SEISMIC STUDIES OF CENTRAL ASIA: SOME CHARACTERISTICS OF EARTHQUAKE MECHANISM AND SEISMIC WAVE VELOCITY STRUCTURE BENEATH THE TIBETAN PLATEAU

by

Wang-Ping Chen

B.S., National Taiwan University (June, 1974)

SUBMITTED IN

PARTIAL FULFILLMENT

OF THE REQUIREMENTS FOR THE

DEGREE OF DOCTOR OF PHILOSOPHY

at the

September 1979

Signature of Author.....
Department of Earth and Planetary Sciences, September 1979

Certified by.....
Thesis Supervisor

Accepted by.....
Chairman, Departmental Committee on Graduate Students

SEISMIC STUDIES OF CENTRAL ASIA: SOME CHARACTERISTICS OF EARTHQUAKE MECHANISM AND SEISMIC WAVE VELOCITY STRUCTURE BENEATH THE TIBETAN PLATEAU

by

Wang-Ping Chen

Submitted to the Department of Earth
and Planetary Sciences in September 1979
in partial fulfillment of the
requirements for the degree of
Doctor of Philosophy

ABSTRACT

This thesis consists of three papers on the seismic studies of the continental tectonics of Asia. In the first paper (J. Geophys. Res., 82, 2945-2969, 1977), seismic moments of thirteen major earthquakes, which occurred in central Asia since 1911 to 1967, are calculated from spectral densities of long-period Love and Rayleigh waves. The seismic moments are then used with fault lengths obtained from other seismic and geological data to place bounds on the average displacements and fault widths of the earthquakes. Differences in arrival times between P and pP for some other earthquakes in Asia indicate focal depths of 40 km. For such a layer, the average rate of seismic slip between India and Eurasia is estimated to be about 20 mm/yr from these seismic moments summed in their tensor form.

The other two papers are submitted to the Journal of

Geophysical Research for publication. The crustal thickness of Tibet is constrained to be about 65 to 80 km with a low average shear wave velocity of less than 3.5 km/sec. The uppermost mantle P and S wave velocities are 8.12±0.06 km/sec and 4.8±0.1 km/sec, respectively, but this high velocity layer does not seem to extend to a great depth. The temperature at the Moho beneath Tibet is compatible with being at about 750°C if the temperature beneath the platforms is close to 500°C. Such a temperature could reach or exceed the solidus of the lower crust. From the flow laws of olivine, the mechanical strength of the uppermost mantle with such a temperature would not be more than about 1 kb. Simple one-dimensional heat conduction calculations suggest that the tectonic and volcanic activity of Tibet could be explained by the recovery of the geotherm maintained by a mantle heat flux of about 0.9 HFU at the base of the crust.

The focal depth of the intermediate depth earthquake of September 14, 1976 is determined to be 90±10 km in the uppermost mantle of Tibet with predominantly normal faulting on north-south striking planes. This mechanism is consistent with the active deformation near the surface of Tibet. The occurrence of this earthquake and earthquakes 60 km beneath Hawaii indicates that rapid deformation process could occur at 700-800°C and pressures over 20 kb.

Thesis Supervisor: Peter Molnar
Associate Professor of Earth Sciences

ACKNOWLEDGEMENTS

First of all, I would like to thank my advisor Peter Molnar for his enthusiasm towards Tibet and earth sciences in general which has been a constant source of inspiration throughout the completion of this study.

I am also grateful to T.J. Fitch and J.L. Nabelek for introducing me to their computer programs on seismic moment tensor inversion and body wave synthesis. K. Aki provided much of the author's background on the theoretical aspects of seismology. Discussions with S. Uyeda on plate tectonics in general is greatly appreciated especially because the Japanese edition of his book 'The New View of the Earth' is partially responsible for my involvement in plate tectonics. While Y.B. Tsai initiated my interests in seismology.

P. Farley, J. MacEachern and M. Slavin provided some unique support during my graduate student career. I would like to extend my thanks to other members of the department who provided support on various levels during the course of this research including many of my graduate student colleagues especially to those on the 7th, 5th and 8th floors of the Green Building.

Finally, I would like to express my special gratitude to my family in Taiwan and C.Y. Chen for consistent morale support throughout the years.

TABLE OF CONTENTS

CHAPTER I INTRODUCTION

The following three chapters in this thesis correspond to three papers on the general subject of continental tectonics of Asia. The motivation behind these studies is a better understanding of large-scale active tectonics in continental areas and especially the tectonic processes related to the collision between India and Eurasia about 40 m.y. ago. Many aspects of earthquake seismology are applied as important methods in this study.

In Chapter II, seismic moments of thirteen major earthquakes in central Asia are calculated from spectral densities of long-period Rayleigh and Love waves. The seismic moments allow us to constrain the average slip and fault widths provided that information on fault length is available from other forms of geophysical and geological data, such as field observations and aftershock relocations. The average rate of seismic slip between India and Eurasia is estimated from the seismic moment data which has a time span of about 50 years. This estimate involves slips on many faults with different orientations and the static seismic moment is expressed in its tensor form, corresponding to a double couple source, in order to perform such an estimate. The estimated slip rate is

inversely proportional to the thickness of the layer where earthquakes can occur. This question is briefly investigated by observing the differences in travel times between P and pP to constrain the focal depths of some other earthquakes in Asia. Then the average seismic slip rate is estimated and compared with the total convergence rate of about 50 mm/yr between India and Eurasia.

Much attention has been paid to the Tibetan plateau because of its unique active deformation, conspicuous location and elevation and its controversial (but most important) role in the understanding of the continental collision process.

The seismic velocity structure of the Tibetan plateau is discussed in Chapter III from a combined interpretation of surface wave dispersion, a synthesis of one P_L-phase, refraction profiles and teleseismic S-P travel time residuals for earthquakes in and around Tibet. The result is consistent with the proposal of a double crustal thickness beneath Tibet. But the uppermost mantle P and S wave velocities are fairly high. We further discuss the tectonic implications of these results starting with an estimate of the uppermost mantle temperatures which, in fact, could reach the solidus of the lower crust and cause volcanism. The mechanical strength of the uppermost mantle

is also estimated from flow laws of olivine at the estimated temperatures. Analytical solutions are found for simple one-dimensional heat conduction problems approximating the situation of a thickened crust and these calculations suggest that the tectonic and volcanic activity could be explained by the recovery of the geotherm maintained by a heat flux at the base of the crust. Radioactive heating can be treated separately from the boundary condition with prescribed heat flux. It could also contribute to the rising of the geotherm as a result of a thickened crust if the distribution of radioactive heat producing elements is not concentrated near the surface.

The focal depth and source mechanism of an intermediate depth earthquake in southern Tibet on September 14, 1976 is studied in detail in Chapter IV. With differences in travel time of P, pP and sP phases, shapes of Rayleigh wave spectra and a synthesis of the P phases, the focal depth is constrained to be 90 ± 10 km and is most likely in the Tibetan uppermost mantle. With P wave first motion polarities, an inversion of the amplitudes of the P phases, and synthetic seismograms of these phases, the fault plane solution is constrained to be a predominantly normal faulting with an approximately east-west trending T-axis. The tectonic implications of this event is discussed.

CHAPTER II

SEISMIC MOMENTS OF MAJOR EARTHQUAKES AND THE AVERAGE RATE OF SLIP IN CENTRAL ASIA

Wang-Ping Chen and Peter Molnar

Department of Earth and Planetary Sciences, Massachusetts Institute of Technology
Cambridge, Massachusetts 02139

Abstract. Seismic moments for 12 major earthquakes ($M \geq 7.6$) in central Asia from 1911 to 1967 were calculated from long-period Rayleigh and Love wave spectral densities. With fault lengths estimated from geological field observations of surface faulting, intensity distributions, or master event relocations of aftershocks, the calculated moments place bounds on the average slip and fault widths. The following table summarizes the calculated moments, estimated fault lengths, and inferred possible average displacements.

Earthquake Location	Year	M_o, dyn-cm	Length, km	Slip, m
Kebin, Kirgizia	1911	4.9×10^{27}	180	2.3
Haiyuan, Kansu	1920	3.0×10^{28}	200	10
Ku-long, Kansu	1927	4.3×10^{27}	150	2.4
Fuh-Yun, Sinkiang	1931	8.5×10^{27}	300	1.9
Bihar-Nepal	1934	1.1×10^{28}	130	5.4
Eastern Himalaya	1947	9.8×10^{26}	?	?
Khait, Tajikistan	1949	2.4×10^{27}	70	3.7
Assam, India	1950	4.0×10^{28}	250	6.6
South Tibet	1951	4.6×10^{27}	200	?
Muya, Siberia	1957	1.4×10^{27}	35	4.5
Gobi-Altai, Mongolia	1957	1.3×10^{28}	270	3.2
Mogod, Mongolia	1967	3.8×10^{26}	40	1.0

The inferred average displacements on the faults, in general, agree with field observations, if in some cases rupture zones extend to 40-km depth. Differences in arrival times between P and $_pP$ for some other earthquakes in Asia indicate focal depths of 40 km and support the inference of brittle failure to the same depth. The average strain pattern caused by seismic slip shows a nearly north-south horizontal compression (or shortening), a considerable amount of vertical expansion of the crust (uplift and crustal thickening), and some nearly east-west horizontal extension. For different assumptions about recurrence rates of large and small earthquakes the calculated shortening for a layer 40 km thick is about 20 mm/yr. It is tempting to infer that the remainder of the 50-mm/yr convergence between India and Eurasia occurs as fault creep. As this rate is inversely proportional to the assumed thickness of the layer, given the uncertainties in the estimates of the moments, all of this convergence could occur as seismic slip without fault creep in a layer 40 but not 100 km thick. Similarly, the calculated seismic slip rate seems to be too high for all of the seismic slip to be confined to a thin layer such as the San Andreas fault (~10 km).

Introduction

The current tectonic activity in central Asia is interpreted as a consequence of a continental collision between India and Eurasia [e.g., Dewey and Burke, 1973; Molnar et al., 1973; Molnar and Tapponnier, 1975]. Since the late Eocene, approximately 2000 km of crustal shortening seems to have taken place after the collision between India and Eurasia. Major east-west trending left-lateral strike-slip faults and other major tectonic features in China and Mongolia are revealed by the interpretation of Landsat photographs, fault plane solutions, and the surface deformation during earthquakes. Molnar and Tapponnier [1975] infer that the pattern of deformation is such that a considerable amount of the convergence between India and Asia is absorbed by lateral motion along these strike-slip faults.

In the present study we determined the seismic moments of major earthquakes ($M \geq 7.6$) (Table 1 and Figure 1) in this area since 1911 and calculated the average rate of deformation caused by slip during earthquakes. The seismic moment (M_o) is the fundamental parameter describing static changes in the earth caused by earthquakes. $M_o = \mu A \Delta\bar{u}$, where μ is the rigidity, A is the fault area, and $\Delta\bar{u}$ is the average displacement along the fault [Aki, 1966]. By summing the seismic moments for many earthquakes during the last 100 years we calculate the average seismic slip rate and compare it with the relative convergence rate between India and Eurasia.

Data and Analysis

We collected as many seismograms as we could for earthquakes in central Asia since 1911 with $M \geq 7.6$ (Table 1) and determined their seismic moments from long-period surface wave spectral densities [Aki, 1966]. All the seismograms used in this study for the earthquakes occurring before the installation of the World-Wide Standardized Seismograph

TABLE 1. Major Events in central Asia, 1911-1957

Station	Component	Epicentral Distance, deg	Az, deg	Phase	Period, s	Instrument	Magnification	Corrected Spectral Density,[a] cm-s	Moment, dyn-cm	Source Parameters,[b] deg
		January 3, 1911 23h 25m 45s 42.8°N, 77.3°E (M = 8.4,[c] 8.7[d])								
RIV	NS	102.2	125	R1	100	Wiechert	2.2	10.9	5.0×10^{27}	90, N70E, 45N;
RIV	EW	102.2	125	R1	100	Wiechert	1.5	7.4	3.4×10^{27}	low angle thrust
PAR	EW	50.6	-56	R1	100	Wiechert	6.0	15.5	7.0×10^{27}	
		December 16, 1920 12h 05m 48s 36.62°N, 105.40°E (M = 8.6[d])								
RIV	NS	81.9	143	G1	100	Wiechert	1.1	23.1	2.8×10^{28}	45, N70W, 45S;
RIV	EW	81.9	143	G1	100	Wiechert	1.2	23.0	2.8×10^{28}	oblique thrust
UPP	NS	58.2	-36	G2	100	Wiechert	1.8	33.8	3.5×10^{28}	
		May 22, 1927 22h 32m 42s 38.05°N, 102.37°E (M = 8.0,[c] 8.3[d])								
HOH	NS	65.0	-47	R1	50	Wiechert	4.5	3.1	1.3×10^{27}	45, N60W, 45S;
GTT	NS	62.5	-45	R1	50	Wiechert	5.4	18.5	8.0×10^{27}	oblique thrust
GTT	EW	62.5	-45	R1	50	Wiechert	7.8	6.4	2.8×10^{27}	
LPZ	EW	158.0	-26	G1	100	Wiechert	5.1	11.8	1.2×10^{28}	
		August 10, 1931 21h 18m 40s 46.89°N, 90.06°E (M = 8.0[c], 7.9[d])								
COP	NS	46.7	-49	G2	100	Wiechert	2.1	39.4	1.1×10^{28}	0, N20W, 90;
SFA[e]		84.5	-13	G2	100	Milne-Shaw[e]	4[e]	31.5[e]	9.7×10^{27}	strike-slip
UPP	NS	42.6	-45	G2	100	Wiechert	1.4	24.5	5.8×10^{27}	
		January 15, 1934 08h 43m 18s 27.55°N, 87.09°E (M = 8.3,[c] 8.4d)								
RAV	NS	62.3	-47	R1	50	Wiechert	3.9	40.3	1.7×10^{28}	90, EW, 20N;
RIV	NS	85.9	131	G1	100	Wiechert	1.3	14.7	6.8×10^{27}	low angle thrust
RIV	EW	85.9	131	G1	100	Wiechert	1.8	29.4	1.4×10^{28}	
VIC[f]		100.0	20	R2	100	Milne-Shaw[f]	4	0.059[g]	9.8×10^{27}	
SJP[e]		127.9	-33	G3	100	Wenner[e]	9.4[e]	8.3[e]	8.2×10^{27}	

TABLE 1. (continued)

Station	Component	Epicentral Distance, deg	Az, deg	Phase	Period, s	Instrument	Magnification	Corrected Spectral Density,[a] cm-s	Moment, dyn-cm	Source Parameters,[b] deg
		July 29, 1947	13h 43m 22s	28.63°N, 93.73°E	(M = 7.7,[c] 7.9[d])					
STU	NS	65.7	-46	R1	50	Wiechert	4.5	5.2	1.8×10^{27}	90, EW, 10N;
RIV	NS	82.4	135	R1	100	Wiechert	1.2	1.7	1.3×10^{27}	low angle thrust
RIV	EW	82.4	135	R1	100	Wiechert	1.2	5.3	4.1×10^{27}	
PAS	Z	110.3	28	R1	100	1-90	21.8	0.66	3.2×10^{26}	
PAS	EW	110.3	28	G1	100	1-90	21.8	0.34	3.0×10^{26}	
		July 10, 1949	03h 53m 36s	39.27°N, 70.59°E	(M = 7.6[c])					
UPP	EW	38.8	-40	R1	50	Wiechert	6.3	8.2	1.3×10^{28}	90, EW, 45S;
PAS	Z	106.4	8	R1	100	1-90	21.8	1.7	4.4×10^{26}	thrust
		August 15, 1950	14h 09m 30s	28.38°N, 96.76°E	(M = 8.6,[c] 8.7[d])					
CHI[e]		109.8	3	G3	100	McComb-Romberg[e]	3.4	59.8[e]	3.7×10^{28} (2.0×10^{29}[h])	
PAS	Z	109.3	30	R3	250	1-90	2.3	115.	5.9×10^{28} (1.4×10^{29})	175, N25W, 55E; nearly strike-slip
PAS	Z	109.3	30	R3	200	1-90	4.5	107.	4.5×10^{28} (1.0×10^{29})	(depth is 30 km)
PAS	Z	109.3	30	R3	150	1-90	9.0	87.	3.3×10^{28} (6.4×10^{28})	
PAS	Z	109.3	30	R4	250	1-90	2.3	115.	5.9×10^{28} (1.4×10^{29})	
PAS	Z	109.3	30	R4	200	1-90	4.5	63.	2.7×10^{28} (6.0×10^{28})	
PAS	Z	109.3	30	R4	150	1-90	9.0	52.	2.0×10^{28} (3.8×10^{28})	
PAS	Z	109.3	30	R5	250	1-90	2.3	124.	6.3×10^{28} (1.5×10^{29})	
PAS	Z	109.3	30	R5	200	1-90	4.5	163.	6.9×10^{28} (1.6×10^{29})	
PAS	Z	109.3	30	R5	150	1-90	9.0	57.	2.2×10^{28} (4.2×10^{28})	
TKY[i]	NS	37	68	G1	200	Omori		30.	7.2×10^{27} (4.0×10^{28})	
TKY	NS	37	68	G1	150	Omori		35.	7.7×10^{27} (3.9×10^{28})	
TKY	NS	37	68	G1	100	Omori		46.	8.7×10^{27} (3.6×10^{28})	

TABLE 1. (continued)

Station	Component	Epicentral Distance, deg	Az, deg	Phase	Period, s	Instrument	Magnification	Corrected Spectral Density,[a] cm-s	Moment, dyn-cm	Source Parameters,[b] deg
		November 18, 1951		09h 35m 47s		30.98°N, 91.49°E	(M = 8.0,[c] 7.9[d])			
RAV	NS	62.5	-48	R1	50	Wiechert	1.9	52.0	2.3×10^{28}	-135, N67W, 45N;
RIV	NS	85.7	134	G1	100	Wiechert	1.2	6.5	7.2×10^{27}	normal and strike-
RIV	EW	85.7	134	G1	100	Wiechert	1.0	8.5	9.4×10^{27}	slip
COP	EW	59.0	-40	R1	50	Wiechert	5.7	2.1	9.4×10^{26}	
PAS	Z	109.7	25	R1	100	1-90	21.8	2.0	8.5×10^{26}	
PAS	EW	109.7	25	G1	100	1-90	21.8	8.7	2.8×10^{27}	
PAS	EW	109.7	25	G3	100	1-90	21.8	14.5	4.6×10^{27}	
PAS	NS	109.7	25	G3	100	1-90	21.8	42.3	1.3×10^{28}	
		June 27,1957		00h 09m 28s		56.20°N, 116.59°E	(M = 7.9[j])			
STU	NS	58.6	-48	R1	50	Wiechert	1.5	1.3	9.1×10^{26}	-34, N119E, 62S;
UPP	NS	47.1	-36	R1	50	Wiechert	7.1	9.6	6.5×10^{27}	oblique normal
PAS	NS	78.4	43	G2	100	30-90	440	4.1	8.3×10^{26}	
PAS	NS	78.4	43	G3	100	30-90	440	4.0	8.1×10^{26}	
		December 4, 1957		03h 37m 45s		45.31°N, 99.21°E	(M = 8.3[j])			
UPP	EW	48.2	-42	R1	100	Wiechert	2.3	10.4	1.2×10^{28}	42, N74W, 42S;
STU	NS	57.8	-51	R1	100	Wiechert	0.3	6.1	6.3×10^{27}	strike-slip
PAS	Z	93.4	30	R4	250	30-90	36.	54.7	2.2×10^{28}	and thrust
PAS	Z	93.4	30	R4	200	30-90	83.	37.8	1.2×10^{28}	
PAS	Z	93.4	30	R5	250	30-90	36.	48.4	1.9×10^{28}	
PAS	Z	93.4	30	R5	200	30-90	83.	30.9	1.0×10^{28}	
PAS	Z	93.4	30	R6	250	30-90	36.	49.5	1.9×10^{28}	
PAS	Z	93.4	30	R6	200	30-90	83.	34.6	1.1×10^{28}	

[a] Values are horizontal displacement spectral densities for G waves, or vertical displacement spectral densities for R waves if using z-component; horizontal displacement spectral densities otherwise. All are normalized for geometrical spreading and attenuation to the source.

[b] The source parameters are the slip angle, the strike and the dip, respectively. Source depth is fixed at 25 km except where otherwise noted.

[c] Value is from Gutenburg and Richter [1954].

[d] Value is from Richter [1958].

[e] Information is from Brune and Engen [1969], and the spectral density is at $\Delta = 90°$ (U_z for R wave).

[f] Information is from Brune and King [1967], and the ground amplitude is at $\Delta = 90°$ (U_z for R waves).

[g] This value is the absolute ground amplitude in cm.

[h] The values in parentheses are calculated for a pure thrust fault striking N81°E, dipping 12°N.

[i] Data for this station are from Ben-Menahem et al. [1974].

[j] Value is from Duda [1965].

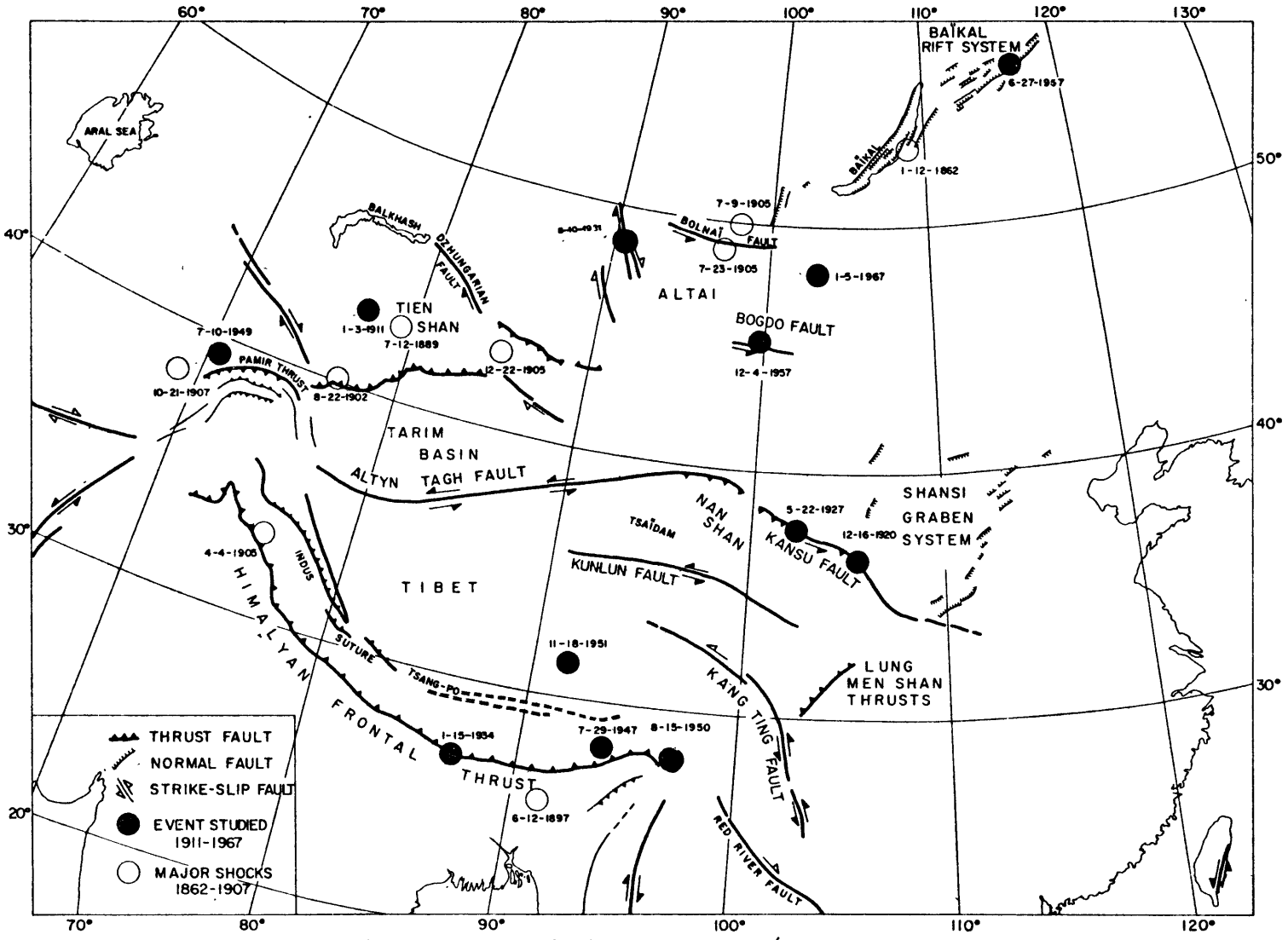

Fig. 1. Map showing major recent tectonic features of Asia (adapted from Molnar and Tapponnier [1975]), events studied from 1911 to 1967, and major shocks from 1862 to 1907.

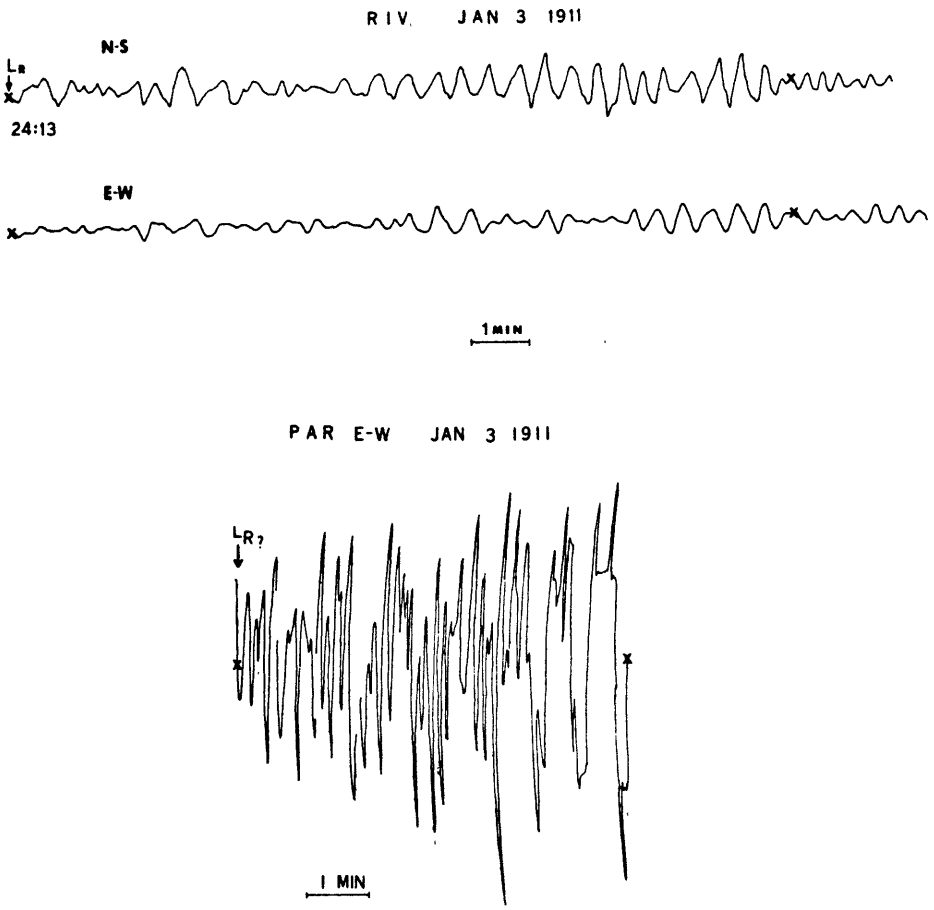

Fig. 2a. Seismograms of Kebin event of 1911, Riverview, Australia, and Paris. Sections between crosses are digitized and used to calculate the spectral densities.

Network (WWSSN) are shown in Figures 2a to 2i. Surface waves with periods up to 60 s are clearly recorded in all cases. We digitized the seismograms, corrected them for the curvature of the trace due to a stylus of finite length, and calculated spectral densities. In general, we used the average spectral density over the period range of 90 to 110 s. Whenever clear signals with periods much longer than 100 s were recorded, particularly for very long paths (e.g., R_2 or G_2), we used the spectral densities at the longer periods. If, on the other hand, signals with periods of 100 s were not directly visible on the seismogram, we used spectral densities only for periods of 50 s; however, in this case spectral densities were used only for stations with relatively simple paths which do not cross continental margins or the heterogeneous structure that exists in much of Asia. We used Love waves (G_2 and G_3) with periods of 200 s recorded by long-period seismographs of the WWSSN to study the Mogod, Mongolia, earthquake of January 5, 1967.

Fault plane solutions were determined from initial motions of P waves or from geologic field observations and macroseismic data or otherwise were inferred from well-determined fault plane solutions of other nearby recent events that presumably occur on the same tectonic features. The seismic moments were then calculated, by assuming a double-couple force configuration and a steplike time function, from the spectral densities by using the tables constructed by Ben-Menahem et al. [1970]. We then took for the seismic moment the geometric average of the different estimates.

Fault lengths were estimated from surface breaks observed in the field, intensity distributions, or master event relocations of aftershocks. The main shock was used as a master event, and station residuals from the master event were subtracted from the arrival times of the aftershocks to calculate the new locations of the aftershocks. Stations not used to locate the main shock were not used to relocate the aftershocks. We used the arrival times listed in the Bulletin of the International Seismological Summary (ISS). We arbitrarily assigned an uncertainty of 2 s for each of the arrival times and used a program written by B. Julian, in which arrival times from particular stations are assigned weights depending on their calculated residuals. Focal depths were restrained to 15 km, as in general there were no nearby stations to constrain the depths. For most events, calculated uncertainties were less for the master event epicenters than for the regular relocations, and we estimate that in general the relative relocations were no more uncertain than 25 km. Sometimes observations of relative displacements on faults were available from field

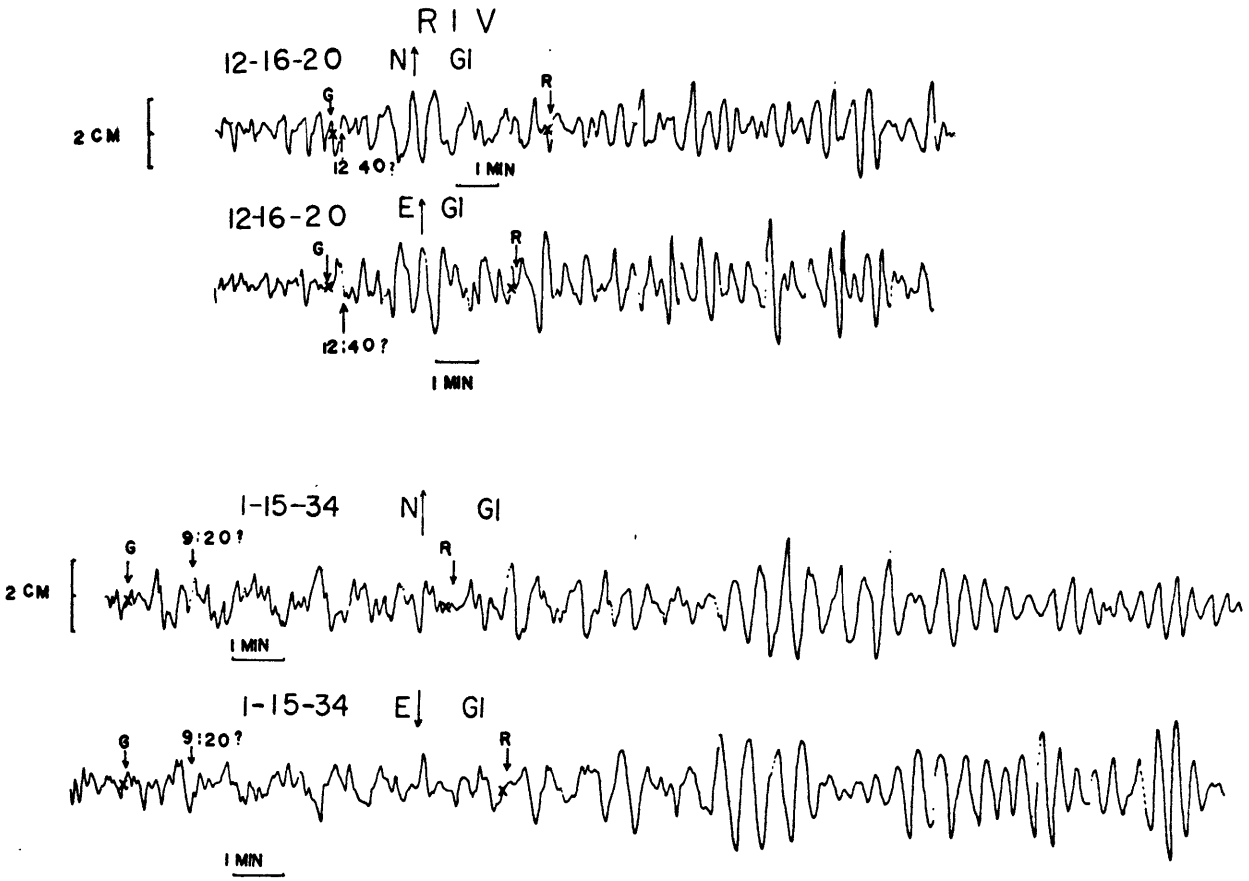

Fig. 2b. Seismograms of Riverview.

studies of the earthquakes. In such cases we used the estimates of moment, fault length, and displacement to infer the fault width.

The principal sources of the uncertainty in the estimation of the seismic moments are (1) the assumed fault plane solutions, (2) the measurements of the surface wave spectral densities, and (3) the assumption of an appropriate stratified earth model or the assumption of the time function of the source in the theoretical calculations. For several cases we explored different fault plane solutions and found that the particular choice did not matter very much. Only for gross errors could this make the calculated moment in error by as much as a factor of 2. Moreover, the uncertainty in the average value from several different stations is likely to be correspondingly less than that for estimates from one station.

Errors in the measured spectral densities arise from a possibly inaccurate knowledge of the instrument responses and from imprecise analog to digital conversion especially for low signal-to-noise ratios. The uncertainty contributed by the instrument response is difficult to estimate but in most cases probably is much less than a factor of 2. To minimize the errors in digitizing, digitized seismograms were plotted and overlain on original seismograms for comparison. When traces were written by pens with finite lengths, after the curvature of the trace was removed, the seismograms again were plotted to be sure that the signal was not distorted. As was mentioned above, only signals for which long-period surface waves were visible to the eye were used. This minimized the possibility of Fourier analyzing only noise or nonlinearly distorted signals.

No correction for the finiteness of the sources was made. For a uniform slip with constant rupture velocity v ($\sim$3.5 km/s) along a long fault the amplitude spectrum is multiplied by an azimuthally dependent factor $\sin X/X$, where

$$X = L\omega(1/v - \cos\theta/c)/2$$

Here L is the fault length, θ is the azimuth between the fault strike and the path to the station, and C is the phase velocity [e.g., Ben-Menahem, 1961]. Only for a limited range of azimuths and only for the largest earthquakes will the spectral density be affected significantly by the finiteness of the sources. For the longest faults, periods much longer than 100 s were generally used. Moreover, for most events the azimuthal coverage is broad enough that the finiteness of the source will have little effect on the average moment. Possibly erroneous earth models and the attenuation factors given by Ben-Menahem et al. [1970] are likely to be less important.

The overall uncertainty of the estimates of the seismic moments varies from event to event and is less for the more recent events than for the older events. In extreme cases,

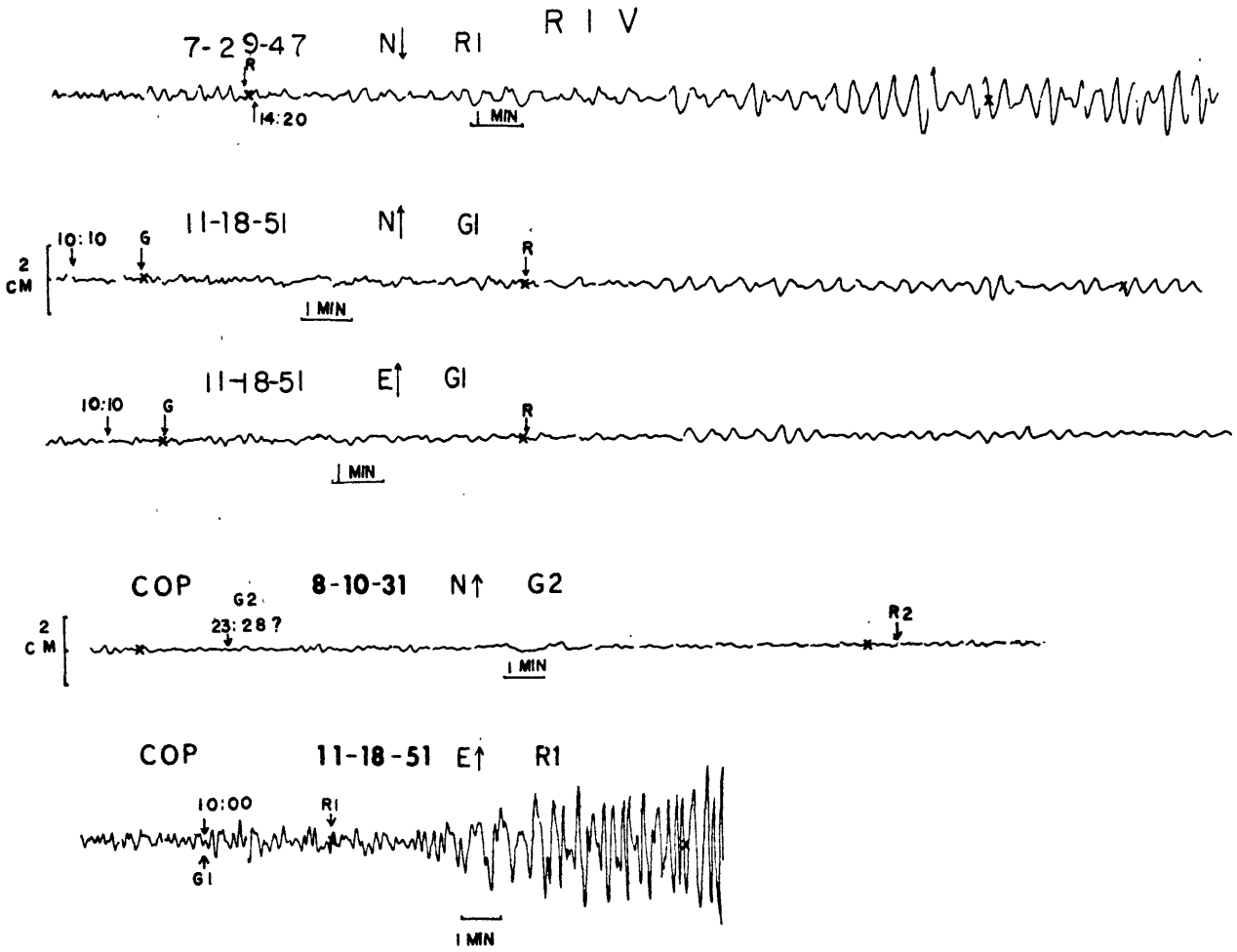

Fig. 2c. Seismograms of Riverview and Copenhagen.

estimates from individual stations may be in error by as much as a factor of 3 or 4. As estimates from several stations and at different periods are generally within this range of each other, the average moment should be more precise. Although for some earthquakes the average estimate may still be in error by this factor, for most cases and in particular for the largest events, we consider the estimates to be precise to within a factor of 2.

Unless there is some gross systematic error in the calculations or assumptions (such as an incorrect fault plane solution), we think that the estimates are accurate to this factor also.

Results for Individual Earthquakes

In this section we describe briefly each earthquake and the assumed fault plane solutions. We then give the average slip based on the calculated moment and inferred fault length, and for an arbitrarily chosen, but reasonable fault width.

Event of January 3, 1911, in Kebin, Kirgizia, USSR (42.8°N, 77.3°E). The geological effects of the Kebin event in the Tien Shan were studied in the field both immediately after the earthquake [Bogdanovich et al., 1914] and more recently [Kuchai, 1969; Shebalin, 1972]. Bogdanovich et al. [1914] observed a clear fault scarp showing thrust sense of motion with vertical displacement of about 4 m near 42.83°N, 77.35°E (Figure 3). This appears to be the maximum displacement that they observed along a zone of destruction, with segments of surface breaks and landslides, trending east-west for about 200 km. Shebalin [1972] inferred a nearly east-west trending fault about 180 km long from the distribution of the maximum intensity (X) isoseismal.

Two clear recordings of Rayleigh waves (Figure 2a) lie on paths in nearly opposite directions from the source. From the measured spectral densities and a fault plane solution inferred from solutions of more recent events [Molnar et al., 1973] the seismic moment is estimated to be 4.9×10^{27} dyn-cm (Table 1), which corresponds to 2.3 m of average slip on a 180 x 40 km^2 fault. In comparison with the 4-m maximum vertical displacement observed in the field [Bogdanovich et al., 1914] this value is reasonable.

Event of December 16, 1920, in Haiyuan, Kansu (36.62°N, 105.40°E). This was one of the most catastrophic events in history. After their expedition, Close and McCormick [1922] described the epicentral zone as 'where the mountains walked'. Landslides accompanying the

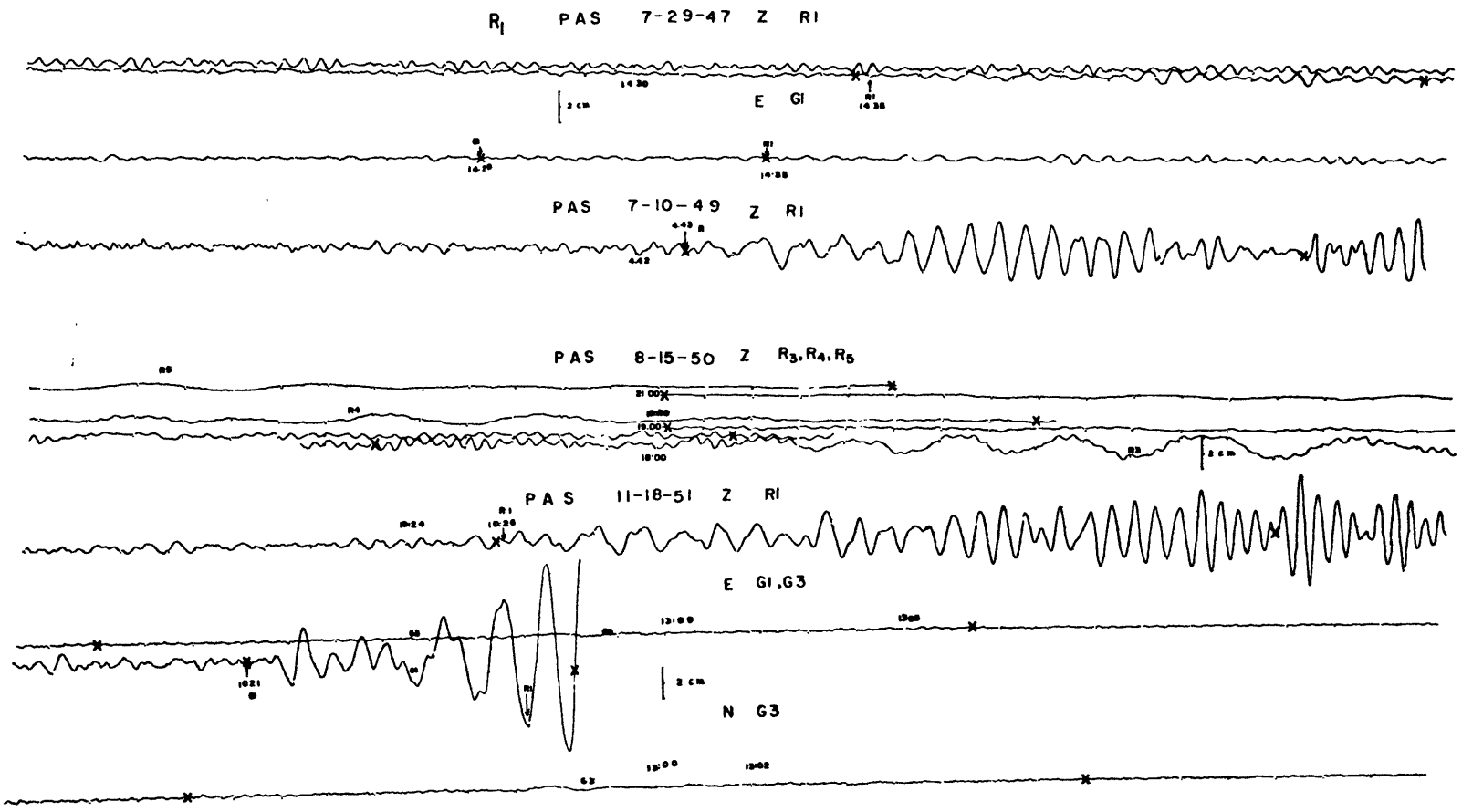

Fig. 2d. Seismograms of Pasadena, California.

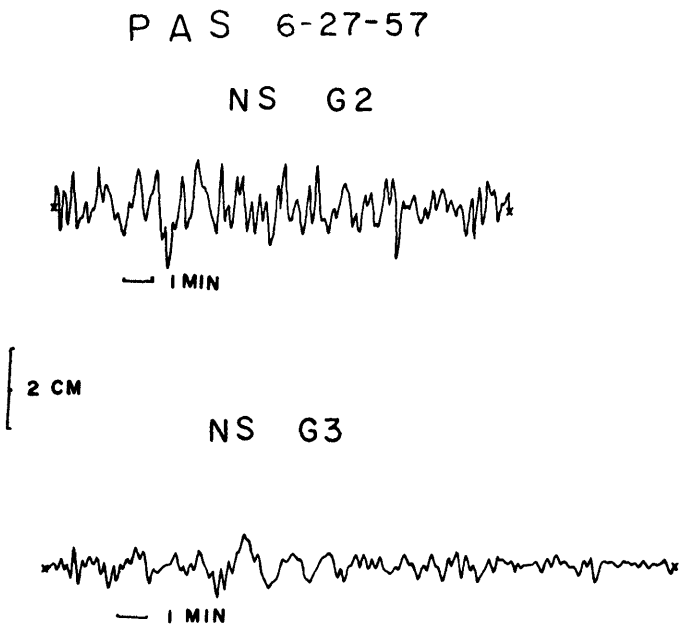

Fig. 2e. Seismograms of Pasadena, California.

shock were reported to have displaced superficial features such as roads and houses up to 1 mi (1.6 km) without apparent damage. Avalanches in an area of 160 x 480 km^2 caused 2 x 10^5 reported deaths on the loess plateau. The maximum intensity reached XI to XII, partly due to unusual surficial conditions [Seismological Brigade of Lanzhou et al., 1976].

Only a few aftershocks were recorded at a small number of stations, and they cannot be relocated accurately. Recent resurveys [Seismological Brigade of Lanzhou et al., 1976] indicate a surface rupture 200 km long with a strike of N50° to 70°W. Some vertical displacement near the epicenter was observed as was left-lateral horizontal displacement, which is consistent with the P wave first motion recorded in Tokyo.

We obtained three seismograms with recordings of long-period surface waves from this event (Table 1 and Figures 2b and 2i) but unfortunately with nearly the same azimuths. The relatively large excitation of Love wave is consistent with a mechanism with a large component of horizontal displacement. If a fault plane striking N70°W is assumed and there is half each of horizontal and vertical motion, the calculated seismic moments for dips of 45° and 90° differed by only 10%. By using the 45° dipping plane the seismic moment is determined to be M_o = 3.0 x 10^{28} dyn-cm, which corresponds to an average slip of 10 m (about 7 m horizontal movement) for a 200 x 50 km^2 fault.

Event of May 22, 1927, in Ku-long, Kansu (38.05°N, 102.37°E). This event occurred approximately 300 km to the northwest of the 1920 Haiyuan shock. The area of destruction forms an ellipse elongated in the northwest direction with a length of 600 km, but by comparing the intensity distribution with that of the Haiyuan shock, we estimated the rupture length to be about 140 km.

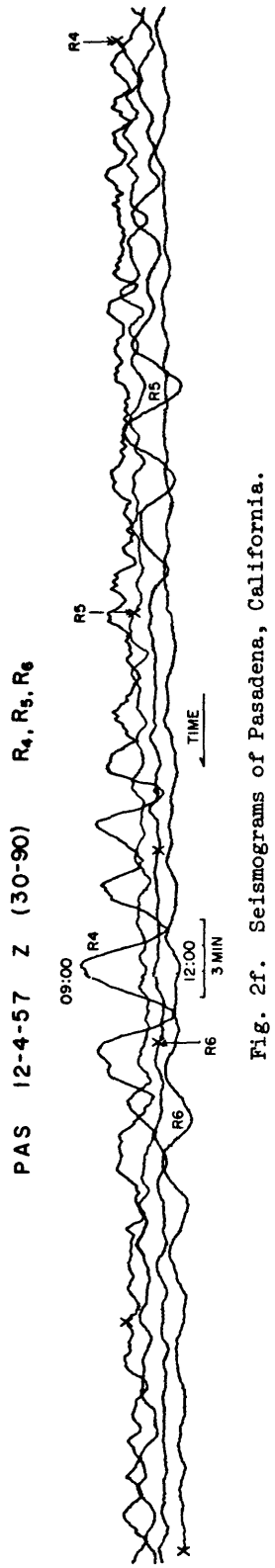

Fig. 2f. Seismograms of Pasadena, California.

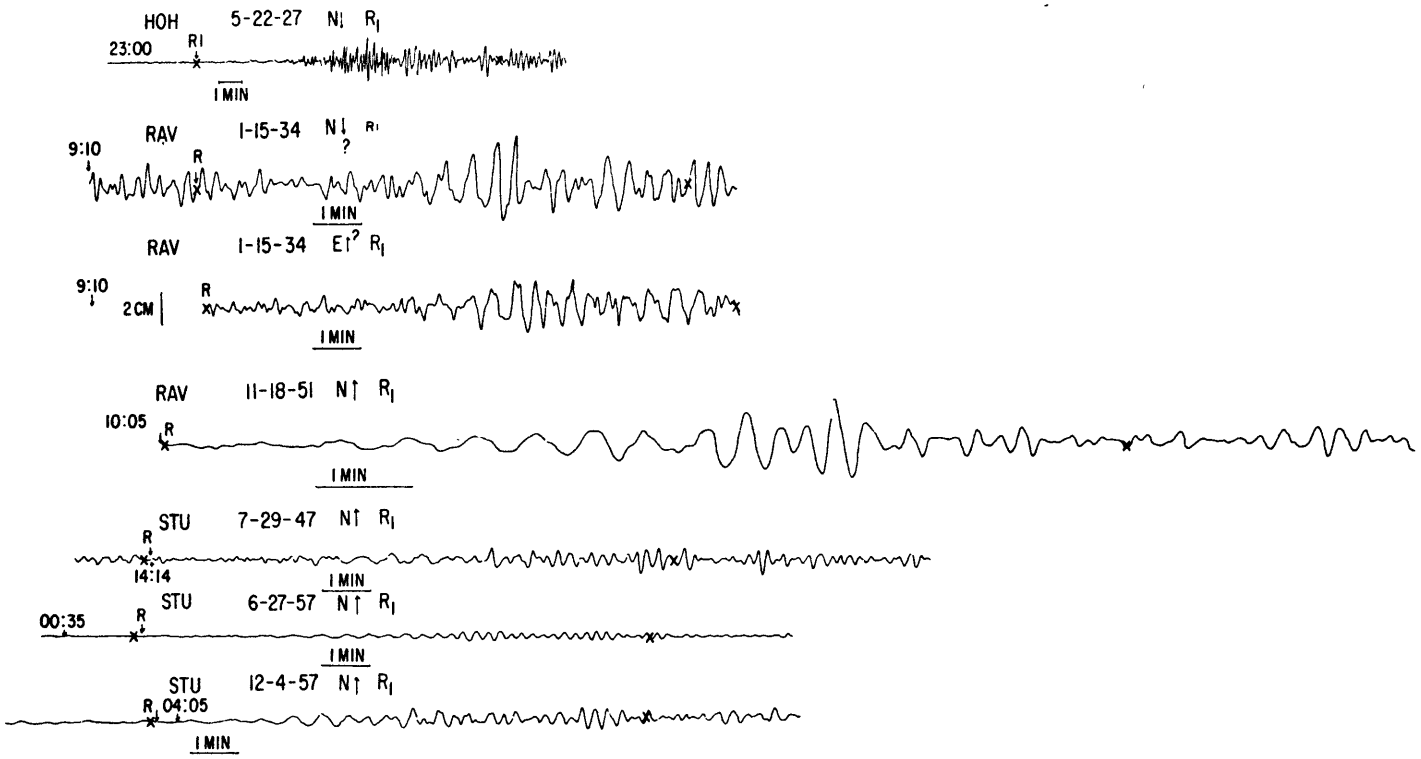

Fig. 2g. Seismograms of Stuttgart, Hohenheim, and Ravensburg, Germany.

Various types of surface ruptures formed. One 10-km-long rupture shows a vertical displacement of 3 to 5 m with the north side down [Seismological Committee of the Academia Sinica, 1956]. In the resurvey report of the Haiyuan event [Seismological Brigade of Lanzhou et al., 1976] this shock was considered to be on the same tectonic feature as the Haiyuan event. Thus we infer that the fuault plane solution for this event is nearly the same as that for the 1920 Haiyuan earthquake.

The moment estimated from recordings at three stations (Figures 2g and 2h) is 4.3 x 10^{27} dyn-cm, which corresponds to an average slip of 2.4 m for a 150 x 40 km^2 fault.

Event of August 10, 1931, in Fuh-Yun, Sinkiang (46.89°N, 90.06°E). Little information is available for this earthquake, probably because of the low population density near the epicentral zone. The Seismological Committee of the Academia Sinica [1956] described high intensities (XI) and a surface rupture 300 km long extending approximately north-south. The epicenter lies near a north-northwest striking fault that is inferred from an interpretation of Landsat photographs to be mostly strike-slip [Molnar and Tapponnier, 1975]. This inference is consistent with the fact that surface wave observations show larger Love waves than Rayleigh waves (Table 1 and Figures 2c and 2i). Among the three stations used, especially large amplitudes for Love waves were recorded at Seven Falls (SFA) [Brune and Engen, 1969], to which the path makes an azimuth of about 8° from the assumed fault strike.

With station azimuth coverage from three stations of only about 40°, the moment is determined to be 8.5 x 10^{27} dyn-cm, which corresponds to an average displacement of 1.9 m for a 50 x 300 km^2 fault or 3.8 m for a 25 x 300 km^2 fault.

Event of January 15, 1934, in Bihar-Nepal (27.55°N, 87.09°E). Isoseismals of maximum intensity X (Mercalli) extended in a west-northwest direction from the epicenter, with a total length of 130 km and a width of 30 km

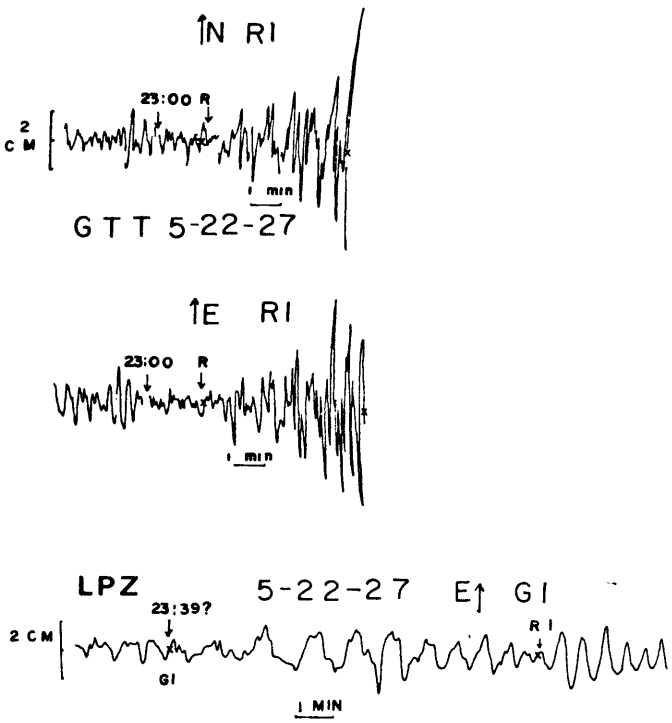

Fig. 2h. Seismograms of Göttingen, Germany, and La Paz (San Calixto), Bolivia.

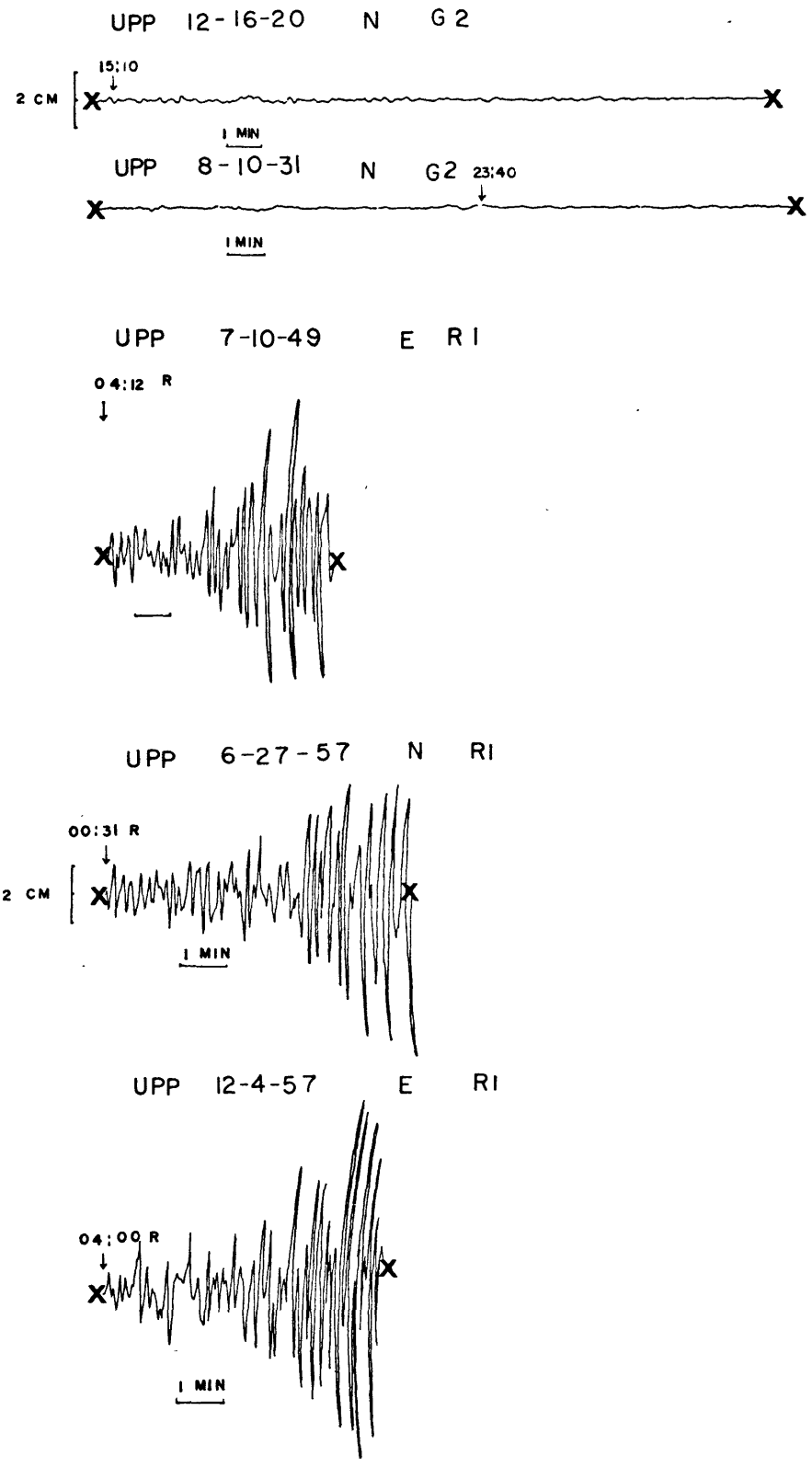

Fig. 2i. Seismograms of Uppsala, Sweden.

[Dunn et al., 1939]. This field survey also showed a 'slump belt' of 300-km length trending in the same direction. Within the belt, tilting or destruction of buildings, emission of sand and water from the ground, and various fissures were widely observed. Dunn et al. [1939] inferred a strike-slip sense of motion along a west-northwest striking fault from the intensity observations. Fault plane solutions of more recent earthquakes in this region, however, show low-angle thrust faulting [e.g., Fitch, 1970; Molnar et al., 1973], and we assume a mechanism of this type.

Note that datum for station Victoria (VIC)

Fig. 3. Fault scarp of the 1911 Kebin earthquake near 42.83°W, 77.33°E looking towards north-northwest (reproduced from Bogdanovich et al. [1914]).

is the amplitude of ground displacement from Brune and King [1967]. The seismic moment from it is evaluated by using another set of tables by Ben-Menahem et al. [1970]. As this amplitude of ground motion depends on the slope of the group velocity dispersion curve explicitly, the structure along the ray path is more important than it is when spectral densities are used. The average seismic moment from five measurements at three stations is 1.1 x 10^{28} dyn-cm, which corresponds to an average slip of 5.4 m for a 130 x 50 km^2 fault.

Event of July 29, 1947, in the eastern Himalaya (28.63°N, 93.73°E). Little information is available for this event, which occurred near the eastern end of the Himalaya, and few aftershocks are reported in the ISS. Thus we cannot estimate the fault dimensions. Fault plane solutions of three more recent earthquakes which occurred within 100 km of this epicenter show east-west trending nearly vertical dipping nodal planes and poorly constrained but shallow dipping nodal planes [Fitch, 1970; Molnar et al., 1973]. We assume shallow angle thrust faulting to the north. The average seismic moment from five measurements at three stations is 9.8 x 10^{26} dyn-cm.

Event of July 10, 1949, in Khait, Tajikistan, USSR (39.27°N, 70.59°E). This event occurred on the Hissaro-Kokhshal fault zone along the border of the southern Tien Shan [e.g., Gubin, 1960, 1967]. Field observations indicated a shallow long source with a considerable amount of vertical motion during the earthquake [Gubin, 1960, 1967]. Isoseismals of maximum intensity (X) extend 65 to 70 km in an east-west direction.

Gubin [1960, 1967] inferred that the faulting was reverse on a nearly vertical plane dipping slightly to the south. Unfortunately, P wave first motions do not uniquely define a single set of nodal planes [Wickens and Hodgson, 1967] but are consistent with this solution. The calculated seismic moment from two stations is not well determined. Its value of 2.4 x 10^{27} dyn-cm corresponds to an average slip of 3.7 m for a 70 x 30 km^2 fault.

Event of August 15, 1950, in Assam, India (28.38°N, 96.76°E). This event was studied extensively by Ben-Menahem et al. [1974], using Rayleigh to Love wave and R_2/R_3 amplitude ratios at Pasadena (PAS), the P/PP amplitude ratio at Tokyo (TKY), and surface wave spectral densities and ground amplitudes at PAS, TKY, and Bergen. They concluded that a fault

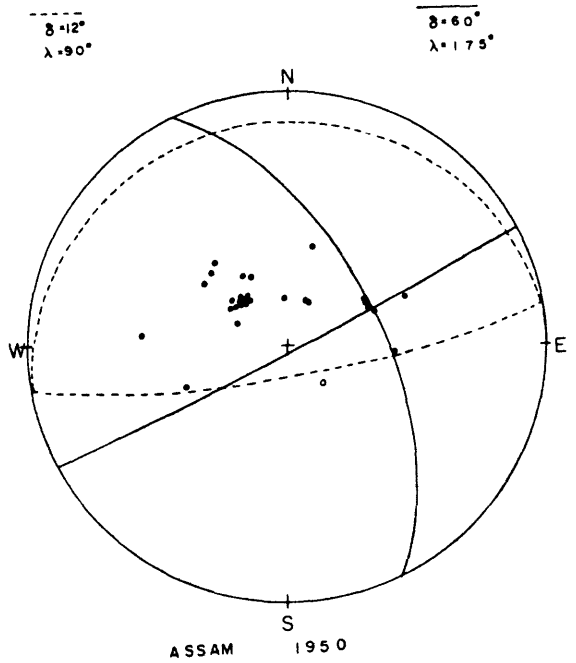

Fig. 4. Fault plane solutions of Assam earthquake of 1950. Lower hemisphere projection of P wave first motions. Open circles indicate dilatation, and solid circles indicate compression. Note that a low-angle thrust (dotted lines) dipping to the north fits the data as well as the strike-slip solution [from Ben-Menahem et al., 1974] (solid lines).

striking N26°W and dipping 60°E with nearly pure strike-slip motion is compatible with all the above observations, as well as with first motions of P waves reported in the ISS, the aftershock distribution, and macroseismic effects.

Using P wave first motions, Tandon [1955] determined a fault plane solution showing normal faulting on an east-west striking plane dipping 75°N. Ben-Menahem et al. [1974] pointed out, however, that three stations (New Delhi, Poona, and Helwan) cited as dilatations in Tandon's study were reported as compressions in the ISS. They determined a fault plane solution shown in Figure 4. A low-angle thrust dipping to the north can explain the P wave first motions equally well (Figure 4) and is similar to fault plane solutions for other earthquakes in this area [e.g., Fitch, 1970; Molnar et al., 1973]. Ben-Menahem et al. [1974] apparently rejected this solution because it disagrees with the Rayleigh/Love wave amplitude ratio at PAS. They also preferred the solution with a large component of strike-slip faulting because of the distribution of aftershocks.

Using the main shock as a master event, we relocated about 100 aftershocks relative to it. We think that the uncertainty of the relocation for about 75 of them is less than 25 km, yet the epicenters scatter over a wide area (Figure 5). This scatter remains when only events occurring within 1 day of the main shock are considered and is too large for all of the aftershocks to lie on a single fault plane. The majority of the aftershocks lie beneath the Himalaya in a zone approximately 250 km long and 100 km wide. A cluster to the southeast suggests a fault zone oriented north-northwest and opens the possibility of a source involving more than one plane. A complicated source involving more than one plane is implied by the distribution and fault plane solutions of aftershocks of the 1964 Alaskan earthquake [Stauder and Bollinger, 1966]. The main shock near Prince William Sound appears to be at the junction of a low-angle thrust extending southwest to Kodiak Island and a hinge fault extending east-southeast. A speculative analogy for the Assam event would be a combination of the two possible solutions shown in Figure 4. Such motion would involve both the underthrusting of the Indian Plate beneath the Himalaya along a shallow dipping fault and northward motion of the Indian plate past material east of it along a right-lateral strike-slip fault.

It turns out that the Rayleigh/Love wave amplitude ratio at PAS is very sensitive to small changes in the assumed fault strike and slip angle. A combination of strike-slip and underthrusting can fit this ratio at PAS with only slightly different parameters for the strike-slip component from those assumed by Ben-Menahem et al. [1974]. It seems that this ratio at PAS is probably not a very strong constraint on the source mechanism of this earthquake.

We calculated seismic moments by assuming both a low-angle thrust and Ben-Menahem et al.'s [1974] strike-slip fault plane solution. In general, the low-angle thrust model gives a moment twice as large as that for the strike-slip faulting, but both are much smaller than the value given by Ben-Menahem et al. [1974]. Ben-Menahem et al. [1974] reported a seismic moment of 2.5×10^{29} dyn-cm. (They give $U_o dS = 7 \times 10^{18}$ cm^3 and $\mu U_o dS = 2.5 \times 10^{30}$ dyn-cm, which are obviously misprints on page 276 of their study.) Using the spectral density data at TKY (the only spectral density data that they reported with units) and their fault plane solution, we obtained a seismic moment of 7.8×10^{27} dyn-cm. If we assume the same fault plane solution and use the data from PAS and Chicago (CHI), the average seismic moment is 4.0×10^{28} dyn-cm, which corresponds to an average slip of 6.6 m for a 250 x 80 km^2 fault. For the low-angle thrust fault the seismic moment is estimated to be 9.5×10^{28} dyn-cm, which corresponds to about a 16 m average slip on a 250 x 80 km^2 fault.

Event of November 18, 1951, in southern Tibet (30.98°N, 91.49°E). Although apparently little is known about this event, it was assigned a large magnitude (M = 8) [Richter, 1958]. Relocation of 10 aftershocks with respect to the main shock suggests a west-northwest trending fault of about 150 to 200 km length (Figure 6). Tapponnier and Molnar [1977] inferred that the regional tectonic pattern near the epicentral zone is mainly east-west trending strike-slip faulting and north-south trending normal faulting. Thus we assumed a fault plane solution with a combina-

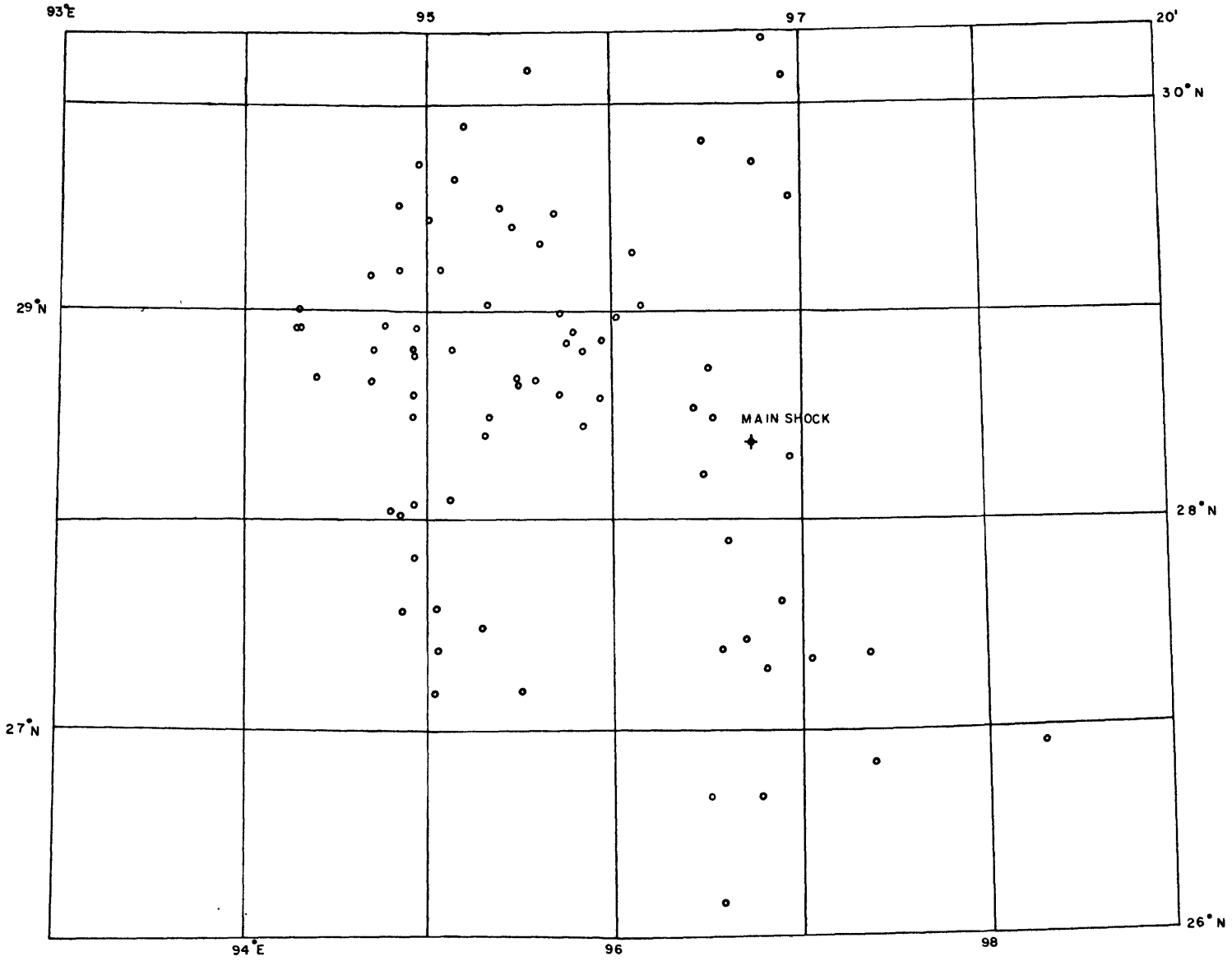

Fig. 5. Aftershock distribution of 1950 Assam earthquake.

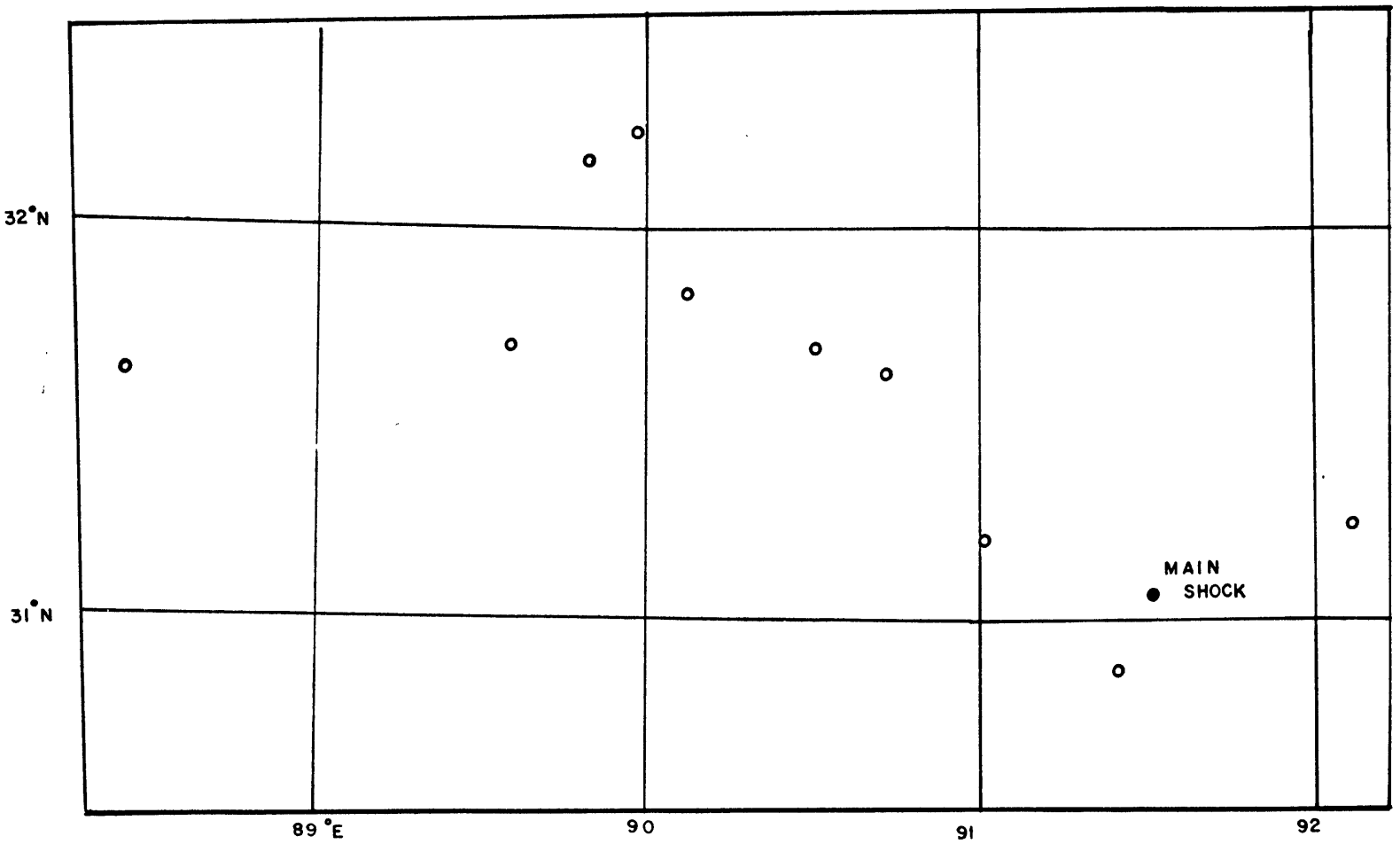

Fig. 6. Aftershock distribution of November 18, 1951, earthquake.

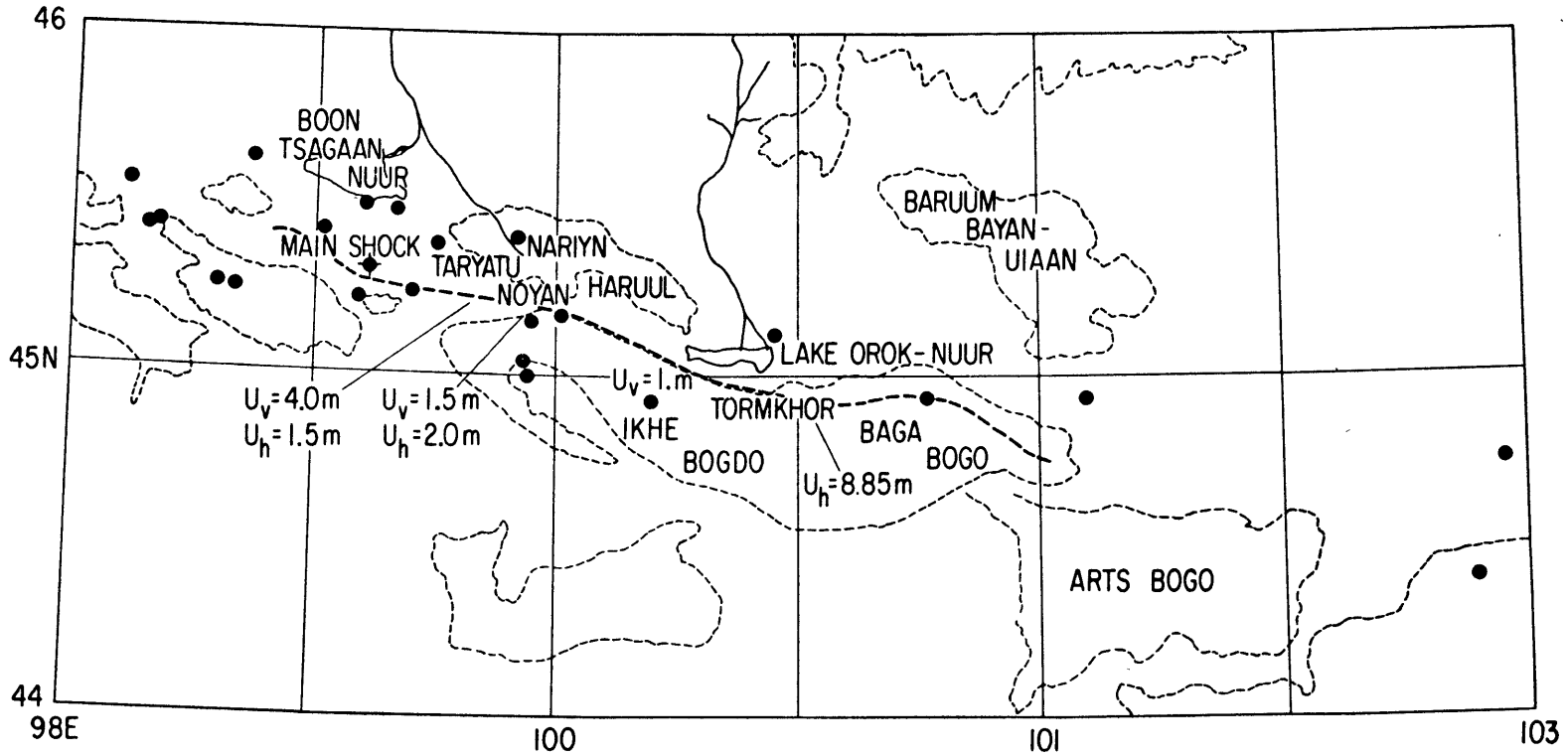

Fig. 7. Map showing fault break observed by Florensov and Solonenko [1963] and aftershocks for the Gobi-Altai earthquake of 1957. U_h is the horizontal displacement, and U_v is the vertical displacement in meters. The dotted contour lines show 1524-m (5000 ft) contour.

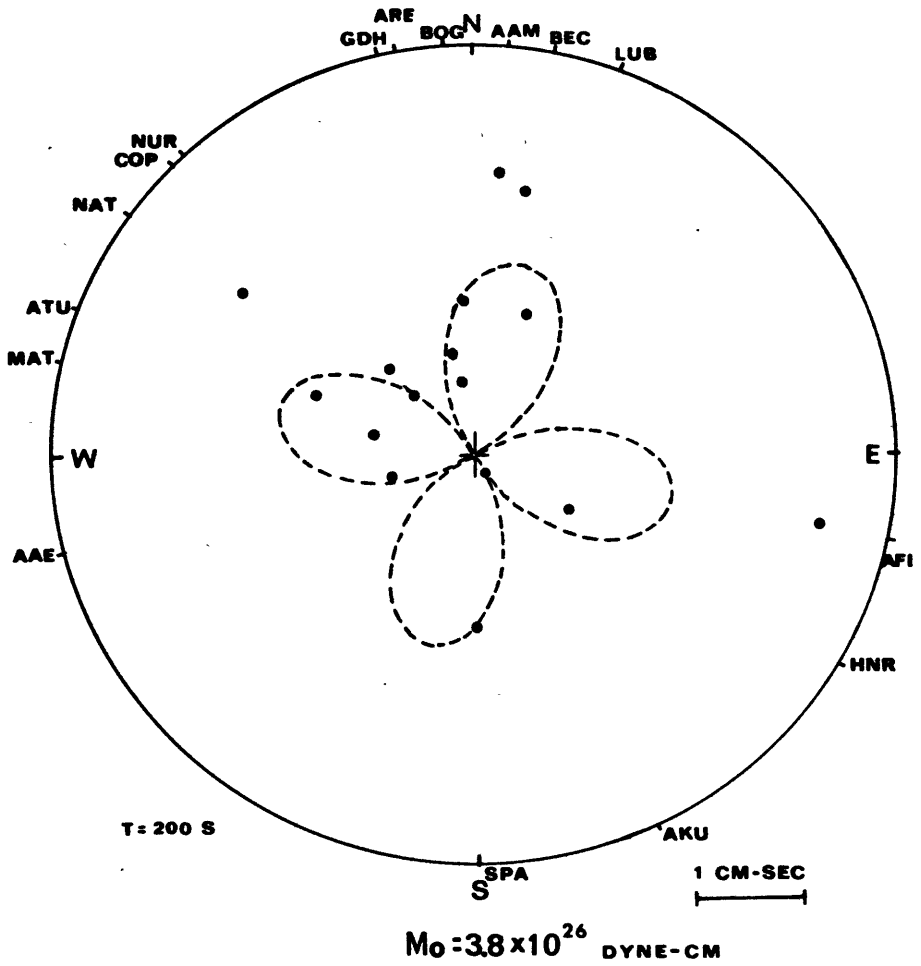

Fig. 8. Observed and calculated spectral densities of G_2 and G_3 waves normalized to the source for the Mogod earthquake. Theoretical spectral density is calculated for the average moment 3.8 x 10^{26}dyn-cm.

tion of right-lateral strike-slip and normal faulting on a plane dipping 45°N with the strike constrained by the aftershock distribution. The seismic moment calculated from eight measurements at four stations is 4.6 x 10^{27} dyn-cm.

Event of June 27, 1957, in Muya, Siberia (56.20°N, 116.59°E). The Muya earthquake was one of the largest known events in the Baikal Rift system. Field studies [Solonenko, 1965; Solonenko et al., 1966] indicate a component of left-lateral strike-slip faulting (~1.5 m) and primarily normal faulting with as much as 5 to 6 m of dip-slip at one site on a 35-km-long fault. The pattern of deformation is complex, and the average slip might have been less than 5 m. The trend of the zone of surface deformation is nearly east-west. P wave first motion data agree with a solution with normal and left-lateral strike-slip motion on a plane striking east-southeast [Vvedenskaya, 1960; Wickens and Hodgson, 1967].

Clear dispersed wave trains of G_2 and G_3 with periods up to 100s or more are recorded at Pasadena (Figure 2e) and are consistent with the assumed fault azimuth and the existence of strike-slip motion.

The average seismic moment from three stations of 1.4 x 10^{27} dyn-cm corresponds to an average slip of 4.5 m on a 35 x 30 km^2 fault, in reasonable agreement with that from the field observations.

Event of December 4, 1957, in Gobi-Altai, Mongolia (45.31°N, 99.21°E). The 1957 Gobi-Altai event occurred on the Bogdo fault of southern Mongolia. The fault plane solution is quite well constrained (work of L. M. Balakina in the work of Florensov and Solonenko [1963] and shows a combination of overthrust and strike-slip motion. This solution is consistent with the observed surface faulting reported by Florensov and Solonenko [1963] and is summarized in Figure 7. The epicentral zone has a surface break at least 270 km long, and the maximum horizontal displacement reaches 8.85 m at one site. This earthquake also caused relative motion on other nearby (as far as 30 km away) tectonic features (e.g., the Tormkhon overthrust). Relocated epicenters of the 23 largest aftershocks relative to the main shock clearly follow the general trend of the surface break, and most of the aftershocks cluster in a zone of 300 km long (Figure 7).

Ben-Menahem and Toksöz [1962] studied this event, using the Rayleigh wave directivity at PAS and inferred a fault length of 560 km. Later, Okal [1976] constructed synthetic seismograms of the Love waves at PAS and found

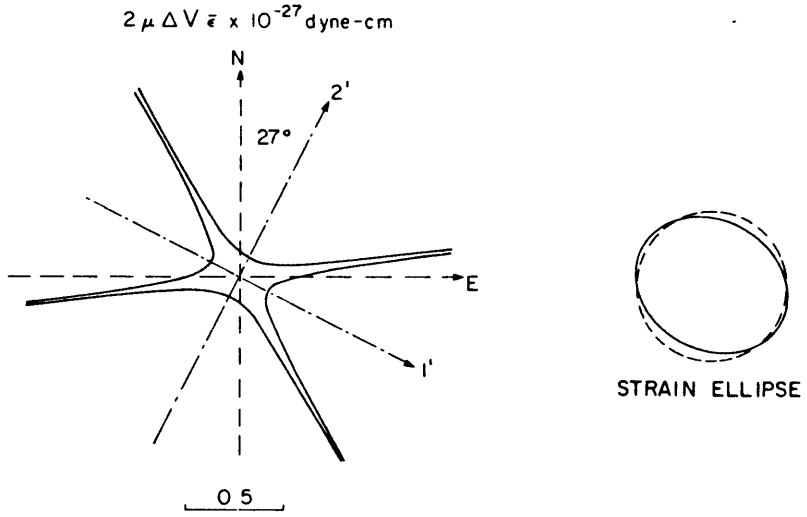

Fig. 9. Horizontal section of the representation quadric of average strain times $2\mu\Delta v$ and strain ellipsoid (highly exaggerated) of the average strain tensor caused by seismic slips from 1911 to 1967. Note that the magnitude of the strain in a given direction is proportional to the reciprocal of the square root of the length of the radius vector r in the drawing of the representation quadric. Equation for the hyperbola intersecting 1'-axis is $37\ X_1'^2 - 85\ X_2'^2 = 1$ (in 10^{27} dyn-cm).

source parameters similar to the fault plane solution from P wave first motion data and that agreed with a fault length of 270 km. These parameters are also consistent with his time domain analysis of Love waves at Palisades and Strasburg and of Rayleigh waves at Pasadena. Our estimate of $M_o = 1.3 \times 10^{28}$ dyn-cm based primarily on recordings of R_4, R_5, and R_6 at Pasadena agrees well with Okal's [1976] estimate ($M_o = 1.8 \times 10^{28}$ dyn-cm).

The average slip calculated from the seismic moment of 1.3×10^{28} dyn-cm is 3.2 m for a 270×50 km^2 source or 6.4 m for a 270×25 km^2 source. The field observations show an average displacement in this range when averaged along the fault [Brune and Allen, 1967].

Event of January 5, 1967, in Mogod, Mongolia (48.15°N, 102.90°E). The Mogod earthquake is the only event used in this study which occurred after the installation of the WWSSN. The fault plane solution given by P wave data is well constrained with nearly pure strike-slip motion on a vertical fault striking north or east [Molnar et al., 1973]. Surface faulting and aftershock epicenters clearly indicate a north-south fault about 40 km in length [Natsag-Yum et al., 1971]. The surface break curves toward the southeast at the south end, where some uplift of the east side was observed. Love waves (mostly G_3) with periods of 200 s recorded on 16 WWSSN stations (Figure 8) were analyzed, and the seismic moment was estimated to be 3.8×10^{26} dyn-cm. Okal [1976] also reported preliminary results on this event, the seismic moment being 3.2×10^{26} dyn-cm. Our estimate of the seismic moment is consistent with about 1 m of average slip, as was observed in the field, on a 40×30 km^2 fault.

Average Rate of Deformation

The seismic moment tensor for the source model with a dipole force acting on a plane cut can conveniently be represented as

$$M_{ij} = M_o(b_i n_j + b_j n_i) \quad i, j = 1, 2, 3 \qquad (1)$$

where M_o is the scalar moment value equal to $\mu A\Delta\bar{u}$ and $\hat{b}$ and $\hat{n}$ are the unit vectors in the direction of slip and normal to the plane of the cut, respectively. The principal axes of M_{ij} are the P, T, and B axes [Gilbert, 1970]. Following this definition, Kostrov [1974] showed the average irrotational strain in a volume due to discrete slips on different cuts within the volume to be

$$\bar{\epsilon}_{ij} = (1/2\mu\Delta V) \sum_{x=1}^{N} M_{ij}^{(x)} \qquad (2)$$

where M_{ij} are summed over all N cuts in the volume and ΔV is the total volume.

When the rate of the change of length due to irrotational strain only in one direction $\hat{\ell}$ is sought, we have

$$\frac{\Delta\ell}{\Delta t} = \left(\frac{1}{2\mu A_p \Delta t}\right)\left(\sum_{x=1}^{N} M_{ij}^{(x)}\right) l_i l_j \qquad (3)$$

where $\Delta V = \ell A_p$ and Δt is the time span during which the seismic slip took place. Because of the symmetry of the seismic moment tensor, the pure rotational strain is ignored in Kostrov's [1974] method. If the orientations of the fault planes involved are randomly distributed throughout the deformed body, however, the rotational strain will cancel and equation (3) gives the total average displacement.

We take the east and north directions as the 1 and 2 axis respectively, and the 3 axis

TABLE 2. Major Events in central Asia 1862-1907

Date	Latitude	Longitude	Location	M	Assumed Source Parameters	Assumed Seismic Moment, dyn-cm
Jan. 12, 1862	53°N	109°E	Proval Bay, Siberia		N60°W, 45°S dipping normal fault	1×10^{27}
July 12, 1889	43°N	79°E	Chilik, Tien-Shan		Same as those for 1911 Kebin event	5×10^{27}
June 12, 1897	26°N	91°E	Assam, Himalayas	8.7	Same as those for 1934 Bihar-Nepal event	4×10^{28}
Aug. 22, 1902	40°N	77°E	Pamir	8.6	Same as those for 1949 Khait event	3×10^{28}
April 4, 1905	33°N	76°E	Kangra, Himalayas	8.6	Same as those for 1934 Bihar-Nepal event	3×10^{28}
July 9, 1905	49°N	99°E	Khangai, Mongolia	8.4	N60°E striking, vertical strike-slip fault	3×10^{28}
July 23, 1905	49°N	98°E	Khangai, Mongolia	8.7	East-west striking vertical strike-slip fault	5×10^{28}
Dec. 22, 1906	43.5°N	85°E	Kashgar, Tien-Shan	8.3	Same as those for 1949 Khait event	5×10^{27}
Oct. 21, 1907	38°N	69°E	Pamir	8.1	Same as those for 1949 Khait event	3×10^{27}

vertically upward. With the assumed fault plane solutions and the seismic moment values summarized in Table 1, the sum of the moment tensors is

$$\sum_{x=1}^{12} M_{ij}^{(x)} = \begin{bmatrix} 1.3 & -4.9 & 3.7 \\ -4.9 & -6.0 & -3.8 \\ 3.7 & -3.8 & 4.8 \end{bmatrix} \times 10^{28} \text{ dyn-cm} \qquad (4)$$

The magnitude of the sum in the direction of 2-axis (north-south horizontal) is 6.0 x 10^{28} dyn-cm.

In our case, the dimensions of the deformed volume in both north-south and east-west directions are about 3000 km (Figure 1). Assuming a thickness of 40 km for the upper part of the lithosphere where brittle deformation can occur, we have an average slip rate due to strain of 15 mm/yr for the time span of 1911 to 1967 or 13 mm/yr for 1911 to 1976 in comparison with the relative convergence rate of about 50 mm/yr between Indian and Eurasian plates [Le Pichon, 1968; Minster et al., 1974].

Diagonalizing $M_{ij}^{(x)}$, we obtain

$$\bar{\varepsilon}_{ij}(2\mu\Delta V) = \begin{bmatrix} 9.4 & 0 & 0 \\ 0 & -8.8 & 0 \\ 0 & 0 & -0.6 \end{bmatrix} \times 10^{28} \text{ dyn-cm} \qquad (5a)$$

or

$$\bar{\varepsilon}_{ij} = \begin{bmatrix} 4.4 & 0 & 0 \\ 0 & -4.1 & 0 \\ 0 & 0 & -0.3 \end{bmatrix} \times 10^{-7} \qquad (5b)$$

$V = 40 \times 3000 \times 3000 \text{ km}^3$

with the corresponding principal directions shown in Figure 9. The horizontal cross section of the representation quadric (Figure 9) shows that the calculated average strain caused by seismic slip in central Asia is nearly north-south compressional. In addition to uplift and crustal thickening, some east-west extension also exists.

Effect of small earthquakes.. The values calculated here include the contributions of only the largest events. The contribution of smaller events can be estimated by using frequency-magnitude and magnitude-moment relations. If we assume that b = 1 in the frequency-magnitude relation (log N = a - bM) and a magnitude-moment relation,

$$\log M_o = 1.5\, M_s + 16.0 \qquad (6)$$

from Aki [1972] on the basis of the ω^{-1} model of Brune and King [1967] for $M_S \geq 5.0$, the total moment for events with magnitude ranging from 5.0 to 7.6 is about 37% of that for events with magnitudes ranging from 7.6 to 8.7 studied here. By further assuming that for smaller events the magnitude-moment relation has a slope of 1, the total moment for events with magnitudes ranging from 3.0 to 5 is about 5% of that for events with magnitudes from 7.6 to 8.7. These percentages are doubled or halved if b = 1.2 or 0.8, respectively. There is a suggestion that b is somewhat lower in Asia than it is elsewhere [Molnar et al., 1973; Sykes, 1970], so that the effect of smaller

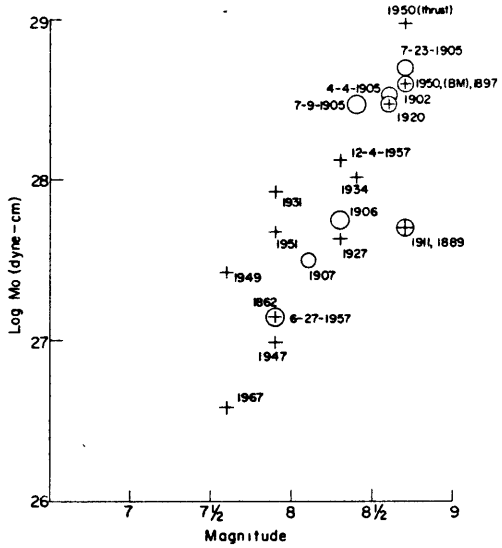

Fig. 10. Magnitudes versus seismic moments for events studied here (pluses). Circles represent assumed seismic moments for events from 1862 to 1907.

earthquakes probably increases the calculated values of ΣM_{ij} or $\bar{\varepsilon}_{ij}$ by only 40% or less.

Effect of incorrect fault plane solutions. The assumed fault plane solutions contribute to the uncertainties in the estimation of slip rate both directly and indirectly through their effect on the estimates of seismic moments. The Assam earthquake of 1950, which has the highest seismic moment of all the events studied (Table 1) and for which the assumed slip vector is nearly horizontal, contributes nearly 50% of the total slip from 1911 to 1967 along the north-south direction. Although the slip vector differs slightly for the two possible fault plane solutions (Table 1) and the corresponding moments differ by a factor of 2, the slip rate in the north-south direction remains essentially unchanged. The calculated vertical and east-west stretching depend very much on which fault plane solution is assumed. If we assume that only shallow angle underthrusting occurred with no component of strike-slip motion, then the vertical expansion is increased by 70%, but there is no calculated east-west stretching. This calculation probably shows the largest possible effect of an erroneous fault plane solution.

Effect of nonstationarity of seismicity. Clearly, the recurrence rate of very large shocks has a large effect on the estimated average slip rate, and perhaps the level of seismicity during the last 66 years is not representative of a longer time average. In fact, Richter [1958] listed seven major shocks in this area between 1897 and 1907, and two others in 1862 and 1889, are clearly comparable in magnitude to those studied here (Figure 1 and Table 2). The two 1905 Mongolian earthquakes were studied by Okal [1977] and moments calculated by him agree well with the displacements and lengths of surface faults observed by A. V. Voznesenskii (cited by Florensov and Solonenko [1963])and more recently by N. A. Florensov, S. D. Hilko, and others. The July

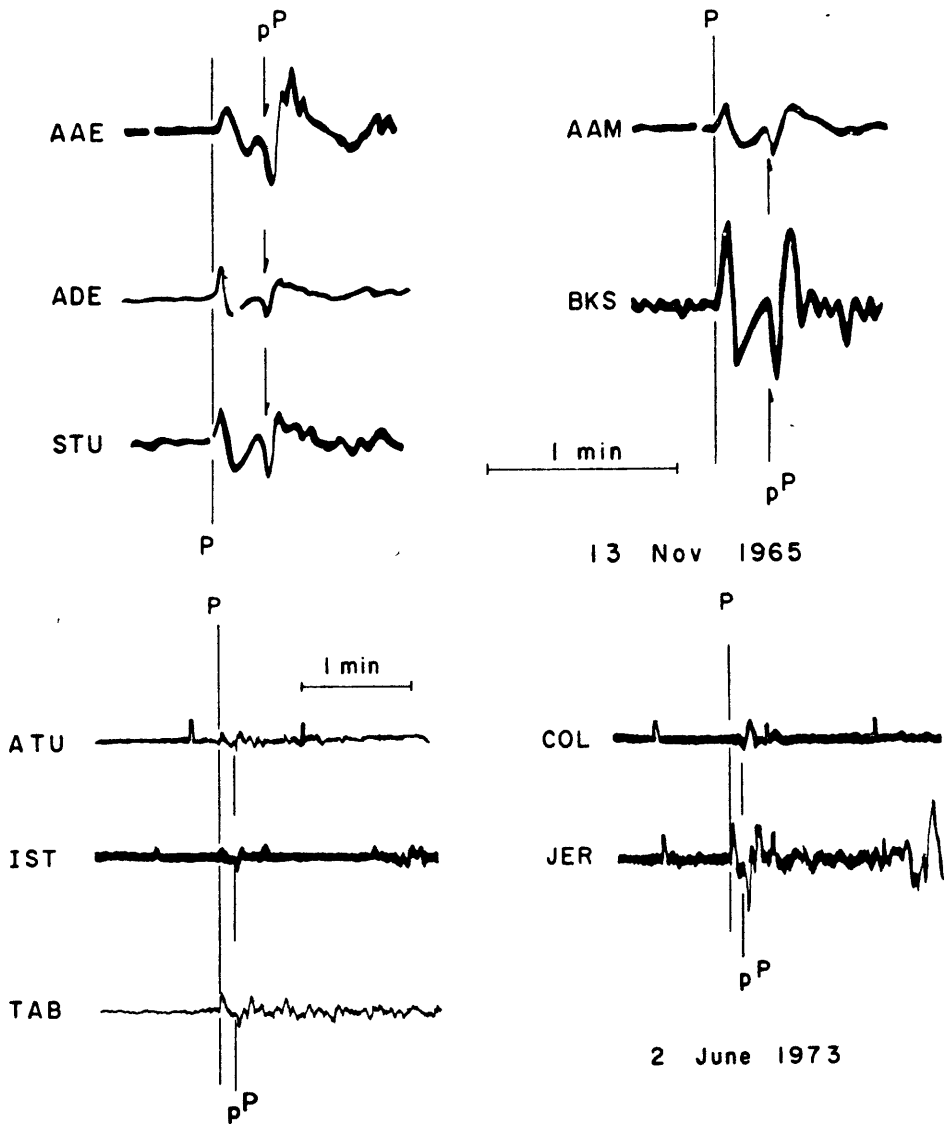

Fig. 11. Long-period vertical component seismograms of the WWSSN showing pP arrivals of two selected events with focal depths of approximately 45 and 30 km, respectively. Relevant information on those readings is given in Table 3.

23, 1905, event appears to have caused no less than 2.5 m of left-lateral slip as well as an unknown component of reverse faulting on a 370 km-long east-west fault. The July 9, 1905, event seems to have ruptured a shorter fault, striking about N60°E with a complicated pattern of deformation (S. D. Hilko, personal communications, 1974, 1975).

The geological effects of the 1862 Proval Bay event on Lake Baikal appear to be comparable or perhaps larger than those of the Muya event [Solonenko, 1968]. A large bay formed when part of the Selenga River delta dropped relative to the lake level. (Proval translates from Russian to 'gap' or 'sink'.) The intensity distribution from the 1889 Chilik earthquake [Mushketov, 1891] is comparable in maximum intensity and area to that of the 1911 Kebin earthquake [Bogdanovich et al., 1914], and we assume that they have the same moment. Seismic moments for the remaining events are estimated approximately from the magnitude-moment relation for the Asian events discussed above (Figure 10). Fault plane solutions are assumed to be the same as for adjacent events studied in the previous section.

If a 40-km-thick layer is assumed, the calculated slip rate, averaged from 1862 to 1967, is 23 mm/yr in the north-south direction in comparison with 15 mm/yr for 1911 to 1967. As Davies and Brune [1971] suggested that the seismicity in around 1900 in this area was particularly high, the difference between the rates that include and exclude these earlier data gives an estimate of the uncertainty in the calculated rates due to the nonstationarity of the seismicity. When averaging over 1862 to 1967 the contribution from the Assam event is relatively small, but the pattern of deformation remains essentially north-south compressional, the smaller extension being in the east-west and vertical directions. In the absence of other information we tentatively assume that the effect of the nonstationarity

of seismicity contributes less than a factor of 2 error to our calculated strain field and slip rate.

Comparison of seismic slip rate with the India-Eurasia convergence rate. The calculated seismic slip rate for a layer 40 km thick and including smaller earthquakes for 1911 to 1967 is about 20 mm/yr, whereas India moves north with respect to Eurasia at 50 mm/yr. When one considers the uncertainties in the calculated strain fields due to errors in the moments themselves, erroneous fault plane solutions, and the nonstationarity of the seismicity, this rate could be in error by a factor of nearly 5 in the case where all the errors conspired to underestimate or to overestimate the calculated strain field. Even if the seismic slip rate were overestimated by this much, the rate (or the thickness of the brittle deforming layer) is considerably larger than that for Iran, where seismic slip accounted for a negligible fraction of the convergence rate with Arabia [North, 1974]. Alternatively, if the calculated seismic slip rate were 5 times too small, then brittle deformation would necessarily extend to 40-km depth and probably deeper. Regardless of the error in the calculated slip rate the convergence between India and Eurasia requires a considerable amount of aseismic slip in the upper 100 km of the mantle, a result that is perhaps not surprising but is different from that of most island arcs [Davies and Brune, 1971].

Depth of brittle zone. Because of the inverse proportionality between slip rate and layer thickness in the estimate of the calculated strain field it perhaps makes more sense to ask what the thickness of the layer is in which brittle deformation must occur. Given a convergence rate of 50 mm/yr, all brittle deformation could be contained in a layer of several kilometers thick with the same extreme uncertainty of a factor of 5. However, if all of the earthquakes ruptured only the upper 10 km as is observed for the San Andreas fault system, the calculated seismic moments would require an average slip much greater than that observed in the field. Moreover, stress drops for nearly all of the earthquakes would be in excess of 100 bars and therefore greater than the values typically reported. In fact, we found that to keep the calculated average slip in the faults in accord with the observed slip, in several cases it was necessary for faults to rupture to about a 40-km depth. Even for depths of 20 km, stress drops for some events were calculated to be unusually high. However, given the uncertainties in the seismic moments and the few events studied, this inference of rupture zones extending to 40 km is perhaps not convincing.

To examine the depth of faulting further, we searched for events in Asia with clear pP phases and found many events with time intervals between P and pP of about 10 s (Figure 11 and Table 3), suggesting focal depths of about 30 to 35 km. One event might have been as deep as 50 km (Figure 11). Probably, brittle deformation does not extend to this depth in all parts of Asia, yet Armbruster et al. [1977] showed that small earthquakes in the Himalaya of Pakistan occur as deep as 60 km. It is because of these observations that we assumed a thickness of 40 km above.

TABLE 3. Selected pP observations

Station	Distance, deg	Azimuth, deg	T^*_{P-pP} s
November 13, 1965	04h 33m 53.2s		43.8°N, 87.7°E
AAE	54.8	246	15
AAM	93.9	354	15
ADE	91.1	140	14
BKS	94.2	23	15
STU	52.2	305	16
June 2, 1973	23h 57m 04.2s		44.1°N, 83.6°E
ATU	44.5	284	9
COL	64.2	22	7
IST	39.7	285	8
JER	39.6	269	9
TAB	28.6	271	9

*Arrival time difference between P and pP.

Conclusion

We estimated the seismic moments for 12 major earthquakes in central Asia since 1911 and compared them with the offsets and fault lengths observed in the field or with fault lengths inferred from intensity and aftershock distributions. For some events, these data suggest that depths of faulting reach 40 km, considerably greater than depths of earthquakes and seismic slip along the San Andreas fault. Differences in time between P and pP confirm that brittle failure does extend to this depth in parts of Asia.

The pattern of deformation caused by the seismic slip shows north-south compression, vertical expansion (uplift and crustal thickening), and a smaller amount of east-west extension. If deformation in Asia includes a large component of eastwards displacement of China with respect to India and Eurasia on strike-slip faults, this displacement seems to occur mostly by fault creep instead of by seismic slip. The calculated average seismic slip rate in the north-south horizontal direction is about 20 mm/yr for a 40-km-deep brittle zone of lithosphere averaged from 1911 to 1967. In comparison with the 50-mm/yr relative motion between Indian and Eurasian plates, only a fraction of the relative convergence is released in the form of seismic slip. The uncertainties in the calculated slip

rate do not allow for an accurate estimate of this fraction or, alternatively, of the thickness of the brittle zone. Nevertheless, this fraction of the relative convergence is much larger than that in Iran, where most of the convergence seems to occur by fault creep [North, 1974], and it is consistent with the inference that brittle deformation extends to 40-km depth in much of Asia.

Acknowledgments. We benefited from numerous discussions with P. Tapponnier. We thank J. Filson and R. North for assistance in computations, G. Stewart for pointing out an error in one of the moment determinations, and D. McKenzie for pointing out that Kostrov's method ignores rotational strain. We also thank M. Båth, J. Brune, R. Cabré, L. A. Drake, S. Gregerson, J. B. Minster, E. A. Okal, G. Schneider, J. H. Whitcomb, and H. Wilhelm for providing the records and instrument response information used in this study. S. D. Hilko, V. I. Kuchai, N. V. Shebalin, and V. P. Solonenko gave us valuable information about surface faulting and intensity distributions for some of the earthquakes studied. The reading of obscure publications was done while Molnar was a guest of the Academy of Sciences of the USSR through exchange with the U.S. National Academy of Sciences and through exchange in earthquake prediction. Thanks are due to numerous individuals who helped during these exchanges. We appreciate the critical comments of W. Pennington and an anonymous referee. This research was supported primarily by National Science Foundation grant 74-02550EAR.

References

Aki, K., Generation and propagation of G waves from the Niigata earthquake of June 16, 1964, 2, Estimation of earthquake moment, released energy, and stress-strain drop from G wave spectrum, Bull. Earthquake Res. Inst. Tokyo, 44, 73-88, 1966.

Aki, K., Scaling law of earthquake source time function, Geophys. J. Roy. Astron. Soc., 31, 3-25, 1972.

Armbruster, J., L. Seeber, and K. H. Jacob, The northwestern termination of the Himalayan mountain front: Active tectonics from microearthquakes, J. Geophys. Res., in press, 1977.

Ben-Menahem, A., Radiation of seismic surface waves from finite moving sources, Bull. Seismol. Soc. Amer., 51, 401-435, 1961.

Ben-Menahem, A., and M. N. Toksöz, Source mechanism from spectra of long-period seismic surface waves, 1, The Mongolian earthquake of December 4, 1957, J. Geophys. Res., 67, 1953-1955, 1962.

Ben-Menahem, A., M. Rosenman, and D. G. Harkrider, Fast evaluation of source parameters from isolated surface-wave signals, 1, Universal tables, Bull. Seismol. Soc. Amer., 60, 1337-1387, 1970.

Ben-Menahem, A., E. Aboudi, and R. Schild, The source of the great Assam earthquake - An interplate wedge motion, rhys. Earth Planet. Interiors, 9, 265-289, 1974.

Bogdanovich, K. I., I. M. Kark, B. Ya. Korolkov, and D. I. Mushketov, The earthquake in the northern part of the Tien Shan of 22 Dec. 1910 (4 Jan. 1911) (in Russian), Trans. Geol. Comm., 89, 1-270, 1914.

Brune, J. N., and C. R. Allen, A low-stress drop, low-magnitude earthquake with surface faulting, The Imperial, California, earthquake of March 4, 1966, Bull. Seismol. Soc. Amer., 57, 501-514, 1967.

Brune, J., and G. R. Engen, Excitation of mantle Love waves and definition of mantle wave magnitude, Bull. Seismol. Soc. Amer., 59, 923-933, 1969.

Brune, J. N., and C. Y. King, Excitation of mantle Rayleigh waves of period 100 seconds as a function of magnitude, Bull. Seismol. Soc. Amer., 57, 1355-1365, 1967.

Close, U., and E. McCormick, Where the mountains walked, Nat. Geogr. Mag., 41, 445-464, 1922.

Davies, G., and J. N. Brune, Regional and global slip rates from seismicity, Nature Phys. Sci., 229, 101-107, 1971.

Dewey, J. F., and K. C. Burke, Tibetan, Variscan and Precambrian basement reactivation: Products of continental collision, J. Geol., 81, 683-692, 1973.

Duda, S. J., Secular seismic energy release in the Circum-Pacific belt, Tectonophysics, 2, 409-452, 1965.

Dunn, J. A., J. B. Auden, A. M. N. Ghosh, and D. N. Wadia, The Bihar-Nepal earthquake of 1934, chaps. 2, 3, 5, India Geol. Surv. Mem. 73, 1939.

Fitch, T. J., Earthquake mechanisms in the Himalayan, Burmese, and Andaman regions and continental tectonics in central Asia, J. Geophys. Res., 75, 2699-2709, 1970.

Florensov, N. A., and V. P. Solonenko, (Eds.), The Gobi-Altai Earthquake, chaps. 10, 12, Siberian Department of Academy of Science, Moscow, 1963, (English Translation, U.S. Department of Commerce, Washington, D. C., 1965.)

Gilbert, F., Excitation of the normal modes of the earth by earthquake sources, Geophys. J. Roy. Astron. Soc., 22, 223-226, 1970.

Gubin, I. E., Regularities of Seismic Activity in the Territory of Tajikistan, pp. 279-303, Academy of Sciences Publishing House, Moscow, 1960.

Gubin, I. E., Lecture notes on basic problems in seismotectonics, pp. 67-68, Int. Inst. of Seismol. and Earthquake Eng., Tokyo, Japan, 1967.

Gutenberg, B., and C. F. Richter, Seismicity of the Earth and Associated Phenomena, pp. 133-150, Hafner, New York, 1954.

Kostrov, V. V., Seismic moment and energy of earthquakes, and seismic flow of rock, Izv. Acad. Sci. USSR, Phys. Solid Earth, 1, 23-44, 1974.

Kuchai, V. I., Results of repeated examination of the remaining deformation in the pleistoseist of the Kebin earthquake (in Russian), Geol. Geophys., 101-108, 1969.

Le Pichon, X., Sea floor spreading and continental drift, J. Geophys. Res., 73, 3661-3697, 1968.

Minster, J. B., T. H. Jordan, P. Molnar, and

E. Haines, Numerical modeling of instantaneous plate tectonics, Geophys. J. Roy. Astron. Soc., 36, 541-576, 1974.

Molnar, P., and P. Tapponnier, Cenozoic tectonics of Asia: Effects of a continental collision, Science, 189, 419-426, 1975.

Molnar, P., T. J. Fitch, and F. T. Wu, Fault plane solutions of shallow earthquakes and contemporary tectonics in Asia, Earth Planet. Sci. Lett., 19, 101-112, 1973.

Mushketov, I. V., Materials for the Study of Earthquakes of Russia, pp. 11-42, A. Suvorin, Saint Petersburg, USSR, 1891.

Natsag-Yum, L., I. Balzhinnyam, and D. Monkho, Earthquakes of Mongolia, in Seismic Regionalization of Ulan Bator, Nauka, Moscow, 1971.

North, R. G., Seismic slip rates in the Mediterranean and Middle East, Nature, 252, 560-563, 1974.

Okal, E. A., A surface-wave investigation of the rupture mechanism of the Gobi-Altai (4 December, 1957) earthquake, Phys. Earth Planet. Interiors, 12, 319-328, 1976.

Okal, E. A., The July 9 and 23, 1905 Mongolian earthquakes: A surface-wave investigation, Earth Planet. Sci. Lett., 34, 326-331, 1977.

Richter, C. F., Elementary Seismology, Freeman, San Francisco, Calif., 1958.

Seismological Brigade of Lanzhou, National Seismological Bureau, and the Seismological Brigade of the Ningxia Hui Nationality Autonomous Region, Great Haiyuan earthquake on December 16, 1920 (in Chinese), Acta Geophys. Sinica, 19, 42-49, 1976.

Seismological Committee of the Academia Sinica, Chronological Tables of Earthquake Data of China (in Chinese), Science Press, Peking, 1956.

Shebalin, N. V., Macroseismic data as information on source parameters of large earthquakes, Phys. Earth Planet. Interiors, 6, 316-323, 1972.

Solonenko, V. P., Tectonics of Muya earthquake area (in Russian), Izv. Acad. Sci. USSR, Geol. Ser., 4, 58-70, 1965.

Solonenko, V. P., Strong earthquakes by means of seismostatistics, in Seismotectonics and Seismicity of the Pri-Baikal Rift System (in Russian), pp. 60-67, Nauka, Moscow, 1968.

Solonenko, V. P., R. A. Kurushin, and S. D. Khilko, Strong earthquakes, in Recent Tectonics, Volcanism and Seismicity of the Stanovoy Upland (in Russian), pp. 145-170, Nauka, Moscow, 1966.

Stauder, W., and G. A. Bollinger, The focal mechanism of the Alaska earthquake of March 28, 1964, and its aftershock sequence, J. Geophys. Res., 71, 5283-5296, 1966.

Sykes, L. R., Seismicity of the Indian Ocean and a possible nascent island arc between Ceylon and Australia, J. Geophys. Res., 75, 5041-5055, 1970.

Tandon, A. N., Direction of faulting in the great Assam earthquake of 15 August 1950, Indian J. Meteorol. Geophys., 6, 61-64, 1955.

Tapponnier, P., and P. Molnar, Active faulting and Cenozoic tectonics in China, J. Geophys. Res., 82, in press, 1977.

Vvedenskaya, A., and L. M. Balakina, Methods and results of the determination of stress acting in the foci of earthquakes of Pri-Baikal and Mongolia (in Russian), Bull. Sov. Seism., Acad. Sci. USSR, 9, 73-84, 1960.

Wickens, A. J., and J. H. Hodgson, Computer re-evaluation of earthquake mechanism solutions 1922-1966, Publ. Dominion Observ., 33 (1), 1967.

(Received June 14, 1976;
revised November 22, 1976;
accepted December 15, 1976.)

CHAPTER III

CONSTRAINTS ON THE SEISMIC WAVE VELOCITY STRUCTURE BENEATH THE TIBETAN PLATEAU AND THEIR TECTONIC IMPLICATIONS

Wang-Ping Chen and Peter Molnar
Department of Earth and Planetary Sciences
Massachusetts Institute of Technology
Cambridge, MA 02139

Abstract

We combine observations of group and phase velocity dispersion of Rayleigh waves, of the wave form of a long period P_L phase, of P_n and S_n velocities from unreversed refraction profiles using earthquakes, and of teleseismic S-P travel time residuals to place bounds on the seismic wave velocity structure of the crust and upper mantle under Tibet. From surface wave measurements alone, the Tibetan crustal thickness can be from 55 km to 85 km, with corresponding uppermost mantle shear wave velocities of about 4.4 km/s to 4.9 km/s, respectively. The P_n and S_n velocities were determined to be 8.12 ± 0.06 km/s and 4.8 ± 0.1 km/s respectively using travel time data at Lhasa from earthquakes in and on the margins of Tibet. With these estimates of the uppermost mantle velocity and with the surface wave dispersion, the crustal thickness is most likely to be between 65-80 km with an average shear wave velocity in the crust less than 3.5 km/s. A synthesis of one P_L wave form does not provide an additional constraint to the velocity structure but is compatible with the range of models given above.

Measurements of both teleseismic S wave and P wave arrival times for nine earthquakes within Tibet show unusually large intervals between P and S compared with the

Jeffreys-Bullen Tables. We infer that most of the large interval is due to delays in the S wave travel times. These delays are not a consequence of errors in the Tables, because S wave and P wave arrival times from eight earthquakes in the nearby Himalaya agree quite well with them. A minimum delay of the S waves of two to three seconds exists even if the focal depth of Tibetan events were only 5 km, while Himalayan events were 33 km. Thus the P_n and S_n velocities apparently do not reflect high velocities in the mantle to a great depth beneath Tibet.

From the dependence of the seismic velocities of olivine on pressure and temperature and from the similarity of the measured P_n and S_n velocities beneath Tibet and beneath shields and platforms, the temperature at the Moho beneath Tibet is compatible with being 250-300° warmer than beneath shields and platforms, i.e. 750°C if the temperature beneath the platforms is close to 500°C. Such a temperature could reach or exceed the solidus of the lower crust. From the flow laws of olivine, the mechanical strength of the uppermost mantle with such a temperature would not be more than about 1 kb and would decrease rapidly with depth. Simple one-dimensional heat conduction calculations suggest that the tectonic and volcanic activity could be explained by the recovery of the geotherm maintained by a mantle heat flux of about 0.9 HFU at the base of the crust. If the

distribution of radioactive heat production elements were not concentrated at the top of the crust, radioactive heating could also contribute significantly to the recovery of the geotherm and thus lower the required mantle heat flow. Thus the idea of a thickened crust in response to horizontal shortening is compatible both with these data and with these calculations.

INTRODUCTION

With an average elevation of about 5 km above sea level over an area of 7×10^5 km^2, the Tibetan plateau is certainly one of the most conspicuous topographic features on earth. To the south and southwest, it is bounded by the Himalayan convergent zone where the continental collision between India and Eurasia plates manifests itself predominantly by low angle thrusting [e.g. Fitch, 1970; Molnar et al., 1973, 1977]. The Altyn Tagh and the Kun-Lun left-lateral strike-slip faults form its northern boundary [e.g. Molnar and Tapponnier, 1975; Tapponnier and Molnar, 1977]. In contrast, recent normal faulting [e.g. Molnar and Tapponnier, 1975, 1978; Ni and York, 1978] and volcanism are widespread over the plateau [Burke et al., 1974]. With its complex variations of active tectonic styles and its massive volume, the evolution of the Tibetan plateau has been recognized as a key to the understanding of continent-continent convergent processes [e.g. Dewey and Burke, 1973; Molnar and Tapponnier, 1975, 1978; Toksöz and Bird, 1977].

Primarily because of its inaccessibility, geological data available about Tibet are very limited. Upper Cretaceous limestones seem to cover much of Tibet [Hennig, 1915; Norin, 1946]. This observation places a lower bound on the time of uplift, but we are not aware of evidence that constrains the timing more tightly. Volcanism, which is apparently quite

young is widespread on the plateau [e.g. Burke, et al., 1974; Kidd, 1975]. Recently Deng [1978] reported Quaternary calc-alkaline to alkaline volcanics in northern Tibet at sites close to those of the earlier findings of Norin [1946]. Similar rock types have also been reported along the southern part of Tibet [Chang and Cheng, 1973; Hennig, 1915; Kidd, 1975]. Apparently, so far, no basalt has been found in these field studies, which are of limited geographic coverage. From the lack of basalts, Dewey and Burke [1973] inferred melting only of crustal materials as the source of the volcanics.

Given the unusual elevation and the limited geologic data, the crustal and upper mantle structures are important constrains on the geologic evolution of the plateau. Gravity data are too limited to provide a tight constraint. Amboldt [1948] reported one gravity measurement within the plateau that is consistent with isostatic equilibrium. Chang and Cheng [1973] also inferred isostatic equilibrium from more recent, but unpublished gravity data. As pointed out by Bird and Toksöz [1977] the crustal thickness of Tibet is likely to be from 55 to 70 km assuming isostatic compensation with mantle properties varying from a mid-ocean ridge-like conditions to stable shield-like environments.

Almost all the previous seismic studies of Tibet are based on group velocity dispersion curves of surface waves [Bird, 1976; Bird and Toksöz, 1977; Chun and Yoshii, 1977;

Patton, 1978; Tung and Teng, 1974; Tseng and Sung, 1963]. In general, these investigators concluded that the crust is about 70 km thick with a relatively low upper mantle shear wave velocity (near 4.5 km/s). The mantle velocities, however, cannot be well constrained with surface wave data alone [Der et al., 1970]. The possible trade-off between upper mantle velocities and crustal thickness was not investigated in most of these studies, and little attention has been given to the uncertainties and bounds of allowable velocity structures. We do not consider the results in the published studies to be conclusive evidence for crustal thicknesses of 70 km, and consequently we have carried out a study of not only surface wave dispersion but of other seismic phases.

Considering that the crust is thick now, but probably was not thick before the collision between India and Eurasia in the early Tertiary, there have been two extreme mechanisms proposed for the thickening of the crust and the uplift of the plateau. Dewey and Burke [1973], Toksöz and Bird [1977] and probably others suggested that Tibet formed by relatively uniform crustal shortening and thickening (like an accordion) in response to horizontal compression. Others [e.g., Argand, 1924; Powell and Conaghan, 1973, 1975] inferred that low angle underthrusting of one crustal block (India) beneath another (Tibet) is the dominant mechanism for creating the high

plateau. Both models require a decrease, if only temporary, in the crustal temperature gradient due to the crustal thickening. Therefore a more quantitative treatment of either situation is required to explain how volcanism could occur on the plateau. Furthermore, the latter model is thought by many to be mechanically unlikely.

The existence of the volcanoes and the inference of relatively low seismic wave velocities led logically to the suggestion that the upper mantle beneath Tibet is relatively hot and light. Part of the high elevation but not the crustal thickening could be a consequence of thermal expansion of the underlying mantle. Although these various opinions diverge considerably, and the specific physical processes are vaguely described at best, the ultimate cause of Tibet's elevation, thick crust and volcanism is virtually unanimously attributed to the India-Eurasia collision.

The existing data for Tibet are too scarce to disciminate among the various proposed evolutionary mechanisms, but tectonic models of the evolution of the India-Eurasia continental collision must provide satisfactory explanations for the structure of the plateau. Furthermore, studying the geophysical characteristics of the Tibetan plateau and the active Himalaya probably provides basic information that constrain the processes of large scale continental tectonics in general.

The purpose of this study is to present a comprehensive seismological dataset that places improved constraints on the seismic velocity structure of the crust and upper mantle beneath the Tibetan plateau. We discuss separately the four relatively independent seismic methods employed: surface wave dispersion for paths crossing the plateau, synthesis of a P_L phase crossing the plateau, P_n and S_n refraction profiles using earthquakes in Tibet and the Himalaya, and teleseismic S wave travel time residuals from earthquakes in and near Tibet. In each section describing the individual seismic phases, a brief introduction and, in some cases, a review of the theories is given, followed by the results of observations. Constraints on possible models and discussions of them are then presented. At the end, we present an interpretation of all the observations and discuss their tectonic implications.

None of the studies of individual seismic phases requires a unique velocity structure, but a consistent model of the crustal thickness and uppermost mantle velocities can be obtained from the combined observations. In particular, the non-uniqueness of the velocity structure has been reduced considerably by the determination of the uppermost mantle velocities from refraction profiles.

SURFACE WAVE DISPERSION

a) Dispersion Curves

We analyzed long-period seismograms for nine earthquakes in and near Tibet recorded at one or more of the four stations of the World Wide Standardized Seismograph Network (WWSSN) just south of the Himalaya (Table I). More than 80% of each of the great circle paths is within the plateau. We chose not to use long paths across much of Asia because of the difficulties in deciding how to regionalize them and because of the likelihood of marked lateral refraction at the boundaries of Tibet and elsewhere. We trust more the results obtained from paths confined as much as possible to Tibet. Thus, the range of epicentral distances is limited to about 20° (Fig. 1). We analyzed only seismograms that have high signal to noise ratios and for which a minimum amount of multi-pathing was apparent (Fig. 2). For only two paths were clear long-period ($\geq$60 sec) Rayleigh waves recorded with large amplitudes (Fig. 2a).

The multi-filtering technique [Landisman et al., 1969] was used to obtain the group velocity dispersion curves. Gaussian band-pass filters centered at each given frequency were applied to the seismograms and the arrival times of the peaks of maximum energy on the filtered traces give the group arrivals. The group velocity resolution is inversely proportional to the bandwidth of the filter at a given frequency.

We analyzed only fundamental modes of both Love and Rayleigh waves with periods from 10 to 90 sec. Group velocity dispersion curves for Rayleigh waves differ from one another by about 3% (Fig. 3a), which is comparable with that in some previous studies [e.g., Chun and Yoshii, 1977]. The dispersion curves between 30s and 60s are poorly defined because of a low signal to noise ratio, which is apparent from visual inspection of the seismograms. The amplitudes on the seismograms are reduced, at least in part, because the group velocity dispersion curve is very steep in this particular frequency band, but Bird and Toksöz [1977] inferred an extremely high attenuation in this band as well. Thus the uncertainty of this part of the dispersion curve is very large, and we assume that this part is essentially undetermined. Compared with the previous studies mentioned above [e.g., Chun and Yoshii, 1977; Bird and Toksöz, 1977] our long-period Rayleigh wave group velocities are about 2 to 3% faster at 70 to 80 sec but slower at longer periods by about the same amount. This difference contributes partly to the differences in preferred mantle velocity models. Love wave group velocities observed here also differ from one another by from 5 to 10% (Fig. 3b). No clear Love wave with period longer than 70 sec was observed.

We also used phase velocities to aid in the discussion of these observations. Phase velocity dispersion curves (Fig. 4) can be calculated using the standard single station method:

$$C(\omega) = \omega X/(\phi_o + \omega t - \phi_F - \phi_I \pm 2n\pi)$$

where C is the phase velocity as a function of angular frequency ω, x the propagation distance, ϕ_o, ϕ_F and ϕ_I are the observed phase delay, calculated focal phase delay and the instrumental phase delay respectively, t is the time interval between the origin time of the earthquake and the beginning of digitization, and n is the integer determined by assuming known phase velocity at long periods, where an integral change in n gives large change in phase velocity.

A combination of a mislocation of 10 km and a 2 sec error in origin time can cause an error of 0.8% in determinations of both group and phase velocities at a distance of 20°. An uncertainty in the group arrival time or phase delay of one-eighth of the period at periods near 80 sec leads to an uncertainty of 1.6% in group or phase velocity at this distance. We assume a total combined maximum error of up to 3% in both is possible for the long period end of the dispersion curves. The uncertainty in the group velocity at short-periods should be less. However, lateral heterogeneity will have a much large effect on relatively shorter wavelength components than the larger wavelength components. This might be part of the reason why there is a fairly large scatter in the data at short periods.

For shallow events, the source depth is not important at long periods. Because both events have nearly vertical strike-slip fault plane solutions, obtained primarily from P wave first-motion polarities, [Molnar et al., 1973; Tapponnier and Molnar, 1977] the uncertainty in the calculated phase delay ϕ_F is small. At extreme conditions, assuming an error of 0.2 cycles in various phase delays, an error of 3.4% in phase velocity is possible if all the errors conspired together for periods near 80 sec and a distance of 20°. The relatively large error in the phase delay assumed here takes into account the effect of a possible non-step-like source time function.

Note that the two Rayleigh wave seismograms with large signal-to-noise ratios at long periods have different paths (Fig. 1). The I-NDI path is almost entirely within Tibet except at the southwestern end where it crosses the Himalaya at a high angle. The II-SHL path across part of the Pamir before it entered Tibet and then met the Himalaya at a low angle. The difference between the two observations at periods longer than 60 sec could be simply due to observational errors, but it might actually reflect real differences in average velocity structures for different paths.

b) Velocity Models

Resolving power of data and assumptions in models:

Before interpreting the data, we briefly review the resolution of surface wave observations on velocity structures. Assuming a laterally homogenous earth structure, Der et al., [1970] investigated effects of observational errors on the resolving power of surface waves using synthetic data with periods and distances comparable to those used here. Their most relevant conclusions are:

1. Over similar period ranges the fundamental Rayleigh mode yields considerably better resolution than the fundamental Love mode. The latter contributes little to the resolution of the upper mantle velocity.

2. If observations are restricted to fundamental modes only, crustal models with no more than 3 layers are justified.

3. With both fundamental mode Rayleigh and Love waves and their first higher modes, the shear-wave velocity (V_S) resolution in the upper crust, lower crust, and uppermost mantle are about 0.05, 0.08, and 0.1 km/sec, respectively. In particular, the shear wave velocity resolution is only 0.1 km/sec for a layer 100 km thick centered at a depth of 125 km. With both the fundamental and the first higher mode Rayleigh wave, the resolving power is close to that of the combination of all four modes.

4. Unless the period range of group velocity observations for Rayleigh and Love wave fundamental modes exceeds 80 sec, the upper mantle velocity resolution is poor.

5. The above summary is appropriate for group velocities. Phase velocity observations provide somewhat less resolution than group velocity observations with the same observational errors.

Der et al. [1970] assumed standard deviations of group velocities of approximately 0.3% near 15 sec and 1.5% at 80 sec; these errors are probably smaller than ours. With reliable group velocity observations of fundamental Rayleigh and Love waves at limited frequency band and with fairly large scatter (Fig. 3), and phase velocity measurements of fundamental Rayleigh mode between 60 to 90 sec only (Fig. 4), we did not perform a formal inversion. Instead, we examined a range of plausible models; and then from a comparison with the observation, we placed bounds on the range of possible structures.

In constructing these models, we further assumed that:

1. The velocity structure below 90 km for most models and density structure for all models are the same as Gutenberg's continental model [Dorman et al., 1960].

2. The ratio of P wave velocity to S wave velocity is fixed at 1.73 in the crust and 1.80 in the uppermost mantle.

3. The shear wave velocity of the top 3.75 km is fixed at 2.55 km/sec [Chen and Molnar, 1975]. We did not consider the period range 5 to 10 sec here.

4. No more than 3 layers in the crust, excluding the top sedimentary layer, are included and the mantle between the Moho and a depth of 90 km is assumed to be homogeneous.

Since the resolution of P wave velocities is very poor compared with the resolution of S wave velocities, we examined dependencies of the dispersion curves only on V_S in the mantle, the crustal thickness, and the shear wave velocity structure in the crust. Theoretical dispersion curves were compared primarily with Rayleigh wave group velocity observations, but for selected structures comparison was also made with Rayleigh wave phase velocity observations. Love wave group velocity observations served only as a loose constraint. As long as theoretical values fall within the scatter of these data, no further comparison with them was made. Surface wave dispersion at the short period range (<30 sec) does not constrain the crustal thickness or the upper mantle shear wave velocity much. Little attention will be paid to these short period range observations in the following discussion of these two subjects.

Crustal thickness and upper mantle S wave velocities:

Rayleigh wave dispersion curves for three different crustal thicknesses (55, 70, and 85 km) were calculated for a range of uppermost mantle shear wave velocities (β_m) from 4.4 to 4.9 km/s (Figs. 5-10). At long periods, higher values of β_m cause faster Rayleigh wave group velocities (Figs. 5-7), and greater crustal thicknesses cause lower group velocities (Figs. 8-10). For a crustal thickness of 55 km, only the model with the lowest value of β_m (4.4 km/s, model F4) fits the upper curve of the Rayleigh wave group velocity observations (Figs. 5 and 8). A lower value of β_m would be required to fit the lower curve, and if the assumed thickness of the crust is less than 55 km, β_m must be lower than 4.4 km/s. For a 70 km thick crust (Fig. 6), however the β_m seems to be constrained to be near 4.7 km/s (Model S7) or higher in order to be consistent with observed group velocity dispersion curves. Values of β_m as small as 4.4 km/s seem to be incompatible with a 70 km crust (Figs. 6 and 8). If we further increase the crustal thickness to 85 km (Fig. 7), the observations constrain the β_m to be 4.8 km/s or even 4.9 km/s, (Figs. 7 and 10), but the fit between the observed and theoretical curves appears to us to be worse than for the previous cases of 55 km and 70 km thick crust. These results confirm Der et al.'s [1970] numerical experiments that show that surface wave dispersion alone is inadequate to constrain both the crustal thickness and the upper mantle shear wave velocity tightly.

Phase velocity dispersion curves for four velocity models are plotted with the two observed dispersion curves in Fig. 4. The curve for model F4 (55 km thick crust, β_m = 4.4 km/s) lies within the scatter of the observations. Both model S7 (70 km thick crust, β_m = 4.7) and model SE (70 km thick crust, β_m = 4.8, with the lowermost crustal velocity lower than that of model S7) fit the observed phase velocities for the I-NDI path well and were within the uncertainties of the observations for the II-SHL path. Model S4 (70 km thick crust, β_m = 4.4 km/s) does not fit the II-SHL observed phase velocities and is systematically lower than the data for I-NDI. It turns out that if $\beta_m \geq 4.8$ km/s, however, the phase velocity data cannot rule out a crustal thickness of 85 km.

Velocity structure of the crust: The crustal structure is constrained primarily by the shorter period portion of the dispersion curves. Fig. 11 shows the theoretical Rayleigh wave group velocity dispersion curves for 7 different models with fixed crustal thickness of 55 km and β_m = 4.4 km/s. If the acceptable values of the calculated Rayleigh wave group velocities are those that lie within the scatter of our data, an average crustal shear wave velocity ($\overline{\beta}$) of 3.5 km/s seems to be too high (Fig. 11a). A single layer between the top low velocity layer and the Moho will not fit the data either at this low value of $\overline{\beta}$ (Fig. 11b). By adding a higher

velocity layer at the base of the crust and maintaining a constant $\overline{\beta}$, dispersion curves can be constructed that agree well with the data (Fig. 11b).

Calculated Rayleigh wave group velocity dispersion curves for 5 different crustal structures with a 70 km thick crust and β_m = 4.7 km/s, also suggest that $\overline{\beta}$ is less than 3.5 km/s (Fig. 12). Thus an average shear wave velocity in the crust of less than 3.5 km/sec is consistent with the data despite the assumed crustal thicknesses. The long-period end of the dispersion curve, however, is sensitive to the shear wave velocity in the lower crust. For instance, the addition of a relatively high velocity layer (such as V_S = 3.9 km/s) between 60 and 70 km depth has the same effect on the long period portion of the dispersion curve that an increase of β_m (such as from 4.7 to 4.8 km/sec) below 70 km has (Fig. 12b,c). These variations are, of course, only examples of many other possibilities. Thus there are trade-offs between the lower crustal shear wave velocity and β_m which is in turn coupled with the crustal thickness.

For crustal thickness of 85 km, the constraints on the crustal structure placed by surface waves will be even looser than the previous discussions for 55 and 70 km thick crust cases. We did not investigate any detailed models for this crustal thickness.

The most important constraint that surface wave dispersion places on the crustal structure is that the average crustal shear wave velocity is low (<3.5 km/s). The data also seem to be better fit by a series of layers of increasing velocity than by a single layer of uniform velocity in the crust below sediments. Our data do not require a low velocity zone in the crust [cf. Chun and Yoshii, 1977]. The crustal thickness and uppermost mantle shear wave velocity combinations obtained earlier are not very sensitive to the possible variations in the crustal structure.

c) Synthesis of Rayleigh wave signals

The group and phase velocity dispersion curves contain very little information about the amplitude of the surface waves other than the fact that there must exist a substantial amount of Fourier amplitude (spectral density) at a particular frequency in order to obtain a reliable determination of the group arrival time. As a further check on the velocity structure, we have used the summation of normal modes to generate synthetic seismograms of vertical components of Rayleigh waves to investigate the possibility of detecting structural differences from these synthetic seismograms. This method was originally designed by Kanamori [1970] to investigate the long-period source characteristics of earthquakes at large distances.

The generation of synthetic seismograms requires a knowledge of the source depth, the fault plane solution, the source time function, the seismic moment, and parameters describing attenuation and a velocity structure. Usually, one assumes a knowledge of several of the factors and tries to deduce the others from the agreement of the synthetic seismogram with the observed one. We summed fundamental Rayleigh modes with periods between about 20 to 120s and generated synthetic seismograms for I-NDI and II-SHL observations (Fig. 1 and 2). Both the synthetic seismograms and the observed seismograms (paths I-NDI and II-SHL, Fig. 2) were low-pass filtered with a cut-off frequency at 0.04 Hz (25 sec) to eliminate excess high frequency oscillations that are superimposed on the long period signals of interest. The finite filter length tends to introduce different effects on the ends of the synthetic seismograms from those of the observations and is a shortcoming for relatively short distances as in our case. We probably do not know the input parameters well enough to obtain a close match between the observed and calculated seismograms. The following discussion deals with simple experiments of the effects of the different parameters on the time domain observations.

Fault plane solutions for both events are held fixed and the uncertainties associated with them have small effect

on the calculated wave form. A point source time history is assumed to be a step for simplicity. The severe attenuation proposed by Bird and Toksöz [1977] was applied to generate the theoretical seismogram marked with 'low Q' in Fig. 13a. The one marked 'normal Q' was generated with the observed attenuation for Rayleigh waves in an average earth structure [summarized in Kovach, 1978]. The observed wave form of the II-SHL path is also shown in Fig. 13a. Although the amplitude for the 'normal Q' synthetic seismogram is 35% larger than that of the 'low Q' synthetic seismogram, the wave forms are quite similar in the bandwidth of interest here, 60 to 90 sec (Fig. 13a). For both synthetic seismograms the same velocity model S7 (70 km thick crust, β_m = 4.7 km/s, Fig. 6) and a source depth of 5 km were used. Part of the mismatch between the synthetic and observed signals arises from the end effects due to a finite filter length. The coda of the S wave and the 20 sec period Rayleigh wave are the most noticeable sources of noise (Fig. 2a). The calculated Rayleigh waves are delayed in time with respect to the observed one in Fig. 13a. The maximum mismatch in group arrival time corresponds to 2.7% difference in group velocity, which agrees with the dispersion curves in Fig. 6 and is within the observational errors.

Fig. 13b shows three synthetic seismograms, with their peak-to-peak maximum amplitude normalized to a common size, assuming model S7 with different source depths of 5, 10 and 30 km

(the actual amplitude ratio is about 3:2:1 respectively). The difference in wave forms for sources at 5 km and 10 km is small. There is a slight difference in wave form for a source at 30 km depth. This can be attributed to the interference of the short period Rayleigh waves, which have a phase shift of π with respect to the longer periods and much weaker amplitudes than for a depth of 10 km [Tsai and Aki, 1970].

Synthetic seismograms were generated for three different velocity models: β_m = 4.4 km/s and 4.7 km/s for a crustal thickness of 70 km (S4 and S7) and β_m = 4.4 km/s for a crustal thickness of 55 km (F4) (Fig. 13c). A 5 km source depth and 'average-earth' Q structure were used. With constant β_m (4.7 km/s) models with 55 km and 70 km thick crusts (model F7 and S7) gave quite different synthetic seismograms (Fig. 13c). We consider Model F7 to be inadequate to explain the observation but that Model S7 is satisfactory in matching the observed wave form of the I-NDI path (Fig. 13c).

d) Summary of surface wave results

1. From group velocity dispersion curves in the period range of 10 to 30 sec, the average crustal shear wave velocity is lower than 3.5 km/s.

2. From observed and calculated Rayleigh wave group and phase velocity dispersion curves and from synthesized Rayleigh waves with periods between about 60 to 90 sec, the

uppermost mantle shear velocity cannot be constrained well even with an assumed crustal thickness. If we assume a β_m of 4.4 km/s, the crustal thickness is probably no more than 55 km. If β_m is about 4.7 km/s, the crustal thickness is likely to be greater than 65 km. A crustal thickness of 85 km is not impossible if β_m = 4.8 km/s and would be required if β_m were yet larger.

P_L PHASE SYNTHESIS

We observed one very clear P_L phase that crossed Tibet (Fig. 2a). P_L propagates as a leaky mode in the crust and travels with velocity higher than the shear wave velocity of the underlying mantle [Gilbert, 1964; Oliver and Major, 1961]. The P_L wave train arrives between the P and S phases and is normally dispersed. P_L can be viewed as the result of multiple reflected and refracted P and SV waves, each of which is, at least once, an SV wave along the ray path [Helmberger, 1972].

Despite the energy leakage, the form of the P_L wave train can be used to infer the crustal structure. Both the phase and group velocity dispersion curves are fairly steep and the P_L wave train is generally short. This makes accurate measurements of dispersion difficult [e.g., Poupinet, 1972]. Instead, we have synthesized seismograms of P_L using different velocity structures in order to constrain the structure. Helmberger [1972] generated synthetic seismograms for P_L at distances between 4° to 13° from explosions using generalized

ray theory, which employs a Cagniard-DeHoop algorithm, He assumed a layer over half-space. We followed his approach and used a double-couple earthquake source [Langston and Helmberger, 1975].

We calculated synthetic seismograms by summing generalized rays of up to suite order number 7 (7 segments in a ray) with a double-couple source at 5 km depth. The fault plane solution is the same as that used in the surface wave calculations before. No attenuation operator is applied to the synthetic seismograms. When we applied Futterman's [1962] constant Q operator with $t/Q \sim 1$ (where t is the travel time) the difference in the waveforms was barely discernible. (This corresponds to an average $Q \sim 300$ for our case). The assumed far-field source time history is given by exp[-t/10 (sec)]t, which would correspond to a fault length of about 30 km in Brune's [1970] formulation.

At first, synthetic seismograms were generated for models with a layer over half-space, each of which represented an average of the velocities in models obtained from surface wave dispersion. Figures 14a and 14b show the synthetic seismograms for two models with 70 km and 85 km thick crusts respectively, together with the observed signal. The first large peak in the synthetic seismograms results from S to P and P to S reflections off the Moho. The large amplitudes at the beginning of the observed seismogram are the direct, P, pP

and sP, which penetrated into the upper mantle to 400-600 km and were not synthetized here. Numrical experiments showed that variations in the mantle velocities between 8.2 to 8.5 km/s have a negligible effect on the large amplitude pulse in the synthetic seismograms. Despite the poor fit between the theoretical and observed seismograms (Fig. 14a), we notice that two quite different models (with a difference of 15 km in crustal thickness) gave similar wave forms in the synthetic seismograms (Fig. 14b). The maximum difference in group velocity between the two synthetic seismograms is only about 2%. This suggests poor resolution of velocity structures with P_L observations alone.

Next, we examined a series of multi-layered models similar to those based on surface wave dispersion in the last section. Helmberger [1972] concluded that for a layer over half-space, the source depth is not crucial, as long as the source is in the layer. A top low velocity layer has a small effect on the long period character of the synthetic seismograms. From a series of numerical experiments with model SE (Fig. 12b) we found that the effect of source depth and that a low velocity layer are insignificant as long as the source is in the layer next to the low velocity surface layer. We tried several models based on surface wave dispersion that included crustal reflectors. Only rays reflected between the free surface and the interfaces including and above the Moho were used. Fig. 14c shows one

example of such a synthesis. This particular model SEM1 has the same shear wave velocity structure as model SE (Fig. 12b), except the upper crustal layer has a P wave velocity 7% less than that of model SE. The large Moho reflections seen in Fig. 14b are suppressed. In addition, the late large arrivals, which resulted from the mid-crustal reflector, have a significant effect on the long-period wave form (compare Figs. 14c and 14b). The synthetic seismogram from this three-layered crustal model fits the long period characteristics of the P_L observation much better than the single layered crust cases. Other models were tested and both velocities and layer thicknesses were modified in a trial and error process. No significant improvement was found with models of different crustal thicknesses and structures from that of model SE, and with a modified model S7 with a linear crustal-mantle transition. The model 'TP-2', with a low velocity zone in the crust preferred by Chun and Yoshii [1977], does not provide a better fit either, even after some variations in its crustal and mantle structures. Presumably, with more layers in the velocity models we might achieve a better match to the observed P_L signal. Yet considering the poor resolving power of the structure, further trial seems fruitless. It is likely that the gross form of P_L can be matched with crustal thickness of 55 to 85 km if there is a velocity gradient in the crust, but that the observations do not constrain the structure very much.

REFRACTION PROFILES

It is well-known in classical seismology that the P_n and S_n velocities can be estimated from the travel time vs. distance plot using close earthquakes [e.g. Bullen, 1963, p. 194]. This involves using many stations for each event. Although, to our knowledge, Lhasa (LHA) has been the only permanent seismograph station in Tibet, the usual method can be applied using travel times from many close earthquakes at a single station.

For refraction in a layered spherical earth model, the travel time t can be expressed in the form

$$t = r_p \Delta / v_p + Ap \qquad (1)$$

where r_p is the radius of the earth to the given interface (the Moho in our case), Δ is the epicentral distance in radians, and V_p is the head wave velocity. The intercept time, Ap, can be expressed by the integral:

$$Ap = \int_o^{z_p} [1/V^2 - (r_p/r)^2/V_p^2]^{1/2} dZ + \int_h^{z_p} [1/v^2 - (r_p/r)^2/V_p^2]^{1/2} dz \qquad (2)$$

r, z_p, h and v are the radius of the earth, the depth of the deepest point on the ray, focal depth and velocity (as a function of depth z) above the Moho, respectively [see e.g., Bullen, 1963, p. 194]. Note that Ap is not related to the horizontal distance. From eq. (1) we have the following expression for the ith event at the given station:

$$t_i - [(Ap_i + \tau_i) + r_p \Delta_i v_p^{-1}] = \varepsilon_i \qquad (3)$$

where t_i is the measured travel time, τ_i is the difference between the calculated and actual origin time, and ε_i is the travel time residual. The usual least square solution can be applied to minimize $\sum_i \varepsilon_i^2$ and thus estimate V_p^{-1}.

In practice, earthquakes are reported with different focal depths. Moreover, the focal depths can easily be in error causing a corresponding error in the origin time. In either case, to use equation (3), it is necessary to normalize the focal depth to a common depth in order to avoid introducing artificially large residuals due to different focal depths and therefore path lengths. This can be done by adjusting the origin time with a depth correction calculated from equation (2), assuming an approximate velocity structure. The term τ_i in eq. (3) is assumed to be absorbed by this depth correction completely. Any incomplete trade-off between the focal depth and the origin time, together with a small error induced by the assumed velocity structure will cause a possible systematic error, which is presumably independent of distance, in the normalized travel times. We assume this only introduces random errors so that only the variance associated with the velocity determination is affected, not the estimate of the velocity.

P_n and S_n arrival times were taken from the Lhasa station reports available between 1960 and 1965 and again

between 1971 and 1973 [Institute of Geophysics, 1966, 1974]. We selected well-located events, for which more than 35 readings from teleseismic stations were used in the location. We used the epicenters, origin times, and depths given in the Bulletins of the International Seismological Summary (ISS) and the International Seismological Center (ISC).

P_n across Tibet: All 61 P_n arrival times between 3° to 17° from Lhasa are plotted in Fig. 15. A model with a crustal layer with P wave velocity (V_p) of 6.1 km/s over a half-space with v_p = 8.0 km/s was assumed to normalize the focal depth to 33 km, which is near the mean reported depth. We took r_p in equation (2) to be 6306.2 km. For a Moho at 35 km depth, instead of 70 km, the estimated velocity should be increased by 0.5%. The P_n velocity is determined to be 8.15 $\pm$ 0.04 km/s, compared with 8.27 $\pm$ 0.07 km/s if no depth correction is applied (Table II). If the apparent velocity were in fact 7.9 km/sec, then the data should be more nearly parallel to the dashed line in Fig. 15. A low P_n velocity will not fit the data well unless there is some special distance dependent systematic error in locations, depths or origin times. If we limit ourselves to sharp P_n arrivals (excluding those reported as eP or eP_n in the station reports), we obtain a P_n velocity of 8.20 $\pm$ 0.04 km/s from 42 arrivals. Without the depth correction, we obtain 8.24 $\pm$ 0.09 km/s (Table II).

If we consider only the 39 sharp arrivals between 3° to

10° (Fig. 16), the P_n velocity is estimated to be 8.12 ± 0.06 km/s for the depth corrected case (Fig. 16b). This is the only case in all the profiles discussed in this section for which the P_n velocity determined without a depth correction, 8.0 ± 0.1 km/s (Fig. 16a) is the smaller. A total of 19 emergent arrivals between 3° to 17° gave an estimate of the velocity of 8.18 ± 0.13 km/s. Thus the entire data set is very consistent (Table II).

P_n across the Himalaya: The data discussed above includes only events north of the Indus Tsang-Po suture because of the possibility of a different structure beneath the Himalaya. However, recordings at Lhasa for 24 events, south of the suture, for nearly all of which sharp readings were reported yields a P_n velocity of 8.11 ± 0.07 km/s. The epicentral distances range from 3° to 17°. Among these, 21 events occurred within 10° of Lhasa (Fig. 17). Despite the scatter, the same estimate for P_n velocity is obtained. Thus no significant difference in the P_n velocity is observed for regions north and south of the suture zones.

S_n across the Tibet and the Himalaya: There are also 23 sharp S_n arrivals reported at Lhasa from events north of the suture in the distance range 3° to 10°. (Only three such arrivals were reported for distances greater than 10°). After the depth normalization, the S_n velocity is estimated to be 4.8 ± 0.1 km/s (Fig. 18). There is a much larger scatter in the S_n residuals

than the P_n residuals probably because of the slower S_n velocity and because of difficulties in identifying the arrival on the seismograms. A low S_n velocity of 4.5 km/s does not fit the data well (Fig. 18). The 11 sharp arrivals for events south of the suture, reported at Lhasa within 3° to 10° gave the same S_n velocity (Table II).

Intercept times and crustal thicknesses: Despite the large uncertainties, the intercept times for P_n all suggest the depth of the interface (the Moho) to be 65 $\pm$ 30 km. S_n intercept times have even larger uncertainties, but the depth of the interface calculated from them fall within the range (Table II) of 80 $\pm$ 50 km. The epicenters of all the events used in this refraction study show a broad azimuthal coverage and distribution of epicentral distances with respect to Lhasa (Fig. 19). Nevertheless, because as purely reversed profile cannot be made, it is remotely conceivable that a dipping Moho might render the real mantle velocities different from the measured apparent velocity. For models with a crustal layer with v_p ranging from 5.9 to 6.5 km/s overlying a mantle half-space with v_p ranging from 7.9 to 8.4 km/s, a uniform dip of about 0.8° of the Moho could add an uncertainty of $\pm$0.1 km/s to estimated P_n velocity, depending on the direction of the dip. Such a dip would correspond to a difference in crustal thicknesses of 15 km over 10° distance. Therefore, if Lhasa were to overlie a maximum depth to the Moho beneath Tibet, such that the

crustal thickness decreased by 15 km, 10° to both the north and west, then the P_n velocity could be overestimated by 0.1 km/s. We think that because the average elevation of Tibet is so uniform, a drastic variation in crustal thickness is unlikely, and it would be fortuitous if Lhasa were to overlie the deepest crust. Notice that here Lhasa is the 'shot point' for the refraction profiles.

Summary of refraction results: High values of the P_n and S_n velocity beneath Tibet are obtained from refraction profiles using earthquakes in Tibet and arrival times at Lhasa. Assuming a Moho at 70 km depth, the P_n velocity is estimated to be 8.12 km/s with a minimum formal standard deviation of 0.06 km/s covering the region north of the suture from 3° to 10° from Lhasa. No significant difference in P_n velocity was found for the regions north and south of the suture. With a somewhat larger uncertainty, the velocity of S_n is similarly determined to be 4.8 ± 0.1 km/s. Both P_n and S_n velocities are about the same as those of the shields and stable platforms. All the intercept times have large uncertainties and they indicate a depth of the Moho of 65 ± 30 km.

TELESEISMIC S-P TRAVEL TIME RESIDUALS

To our knowledge, the high velocities for the uppermost mantle under Tibet discussed in the last section have not been proposed before. The vertical extent of the high velocity zone is of great importance in the interpretation

of the tectonics. The refraction profiles require a layer beneath the Moho with a thickness of only about 10 km. P_L is relatively insensitive to mantle properties [Poupinet, 1972] and the surface wave dispersion curves are not very sensitive to the velocity structure below about 100 km. The teleseismic travel time measurements discussed in this section are intended to serve as a crude estimate of the vertically averaged velocity structure to a greater depth ($\sim$300 km).

Teleseismic P and S wave arrival times were measured from the records of the WWSSN stations for 9 earthquakes in Tibet and 8 earthquakes in the Himalaya (Fig. 20, Table III). Arrival times were measured only for S wave signals that are clear on the long-period records (Fig. 21). Uncertainties are about one second. To avoid inclusion of converted phases (e.g., Sp), we tried to measure only the transverse components of the S waves. S-wave polarization angles were checked with known P wave fault plane solutions [Molnar and Tapponnier, 1978; Molnar et al., 1973, 1977; Ni and York, 1978]. We considered only the distances range between 30° and 80° to avoid triplication in the S wave travel time curve, and possible misidentification of SKS for S.

Both P and S wave travel time residuals, with respect to the Jeffreys-Bullen [1940] (J-B) travel time tables, were plotted as a function of epicentral distance using locations and origin times given by the ISC. Since the hypocenters and origin times reported by ISC were calculated primarily using the J-B P wave travel times, the P wave residuals were automatically minimized. Therefore the S-P travel time residuals are an approximation to the S wave travel time residuals. Because late (or early) S waves are likely to be associated with late (or early) P waves, the S-P residuals measured here probably give lower bounds to the S wave residuals.

For 9 earthquakes in Tibet, P wave residuals scatter around the mean as expected from the hypocenter location procedure, whereas S waves travel times show large delays (Fig. 22). The S-P travel time residuals have correspondingly large delays (Table III, Figs. 22 and 24). Applying station corrections [Sengupta, 1975; Sengupta and Julian, 1976] to these data does not significantly reduce the scatter, but increases the S-P travel time residuals by about 1 sec (Table III, Figs. 22 and 24).

With the same procedure, we studied 8 earthquakes in the Himalaya (Fig. 23) and observed smaller S-P travel time residuals than for earthquakes in Tibet (Table III, Figs. 23 and 24). The rays from earthquakes in Tibet and the

Himalaya to a given station more than 30° from the epicenters will have nearly identical paths except near the source region. Thus we infer that the large S-P travel time delays for earthquakes in Tibet are due to the medium properties of the region beneath Tibet and not to systematic errors in the travel time tables or to the medium along the rest of the ray paths.

In general, there is a strong trade-off between the focal depth and the origin time for events located teleseismically. Erroneous depths could also, at least partially, be responsible for the large S-P travel time delays for earthquakes in Tibet, if these earthquakes actually occurred at a shallower depth than was obtained in the location procedure. The S-P travel time residuals were calculated for each event assuming three possible depths: their depths given by the ISC, 5 km, and 33 km (Fig. 24). To make an extreme comparison, assume all earthquakes in Tibet occurred at 5 km depth, but all earthquakes in the Himalaya occurred at 33 km depth. On the average, there is still a difference of approximately 2 sec between the S-P residuals from earthquakes in these two regions (Fig. 24, Table III).

Thus the average S-P travel times are late for events in Tibet not only with respect to the J-B tables which represent an averaged earth model but also with respect to those for events in the Himalaya. Because low P wave

velocities probably cannot be detected through routine location procedures using the P wave arrival times alone, a delay of ls in P wave travel times from the average earth could easily exist. This would lead to another second in delay in the S wave travel time. These lower bounds on the S-P travel time residuals are given in 1 sec intervals in Figure 20 together with the location of the 17 earthquakes. For this figure, the focal depths for Tibetan events are normalized to 5 km and for Himalayan events, at 33 km. Although our data points certainly do not allow a meaningful contouring of these residuals in Tibet, the two earthquakes in the center of Tibet have especially large S-P travel time residuals (>5 sec). Moreover, the distribution of S-P travel time residuals in the Himalaya is uniform. The immediate inference from the late S-P travel times in Tibet is that the relatively high P_n and S_n velocities obtained from the refraction profiles discussed in the last section are not likely to extend to a great depth beneath Tibet.

SEISMIC WAVE VELOCITY STRUCTURE

Observed group and phase velocity dispersion curves of Rayleigh waves provide constraints on crustal thickness and the uppermost mantle shear wave velocity. For possible thicknesses of 55 km to 70 km, or even 85 km, the corresponding uppermost mantle shear wave velocities of 4.4 km/s or less to 4.7 $\sim$ 4.8 km/s, or even as large as 4.9 km/s, are required

respectively. We consider an S_n velocity of 4.9 km/sec to be unlikely and therefore conclude that the crust probably is not as thick as 85 km.

The paths for the observations of surface waves and P_L phase all cross the Himalaya. This apparent lateral inhomogeneity introduces an additional uncertainty that is difficult to quantify. The two clear long-period Rayleigh wave signals studied here cross the Himalaya at very different angles (Fig. 1). The 3% difference in the group velocities could be a consequence of lateral heterogeneity. We cannot confidently attribute this difference solely to real structural differences because of the uncertainties in the group velocity determinations.

Since both the P_n and S_n velocities were estimated to be high from the refraction profiles, P_n velocity 8.12 $\pm$ 0.06 km/s, S_n velocity 4.8 $\pm$ 0.1 km/s, the crustal thickness is apparently about 70 km. It is difficult to attach a formal uncertainty to this thickness, but from the comparison between the observed and theoretical dispersion curves, we estimate that the crustal thickness is between 65 km and 80 km (Figs. 9 and 10). These models seem to be compatible with the P_L wave form, but it does not provide a strong constraint on the velocity structures by itself.

Travel time measurements for earthquakes in Tibet to stations at distances of 30° to 80° indicate late S waves and long delays between P and S. Since the Tibetan earthquakes

have late S-P travel times compared with earthquakes in the Himalaya, the average velocity beneath Tibet must be lower than that of the Himalaya. The relatively high velocity zone beneath the Moho of Tibet, estimated from the refraction profiles therefore probably is not thick.

With some additional assumptions, the data can be used to estimate differences in average upper mantle velocities beneath Tibet and stable platforms or shields. Suppose all such differences were confined to the upper 240 km as inferred for shields and ocean basins [Dziewonski, 1971; Okal, 1977]. Also assume that the measured S-P travel time residuals are estimates of S wave travel time residuals. Let us compare the Tibetan models with model S2 of Dziewonski [1971] for the shield regions, but with a 70 km thick crust. The additional 35 km of crust beneath Tibet or the Himalaya, replacing the uppermost mantle in model S2, corresponds to about 2 sec in S wave travel time delay. This effect could explain the average delay of about 2 sec (with respect to the J-B tables) for the Himalayan events, but it cannot account for the difference between the data from Tibet and the Himalaya. As an extreme let us assume that the earthquakes in Tibet occurred at a depth of only 5 km. If one increases the velocities of model S2 by about 1% to correct for the effect of velocity dispersion due to attenuation [Hart et al., 1977], then the vertical one way S wave travel time between the depths of 0 and 240 km for model S2 is 53.8 sec. This is about 1.1 sec faster than that for the Jeffreys-Bullen model. Therefore the

observed average S-P travel time delay of 3.6 sec with respect to the J-B tables for earthquakes in Tibet corresponds to an average difference of 4.7 sec in S wave travel time of which 2 sec can be attributed to the effect of a thick crust. The resulted S wave travel time difference of 2.7 sec corresponds to a reduction of the shear wave velocity of 6% between 70 to 240 km compared with model S2. If we assume that models S7, SE (70 km thick crust, β_m = 4.7-4.8 km/s, Figs. 6 and 12) and F4 (55 km thick crust, β_m = 4.4 km/s, Fig. 5) could be appropriate for Tibet in the depth range from 0 to 100 km, then the average shear wave velocity beneath Tibet must still be about 4 to 5% lower than that of model S2 for shields between the depths of 100 km and 240 km. Insofar as Dziewonski's [1971] model S2 is appropriate for the shields, this corresponds to the average shear wave velocity of about 4.3 km/s between 100 and 240 km depth beneath Tibet. Because of S-P residuals are lower bounds to the S wave delays and because we assumed extreme for the depths of the events in Tibet, the average shear wave velocity beneath Tibet could be lower.

The effect of velocity dispersion due to attenuation has been neglected in the above discussions of crustal thickness. It is difficult to estimate the contribution from such velocity dispersion without sufficient data on both attenuation and phase velocity [e.g., Lee and Solomon, 1978]. Qualitatively, if strong attenuation exists, the estimate of shear wave velocities from surface waves should

be increased by a small amount (∿1%) above those considered here before comparing them with body wave observations [Hart et al., 1977]. Thus there might be a small systematic overestimate of a few km of the crustal thickness, but this overestimate is probably much less than the uncertainty quoted above.

TECTONIC IMPLICATIONS

A. The Thick Crust

The apparently very thick crust (∿70 km) beneath Tibet implies that the crust has been thickened approximately by a factor of 2 since the collision between India and Eurasia. This is consistent with the idea of horizontal compression and shortening [Dewey and Burke, 1973]. The hypothesis of underthrusting the Indian plate beneath the Eurasian plate can be argued as still possible if somehow either the crust of Tibet were detached from its underlying mantle while the Indian plate was subducted along the base of the crust or if the Indian crust plunged into the mantle and then migrated, probably as a melt, up to the base of Tibet's crust. In other words, continental crust of 1000 km length would have been consumed and recycled back near the surface in a time span of about 40 m.y.

B. Uppermost Mantle Seismic Velocities

Both P_n and S_n velocities indicate a high velocity uppermost mantle under Tibet. The late S-P travel time

residuals for earthquakes in Tibet indicate that these high velocities do not reflect the properties of the deeper part of the upper mantle. Although the interpretation of the travel time residuals are highly non-unique; a lithosphere, defined by seismic velocities, of about 100 km thickness under Tibet is consistent with the observations.

Implications for the temperature in the mantle: The apparently high uppermost mantle velocities under Tibet are not directly comparable to those under the stable platforms and shields because the extremely thick crust in Tibet will create about 10 to 12 kb additional lithostatic pressure at the base of the thickened Tibetan crust. Assuming that the pressure and temperature dependence of seismic wave velocities for olivine are representative of the mantle [e.g., Anderson et al., 1968; Birch, 1969], 10 kb of pressure causes an increase in V_p of about 0.1 km/s and a temperature increase of about 250°C causes a similar decrease. V_s has very similar pressure-temperature dependence to that of the V_p for most olivine group minerals, but with the exception of forsterite samples measured by Anderson et al. [1968], which have been questioned by Birch [1969]. Thus, if the P_n and S_n velocities were the same beneath stable platforms and Tibet and if the temperature and pressure dependencies of the seismic velocities were those appropriate for olivine, then the temperature of the Moho beneath Tibet would be about 250°C

hotter than that of the platform. This estimate of relative temperature would have an uncertainty as large as 120°C, even if the resolution of the difference in P_n velocity for Tibet and shields were only $\pm$0.05 km/sec. Thus this suggested difference in temperature is only a crude estimate, not a precise measurement.

The temperature under platforms and shields are difficult to estimate. From heat flow measurements, Sclater et al. [1979] estimated a lower bound on the temperature for the Canadian shield to be less than 400°C at the base of the crust. On the other hand, if we take the measured reduced heat flow as an upper bound of the mantle heat flow for Eastern U.S. (0.80 $\pm$ 0.05 HFU, [Lachenbruch and Sass, 1976]) and the Indian shield (0.93 HFU, [Rao et al., 1976]), the mantle heat flow alone gives 470°C and 540°C at the base of the crust, respectively, assuming a crustal thickness of 35 km and thermal conductivity of 6×10^{-3} cal/cm°C-sec. Uncertainties in conductivity and heat flow measurements alone will probably add 20% uncertainties to those estimates. In any case, if the temperature at the base of the crust beneath platforms and shields were about 500°C, then at the Moho beneath Tibet it could be about 750°C. Although the uncertainty in this number is very large, our point is that the high P_n and S_n velocities do not require an unusually cold upper mantle.

Implications for the strength of the mantle: The temperature at the Moho strongly affects on the mechanical behavior of the lower crust and upper mantle. One can estimate the mechanical strength of the uppermost mantle beneath Tibet assuming that the flow laws for steady state creep of olivine are representative of the uppermost mantle rheology [Goetze and Evans, 1979; Kirby, 1977; Tapponnier and Francheteau, 1978]. For differential stress $(\sigma_1-\sigma_3)$ less than 2 kb, the flow law can be written in the form:

$$\dot{\varepsilon} = A(\sigma_1-\sigma_3)^n \exp(-Q/RT) \qquad (4)$$

where $\dot{\varepsilon}$ is the strain rate, A and n are constants, Q is the activation energy, R is the gas constant and T is the absolute temperature. For dislocation creep of olivine, Goetze [1978] reported n = 3, A = 70 (bar^{-3} sec^{-1}), and Q = 122 (kcal/mole). Note that the uncertainties in the estimate of activation energy and temperature will dominate the uncertainty of the estimate of the differential stress or strain rate. Assuming a strain rate corresponding to 100% strain for the past 40 m.y., since the collision, the calculated differential stress is 1.1 kb at 750°C or 430 bars at 800°C. If the temperature were as low as 700°C, the calculated differential stress would be larger than 2 kb. Post [1977] obtained a quite different olivine flow laws for Mt. Burnet dunite. Using his 'dry' flow low under the same assumptions, differential stress is estimated to be 3.7 kbars at 800°C while the 'wet' flow law requires

only 30 bars of differential stress under these conditions. If Coble creep (syntectonic recrystalization), instead of dislocation creep, however, is the predominant deformation mechanism, the calculated differential stress is only 210 bars at 800°C and 430 bars at 700°C at the given strain rate [Goetze, 1978]. Thus the lower bound of the differential stress required to deform the uppermost mantle under Tibet at the given strain rate through steady state ductile flow of olivine is only about 0.4 kb. Although the extimate of temperature beneath Tibet is too uncertain to prove that the uppermost mantle is not strong, the apparently high P_n and S_n velocities beneath Tibet do not require high mechanical strength for the uppermost mantle.

Implications on volcanism in Tibet: It is interesting to note that at temperatures of about 800°C and 20 kb pressure, incipient melting of crustal material (but not the uppermost mantle) is possible in the presence of a small amount of water. Fig. 25 shows solidi for some likely crustal and upper mantle materials based on data from experimental petrology [Lambert and Wyllie, 1970; Merrill et al., 1970; Merrill and Wyllie, 1975]. None of the data have error bars and therefore can only be used qualitatively. Nevertheless, the solidus for

water saturated peridotite is over 1000°C despite the pressure [Merrill et al., 1970]. With only 0.1 weight% of water, partial melting of gabbroic material is possible at 20-25 kb pressure and between 700 to 800°C [Lambert and Wyllie, 1970]. The solidus for peridotite with 0.1 weight% water at this pressure range is over 1250°C. Thus for Tibet, there could be enough heat conducted from the mantle to support a partially molten crust on a subsolidus uppermost mantle. The inference of a high velocity mantle lid on the low velocity zone, then, is not incompatible with the widespread volcanism over Tibet unless the volcanic activity is predominantly of mantle origin or unless the lower crust of Tibet consists of only anhydrous minerals. The geochemical evidence gathered so far is not sufficient to reach any conclusion on whether the lower crust of Tibet is hydrous or not. Simply based on the fact that no basalt was found [Hennig, 1915, Deng, 1978], it is believed that the volcanic activity involved melting of crustal materials only. The unusually low average crustal velocity for Tibet is also consistent with high temperatures and melting.

C. A Discussion of the Thermal Evolution of the Plateau

The presence of widespread volcanic activity and diffuse seismicity with prominent normal faulting in Tibet (Molnar and Tapponnier, 1978) all indicate that Tibet is tectonically active at present. Yet the geothermal gradient in the crust should have been decreased by crustal thickening. Thus the

source of heat deserves some consideration. There are three apparent heat sources that contribute to Tibet's crustal geotherm: strain heating from the thickening of the crust, radioactive heat production in the crust and the mantle heat flux from below the crust.

Since the crust of Tibet seems to be twice as thick as normal continental crust, the average strain rate in the crust is likely to be of the order of 1/40 m.y. Assuming an averaged stress of 1 kb throughout Tibet, the stress heating rate per unit volume (stress x strain rate) is only about 8×10^{-7} erg/cm^3-sec or 0.2×10^{-13} cal/cm^3-sec (0.2 HGU). This is considerably smaller than the presumed radioactive heat production rate of lower crustal materials [e.g., Tilling et al., 1970] and can be neglected.

We investigate the effects of the mantle heat flux and radioactive heating in the crust by considering the simple one-dimensional heat conduction problem with the following assumptions:

1. A constant mantle heat flux (Q_h) is held at the base of the crust.

2. The thickening of the crust is instantaneous and the original geotherm is stretched accordingly. This serves as the initial condition.

3. Tibet defines a heat flow province such that the the empirical relationship $Q_s = Q_o + D\ A_o$, (5) between surface heat flow (Q_s) and surface heat production rate (A_o) is valid.

4. There has been no erosion. This assumption is justified by the facts that the Cretaceous limestone is still widespread [Hennig, 1915, Norin, 1946], and that the present-day drainage system in Tibet is internal [Molnar and Tapponnier, 1978].

We separate the temperature T in the crust into the contributions from the mantle heat flux T_m and from radioactive heat production T_R. Three possible distributions of radioactive heat producing elements in the crust are considered separately: (a) a uniform distribution with depth, (b) an exponentially decaying distribution as a function of depth with the surface heat production rate unchanged by crustal thickening, i.e., with no migration of heat producing elements after crustal thickening, and (c) an exponentially decaying distribution with depth but with the thickness of the layer of the variable heat producing elements unchanged by crustal thickening (i.e., the migration of radioactive heat producing elements is much faster than heat conduction). The detailed derivations are given in Appendix A. Throughout this discussion, the crustal thickness is taken to be thickened by a factor of two to a value of 70 km. We also assumed that the thermal conductivity

(k) = 6 x 10^{-3} cal/cm-°C-sec and the thermal diffusivity (κ) = 0.01 cm^2/sec. Note that T_m can be scaled to any desired crustal thickness rather easily (Fig. A1). We shall concentrate our discussions only on the temperature at the base of the crust where it will be highest in the crust.

First, consider only T_m with two starting temperatures ($T_m°$) 500°C and 600°C, corresponding to mantle heat flow (Q_h) of 0.86 μcal/cm^2-sec (HFU) and 1.03 HFU respectively in a steady state. T_m will reach 800°C in about 45 and 14 m.y. (Fig. A1(a)) respectively. If thickening were not instantaneous but took place in four steps 10 m.y. apart, by using Fig. A1(a) we find that T_m = 800°C after 42 m.y. if $T_m°$ = 500°C or after 22 m.y. if $T_m°$ = 600°C. The reason for the increase in time to reach 800°C for the 600°C starting temperature compared with instantaneous thickening is due to a subtle trade-off between the scaling of time and the ratio of T_m to its asymptotic value T_m^∞ by the crustal thickness (Fig. A1(a)).

The contribution from radioactive heat production strongly depends on the distribution of those elements, parameterized by the constant D, in equation (5). The steady state temperature due to radioactive heat production (T_R^∞) is approximately proportional to D^2. For an exponential distribution of radioactivity, D must be much smaller than the crustal thickness to satisfy equation (5) [Lachenbruch, 1970]. If the differentiation of the radioactive heat producing elements

is much faster than heat conduction so that D does not change during crustal thickening, then T_R contributes little to the crustal geotherm. In this case, where $T_R°$ is the contribution to the initial geotherm due to radioactivity, $T_R^{\infty} \sim 2T_R°$ (case c) not $4T_R°$ as is the case when doubling of the crust also doubles D (cases a and b). Moreover, the rate of change of T_R is relatively slow (Fig. A2). This occurs because in most models, and probably in the earth also, the source of heat is far from the base of the crust.

For cases (a) and (b), $T_R^{\infty} \sim 4T_R°$ and after 40 m.y., $T_R \tilde{\sim} 2T_R°$. For instance, at 70 km depth, for case a, with Q_h = 0.75 HFU, D = 25 km and $A(z) = A_o$ = 1 HGU (i.e., T° = 438 + 52 = 490°C), in 40 m.y. T = 687 + 114 = 801°C (Appendix A, Fig. A2). If we assume for case (b) that D = 7.5 km and $A(z) = 10 \exp(-z/D)$ HGU, (i.e., T° = 438 + 89 = 527°C) T = 654 + 162 = 816°C in 30 m.y. (Appendix A, Fig. A2). The steady state final heat flow at the surface would be only 1.25 HFU for the former case and 2.25 HFU for the latter. Since heat flow measurements are not available for Tibet, these hypothetical values are only meaningful as plausibility arguments and they should not be taken as fact. Nonetheless, the above calculations suggest that it is possible that the lower crust of Tibet could reach 700-800°C in 40 m.y., simply from the recovery of the geotherm provided that the heat flux from the mantle is greater than about 0.9 HFU without any

heat production in the crust. The starting temperature at the base of the crust is crucial in determining whether the temperature in the lower crust reaches 700 to 800°C in 40 m.y. A reasonably warm starting temperature of 490°C at the Moho can be maintained by a mantle heat flux of only 0.75 HFU, if there is sufficient radiogenic heat production in the crust (to produce 0.5 HFU) after the crustal thickening. Then the calculated temperature at the Moho would reach 801°C after 40 m.y., as in the example given for case (a) before. Thus radioactive heat production could be important for the recovery of crustal geotherm in 40 m.y., if radioactive heating also makes a significant contribution to the original goetherm [Bird et al., 1975].

Crustal shortening beneath Tibet by horizontal shortening [Dewey and Burke, 1973] seems to be compatible with both the seismic observations and these thermal calculations. Yet the behavior of the lithosphere as a whole during the continental collision is not clear. In fact, the assumptions in these calculations are directly related to this question. If we assume that at 70 km depth the mantle heat flux is about 0.9 HFU and the temperature is about 800°C, for a coefficient of thermal conductivity (k) of 7.5×10^{-3} cal, cm/sec°C the 1300°C isotherm will be reached at about 112 km. If indeed the lithosphere were maintained at an approximately

constant thickness by a heat flux of about 0.9 HFU at the base of the non-convective layer, then the estimated temperature at the base of the Tibetan crust could be explained simply in terms of the recovery of the geotherm with little contribution by radioactivity. The volcanic activity would be the result of the depression of the lower crust to depths where the temperature is high enough for it to melt. No anomalous heat flow from the asthenosphere would be required.

Presumably small scale convection maintains an essentially constant heat flux at the base of the plate. Parsons and McKenzie [1978] describe this in terms of the stability of a thermal boundary layer above the viscous asthenosphere and with a thickness δ between two isotherms. If a critical Rayleigh number $Ra_c = \frac{g\alpha\Delta T\delta^3}{\kappa\nu}$ is exceeded, the boundary layer becomes unstable so that small scale convection occurs and provides convective heat transport. In Ra_c, g is the gravitational acceleration, α the coefficient of volumetric thermal expansion and ν is the kinematic viscosity. If the whole lithosphere with the thermal boundary layer were thickened by horizontal shortening, δ would increase and Ra_c would increase as δ^3. This instability would be a very effective way of enhancing the instability of the boundary layer and causing small scale convection. Effectively there would be a detachment of the bottom of the thickening lithosphere that might tend to keep the lithosphere from continuing to thicken as the crust does.

CONCLUSIONS

1. The crust beneath Tibet is about 65 to 80 km thick with an averaged shear wave velocity of less than 3.5 km/s from surface wave dispersion, refraction profiles and P_L-phase synthesis.

2. P_n and S_n velocities were estimated to be 8.12 ± 0.06 km/sec and 4.8 ± 0.1 km/sec respectively.

3. The averaged vertical shear wave velocity between 70 to 240 km depth is about 6% lower than that of the shield model S2 [Dziewonski, 1970] and this average velocity beneath Tibet is also lower than that below the Himalaya.

4. From the P_n and S_n velocities and the pressure-temperature dependence of the seismic velocities for olivine, the temperatures at the base of the Tibetan crust could be about 250°C hotter than that beneath shields or stable platforms. Since the temperature at the Moho beneath platforms is about 500°C, the base of the crust beneath Tibet could be near 750°-800°C.

5. At this temperature, and depending on deformation mechanism, the uppermost mantle is likely to have a maximum mechanical strength of less than about 1 kb. This value decreases rapidly with depth in the uppermost mantle.

6. Partial melting of the lower crustal materials but not upper mantle is likely with these estimated temperatures. The low crustal velocities are consistent with a hot or molten lower crust.

7. Simple one-dimensional heat conduction calculations suggest that no anomalous mantle heat source is needed to explain the volcanic and tectonic activity provided that a heat flux of about 0.75 to 0.9 HFU (depending on the amount and distribution of crustal heat production) is available from the asthenosphere and that the thickness of the lithosphere does not increase drastically throughout the collision.

Acknowledgements

We are grateful to A. Dainty who did much work in implementing a double-couple source to the generalized ray program STPSYN-3 by D.V. Helmberger and R.A. Wiggins. M. Bouchon, A. Dziewonski and H. Kanamori kindly made their programs available to us. J. Ni provided several fault plane solutions in Tibet prior to their publication. K. Anderson, T.A. Chou, W.Y. Chung, W. Ellsworth, H. Patton and G. Stewart helped us in computations. We also benefitted from discussions with K. Burke, P. England, B. Parsons, and P. Tapponnier.

This research is supported by the National Science Foundation Grant No. 77-23017 EAR.

References

Amboldt, N., Relative Schwekraftbestimmungen mit Pendeln in Zentralasien, Reports from the Scientific Expedition to the Northwestern Provinces of China under the Leadership of Dr. Sven Hedin, Publ. 30 (II), Geodesy 2, Tryckeri, Aktiebolaget Thule, Stockholm, 1948.

Anderson, O.L., E. Schreiber, R.C. Liebermann, and N. Soga, Some elastic constant data on minerals relevant to geophysics, Rev. Geophys., 6, 481-524, 1968.

Argand, E.C.R., La tectonique de l'Asie, 13th International Geological Congress, Brussels, 1922, Comptes rendu, I, Pt. 5, 171-372, 1924.

Birch, F., Density and composition of the upper mantle: First approximation as an olivine layer, in The Earth's Crust and Upper Mantle, P.J. Hart (ed.), Geophys. Monograph, 13, Amer. Geophys. Union, Washington, D.C., 1969.

Bird, P., Thermal and mechanical evolution of continental convergence zones: Zagros and Himalayas, Ph.D. Thesis, Massachusetts Institute of Technology, Cambridge, MA, 1976.

Bird, P., and M.N. Toksöz, Strong attenuation of Rayleigh waves in Tibet, Nature, 266, 161-163, 1977.

Bird, P., M.N. Toksöz, and N.H. Sleep, Thermal and mechanical models of continent-continent convergent zones, J. Geophys. Res., 80, 4405-4416, 1975.

Brune, J.N., Tectonic stress and the spectra of seismic shear waves from earthquakes, J. Geophys. Res., 75, 4997-5009, 1970.

Bullen, K.E., An Introduction To the Theory of Seismology, 3rd ed., Chap. 12, Cambridge University Press, Cambridge, 1963.

Burke, K.C.A., J.F. Dewey, and W.S.F. Kidd, The Tibetan plateau, its significance for tectonics and petrology, Geol. Soc. Amer. Abstr. Programs, 6, 1027-1028, 1974.

Carslaw, H.S., and J.C. Jaeger, Conduction of Heat in Solids 2nd ed., Chap. 3.8, Oxford University Press, Oxford, 1959.

Chang, C. and H. Cheng, Some tectonic features of the Mt. Jolmo Lungma area, southern Tibet, China, Sci. Sinica, 16, 257-265, 1973.

Chen, W.P. and P. Molnar, Short-period Rayleigh wave dispersion across the Tibetan plateau, Bull. Seism. Soc. Amer., 65, 1051-1057, 1975.

Chun, K.Y., and T. Yoshii, Crustal structure of the Tibetan Plateau: A surface wave study by a moving window analysis, Bull. Seismol. Soc. Amer., 67, 735-750, 1977.

Deng, W., A preliminary study on the petrology and petrochemistry of the Quarternary volcanic rocks of northern Tibet autonomous region, Acta. Geol. Sinica, 52, 148-162, 1978.

Der, Z., R. Massé, and M. Landisman, Effects of observational errors on the resolution of surface waves at intermediate distances, J. Geophys. Res., 75, 3399-3409, 1970.

Dewey, J.F., and K.C.A. Burke, Tibetan, Variscan, and Pre-Cambrian basement reactivation: Products of a continental collision, J. Geol., 81, 683-692, 1973.

Dorman, J., M. Ewing, and F. Press, Study of shear-velocity distribution in the upper mantle by mantle Rayleigh waves, Bull. Seism. Soc. Amer., 50, 87-115, 1960.

Dziewonski, A.M., Upper mantle models from 'pure path' dispersion data, J. Geophys. Res., 76, 2587-2601, 1971.

Fitch, T.J., Earthquake mechanism in the Himalaya, Burmese, and Andaman regions and continental tectonics in central Asia, J. Geophys. Res., 75, 2699-2709, 1970.

Futterman, W.I., Dispersive body waves, J. Geophys. Res., 67, 5279-5291, 1962.

Gilbert, F., Propagation of transient leaking modes in a stratified elastic waveguide, Rev. Geophys. 2, 123-153, 1964.

Goetze, C., The mechanism of creep in olivine, Phil. Trans. Roy. Soc. Lond., 288, 99-119, 1978.

Goetze, C., and B. Evans, Stress and temperature in the bending lithosphere as constrained by experimental rock mechanics, Geophys. J. Roy. Astron. Soc., (in press), 1979.

Hart, R.S., D.L. Anderson, and H. Kanamori, The effect of attenuation on gross earth models, J. Geophys. Res., 82, 1647-1654, 1977.

Helmberger, D.V., Long-period body-wave propagation from 4° to 13°, Bull. Seism. Soc. Amer., 62, 325-341, 1972.

Hennig, A., Zur Petrographie und Geologie von Sudwestibet, in Southern Tibet, Vol. V, Kung, Boktryekeriet, P.A. Norstedt, Stockholm, 1915.

Institute of Geophysics, Preliminary Seismological Report of Central Station Peking and Auxiliary Stations, (1960-1965), (in Chinese), Academia Sinica, Peking, 1966.

Institute of Geophysics, Chinese Seismological Station Reports (1971-1973), (in Chinese), Academia Sinica, Peking, 1974.

Jeffreys, H., and K.E. Bullen, Seismological Tables, Brit. Assoc. Advancement of Sci., Gray-Milne Trust, London, 65 pp., 1940.

Kanamori, H., Synthesis of long-period surface waves and its application to earthquake source studies - Kurile Islands earthquake of October 13, 1963, J. Geophys. Res., 75, 5011-5027, 1970.

Kidd, W.S.F., Widespread late Neogene and Quaternary alkaline volcanism on the Tibetan plateau (abstract), EOS Trans. AGU, 56, 453, 1975.

Kirby, S.H., State of stress in the lithosphere: inferences from the flow laws of olivine, Pure Applied Geophys., 115, 245-258, 1977.

Kovach, R.L., Seismic surface waves and crustal and upper mantle structure, Rev. Geophys. Space Phys., 16, 1-13, 1978.

Lachenbruch, A.H., Crustal temperature and heat production: implications of the linear heat flow relation, J. Geophys. Res., 75, 3291-3300, 1970.

Lachenbruch, A.H. and J.H. Sass, Heat flow in the United States and the thermal regime of the crust, in: The Earth's Crust, J.G. Heacock (ed.), Geophys. Monograph, 20, Amer. Geophys. Union, Washington, DC, 1976.

Lambert, I.B., and P.J. Wyllie, Low-velocity zone of the earth's mantle: incipient melting caused by water, Science, 169, 764-766, 1970.

Landisman, M., A. Dziewonski, and Y. Sato, Recent improvements in the analysis of surface wave observations, Geophys. J. Roy. Astron. Soc., 17, 369-403, 1969.

Langston, C.A., and D.V. Helmberger, A procedure for modeling shallow dislocation sources, Geophys. J. Roy. Astron. Soc. 42, 117-130, 1975.

Lee, W.B., and S.C. Solomon, Simultaneous inversion of surface wave phase velocity and attenuation: Love waves in western North America, J. Geophys. Res., 83, 3389-3400, 1978.

Merrill, R.B., J.K. Robertson, and P.J. Wyllie, Melting reactions in the system $NaAlSi_3O_8$-$KAlSi_3O_8$-SiO_2-H_2O to 20 kilobars compared with results for other feldspar-quartz-H_2O and rock - H_2O systems, J. Geol., 78, 558-569, 1970.

Merrill, R.B., and P.J. Wyllie, Kaersutite and kaersutite eclogite from Kakanui, New Zealand— Water-excess and water-difficient melting to 30 kilobars, Geol. Soc. Amer. Bull., 86, 555-570, 1975.

Molnar, P., W.P. Chen, T.J. Fitch, P. Tapponnier, W.E.K. Warsi, and F.T. Wu, Structure and tectonics of the Himalaya: A brief summary of relevant geophysical observation, in Himalaya: Sciences de la Terre, pp. 269-294, Centre National de la Recherche Scientifique, Paris, 1977.

Molnar, P., T.J. Fitch, and F.T. Wu, Fault plane solutions of shallow earthquakes and contemporary tectonics in Asia, Earth Planet. Sci. Lett., 16, 101-112, 1973.

Molnar, P., and P. Tapponnier, Cenozoic tectonics of Asia: Effects of a continental collision, Science, 189, 419-426, 1975.

Molnar, P., and P. Tapponnier, Active tectonics of Tibet, J. Geophys. Res., 83, 5361-5375, 1978.

Ni, J., and J.E. York, Late Cenozoic extensional tectonics of the Tibetan Plateau, J. Geophys. Res., 83, 5377-5387, 1978.

Norin, E., Geological Explorations in Western Tibet, Reports from the Scientific Expedition to the Northwestern Provinces of China under the Leadership of Dr. Sven Hedin, Publ. 29, (III), Geology 7, Tryckeri Aktiebolaget, Thule, Stockholm, 1946.

Okal, E.A., The effect of intrinsic oceanic upper-mantle heterogeneity on regionalization of long-period Rayleigh wave phase velocities, Geophys. J. Roy. Astron. Soc., 49, 357 -370, 1977.

Oliver, J., and M. Major, Leaking mode and the P_L phase, Bull. Seism. Soc. Amer., 50, 165-180, 1960.

Parsons, B., and D. McKenzie, Mantle convection and the thermal structure of the plates, J. Geophys. Res., 83, 4485-4496, 1978.

Patton, H.J., Source and propagation effects of Rayleigh waves from central Asian earthquakes, Ph.D. Thesis, Massachusetts Institute of Technology, Cambridge, MA, 1978.

Post, R.L., Jr., High-temperature creep of Mt. Burnet dunite, Tectonophysics, 42, 75-110, 1977.

Poupinet, G., P_L waves and crustal structure in Canada, Canad. J. Earth Sci., 9, 1014-1029, 1972.

Powell, C.M., and P.J. Conaghan, Plate tectonics and the Himalayas, Earth Planet. Sci. Lett., 20, 1-12, 1973.

Powell, C.M., and P.J. Conaghan, Tectonic models of the Tibetan Plateau, Geology, 3, 727-731, 1975.

Rao, R.U.M., G.V. Rao, and H. Narain, Radioactive heat generation and heat flow in the Indian Shield, Earth Planet. Sci. Lett., 30, 57-64, 1976.

Sclater, J.G., C. Jaupart, and D. Galson, The heat flow through oceans and continents, Submitted to Rev. Geophys. Space Phys., 1978.

Sengupta, M.K., The structure of the earth's mantle from body-wave observations, Sc.D. Thesis, Massachusetts Institute of Technology, Cambridge, MA, 1975.

Sengupta, M.K., and B.R. Julian, P-wave travel times from deep earthquakes, Bull. Seism. Soc. Amer., 66, 1555-1579, 1976.

Tapponnier, P., and J. Francheteau, Necking of the lithosphere and the mechanics of slowly accreting plate boundaries, J. Geophys. Res., 83, 3955-3970, 1978.

Tapponnier, P. and P. Molnar, Active faulting and tectonics in China, J. Geophys. Res., 82, 2905-2930, 1977.

Tilling, R.I., D. Gottfried, and F.C.W. Dodge, Radiogenic heat production of contrasting magma series: bearing on interpretation of heat flow, Geol. Soc. Amer. Bull., 81, 1447-1462, 1970.

Toksöz, M.N., and P. Bird, Formation and evolution of marginal basins and continental plateaus, in Island Arcs, Deep-Sea Trenches, and Back-Arc Basins, pp. 379-394, AGU, Washington, D.C., 1977.

Tsai, Y.B., and K. Aki, Precise focal depth determination from amplitude spectra of surface waves, J. Geophys. Res., 75, 5729-5743, 1970.

Tseng, J., and Z. Sung, Phase velocities of Rayleigh waves in China, Acta Geophys. Sinica, 12, 148-165, 1963.

Tung, J.P., and T.L. Teng, Surface wave study of crustal structure of southern China, EOS Trans. AGU, 55, 359, 1974.

Table I

Earthquakes used for surface wave dispersions and P_L phase observation

Date	Number	Epicenter Location Lat.(°N)	Longt.(°E)	Origin Time	Stations	Seismic phases
Apr. 19, '63	I	35.7	96.9	07:35:22.7	NDI	LR, P_L
Oct. 16, '63	II	38.6	73.4	15:43:00.8	SHL	LR
Mar. 16, '64	III	36.95	95.50	01:05:19.8	NDI	LR, LG
Oct. 14, '66	IV	36.45	87.43	01:04:42.9	NDI LAH	LR, LG LG
Aug. 30, '67	V	31.57	100.31	11:08:50.0	LAH	LG
Mar. 24, '71	VI	35.46	98.04	13:54:21.0	NDI	LR
Aug. 30, '72	VII	36.65	96.35	15:14:07.5	NDL NIL	LR, LG LG
Aug. 30, '72	VIII	36.56	96.35	18:47:40.3	NDI NIL	LR, LG LG
Feb. 7, '73	IX	31.50	100.33	16:06:25.8	NDI	LG

Hypocenters and origin times as reported by ISC after 1964, by the Coastal and Geodetic Survey before 1964.

Table II

Pn and Sn velocity estimates for Tibet (north of the suture) and regions south of the suture

	Epicentral Distance (deg.) Range	Arrivals	No. of Observations	Travel time (sec) = Distance (km)/velocity (km/s) + Intercept time (sec)
Tibet, north of the suture	3 ∿ 17	all Pn	61	$x/(8.27\pm0.07) + (12.4\pm7.0)$ $x/(8.15\pm0.04) + (10.3\pm4.1)$
		sharp Pn	42	$x/(8.24\pm0.09) + (12.0\pm5.4)$ $x/(8.20\pm0.04) + (10.6\pm2.6)$
		emergent Pn	19	$x/(8.38\pm0.21) + (14.5\pm15.0)$ $x/(8.18\pm0.13) + (11.2\pm9.8)$
	3 ∿ 10	sharp Pn	39	$x/(7.97\pm0.12) + (9.7\pm6.9)$ $x/(8.12\pm0.06) + (10.0\pm3.6)$
		sharp Sn	23	$x/(4.77\pm0.09) + (25.4\pm11.4)$ $x/(4.77\pm0.08) + (23.5\pm9.5)$
Regions south of the suture	3 ∿ 17	all Pn (mostly sharp)	24	$x/(8.20\pm0.11) + (10.4\pm5.2)$ $x/(8.11\pm0.07) + (9.1\pm3.6)$
	3 ∿ 10	all Pn (mostly sharp)	21	$x/(8.29\pm0.15) + (11.0\pm5.8)$ $x/(8.13\pm0.10) + (9.3\pm4.0)$
		sharp Sn	11	$x/(4.94\pm0.11) + (28.3\pm8.8)$ $x/(4.75\pm0.10) + (23.2\pm8.6)$

Results after the depth correction are given on the second line.
All velocities are calculated for a Moho at 70 km depth.

Table III

S-P travel time residuals with respect to the Jeffreys-Bullen Table for earthquakes in Tibet (T) and the Himalaya (H)

Date	Location Lat.(°N)	Long.(°E)	Depth Reported by ISC(km)	No. of Observations	δTs-p (sec) ISC depth	33km Normalized	5km Depth
Mar. 6, '66	31.49	80.50(T)	50	19	11.4±2.4	10.0	7.1
				16	12.1±3.3	10.7	7.8
Oct. 14, '66	36.45	87.43(T)	14	11	6.6±2.2	8.5	5.7
				9	7.9±1.5	9.8	7.0
Jul. 22, '72	31.38	91.41(T)	17	15	4.4±2.9	6.0	3.2
				14	5.3±3.7	6.9	4.1
Jul. 14, '73	35.16	86.40(T)	22	20	7.3±2.7	8.4	5.6
				16	7.8±3.2	8.9	6.1
Jul. 19, '75	32.39	78.50(T)	1	15	1.4±2.4	4.6	1.8
				12	2.9±1.5	6.1	3.3
Apr. 28, '75	35.80	79.86(T)	33	18	3.7±2.2	3.7	0.9
				13	4.1±2.4	4.1	1.3
May 5, '75	33.09	92.92(T)	33	22	5.8±2.3	5.8	2.9
				20	6.7±2.6	6.7	3.8
May 19, '75	35.16	80.80(T)	26	10	4.4±2.8	5.1	3.3
				8	5.3±1.7	6.0	4.2
Jun. 4, '75	35.87	79.85(T)	33	15	4.7±2.7	4.7	1.9
				12	5.6±1.0	5.6	2.8
						Ave.	3.6
							4.5

Table III (cont'd)

Sep. 26, '64	29.96	80.46(H)	50	10	2.7±1.7	1.3	-1.6
				7	3.5±2.2	2.1	-0.8
Oct. 21, '64	28.04	93.75(H)	37	19	2.5±1.8	2.2	-0.8
				18	2.9±2.4	2.6	-0.4
Jun. 27, '66	29.62	80.83(H)	33	15	3.1±1.9	3.1	0.2
				12	2.9±2.8	2.9	0.0
Dec. 16, '66	29.62	80.79(H)	19	14	2.0±2.7	2.3	0.6
				13	1.8±4.0	2.1	0.4
Mar. 14, '67	28.41	94.29(H)	20	19	1.2±2.2	2.3	-0.1
				17	2.4±1.8	3.5	1.1
Feb. 19, '70	27.40	93.96(H)	12	14	-0.5±3.2	1.6	-1.2
				12	1.2±3.1	3.3	0.5
Sep. 3, '72	35.94	73.33(H)	45	16	1.7±1.7	0.7	-2.2
				13	2.3±2.0	1.3	-1.6
Mar. 24, '74	27.66	86.00(H)	20	26	1.3±2.1	2.4	0.0
				21	1.6±2.6	2.7	0.3
						Ave.	
						2.0	
						2.6	

Results after applying the station corrections are given on the second line for each event.

Figure Captions

Fig. 1. Map of Tibet showing earthquake (dots) - station (triangles) combinations used for surface wave dispersions and the P_L phase observation. Events I and II generated large long-period Rayleigh waves. Note the difference in the paths to stations from these two events. Event I was used for the P_L phase observation also. Major strike-slip and thrust faults (see legend) were also plotted following Molnar and Tapponnier [1975].

Fig. 2. (a) Seismograms of clear long period Rayleigh waves and P_L-phase. These are the only Rayleigh wave observations found with a large signal to noise ratio at low frequencies.

(b) Representative seismograms observed at stations south of the Himalaya for earthquakes in Tibet. Note that no clear Rayleigh wave signals with periods beyond about 30 sec were apparent. Love waves vary from a pulse shape signal to dispersed wave trains up to about 60 sec period.

Fig. 3. (a) Group velocity dispersion curves of Rayleigh waves. No clear signal was observed between 30 to 60 sec periods. A 3% maximum error in group velocities would be about 0.1 km/s.

(b) Group velocity dispersion curves of Love waves.

Fig. 4. Phase velocity dispersion curves for Rayleigh waves. Observed values for I-NDI path (crosses) and II-SHL path (dots) were plotted together with three theoretical curves calculated for models F4, S7, and S4. Model SE

generates nearly identical phase velocity dispersion curve as that of the model S7 at the period range shown. Error bar shown is approximately $\pm$2.4% maximum error in phase velocity (see text). See Figs. 5, 6, and 12 for model parameters.

Fig. 5. Theoretical Rayleigh wave dispersion curves (top) for three models (bottom) with a crustal thickness of 55 km for different uppermost mantle shear wave velocities (β_m). The two long-period observations are shown as solid triangles and reversed solid triangles for comparison. Also shown is the theoretical Love wave dispersion curve for model F4.

Fig. 6. Theoretical Rayleigh wave dispersion curves (top) for 3 models (bottom) with a crustal thickness of 70 km for different β_m. Layout same as in Fig. 5.

Fig. 7. Theoretical Rayleigh wave dispersion curves (top) for 3 models (bottom) with a crustal thickness of 85 km for different β_m. Model E4 is used in Fig. 8. Layout same as in Fig. 5.

Fig. 8. Theoretical Rayleigh wave dispersions for 3 models with β_m = 4.4 km/s for different crustal thicknesses. Model parameters were given in Figs. 5, 6, and 7. Layout same as in Fig. 5.

Fig. 9. Two theoretical Rayleigh wave dispersion curves for models with β_m = 4.7 km/s for crustal thicknesses of 55 and 70 km. Layout same as in Fig. 5.

Fig. 10. Two theoretical Rayleigh wave dispersion curves for models with β_m = 4.8 km/s for crustal thicknesses of 70 and 85 km. Layout same as in Fig. 5.

Fig. 11. (a) Theoretical Rayleigh wave dispersion curves (top) for 3 models (bottom) with β_m = 4.4 km/s and a crust of 55 km thick but with different crustal velocity structures. The average crustal shear wave velocity ($\bar{\beta}$) ranges from 3.49 km/s to 3.44 km/s. The model FF3 which fits the observations is the same as model F4 (Fig. 5). The upper and lower bound of our observations are shown in reversed solid triangles and solid triangles respectively. (b) Theoretical Rayleigh wave dispersion curves (top) for 4 models (bottom) with a fixed crustal thickness (55 km), β_m (4.4 km/s) and $\bar{\beta}$ (3.44 km/s). Note that a uniform crust between the Moho and the sediments with this low $\bar{\beta}$ is not appropriate to explain the observations.

Fig. 12. (a) Theoretical Rayleigh wave dispersion curves (top) for 3 models (bottom) with fixed crustal thickness (70 km), and β_m (4.7 km/s). $\bar{\beta}$ ranges from 3.53 to 3.45 km/s. For all cases the velocities are too high. Layout same as Fig. 11. (b) Theoretical Rayleigh wave dispersion curves

(top) for 3 models (bottom). Model SS3 in (a) is plotted for comparison. The addition of a relatively high velocity layer (β = 3.9 km/s) makes model SS5 (= model S7, Fig. 6) fit the data at both long period and short period ends. Model SE is described in (c). (c) Theoretical Rayleigh wave dispersion curves for models SE and SS5. The slight increase in β_m in SE has the same effect as the introduction of a layer at the base of the crust with β = 3.9 km/s in SS5 (see (b)). Also note that model S7 (SS5) and SE have nearly identical phase velocity dispersion curves (Fig. 4).

Fig. 13. (a) Low-pass filtered vertical component Rayleigh wave of the II-SHL path observation together with two synthetic seismograms for different Q structures. Both synthetics employ model S7 (Fig. 6) with source depth 5 km and an arbitrary seismic moment. All the seismograms have been normalized to have the same maximum peak-to-peak amplitude, emphasizing their similarity in wave forms. (b) Three low-pass filtered synthetic seismograms of the vertical component of Rayleigh waves for model S7 with different source depths of 5, 10 and 30 km. Amplitude scales have been normalized as in (a). (c) Low-pass filtered vertical component of the Rayleigh wave observation of the I-NDI path together with three synthetic seismograms for different velocity structures: Models F7, S4, S7 (Figs. 5 and 6). Amplitude scales have been normalized

as in (a). Note the particularly poor fit of model F7.

Fig. 14. (a) Vertical component of the long-period P_L phase for the I-NDI path (solid trace) and one synthetic seismogram (dashed trace) for a 70 km thick crust (single layer over a half-space) model, with an arbitrary seismic moment. The large amplitudes at the beginning of the observation are deep mantle reflections and refractions and were not synthesized. (b) Two synthesized vertical components of P_L phases for layer-over-half space models with different crustal thicknesses of 70 and 85 km. P and S wave velocities for crust and mantle are shown in the lower-right corner. Note the similarity between the two waveforms. (c) Synthesized vertical component of a P_L phase for model SEM1 (dashed trace) together with the observed signal. The inclusion of a crustal reflector alters the long-period waveform considerably from the pulse like character in (b).

Fig. 15. Plots of P_n travel times normalized for a focal depth of 33 km (top) and travel time residuals (bottom) vs. distance to LHA for earthquakes north of the Indus-Tsang Po suture. The distance range is about 3°-17°. The P_n velocity (8.15 ± 0.04 km/s) and travel time residuals were obtained by a least-square fitting of the 61 observations assuming a Moho depth of 70 km. Most of the residuals fall within ± 1 sec of the mean. The dashed line shows the slope of a curve that the data would

follow if the P_n velocity were 7.9 km/s. Travel time residuals can be viewed as reduced travel times in conventional refraction analysis.

Fig. 16. (a) Plots of data for Pn travel times without depth normalization (top) and travel time residuals (bottom) vs. distance to LHA for earthquakes north of the Indus-Tsang Po suture. Distance range is 3°-10°. Layout as in Fig. 15. (b) The same dataset as in (a) but with a normalization for a focal depth of 33 km. Note the reduction of residuals compared with (a). Layout as in Fig. 15.

Fig. 17. Plots of P_n travel times normalized for a focal depth of 33 km (top) and travel time residuals (bottom) vs. distance to LHA for earthquakes south of the suture. Distances range from 3° to 10°. Layout same as in Fig. 15.

Fig. 18. Plots of S_n travel times normalized for focal depths of 33 km (top) and travel time residuals (bottom) vs. distance to LHA for earthquakes north of the suture. Distances range 3° to 10°. Layout as in Fig. 15.

Fig. 19. Map of Tibet showing the location of LHA and the epicenters used for the refraction profiles. Tectonic features are the same as in Fig. 1.

Fig. 20. Map of Tibet and the Himalaya showing the locations of 17 earthquakes (circles) used in telseismic travel time measurements. Roman numerals inside the circles are the lower bounds at 1 sec intervals of S-P travel

time residuals with respect to the J-B tables. Source depths have been normalized to 5 km for earthquakes in Tibet and to 33 km for those in the Himalaya. Tectonic features are the same as in Fig. 1.

Fig. 21. Examples of seismograms used in the teleseismic travel time measurements for earthquakes in Tibet and the Himalaya. Arrows indicate the onset of S wave arrivals. Numbers in the parentheses are S wave travel time residuals in sec with respect to the J-B table for the source depths given by the ISC.

Fig. 22. (a) Plots of teleseismic P and S wave travel time residuals, with respect to the J-B tables vs. distance for earthquakes in Tibet (b) S-P travel time residuals (circles). The crosses are the results after station corrections. Dashed line shows the zero-residual level for a focal depth normalized to 5 km. The averaged S-P delays are given in Table III with estimated standard errors.

Fig. 23. (a) Plots of teleseismic P and S wave travel time residuals, with respect to the J-B table, vs. distance for earthquakes in the Himalaya. (b) S-P travel time residuals. Symbols are the same as in Fig. 22.

Fig. 24. Average S-P travel time residuals for earthquakes in Tibet (left) and the Himalaya (right). Hatched and open columns are average residuals without and with the station corrections, respectively. The residuals are given for three different focal depths: 5 km (top), 33 km (middle) and the depth reported by the ISC (bottom).

Fig. 25. Solidi of selected possible crustal and uppermantle materials of different water content from data obtained from experimental petrology [Lambert and Wyllie, 1970, Merrill et al., 1970, Merrill and Wyllie, 1975]. Dashed lines indicate areas of large uncertainty cited in the original literature.

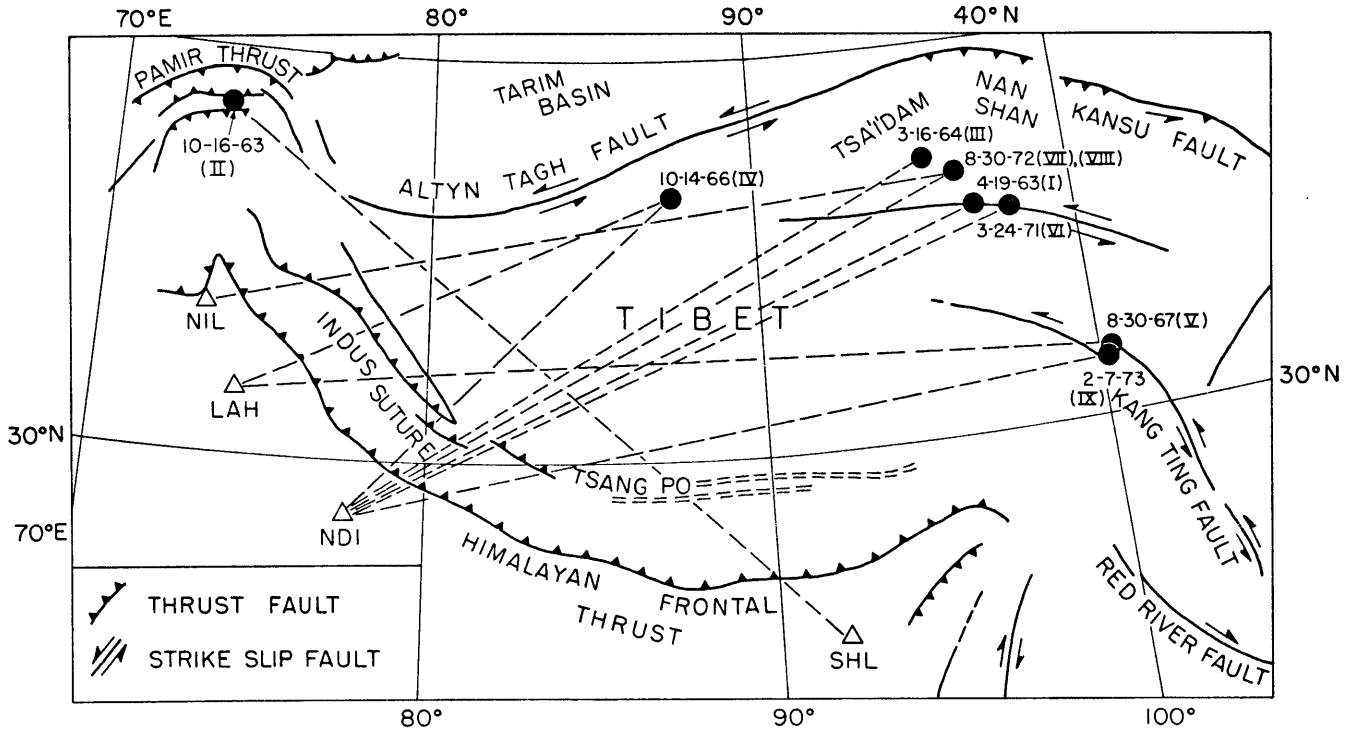
70°E
80°
90°
40°N
PAMIR THRUST
TARIM BASIN
NAN SHAN
KANSU FAULT
10-16-63 (II)
ALTYN TAGH FAULT
TSAIDAM
3-16-64(III)
8-30-72(VII),(VIII)
10-14-66(IV)
4-19-63(I)
3-24-71(VI)
NIL
T I B E T
8-30-67(V)
INDUS SUTURE
LAH
2-7-73 (IX)
30°N
KANG TING FAULT
TSANG PO
NDI
HIMALAYAN FRONTAL THRUST
SHL
RED RIVER FAULT
THRUST FAULT
STRIKE SLIP FAULT
80°
90°
100°

Fig. 1

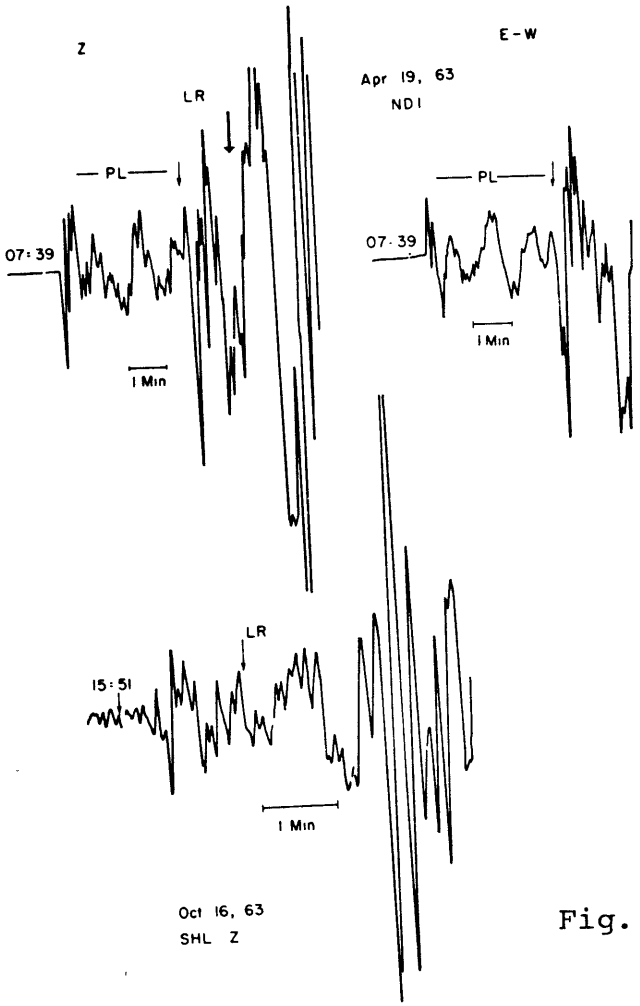
Z
E-W
Apr 19, 63
NDI
LR
PL
07:39
1 Min
PL
07·39
1 Min
LR
15:51
1 Min
Oct 16, 63
SHL Z

Fig. 2(a)

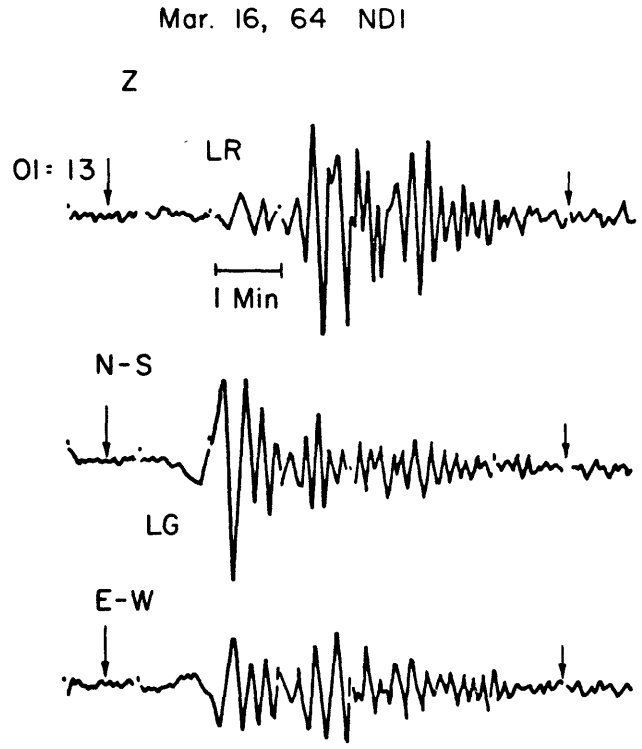
Mar. 16, 64 NDI
Z
01: 13
LR
1 Min
N-S
LG
E-W
Aug. 30, 67 LAH Z
01: 19
LR
1 Min
Aug. 30, 72 NDI
18: 56 LR
Z
18: 56 LG
N
1 Min

Fig. 2(b)

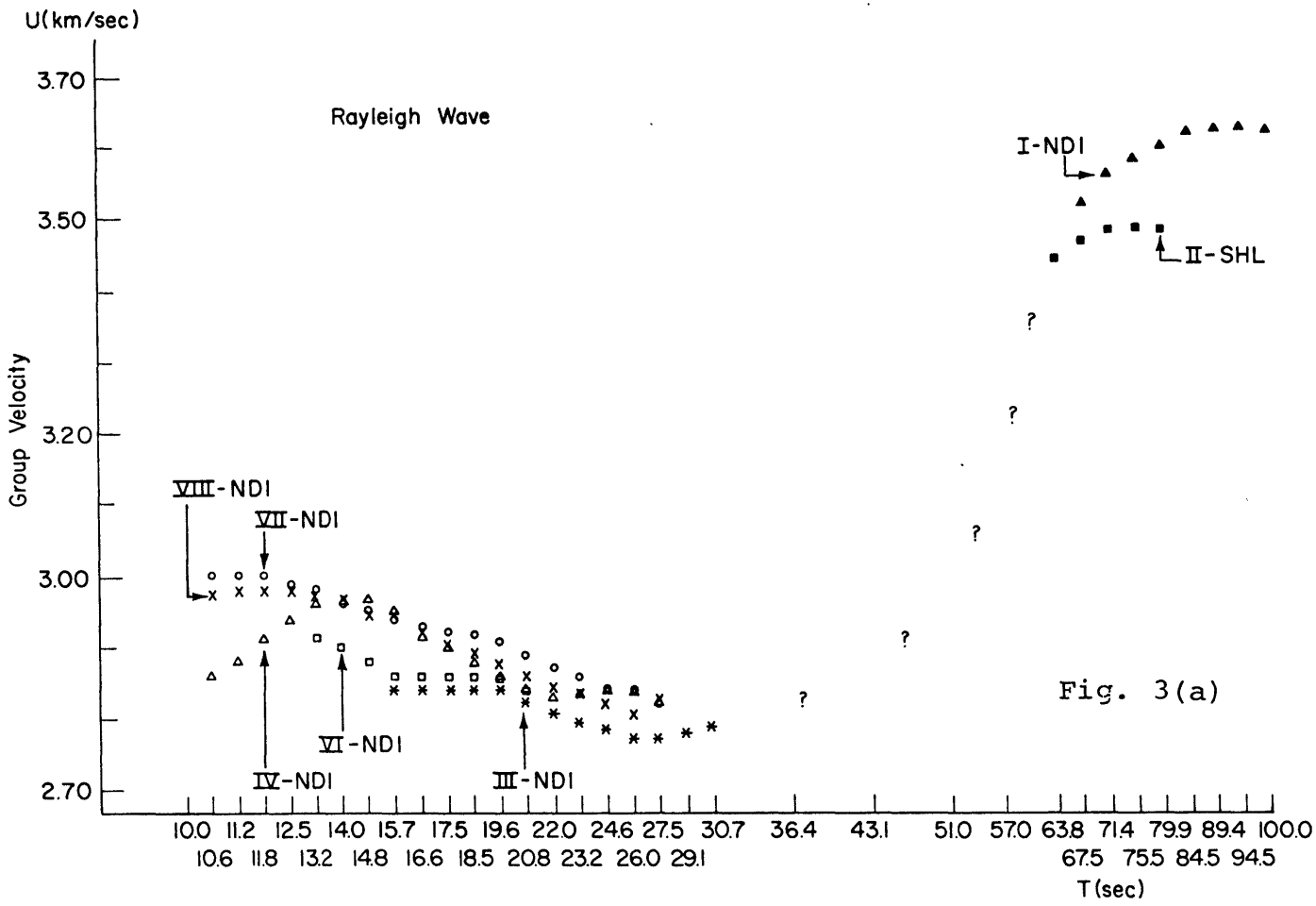
U(km/sec)
Rayleigh Wave
Group Velocity
3.70
3.50
3.20
3.00
2.70
I-NDI
II-SHL
VIII-NDI
VII-NDI
VI-NDI
IV-NDI
III-NDI
?
10.0 11.2 12.5 14.0 15.7 17.5 19.6 22.0 24.6 27.5 30.7 36.4 43.1 51.0 57.0 63.8 71.4 79.9 89.4 100.0
10.6 11.8 13.2 14.8 16.6 18.5 20.8 23.2 26.0 29.1 67.5 75.5 84.5 94.5
T(sec)

Fig. 3(a)

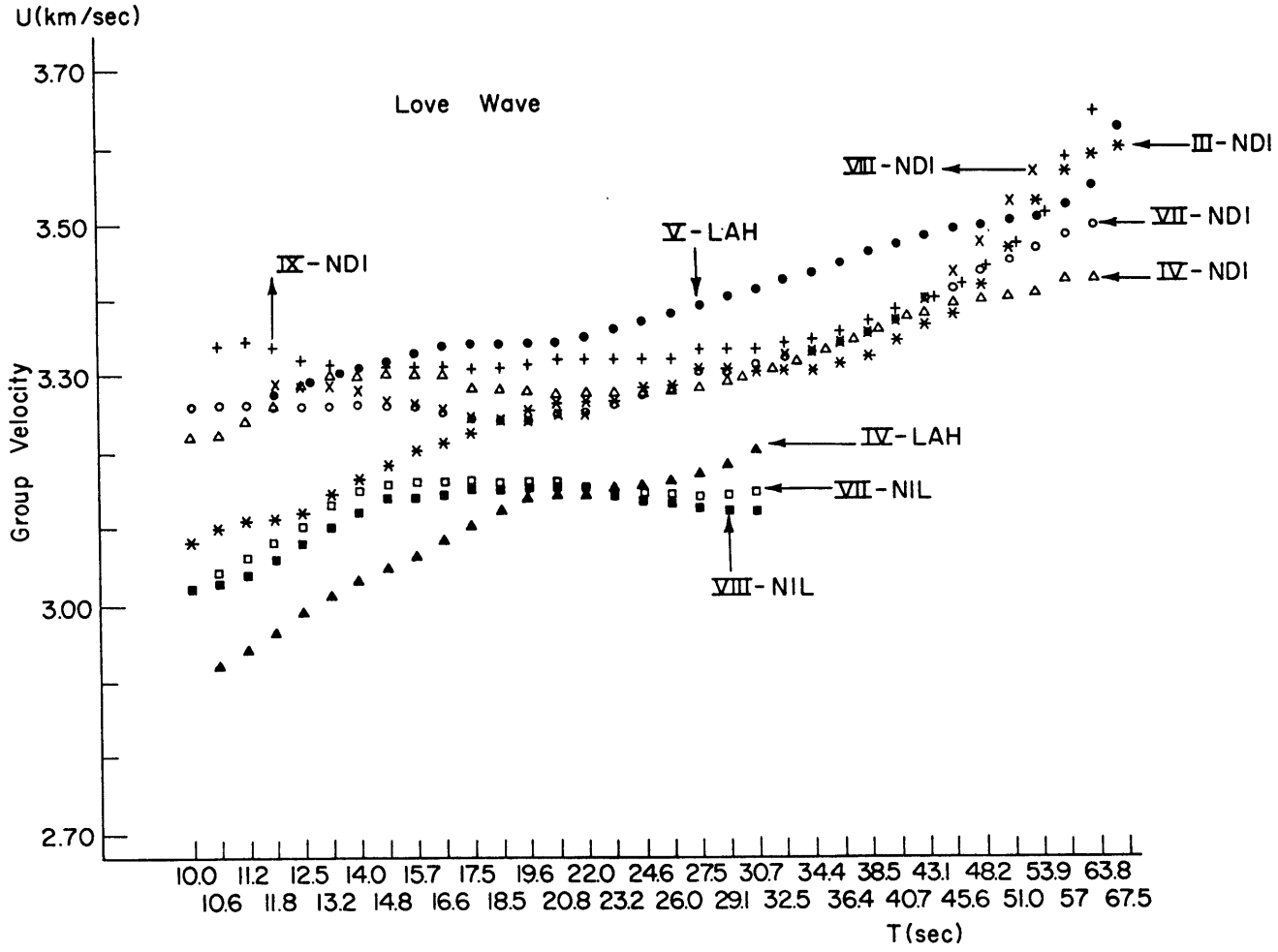
U(km/sec)
Love Wave
3.70
3.50
3.30
3.00
2.70
Group Velocity
III-NDI
VIII-NDI
VII-NDI
IV-NDI
V-LAH
IX-NDI
IV-LAH
VII-NIL
VIII-NIL
10.0 11.2 12.5 14.0 15.7 17.5 19.6 22.0 24.6 27.5 30.7 34.4 38.5 43.1 48.2 53.9 63.8
10.6 11.8 13.2 14.8 16.6 18.5 20.8 23.2 26.0 29.1 32.5 36.4 40.7 45.6 51.0 57 67.5
T(sec)

Fig. 3(b)

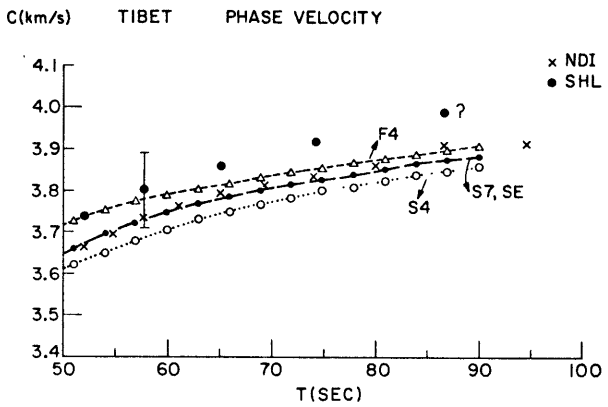
C(km/s)
TIBET
PHASE VELOCITY
× NDI
● SHL
4.1
4.0
3.9
3.8
3.7
3.6
3.5
3.4
50
60
70
80
90
100
T(SEC)
● ?
F4
S4
S7, SE

Fig.4

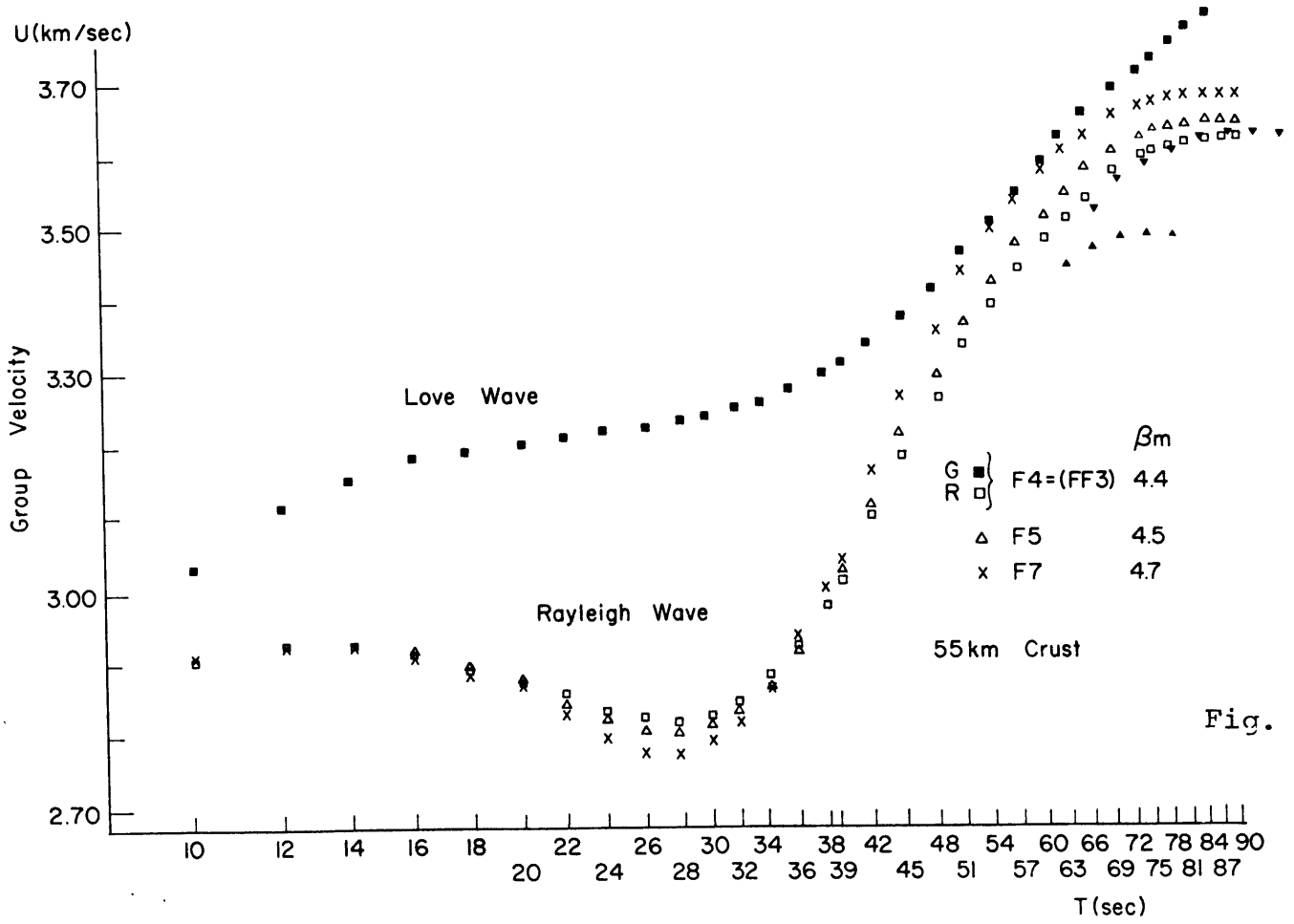
U(km/sec)
3.70
3.50
3.30
3.00
2.70
Group Velocity
Love Wave
Rayleigh Wave
55km Crust
βm
G
R
F4=(FF3) 4.4
F5 4.5
F7 4.7
10 12 14 16 18 20 22 24 26 28 30 32 34 36 38 39 42 45 48 51 54 57 60 63 66 69 72 75 78 81 84 87 90
T(sec)

Fig. 5

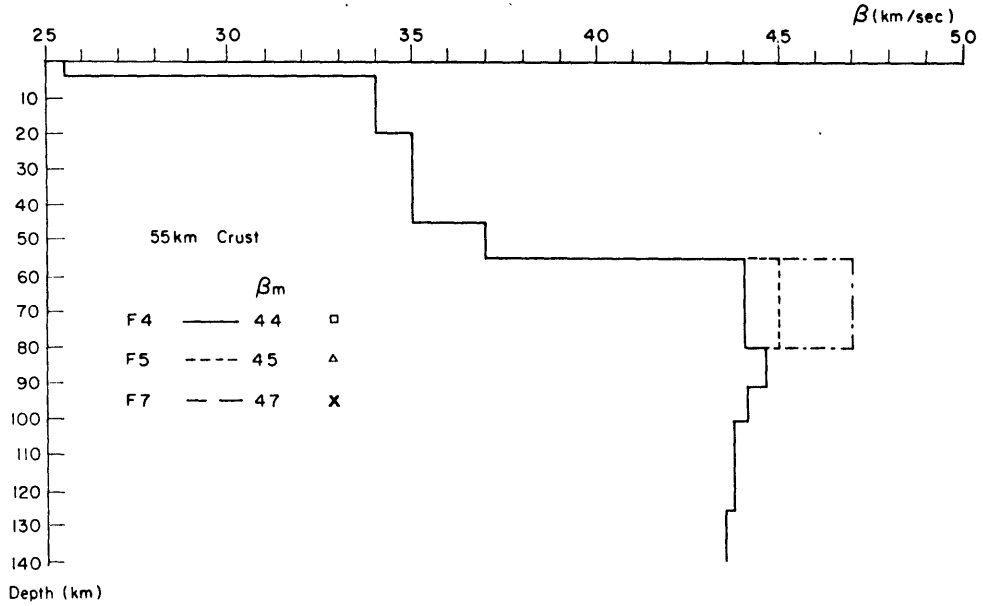
β (km/sec)
25
30
35
40
45
50
10
20
30
40
50
60
70
80
90
100
110
120
130
140
Depth (km)
55km Crust
βm
F4 —— 44 □
F5 ---- 45 △
F7 — — 47 X

Fig. 5
(cont.)

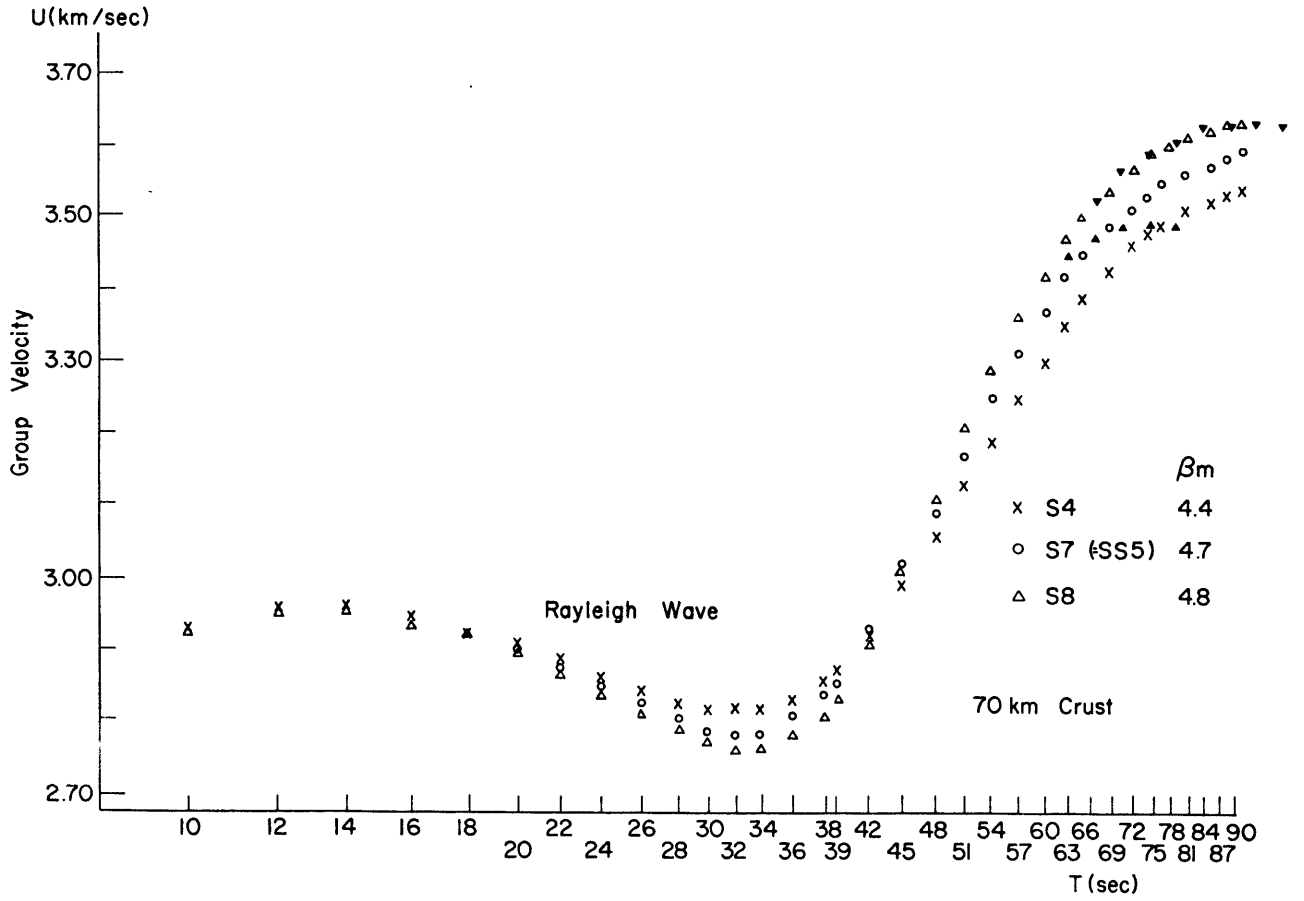
U(km/sec)
3.70
3.50
3.30
3.00
2.70
Group Velocity
Rayleigh Wave
70 km Crust
βm
S4 4.4
S7 (SS5) 4.7
S8 4.8
10 12 14 16 18 20 22 24 26 28 30 32 34 36 38 39 42 45 48 51 54 57 60 63 66 69 72 75 78 81 84 87 90
T(sec)

Fig. 6

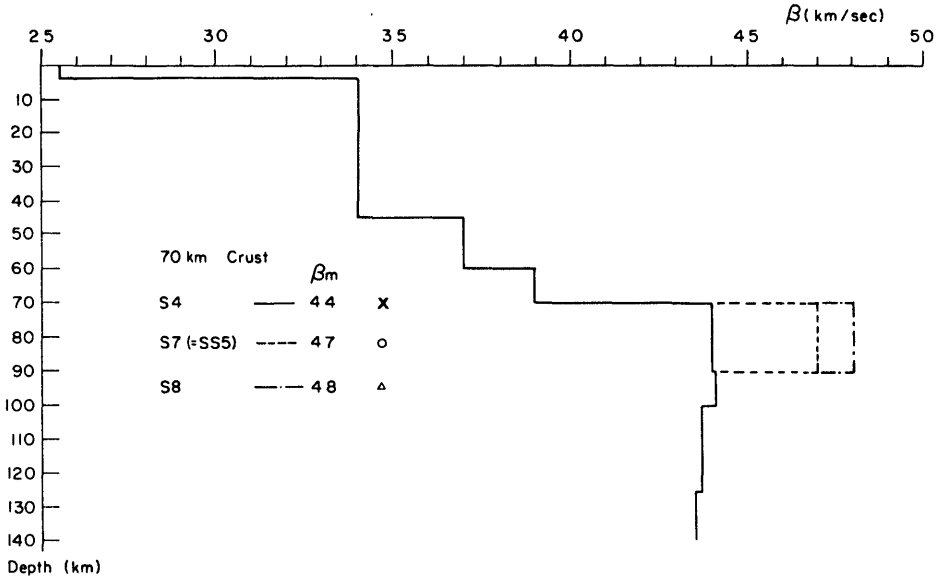
β(km/sec)
25
30
35
40
45
50
10
20
30
40
50
60
70
80
90
100
110
120
130
140
Depth (km)
70 km Crust
βm
S4 — 44 x
S7 (=SS5) ---- 47 o
S8 —·— 48 △

Fig. 6
(cont.)

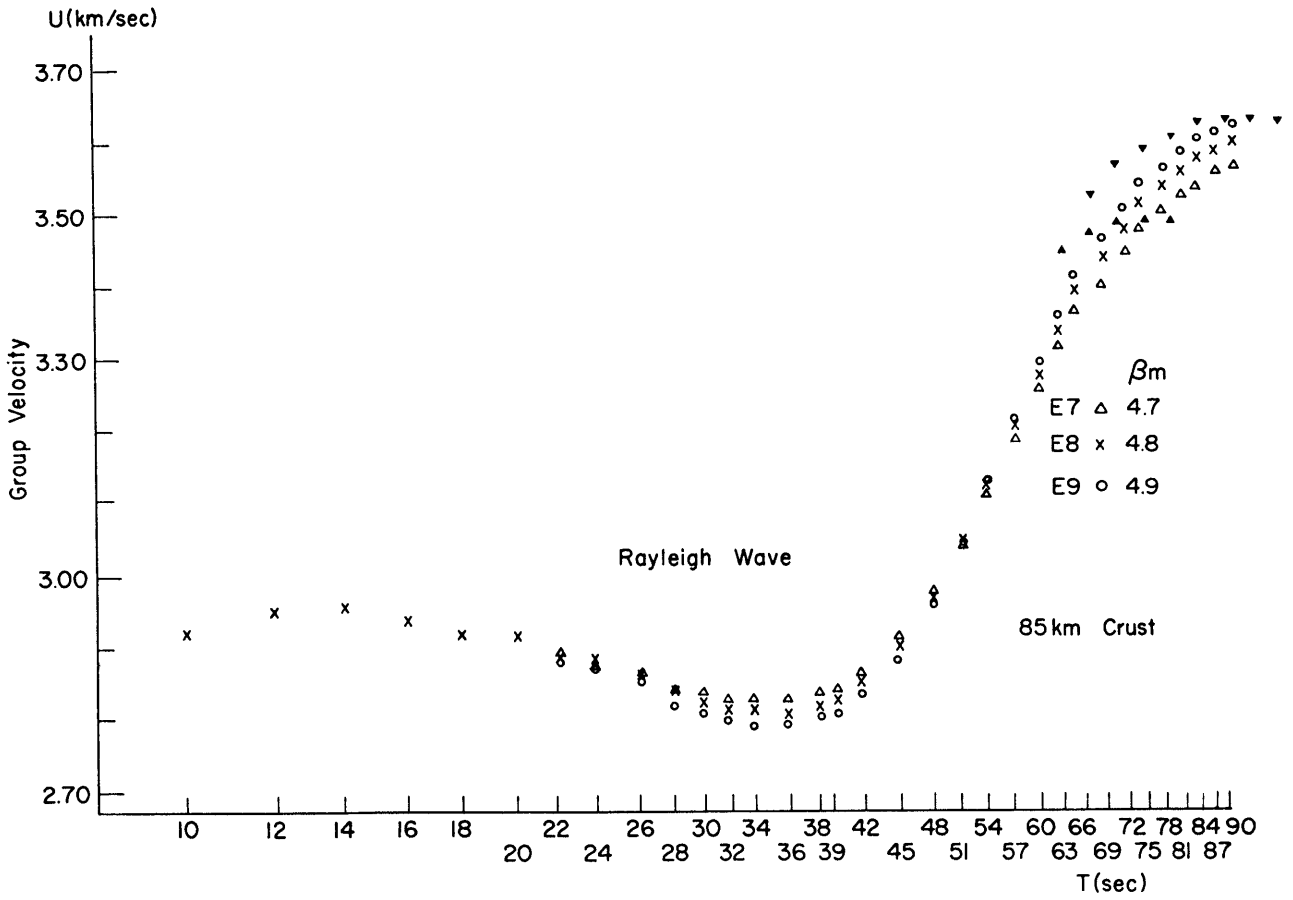
U(km/sec)
3.70
3.50
3.30
3.00
2.70
Group Velocity
Rayleigh Wave
85 km Crust
βm
E7 △ 4.7
E8 x 4.8
E9 o 4.9
10 12 14 16 18 20 22 24 26 28 30 32 34 36 39 42 45 48 51 54 57 60 63 66 69 72 75 78 81 84 87 90
T(sec)

Fig. 7

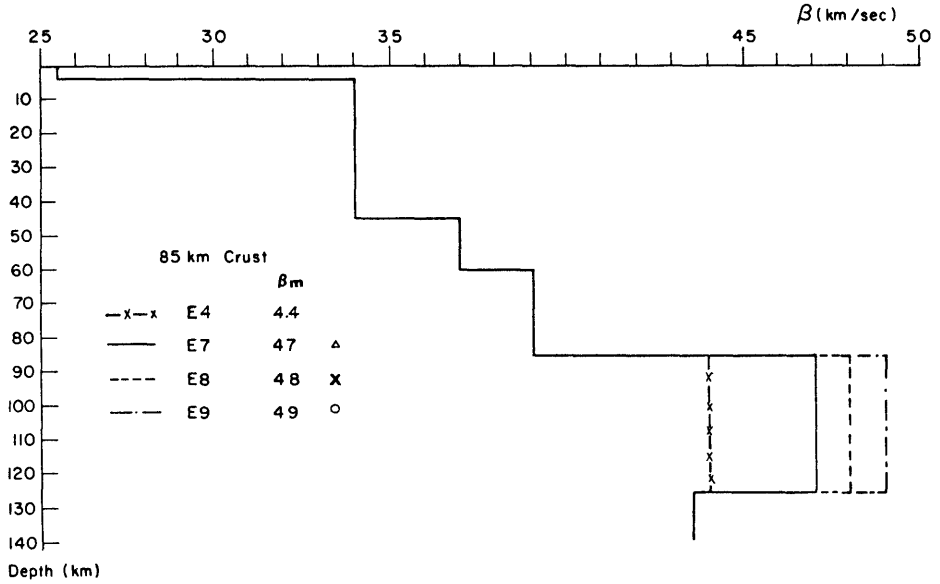
β (km/sec)
25
30
35
45
50
10
20
30
40
50
60
70
80
90
100
110
120
130
140
Depth (km)
85 km Crust
βm
E4 4.4
E7 47 Δ
E8 48 X
E9 49 O

Fig. 7
(cont.)

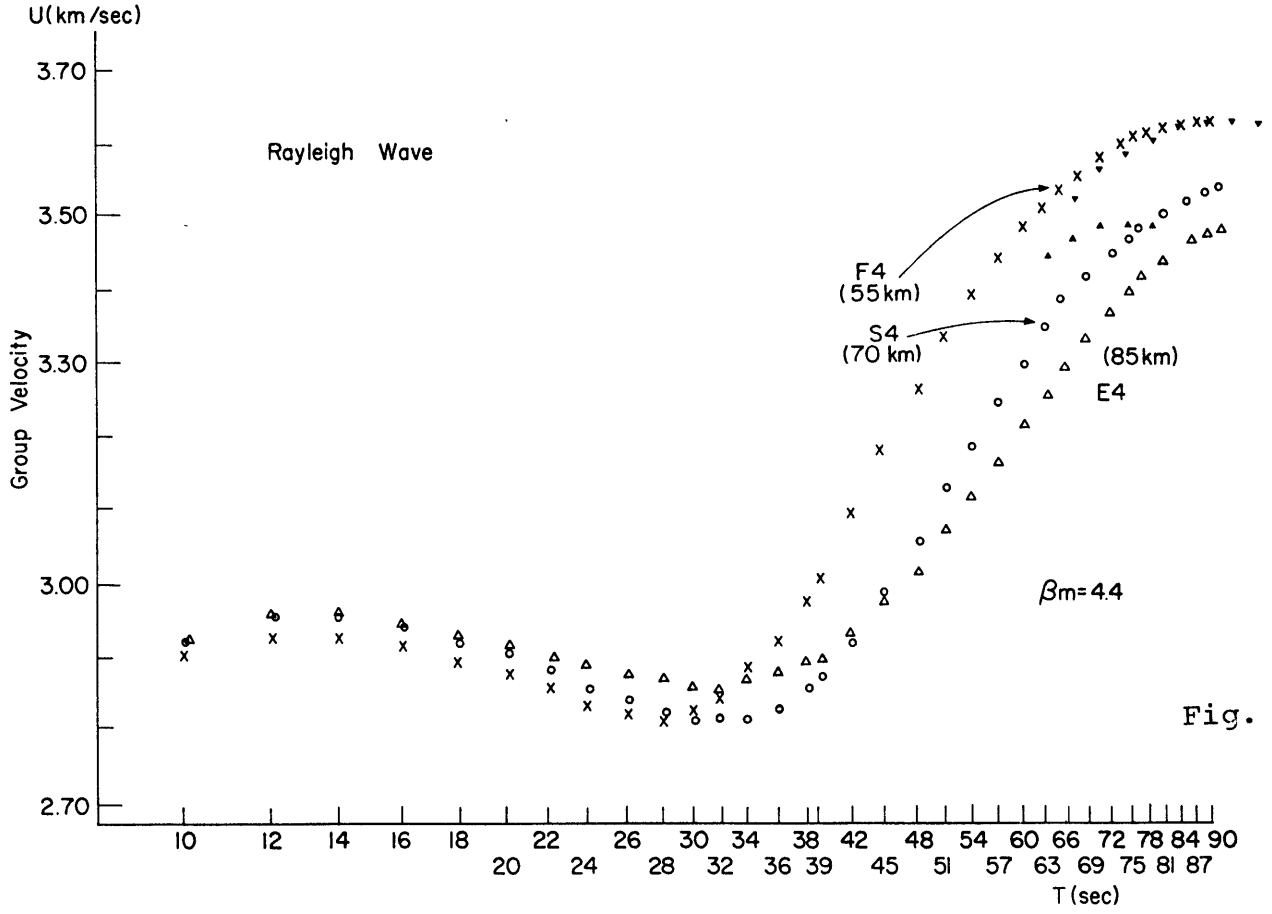
U(km/sec)
3.70
3.50
3.30
3.00
2.70
Group Velocity
Rayleigh Wave
F4
(55km)
S4
(70 km)
(85km)
E4
βm=4.4
10 12 14 16 18 20 22 24 26 28 30 32 34 36 38 39 42 45 48 51 54 57 60 63 66 69 72 75 78 81 84 87 90
T(sec)

Fig. 8

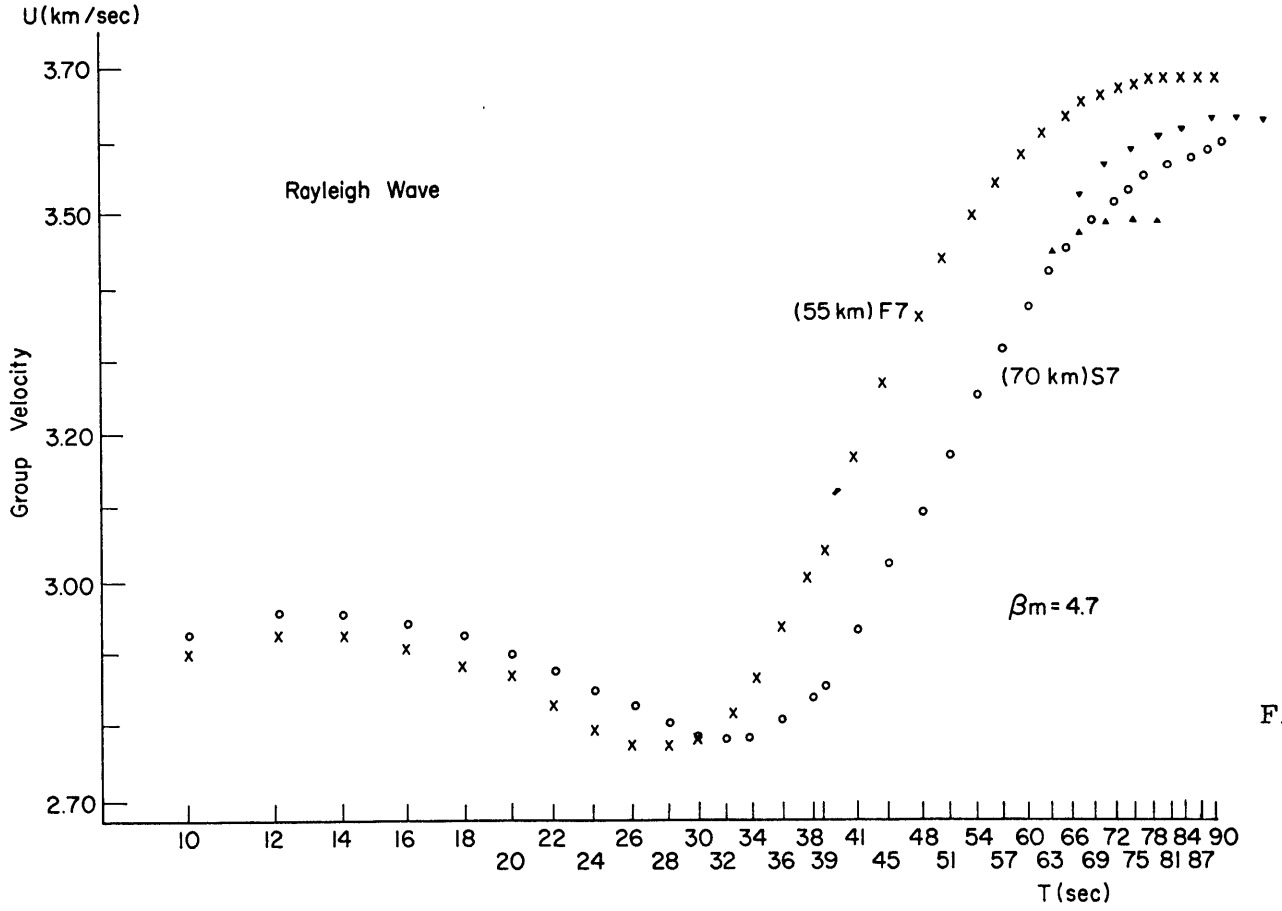
U(km/sec)
3.70
3.50
3.20
3.00
2.70
Group Velocity
Rayleigh Wave
(55 km) F7
(70 km) S7
βm = 4.7
10 12 14 16 18 20 22 24 26 28 30 32 34 36 38 39 41 45 48 51 54 57 60 63 66 69 72 75 78 81 84 87 90
T(sec)

Fig. 9

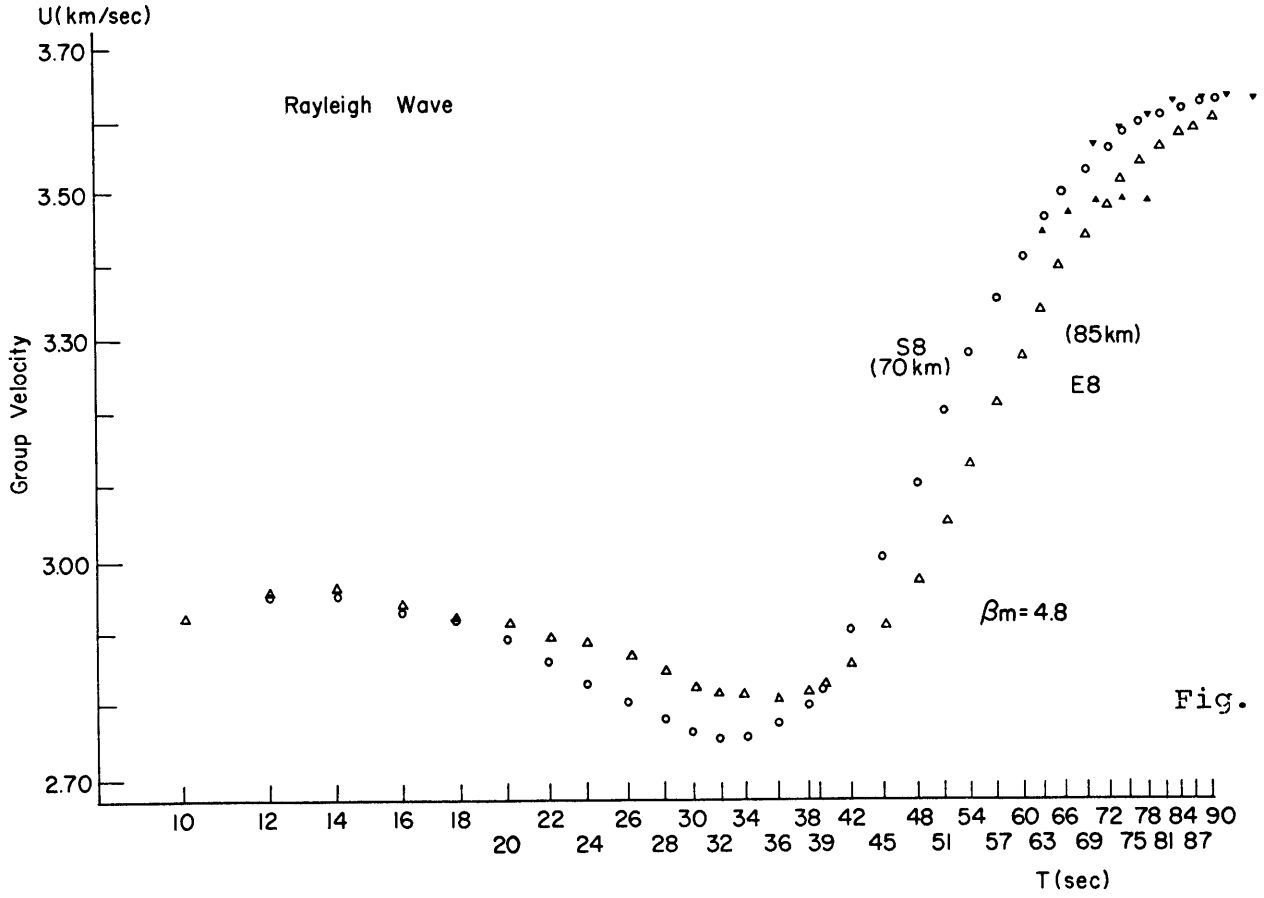
U(km/sec)
3.70
3.50
3.30
3.00
2.70
Group Velocity
Rayleigh Wave
S8
(70km)
(85km)
E8
βm=4.8
10 12 14 16 18 20 22 24 26 28 30 32 34 36 38 39 42 45 48 51 54 57 60 63 66 69 72 75 78 81 84 87 90
T(sec)

Fig. 10

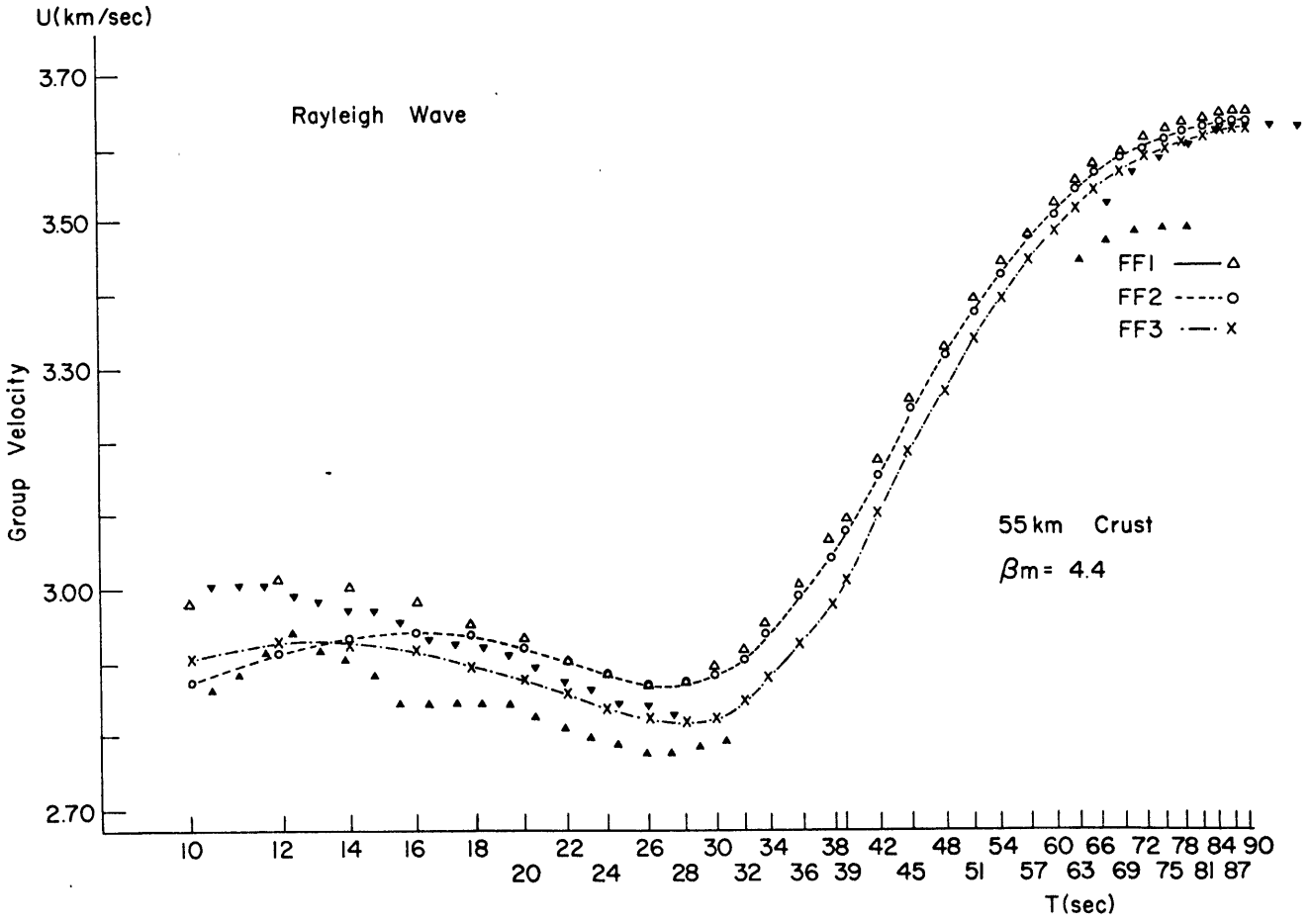
U(km/sec)
3.70
3.50
3.30
3.00
2.70
Group Velocity
Rayleigh Wave
FF1
FF2
FF3
55 km Crust
βm = 4.4
10 12 14 16 18 20 22 24 26 28 30 32 34 36 38 39 42 45 48 51 54 57 60 63 66 69 72 75 78 81 84 87 90
T(sec)

Fig. 11(a)

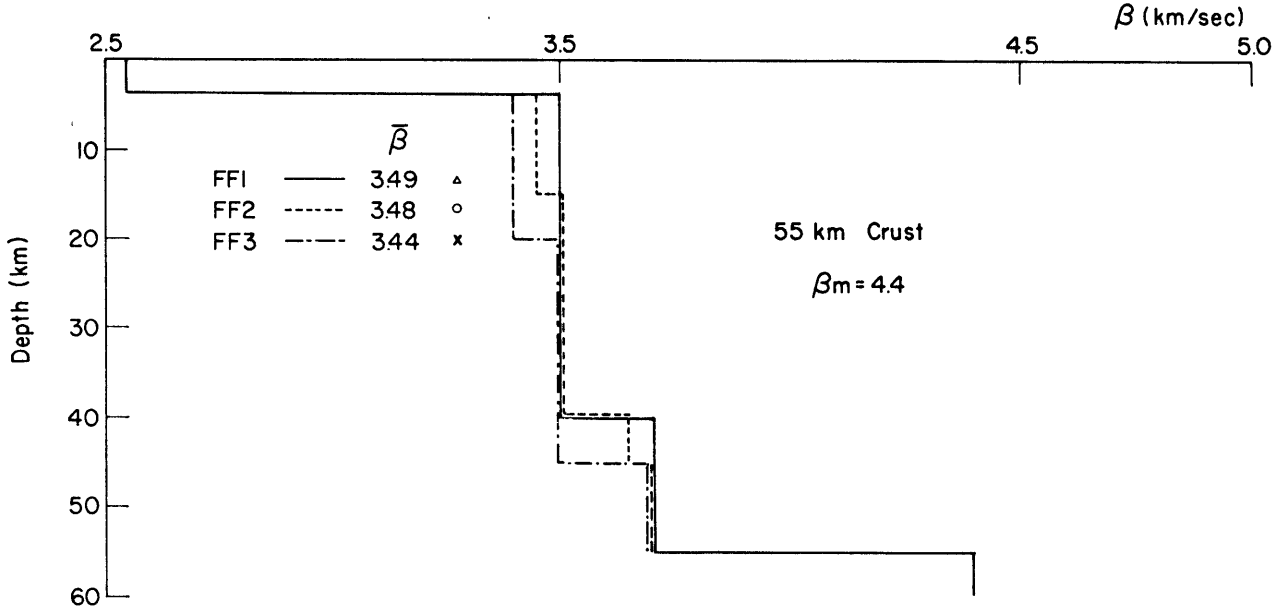
β (km/sec)
2.5
3.5
4.5
5.0
Depth (km)
10
20
30
40
50
60
$\bar{\beta}$
FF1 —— 3.49 △
FF2 ------ 3.48 ○
FF3 —·—· 3.44 ×
55 km Crust
βm = 4.4

Fig. 11(a)
(cont.)

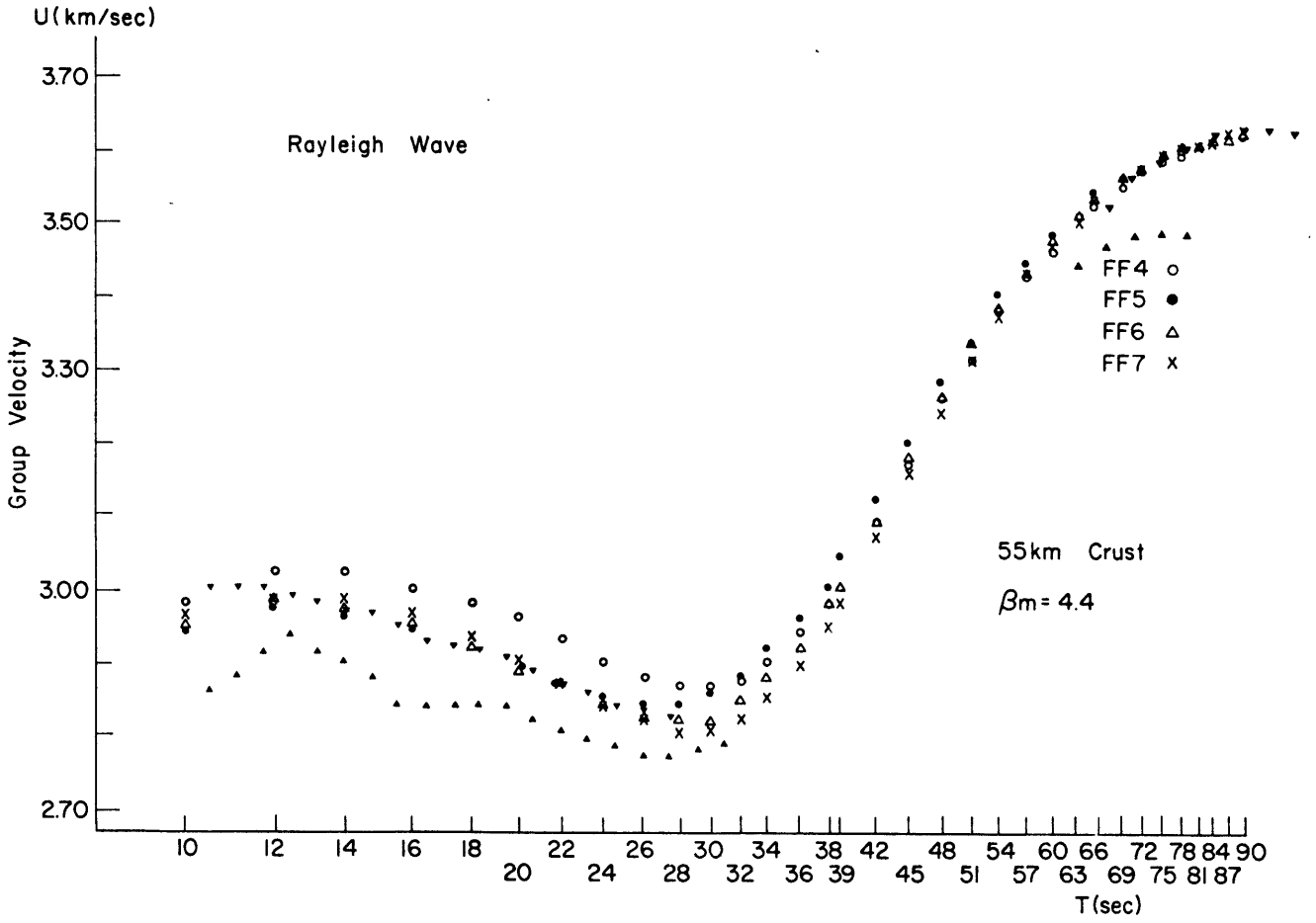
U(km/sec)
3.70
3.50
3.30
3.00
2.70
Group Velocity
Rayleigh Wave
FF4
FF5
FF6
FF7
55km Crust
βm = 4.4
10 12 14 16 18 20 22 24 26 28 30 32 34 36 38 39 42 45 48 51 54 57 60 63 66 69 72 75 78 81 84 87 90
T(sec)

Fig. 11(b)

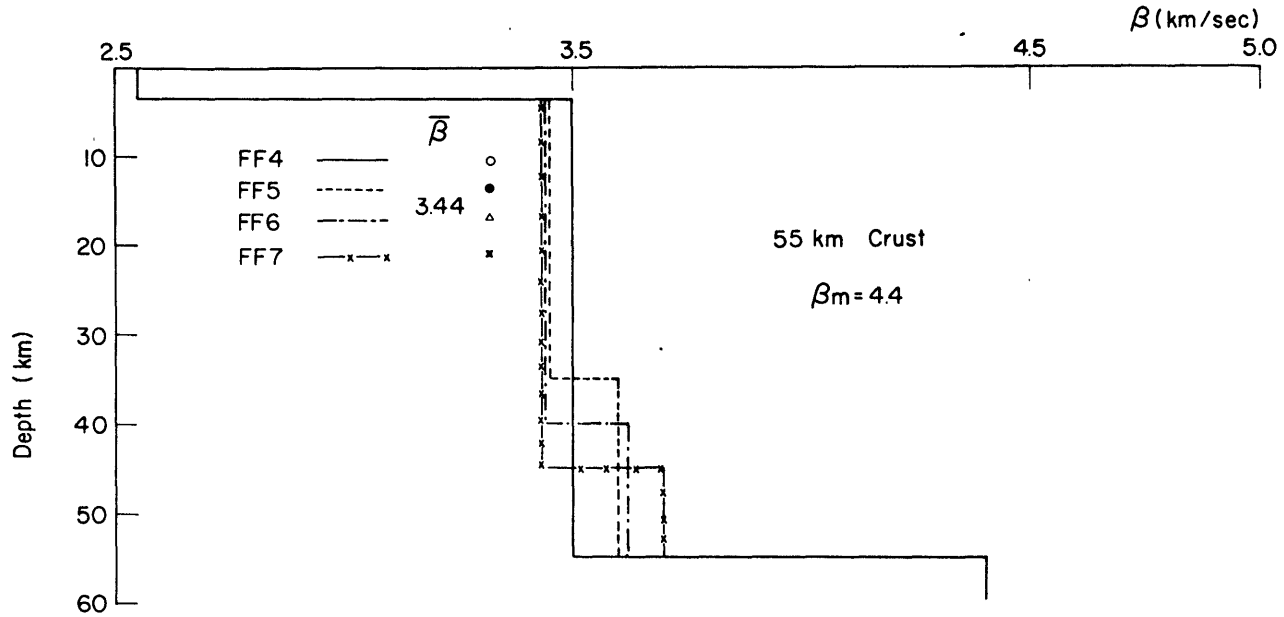
β (km/sec)
2.5
3.5
4.5
5.0
Depth (km)
10
20
30
40
50
60
β̄
FF4
FF5
FF6
FF7
3.44
55 km Crust
βm = 4.4

Fig. 11(b)
(cont.)

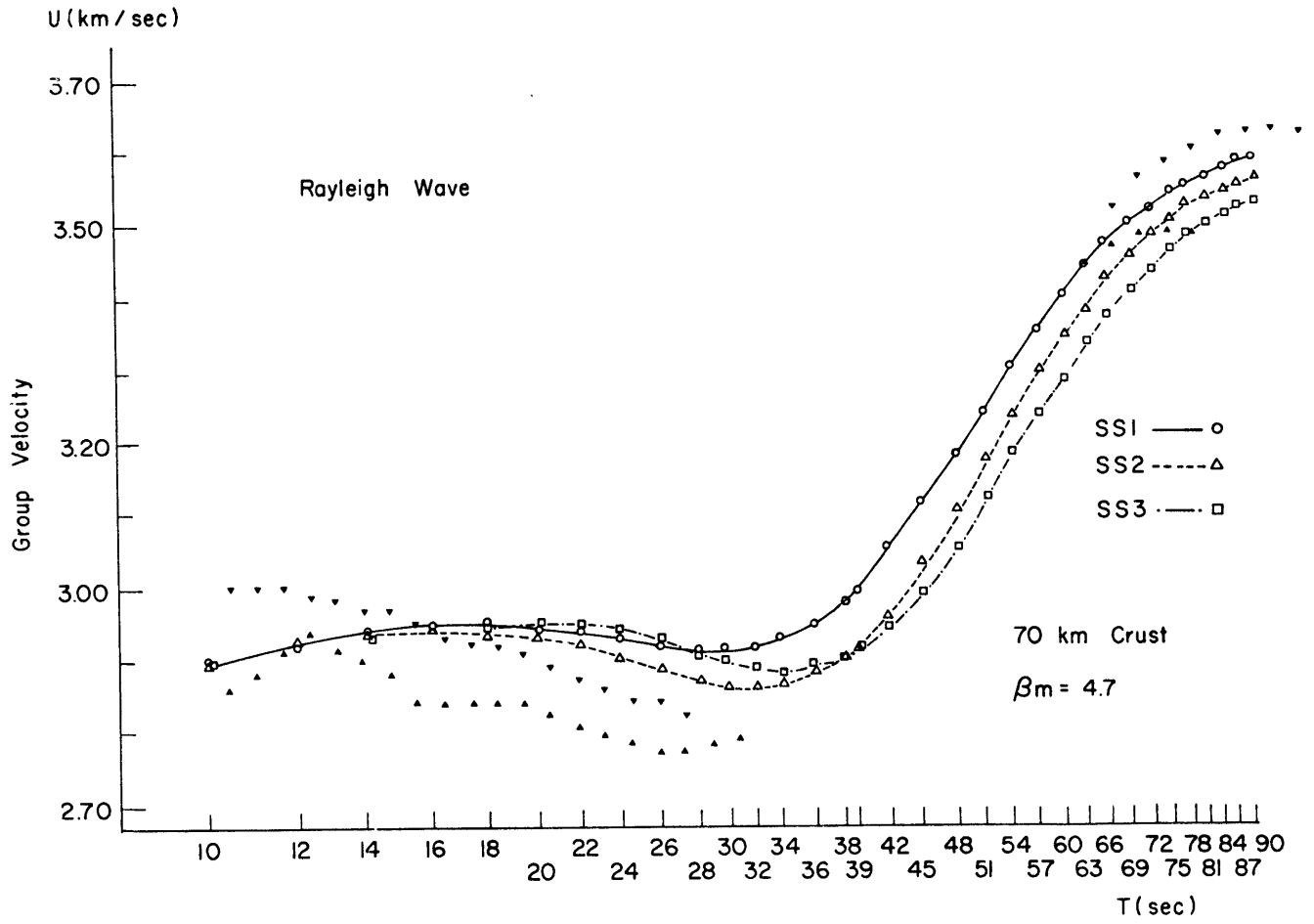
U (km / sec)
3.70
3.50
3.20
3.00
2.70
Group Velocity
Rayleigh Wave
SS1
SS2
SS3
70 km Crust
βm = 4.7
10 12 14 16 18 20 22 24 26 28 30 32 34 36 38 39 42 45 48 51 54 57 60 63 66 69 72 75 78 81 84 87 90
T (sec)

Fig. 12(a)

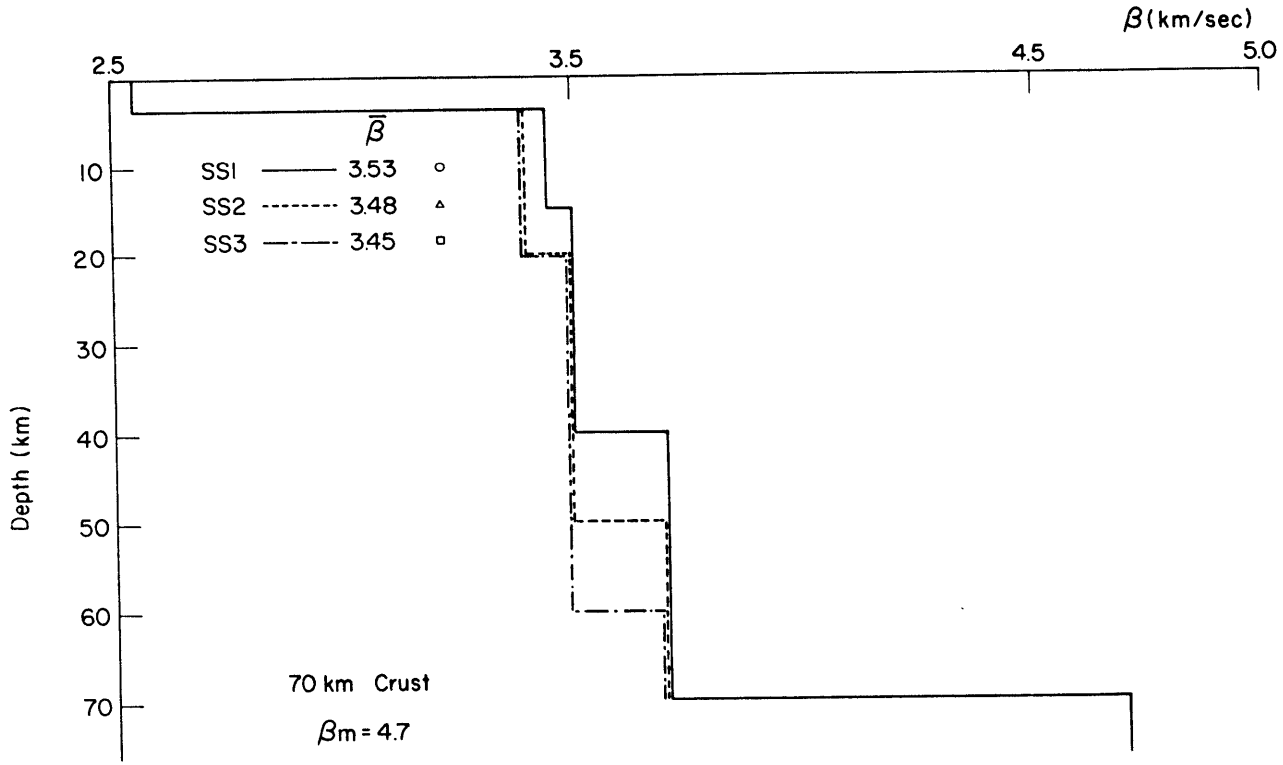
β(km/sec)
2.5
3.5
4.5
5.0
β̄
SSI —— 3.53 ○
SS2 ------- 3.48 △
SS3 —·—· 3.45 □
Depth (km)
10
20
30
40
50
60
70
70 km Crust
βm = 4.7

Fig. 12(a)
(cont.)

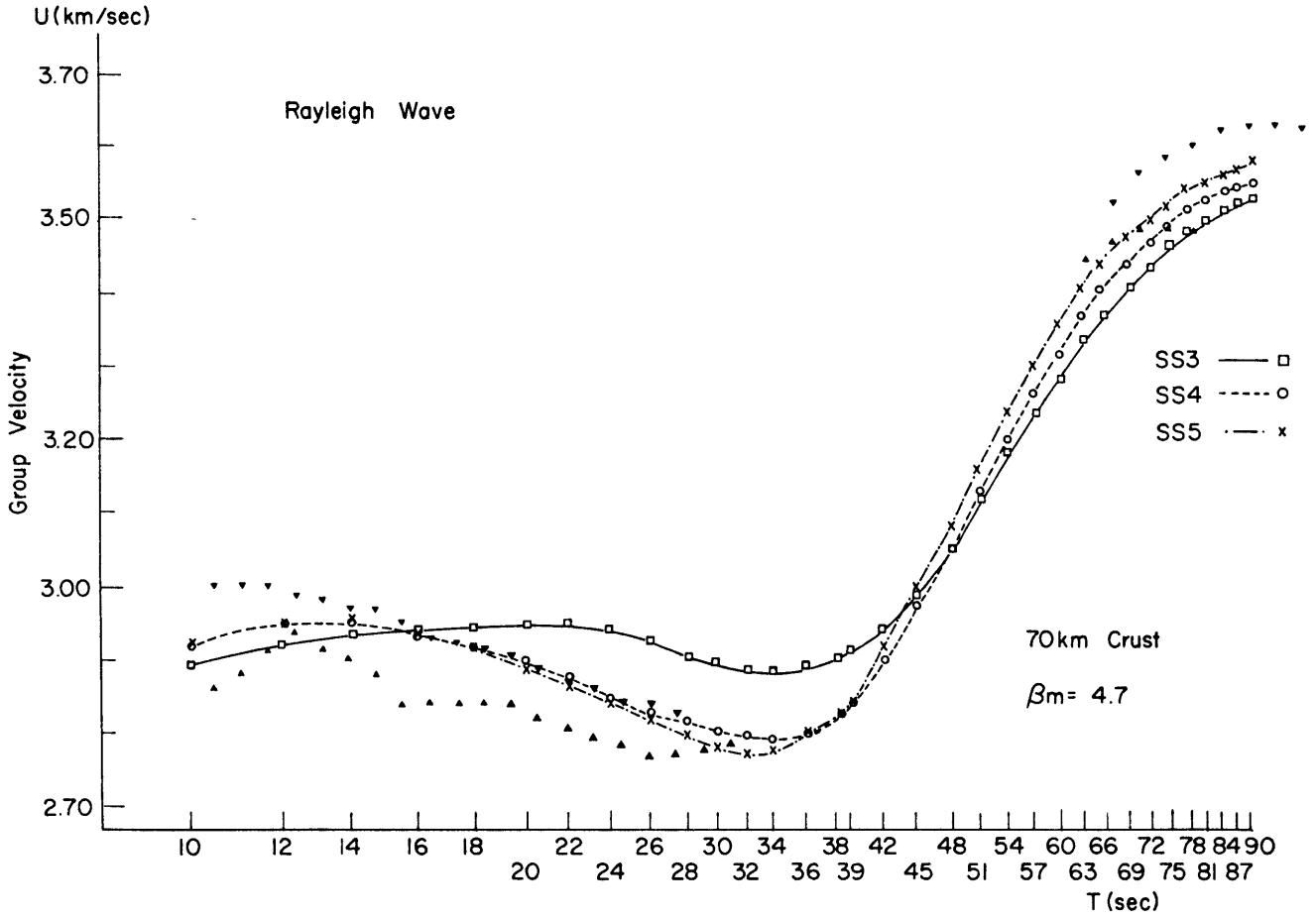
U(km/sec)
3.70
3.50
3.20
3.00
2.70
Group Velocity
Rayleigh Wave
SS3
SS4
SS5
70km Crust
βm= 4.7
10 12 14 16 18 20 22 24 26 28 30 32 34 36 38 39 42 45 48 51 54 57 60 63 66 69 72 75 78 81 84 87 90
T(sec)

Fig. 12(b)

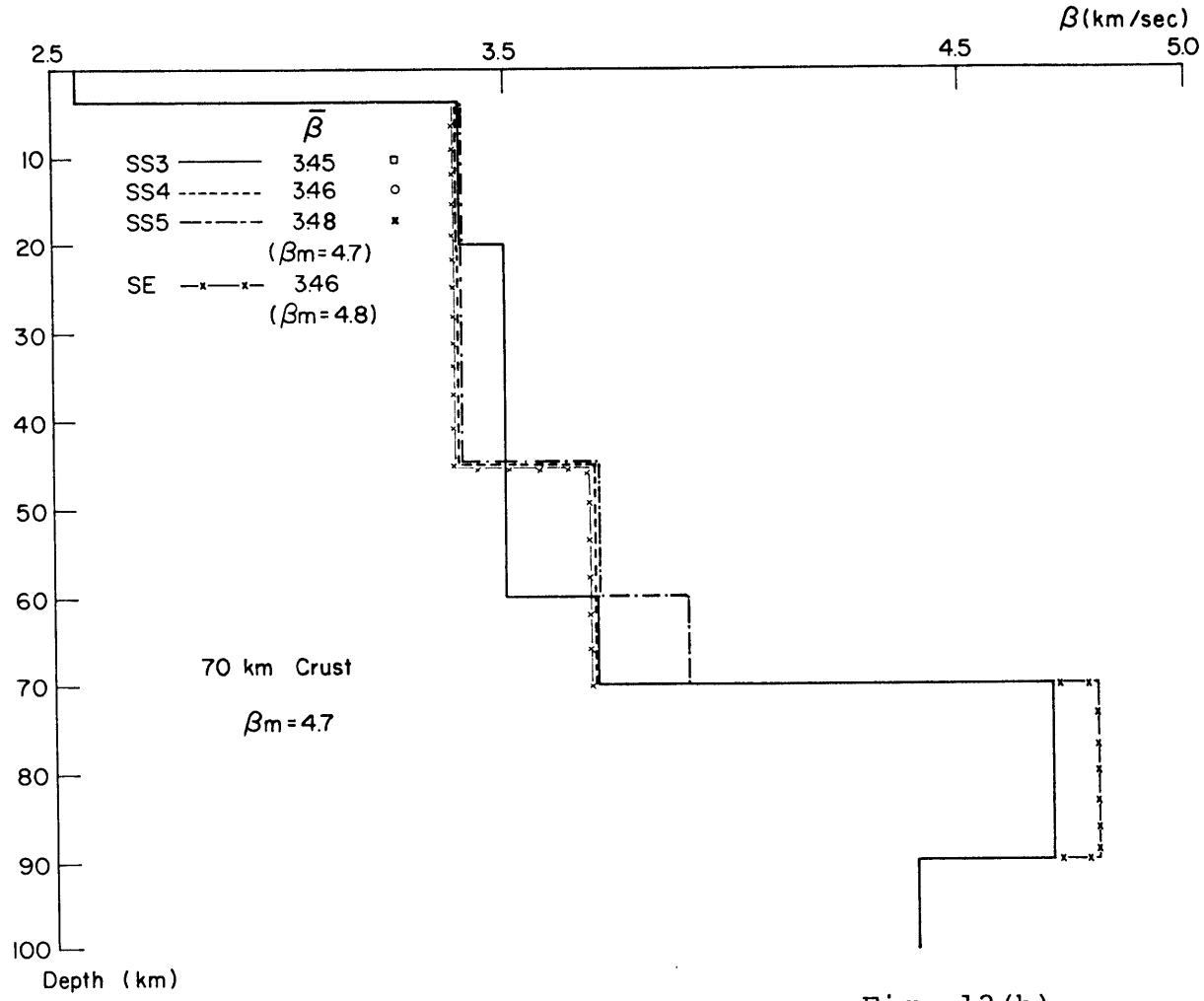
β (km/sec)
2.5
3.5
4.5
5.0
β̄
SS3 ——— 3.45
SS4 -------- 3.46
SS5 —·—·— 3.48
(βm=4.7)
SE —x—x— 3.46
(βm=4.8)
10
20
30
40
50
60
70
80
90
100
70 km Crust
βm=4.7
Depth (km)

Fig. 12(b)
(cont.)

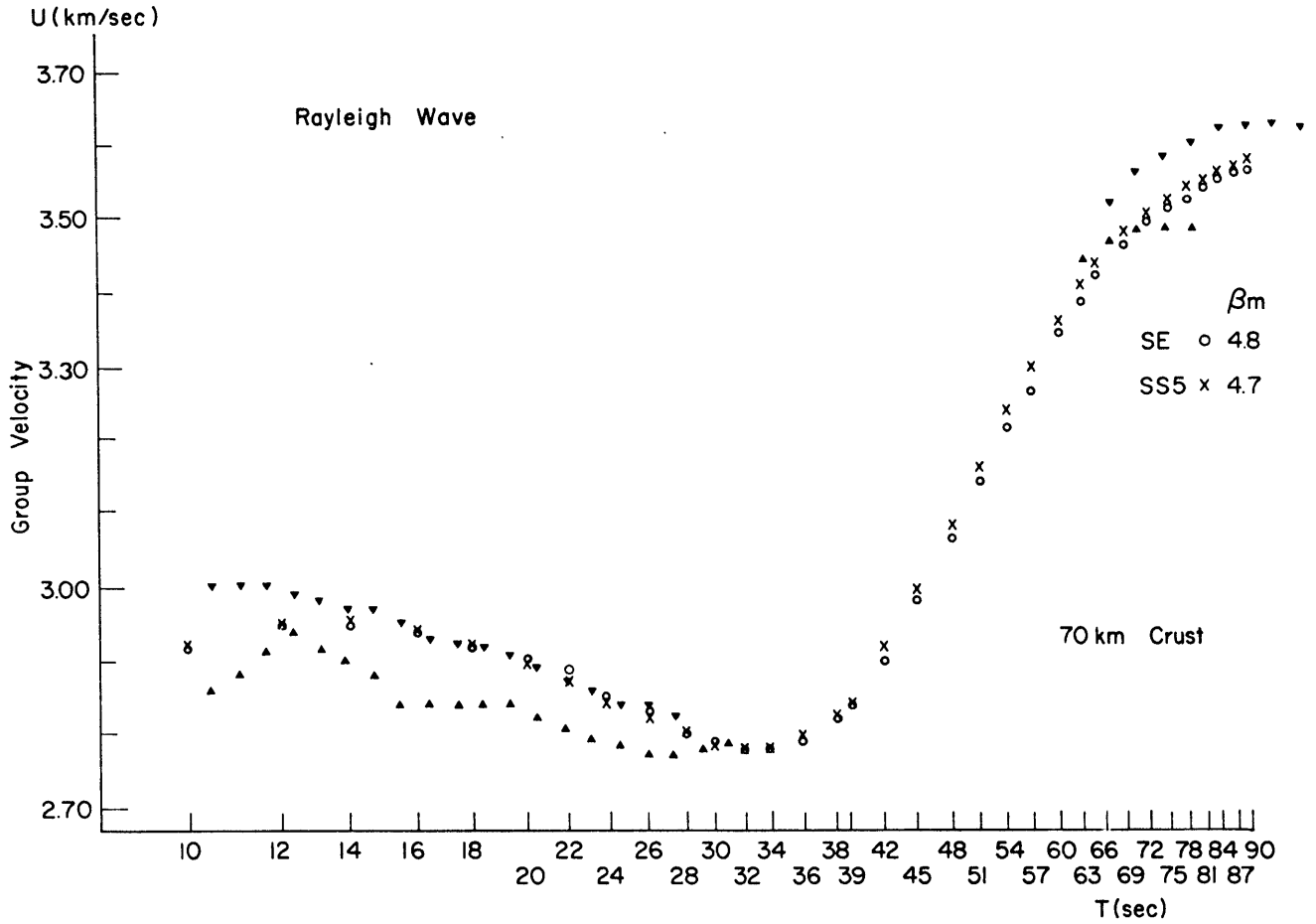
U (km/sec)
3.70
3.50
3.30
3.00
2.70
Group Velocity
Rayleigh Wave
βm
SE ○ 4.8
SS5 × 4.7
70 km Crust
10 12 14 16 18 20 22 24 26 28 30 32 34 36 38 39 42 45 48 51 54 57 60 63 66 69 72 75 78 81 84 87 90
T(sec)

Fig. 12(c)

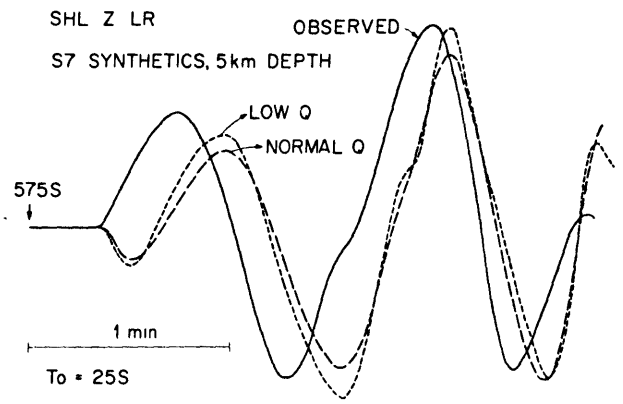
SHL Z LR
S7 SYNTHETICS, 5km DEPTH
OBSERVED
LOW Q
NORMAL Q
575S
1 min
To = 25S

Fig. 13(a)

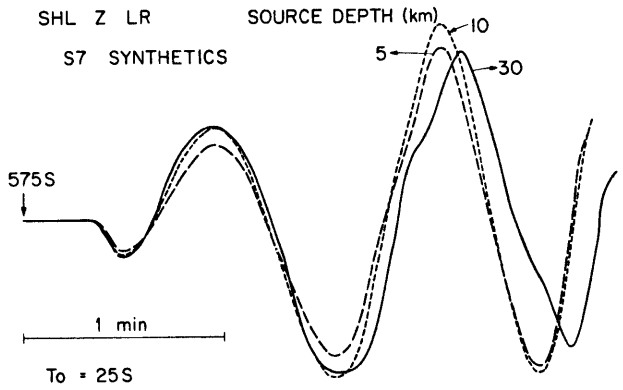

Fig. 13(b)

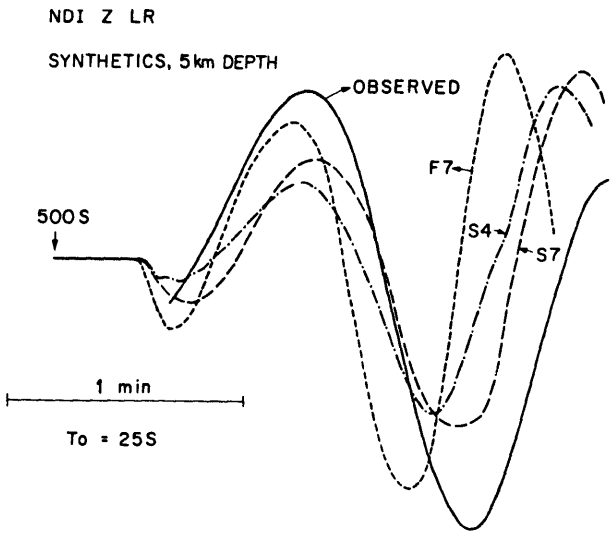
NDI Z LR
SYNTHETICS, 5km DEPTH
OBSERVED
F7
S4
S7
500S
1 min
To = 25S

Fig. 13(c)

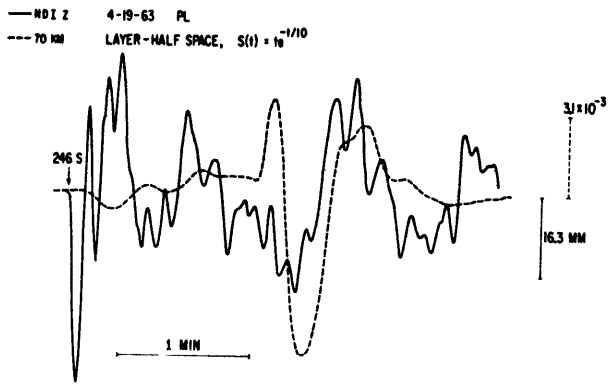
NDI Z
70 KM
4-19-63 PL
LAYER-HALF SPACE, S(t) = t^-1/10
246 S
3.1 x 10^-3
16.3 MM
1 MIN

Fig. 14(a)

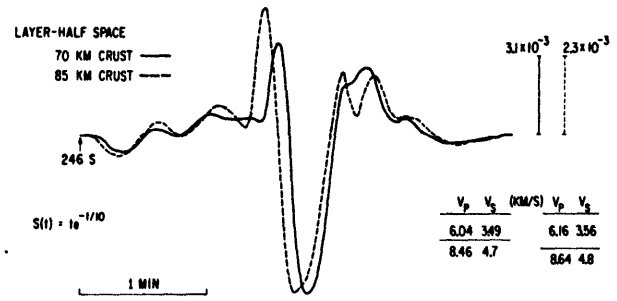
LAYER-HALF SPACE
70 KM CRUST
85 KM CRUST
3.1x10⁻³
2.3x10⁻³
246 S
S(t) = te^-t/10
Vp Vs (KM/S) Vp Vs
6.04 3.49 6.16 3.56
8.46 4.7 8.64 4.8
1 MIN

Fig. 14(b)

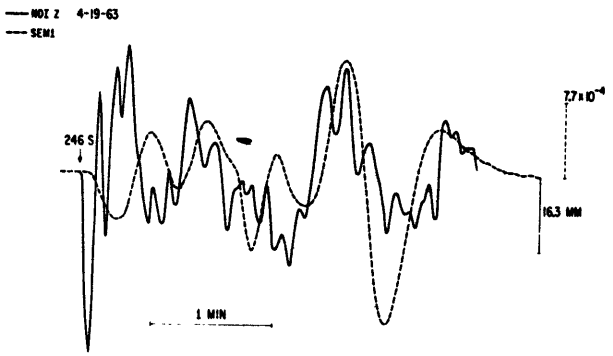

Fig. 14(c)

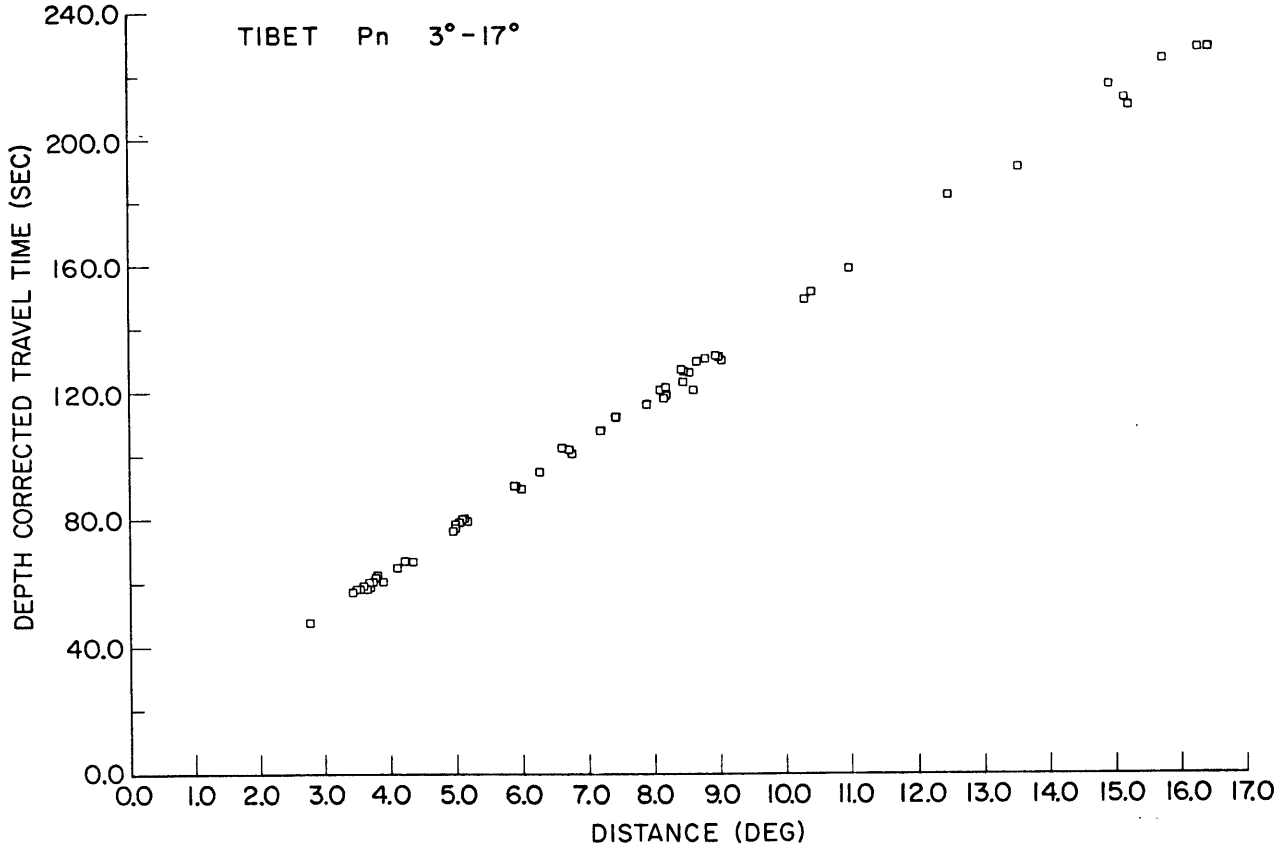
TIBET Pn 3°-17°
DEPTH CORRECTED TRAVEL TIME (SEC)
240.0
200.0
160.0
120.0
80.0
40.0
0.0
0.0 1.0 2.0 3.0 4.0 5.0 6.0 7.0 8.0 9.0 10.0 11.0 12.0 13.0 14.0 15.0 16.0 17.0
DISTANCE (DEG)

Fig. 15

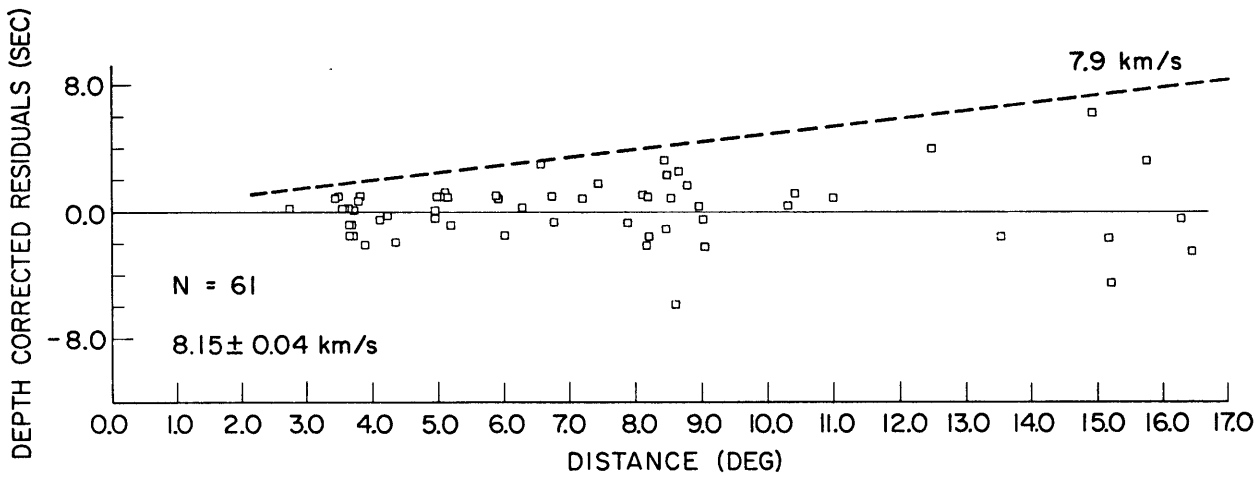
DEPTH CORRECTED RESIDUALS (SEC)
8.0
0.0
-8.0
7.9 km/s
N = 61
8.15± 0.04 km/s
0.0 1.0 2.0 3.0 4.0 5.0 6.0 7.0 8.0 9.0 10.0 11.0 12.0 13.0 14.0 15.0 16.0 17.0
DISTANCE (DEG)

Fig. 15
(cont.)

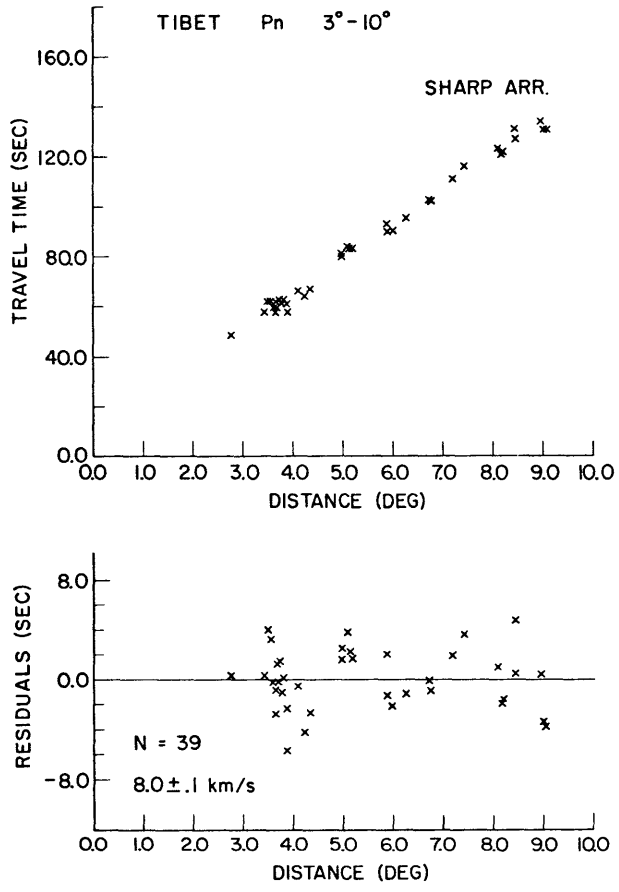
TIBET Pn 3°-10°
SHARP ARR.
TRAVEL TIME (SEC)
160.0
120.0
80.0
40.0
0.0
0.0 1.0 2.0 3.0 4.0 5.0 6.0 7.0 8.0 9.0 10.0
DISTANCE (DEG)
RESIDUALS (SEC)
8.0
0.0
-8.0
N = 39
8.0±.1 km/s
0.0 1.0 2.0 3.0 4.0 5.0 6.0 7.0 8.0 9.0 10.0
DISTANCE (DEG)

Fig. 16(a)

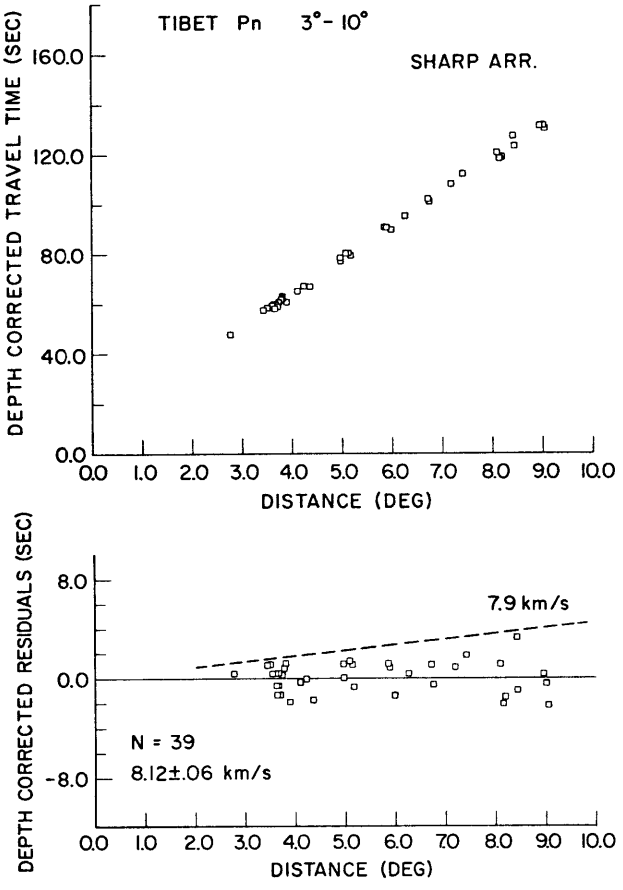
TIBET Pn 3°- 10°
SHARP ARR.
DEPTH CORRECTED TRAVEL TIME (SEC)
160.0
120.0
80.0
40.0
0.0
0.0 1.0 2.0 3.0 4.0 5.0 6.0 7.0 8.0 9.0 10.0
DISTANCE (DEG)
DEPTH CORRECTED RESIDUALS (SEC)
8.0
0.0
-8.0
7.9 km/s
N = 39
8.12±.06 km/s
0.0 1.0 2.0 3.0 4.0 5.0 6.0 7.0 8.0 9.0 10.0
DISTANCE (DEG)

Fig. 16(b)

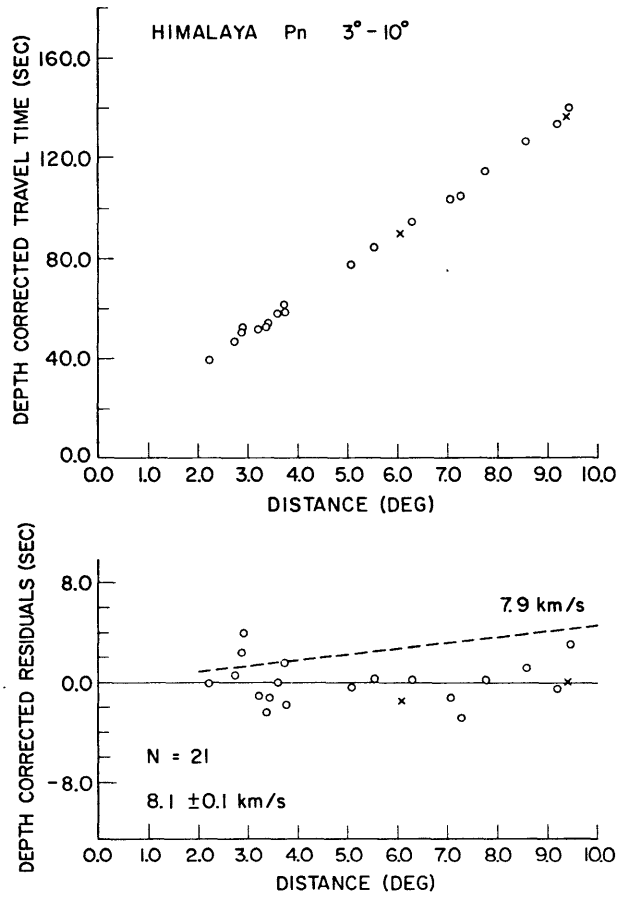
HIMALAYA Pn 3° - 10°
DEPTH CORRECTED TRAVEL TIME (SEC)
160.0
120.0
80.0
40.0
0.0
0.0 1.0 2.0 3.0 4.0 5.0 6.0 7.0 8.0 9.0 10.0
DISTANCE (DEG)
DEPTH CORRECTED RESIDUALS (SEC)
8.0
0.0
-8.0
7.9 km/s
N = 21
8.1 ±0.1 km/s
0.0 1.0 2.0 3.0 4.0 5.0 6.0 7.0 8.0 9.0 10.0
DISTANCE (DEG)

Fig. 17

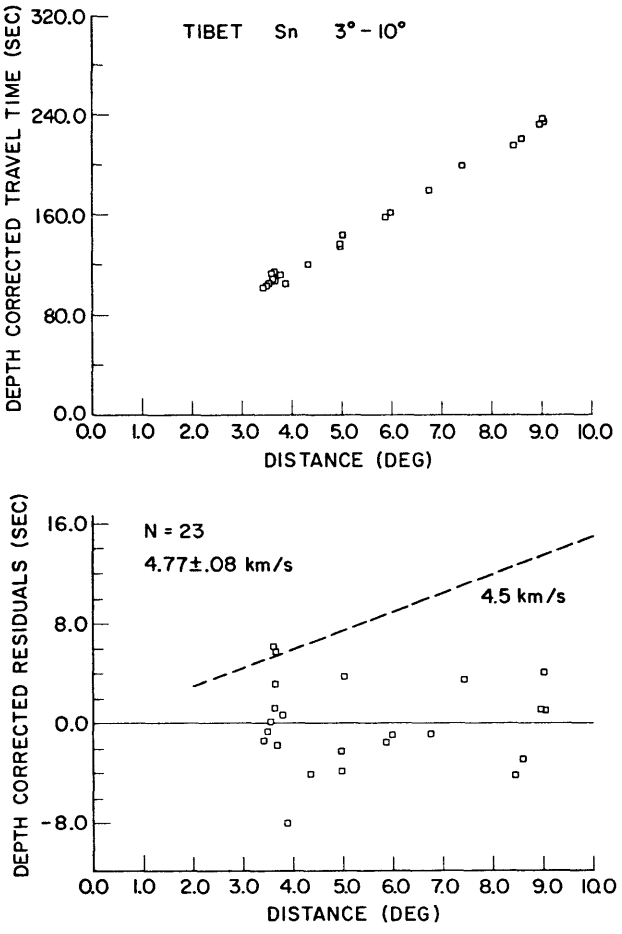
TIBET Sn 3° - 10°
DEPTH CORRECTED TRAVEL TIME (SEC)
320.0
240.0
160.0
80.0
0.0
0.0 1.0 2.0 3.0 4.0 5.0 6.0 7.0 8.0 9.0 10.0
DISTANCE (DEG)
N = 23
4.77±.08 km/s
4.5 km/s
DEPTH CORRECTED RESIDUALS (SEC)
16.0
8.0
0.0
-8.0
0.0 1.0 2.0 3.0 4.0 5.0 6.0 7.0 8.0 9.0 10.0
DISTANCE (DEG)

Fig. 18

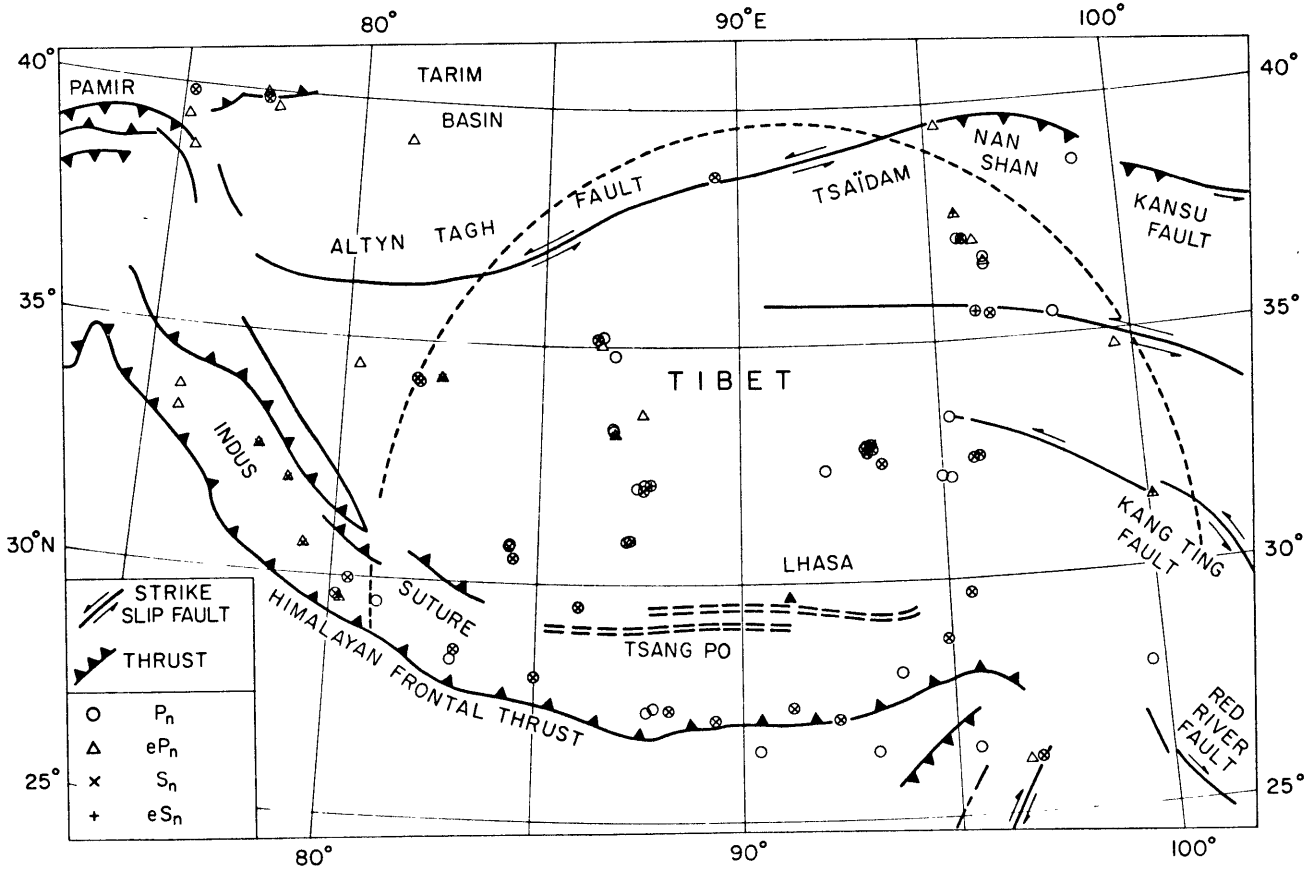
80°
90°E
100°
40°
35°
30°N
25°
PAMIR
TARIM
BASIN
ALTYN TAGH
FAULT
TSAÏDAM
NAN SHAN
KANSU FAULT
TIBET
INDUS
SUTURE
HIMALAYAN FRONTAL THRUST
LHASA
TSANG PO
KANG TING FAULT
RED RIVER FAULT
STRIKE SLIP FAULT
THRUST
Pn
ePn
Sn
eSn

Fig. 19

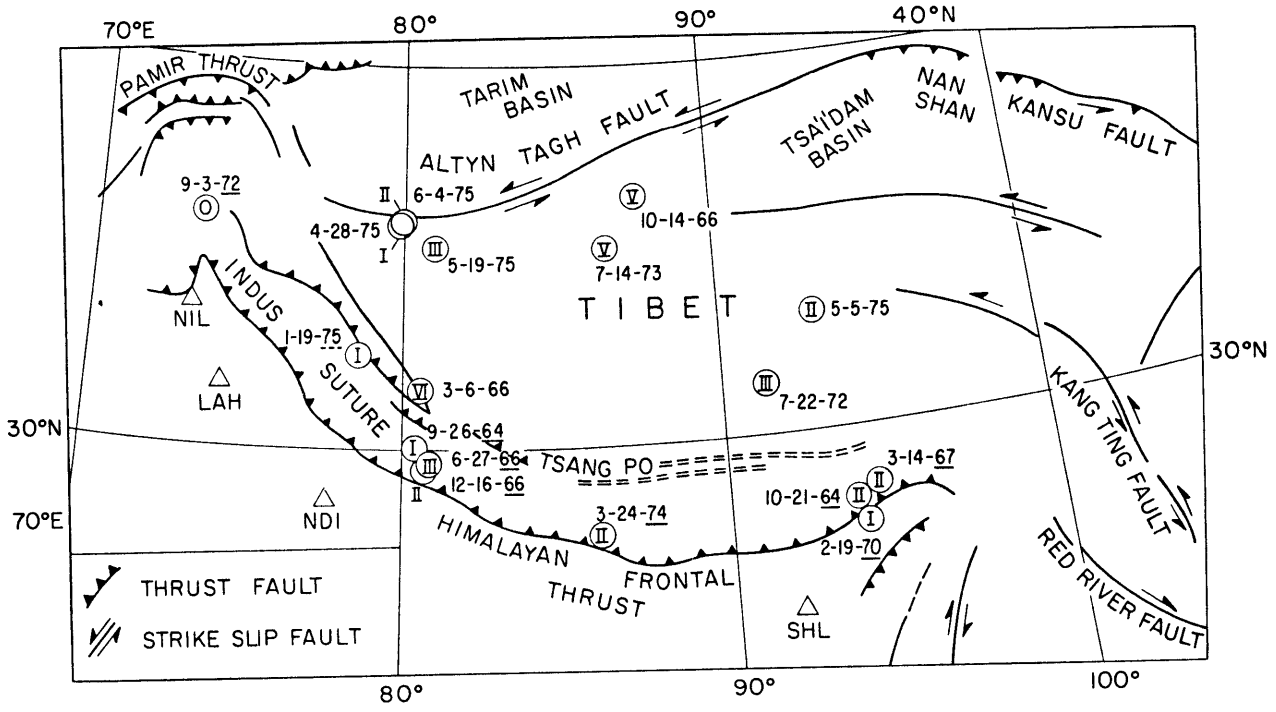
70°E
80°
90°
40°N
30°N
70°E
80°
90°
100°
PAMIR THRUST
TARIM BASIN
ALTYN TAGH FAULT
TSAIDAM BASIN
NAN SHAN
KANSU FAULT
9-3-72
6-4-75
4-28-75
5-19-75
10-14-66
7-14-73
TIBET
5-5-75
INDUS SUTURE
NIL
LAH
NDI
1-19-75
3-6-66
9-26-64
6-27-66
12-16-66
7-22-72
KANG TING FAULT
TSANG PO
3-14-67
10-21-64
3-24-74
2-19-70
HIMALAYAN FRONTAL THRUST
SHL
RED RIVER FAULT
THRUST FAULT
STRIKE SLIP FAULT

Fig. 20

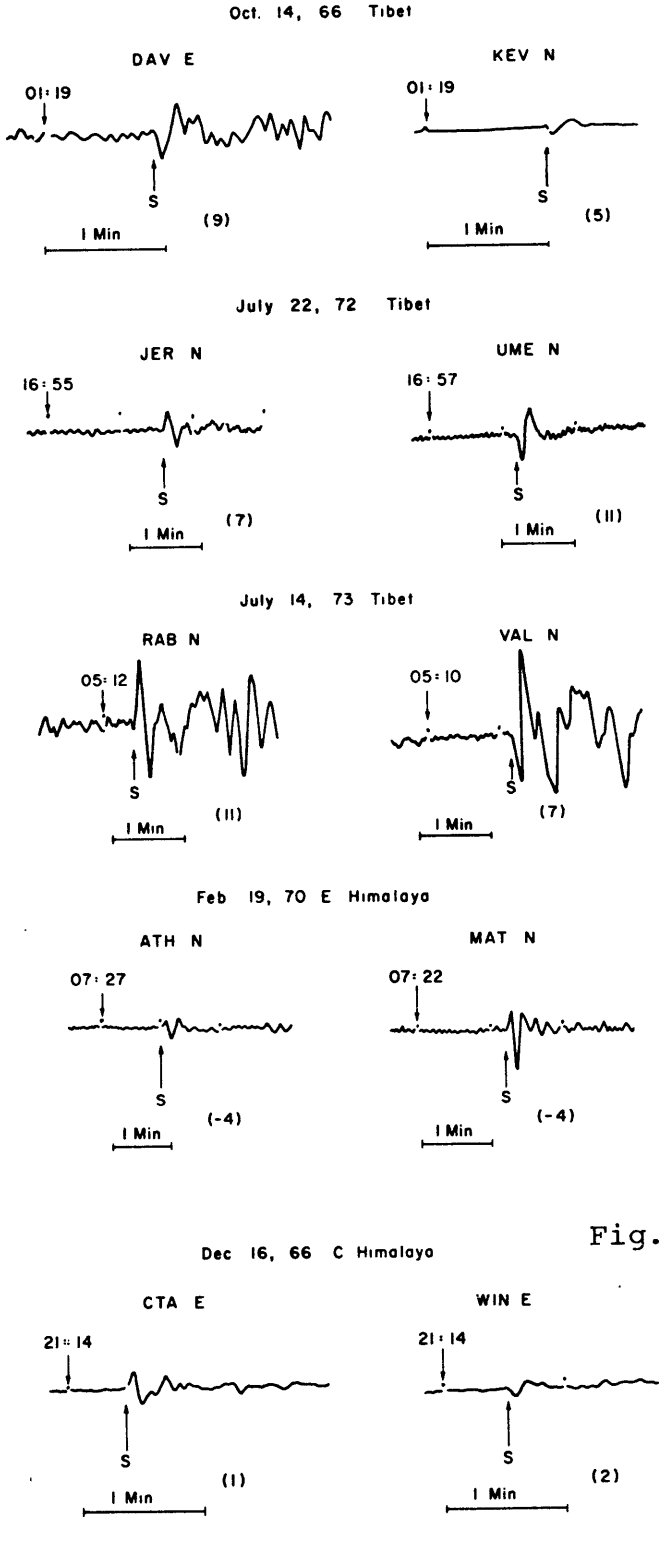
Oct. 14, 66 Tibet
DAV E
01:19
S
(9)
1 Min
KEV N
01:19
S
(5)
1 Min
July 22, 72 Tibet
JER N
16:55
S
(7)
1 Min
UME N
16:57
S
(11)
1 Min
July 14, 73 Tibet
RAB N
05:12
S
(11)
1 Min
VAL N
05:10
S
(7)
1 Min
Feb 19, 70 E Himalaya
ATH N
07:27
S
(-4)
1 Min
MAT N
07:22
S
(-4)
1 Min
Dec 16, 66 C Himalaya
CTA E
21:14
S
(1)
1 Min
WIN E
21:14
S
(2)
1 Min

Fig. 21

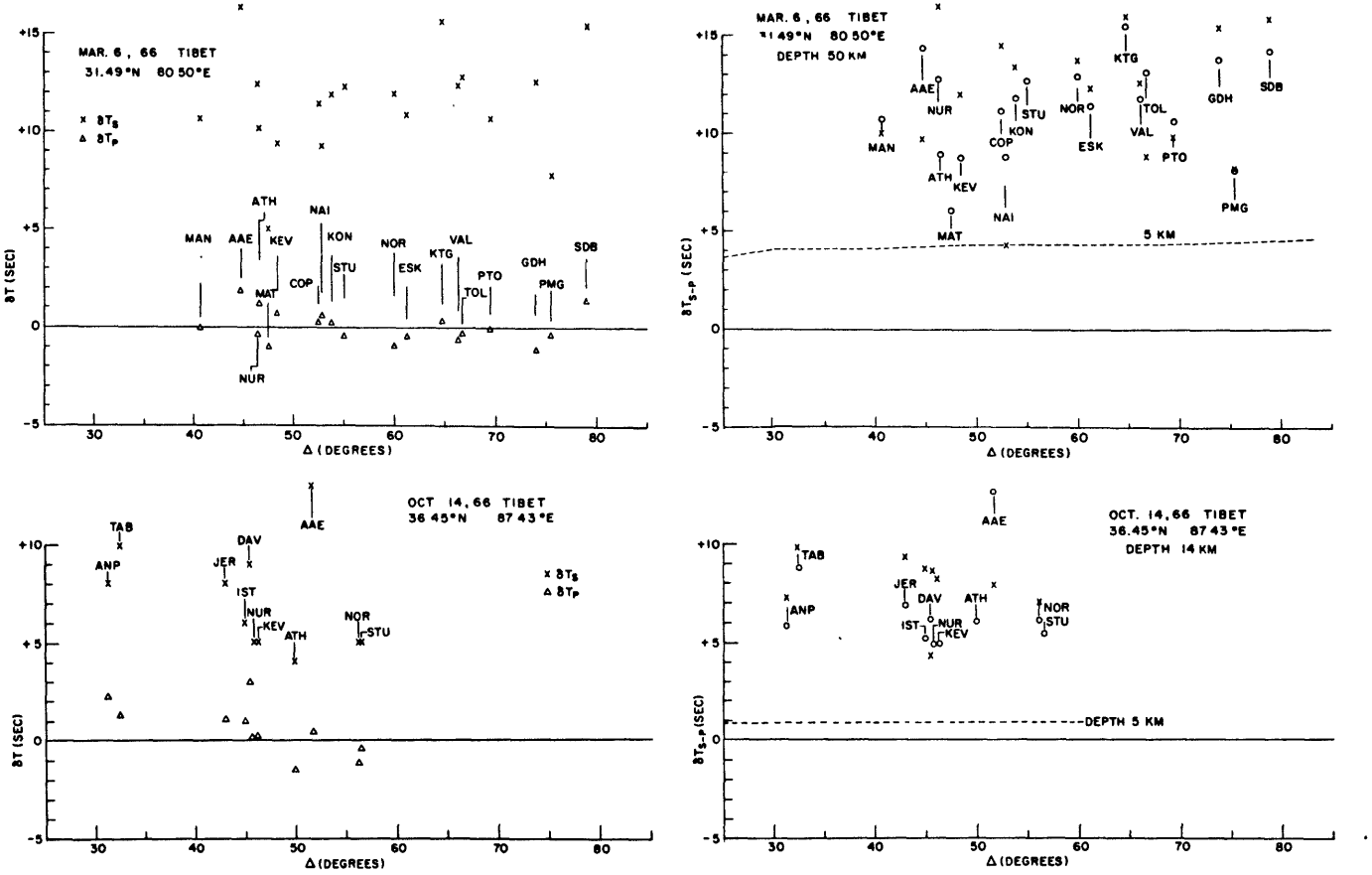

Fig. 22(a)

Fig. 22(b)

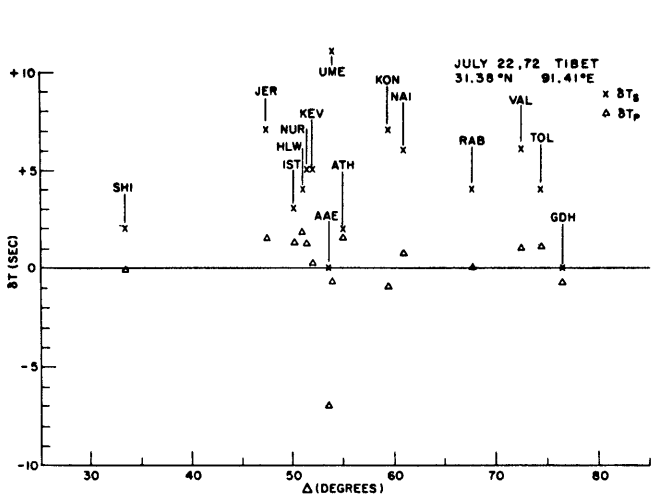

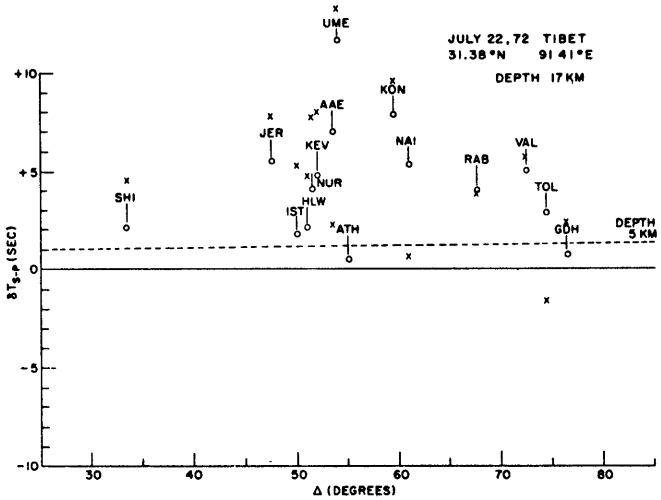

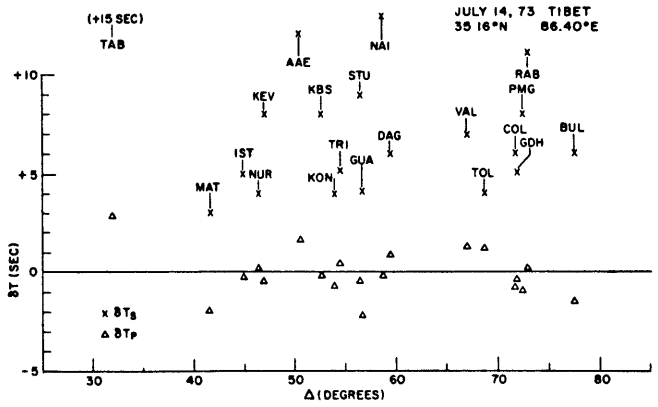

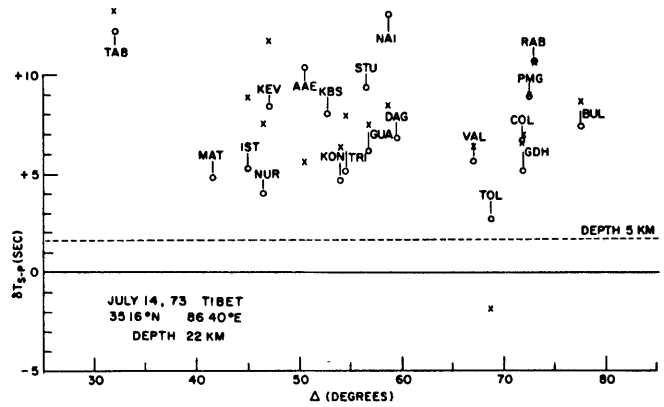

Fig. 22(a) (cont.)

Fig. 22(b) (cont.)

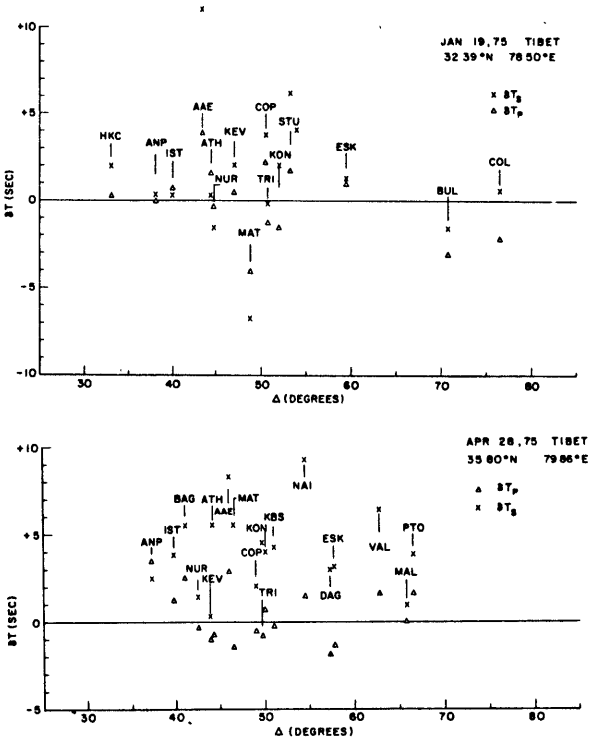

Fig. 22(a) (cont.)

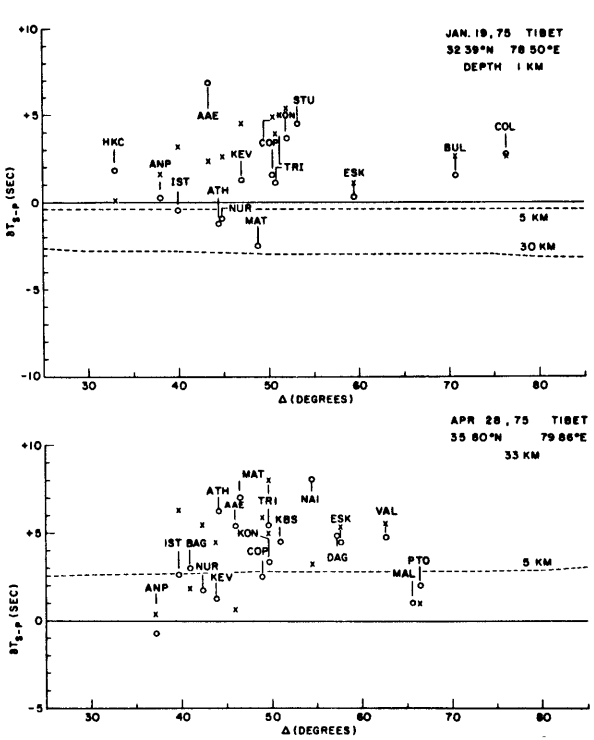

Fig. 22(b) (cont.)

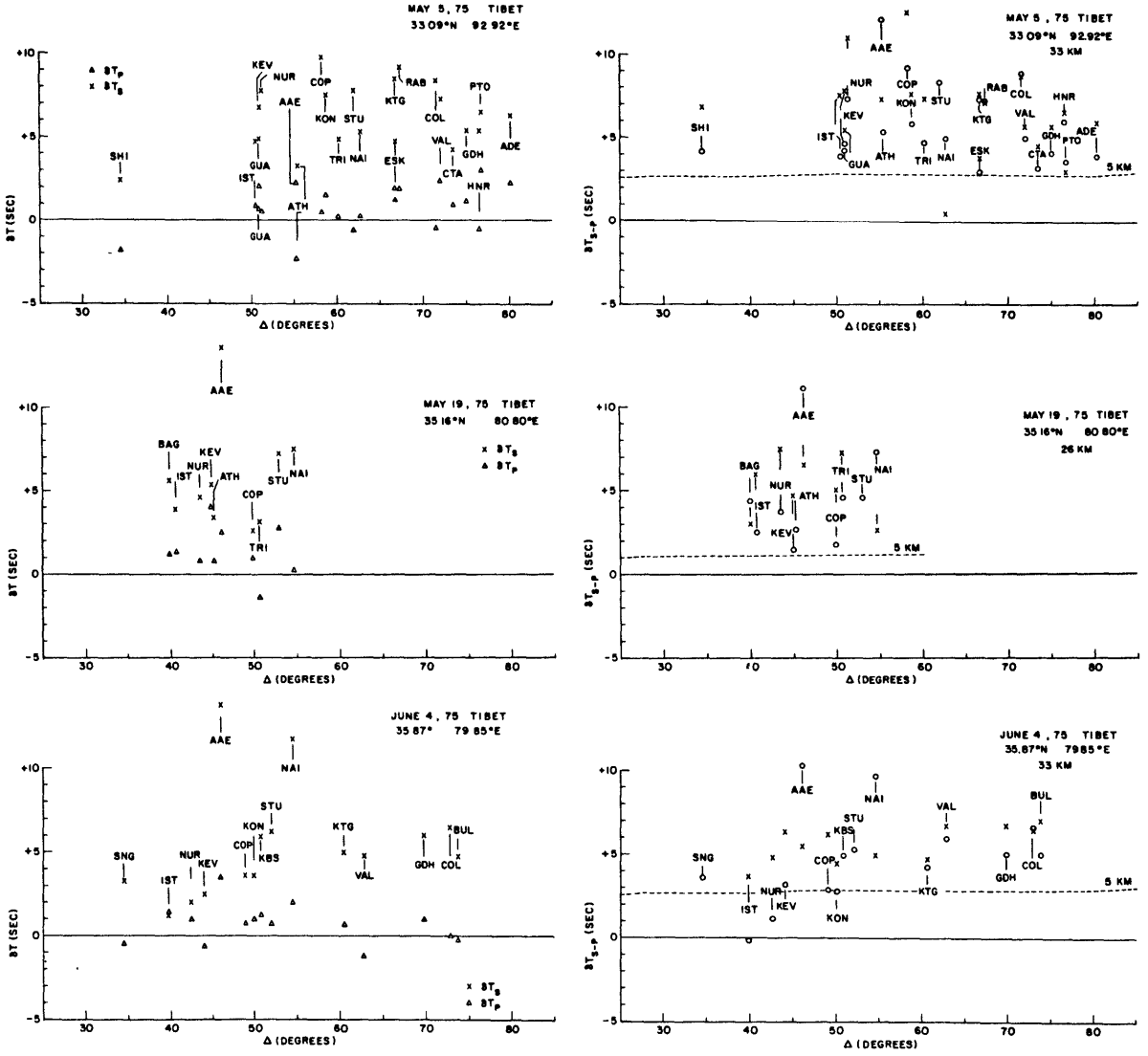

Fig. 22(a) (cont.)

Fig. 22(b) (Cont.)

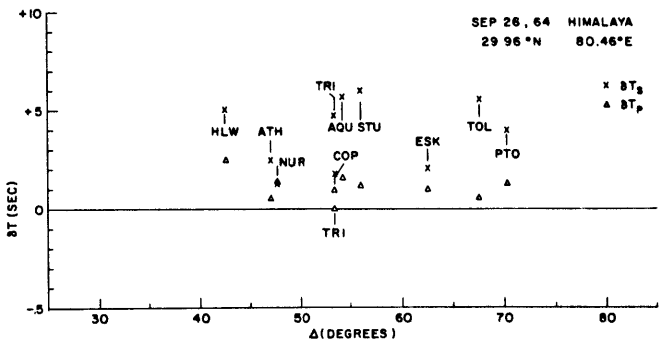

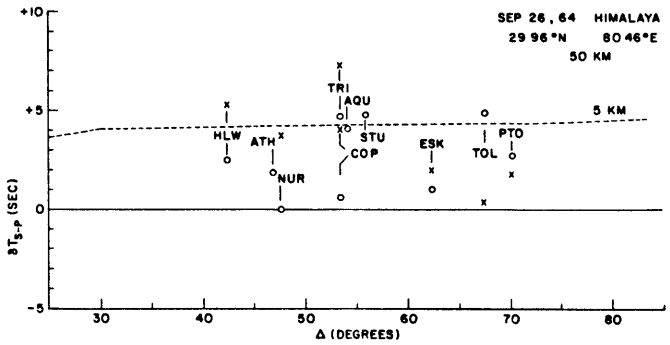

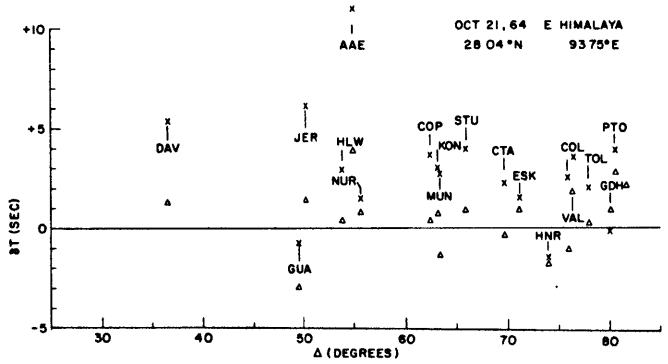

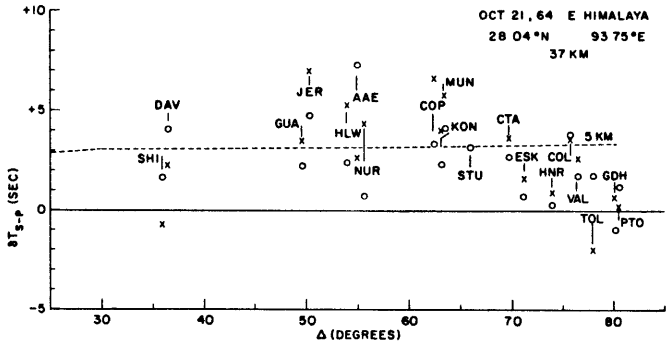

Fig. 23(a)

Fig. 23(b)

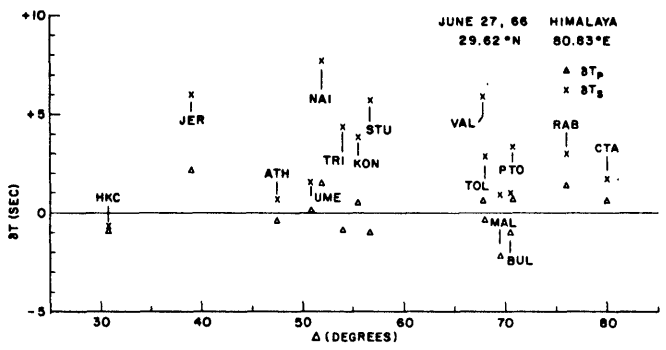

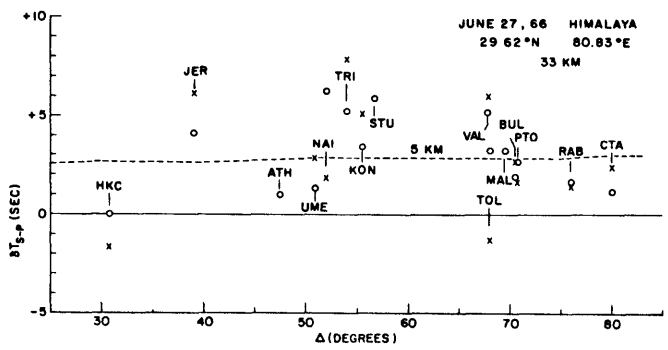

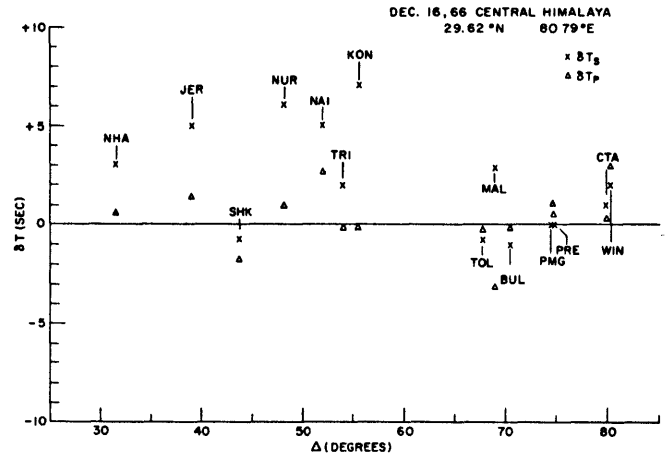

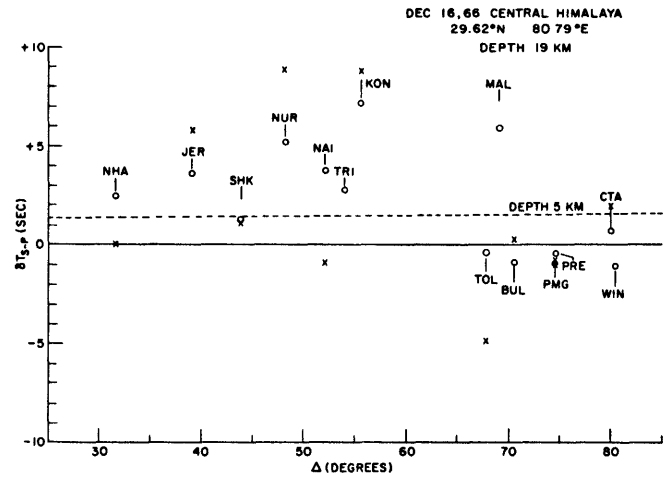

Fig. 23(a)
(cont.)

Fig. 23(b)
(cont.)

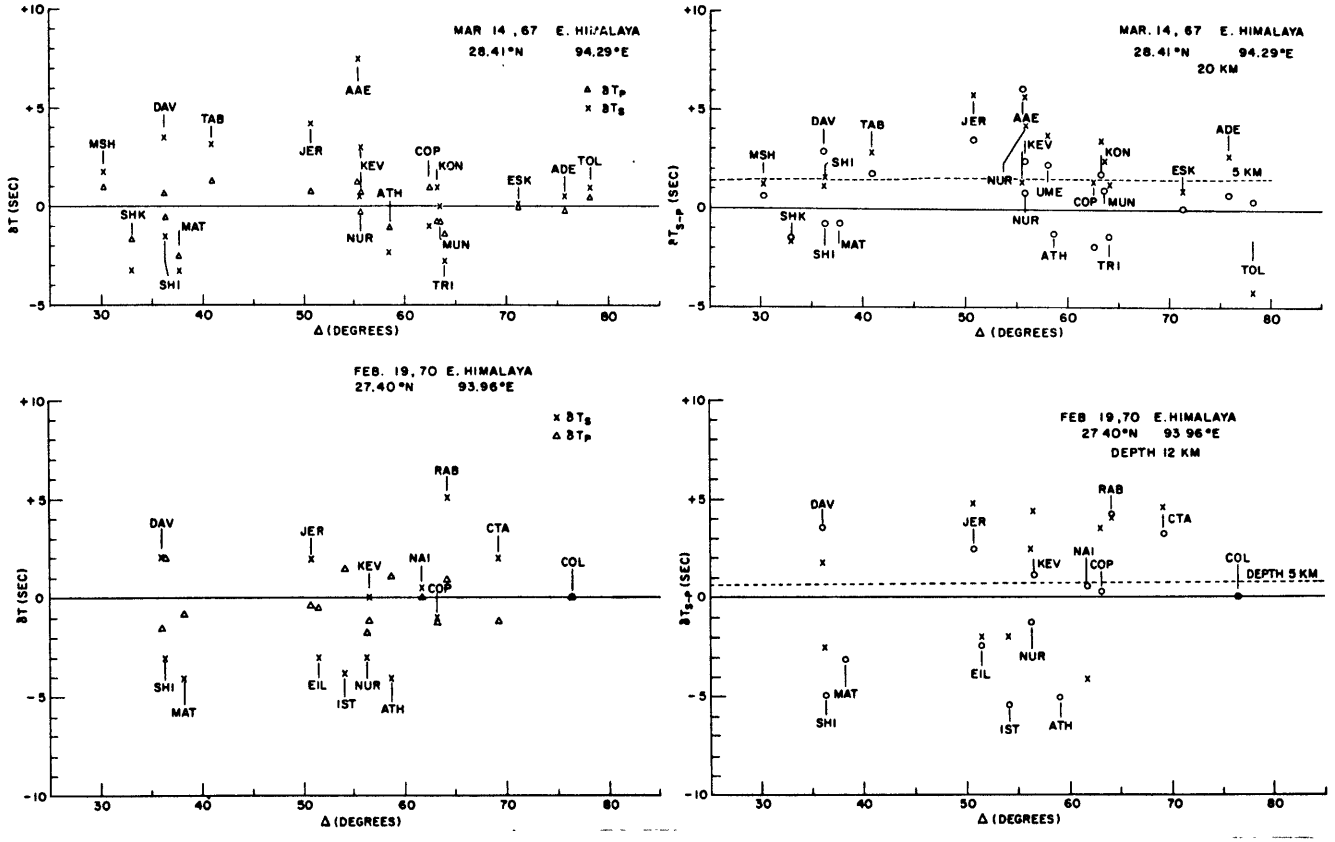

Fig. 23(a) (cont.)

Fig. 23(b) (cont.)

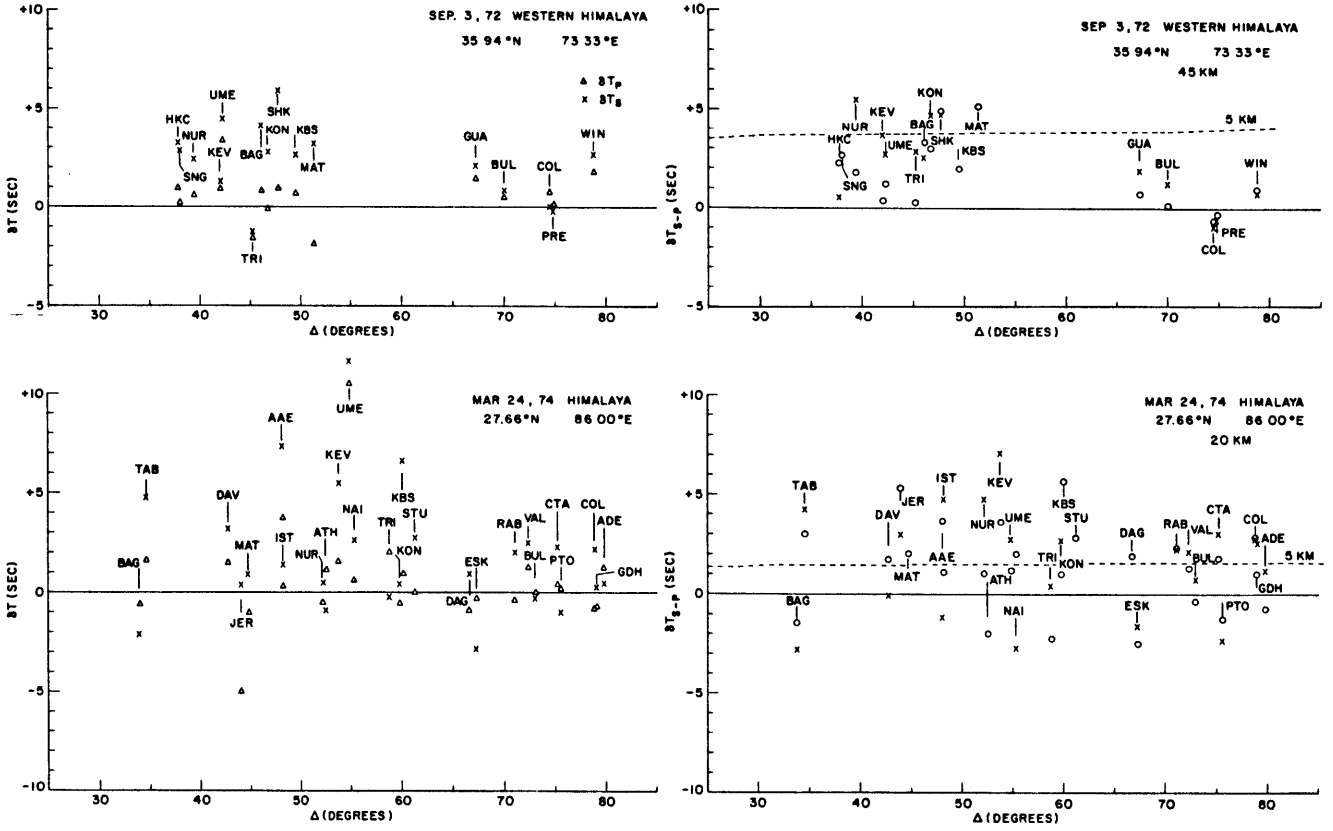

Fig. 23(a) (cont.)

Fig. 23(b) (cont.)

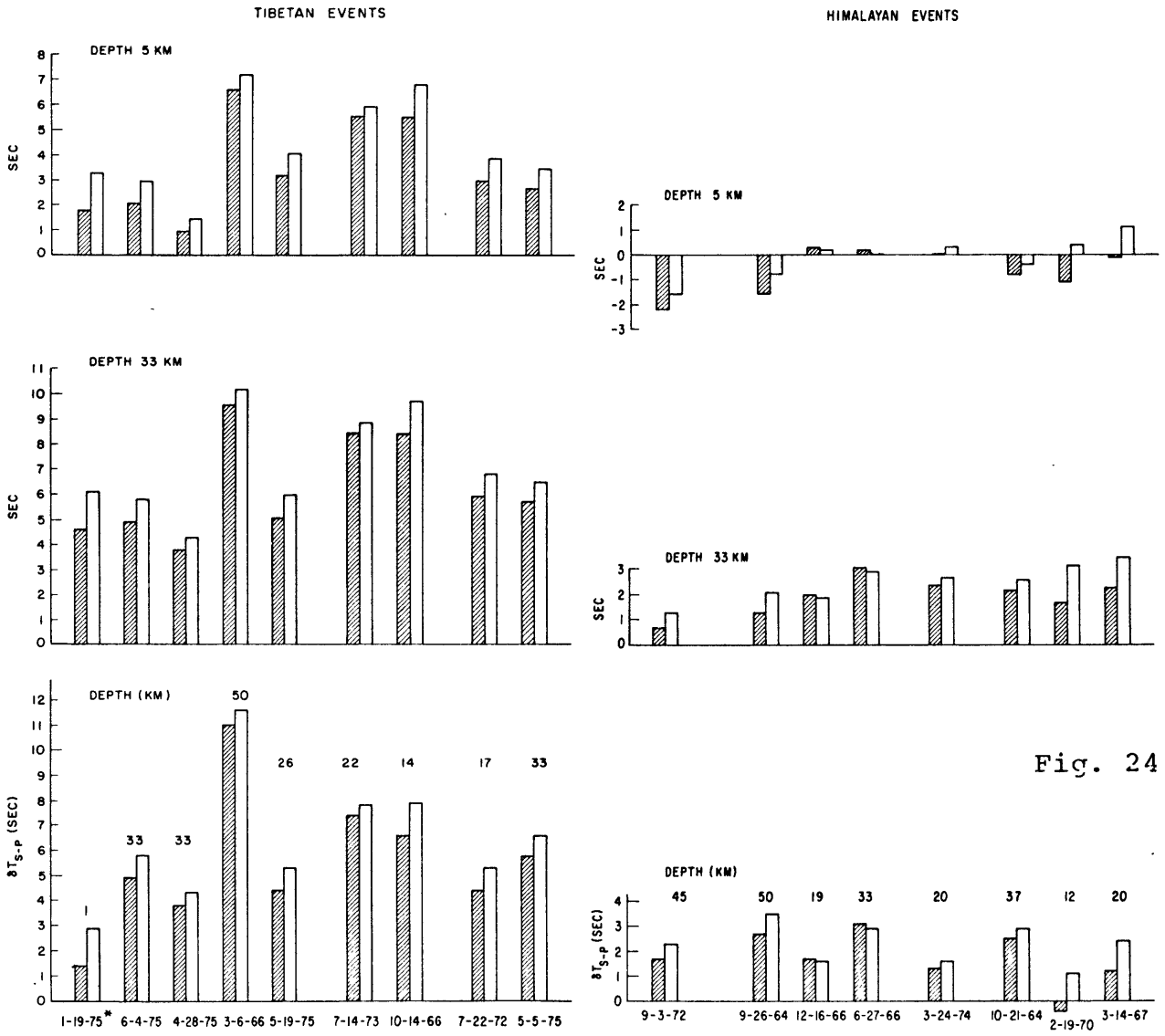
TIBETAN EVENTS
HIMALAYAN EVENTS
DEPTH 5 KM
DEPTH 5 KM
SEC
DEPTH 33 KM
DEPTH 33 KM
DEPTH (KM)
DEPTH (KM)
δT_{S-P} (SEC)
1
33
33
50
26
22
14
17
33
45
50
19
33
20
37
12
20
1-19-75*
6-4-75
4-28-75
3-6-66
5-19-75
7-14-73
10-14-66
7-22-72
5-5-75
9-3-72
9-26-64
12-16-66
6-27-66
3-24-74
10-21-64
2-19-70
3-14-67

Fig. 24

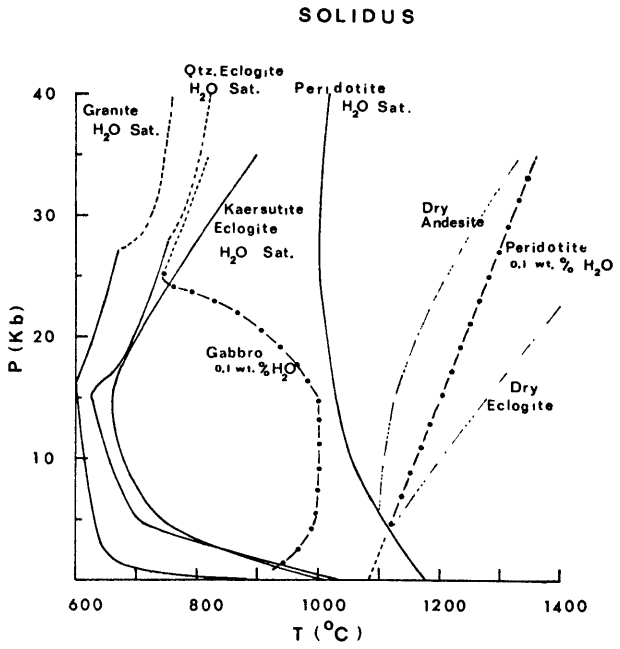
SOLIDUS
Qtz. Eclogite
H2O Sat.
Peridotite
H2O Sat.
Granite
H2O Sat.
Kaersutite
Eclogite
H2O Sat.
Dry
Andesite
Peridotite
0.1 wt. % H2O
Gabbro
0.1 wt. % H2O
Dry
Eclogite
40
30
20
10
P (Kb)
600
800
1000
1200
1400
T (°C)

Fig. 25

CHAPTER IV

An Intermediate Depth Earthquake Beneath Tibet: Source Characteristics of the Event of September 14, 1976

Wang-Ping Chen
Department of Earth and Planetary Sciences
Massachusetts Institute of Technology
Cambridge, MA 02139

Thomas J. Fitch
Applied Seismology Group, Lincoln Laboratory
Massachusetts Institute of Technology
Cambridge, MA 02139

John L. Nabelek
Department of Earth and Planetary Sciences
Massachusetts Institute of Technology
Cambridge, MA 02139

Peter Molnar
Department of Earth and Planetary Sciences
Massachusetts Institute of Technology
Cambridge, MA 02139

Abstract

This paper presents the results of a detailed study of an intermediate depth earthquake beneath southern Tibet (September 14, 1976, 06 hr 43 m 51.6S; 29.81°N, 89.57°E, focal depth 90±10 km, m_b = 5.4).

From the differences in arrival times of P, pP and sP, from a synthesis of the phases, and from Rayleigh wave spectral densities, the focal depth is estimated to be 90±10 km and therefore in the uppermost mantle. From the polarities of the first motions of P waves, an inversion of the relative amplitudes of P, pP and sP and their synthesis, the fault plane solution is constrained to be predominantly normal faulting with the T-axis approximately horizontal and east-west trending. This fault plane solution is similar to those for shallow earthquakes near the surface of Tibet. The occurrence of an earthquake at such a depth is consistent with rapid deformation at a temperature of between 700 to 800°C in the mantle beneath the Tibetan crust. The seismic moment of a double couple point source is estimated to be about 6.5×10^{24} dyne-cm (with an uncertainty of about a factor of 1.4) from the sP amplitudes in the period range of about 10 sec, and 5×10^{24} dyne-cm (with an uncertainty of about a factor of 1.3) from the spectral density of Rayleigh waves with periods of 50 sec.

INTRODUCTION

Intermediate and deep focus earthquakes are typically associated with subduction zones of oceanic lithospheres and they rarely occur beneath continents. Although the intermediate depth earthquakes in the Hindu Kush, Carpathians and Burma and the deep Spanish earthquake of 1954 are good examples of such events beneath continents, they too are generally considered to be evidence for sinking slabs of oceanic lithosphere [e.g., Chatelain et al., 1979; Chung and Kanamori, 1976; Isacks and Molnar, 1971; Roecker et al., 1979]. Presumably, it is only where cold lithosphere is subducted into the asthenosphere that the material at intermediate depths can, in general, be strong enough to support the stresses needed to cause earthquakes and that such stresses can be generated.

Whether intermediate and deep earthquakes result from deformation processes analogous to brittle failure or stick-slip of earth materials observed in laboratory experiments remains controversial. In any case, the depth and fault plane solutions of these earthquakes have been used extensively to study the state of stress in the subducted lithosphere [e.g., Isacks and Molnar, 1971]. In fact they provide the only information that we have for the orientation of the principle stresses a few km

beneath the earth's surface. It follows that the occurrence of unusually deep earthquakes are likely to provide new information on the state of stress deep in the lithosphere. Moreover, since earthquakes do not seem to occur where the temperature is high [Brace and Byerlee, 1970; Molnar et al., 1979], their occurrence can be used to place a constraint on the temperature of the material in the source region.

In this study, we present seismic evidences of an earthquake with a focal depth of about 90 km beneath southern Tibet where active subduction of oceanic lithosphere presumably ceased a few tens of m.y. ago. To our knowledge, the earthquake considered in the present study is the first to be studied that occurred at intermediate depths and that cannot be ascribed to subduction of oceanic lithosphere.

The high Tibetan Plateau, north of the Himalaya convergent zone, is a focal point in understanding the relationship between the onset of the continental collision between India and Eurasia about 40 m.y. ago and the active tectonics of much of Asia [e.g., Dewey and Burke, 1973; Molnar and Tapponnier, 1975, 1978]. South of the plateau, deformation seems to occur primarily by low-angle underthrusting that is presumably responsible for the high mountain ranges [Fitch, 1970; Molnar et al., 1977]. Large left-lateral strike slip faults extend eastward across China from the

northern and northeastern boundaries of Tibet. In the plateau itself, however, the active deformation is primarily by widespread normal faulting with an approximately east-west trending T-axis [e.g., Molnar and Tapponnier, 1975, 1978; Ni and York, 1978]. It is particularly interesting to note that the active normal faults apparently extend south of the suture to the high Himalaya so that the boundary of Tibet, defined by its present tectonics, has grown [Molnar and Tapponnier, 1978].

The epicenter of the earthquake of September 14, 1976 is about 50 km north of the Indus Tsang-Po suture and approximately 300 km north of the Himalayan main boundary fault (Fig. 1). Seismicity in Tibet is quite scattered and the focal depths are not well-studied. The existence of large short-period Rayleigh waves clearly visible on the short-period seismograms of the World Wide Standardized Seismograph Network (WWSSN) [e.g., Chen and Molnar, 1975] suggests that there are probably some very shallow earthquakes. All of those for which Molnar and Tapponnier [1978] determined fault plane solutions appear to be quite shallow (<35 km).

In the following sections, we present the five different methods used to constrain the focal depth and source mechanism and we then discuss the tectonic implications of this particular earthquake.

DATA AND ANALYSIS

We examined all the available WWSSN seismograms for this earthquake and selected records with large signal to noise ratios for body wave and surface wave analysis.

For quantitative analysis of the seismograms, we use the S wave velocity structure of model SE in Chen and Molnar [1980]. The P wave velocity is assumed to be 1.73 times that of the S wave velocity (a Poisson's ratio of 0.25) except for the Pn velocity which was measured independently [Chen and Molnar, 1980] (Table I). The density structure and both P and S wave velocity structures below 90 km, where little observational constraints are available, are those of the Gutenberg's continental model [Dorman et al., 1960].

1. Differential Travel Times of P Waves Between Direct and Depth Phases

The body wave magnitude (m_b) given by the International Seismological Center (ISC) for this event is 5.4. Earthquakes of this size are marginal for P wave first motion studies, because in general, the direct P phase is fairly small. For this event the P phases are especially weak because most seem to be near nodes of the radiation pattern. However, one later phase, which we identify as the sP phase, is apparent on many long-period WWSSN seismograms, and the travel time difference (δT) between these two

phases is about 38 sec (Fig. 2). On several short-period and some long-period records, another apparent depth phase can be clearly recognized (e.g., at COL and STU) with a δT of about 27 sec (Fig. 2). The differential travel times and their uncertainties are summarized in Table II.

For vertical ray paths and for the average velocities in the crust and upper mantle in Table I, a focal depth of 90 km is consistent with both a 28 sec travel time difference between P and pP (δT pP-P) and a 38 sec travel time difference between P and sP (δT sP-P). If the crustal thickness were 80 km instead of 70 km, with the same average velocities as these of model SE in the crust, these differential travel times would indicate a focal depth of 85 km. For the extreme case, in which both the values of δT sP-P were systematically overestimated by 2 sec and the average crustal velocity were overestimated by 5%, could the focal depth be as shallow as 75 km for a crust as thick as this much. Moreover, a non-vertical ray path will cause an underestimate of the focal depth by a few km. Thus given the uncertainties in both the differential travel times and the velocity structure, we conclude that this earthquake occurred in the uppermost mantle with a focal depth of 90 ± 10 km.

2. Fault Plane Solutions

Possible fault plane solutions were constructed for this event using the P wave first motion polarities assuming a double couple source (Fig. 3). The projections of the rays onto the focal sphere are based on take-off angles calculated from the Herrin [1968] P tables. Since the take-off angles would change considerably if the source were in the lower crust instead of the uppermost mantle, we examined two source depths one in the crust and the other below it. Because the Herrin P tables assume a radially symmetrical earth, these depths were 25 km and 75 km to approximate source depths in the lower crust and in the uppermost mantle beneath Tibet, respectively. The differences between the take-off angles for sources in the mantle at 75 km or 90 km or between sources at 25 km in a crust 35 km thick or at 60 km in a crust 70 km thick are negligible. In both cases, one approximately north-south striking plane is well-constrained. To parameterize the solution we can treat this plane as the fault plane, without loss of generality. The P wave first motions constrain the slip angle in this plane to be within about 6° of 222° for a crustal source depth (Fig. 3a), but for an uppermost mantle source, they allow a range from 232° to 270° (Fig. 3b). Table III summarizes the possible solutions including the one that fits the P wave amplitude data best and will be discussed below in section 4. Note that all of these solutions contain a major component of normal faulting.

3. Rayleigh Wave Amplitude Spectra

An obvious indication of the depth of this event is the lack of Rayleigh waves with periods less than about 20 sec on almost all the WWSSN long-period seismograms (Fig. 4). Not surprisingly, there is no surface wave magnitude assigned by the ISC. Tsai and Aki [1970] demonstrated that in the period range of 10 to 50 sec, where the attenuation coefficient is nearly independent of frequency for Rayleigh waves, the Rayleigh wave excitation depends strongly only on properties of the source. In particular, they showed that the shape of the Rayleigh wave amplitude spectra could be used to determine the focal depth without knowing the exact value of the attenuation coefficient.

Thirteen WWSSN vertical component seismograms with visible Rayleigh wave signal with periods of 50 sec were digitized in the group velocity window between 4 km/s to 2.8 km/s. Their unsmoothed amplitude spectra in the period range of 10 to 50 sec, after removing the effect of the instrument response (Fig. 5), show a rapid decrease towards the high frequency end, despite some noise clearly visible on the seismograms (Fig. 4,5).

Tsai and Aki [1970] discussed in detail the possible effects of various source and propagation parameters on

the determination of source depth from Rayleigh wave amplitude spectra. For our case, the assumption of a point double couple source is a good approximation considering the small magnitude of this earthquake. A rise time of about 2 sec gave satisfactory results for synthetic P wave forms (section 5). Therefore, the effects of the source-time function on the surface wave spectra are negligible. Errors in our knowledge of the crust and upper mantle velocity structure beneath Tibet are probably negligible judging from Tsai and Aki's [1970] numerical experiments exploring the effects of different velocity structures.

We examined the effects of different fault plane solutions obtained from the last section and section 4 (Table III), and found negligible effects on the shape of the Rayleigh wave amplitude spectra between 10 to 50 sec at a source depth of around 85 km (Fig. 5). Thus, the principle factor affecting the shapes of the spectra is the depth of focus. Because we are only interested in the shapes of the amplitude spectra in this period range, the theoretical spectra, corresponding to a seismic moment of 1×10^{27} dyne-cm, have not been corrected for attenuation. It is clear that a source depth of 45 km will not fit the observations (Fig. 5). This is consistent with the identification of

the two depth phases and their differential travel times. However, at a source depth around 90 km, the shape of the observed Rayleigh wave amplitude spectra between 10 to 50 sec cannot constrain the source depth better than $\pm$10 km (Fig. 5). For fault plane solution 3, at 90 km depth and from the observed spectral densities at 50 sec the seismic moment is estimated to be about 5×10^{24} dyne-cm, (Fig. 6) with an estimated uncertainty of a factor of 1.3, assuming an attenuation coefficient of 1.5×10^{-4} km^{-1} [Ben-Menahem, 1965; Tsai and Aki, 1970]. Combinations of different possible source depths from 85 to 95 km and fault plane solutions shown in Table III give geometrically averaged seismic moments between 5 to 6×10^{24} dyne-cm and an uncertainty of a factor of 1.3 is estimated from the scatter of the data.

4. Seismic Moment Tensor Inversion of P Wave Amplitudes

The response of an elastic body to an arbitrary static seismic moment tensor at a point souce can easily be found by differentiating the Green's function with respect to the source coordinates. Suppose we have a force couple at the source position $\underline{\xi}$ with the force pointing at the $\hat{i}$ direction and the moment arm pointing at the $\hat{j}$ direction (Fig. 7). (This corresponds to a M_{ij} term in the moment tensor.) If the Green's function $G_{ni}(\underline{\chi}, \underline{\xi}, t)$ is known, where $\underline{\chi}$ is the receiver position and t is time,

then the displacement response u_n at $\underline{\chi}$ in the $\hat{n}$ direction, due to M_{ij}, is simply

$$u_n = \sum_{i,j} M_{ij} \partial/\partial\xi_j \, G_{ni}(\underline{\chi}, \underline{\xi}, t) \qquad (1)$$

Since it is difficult to perform the differentiation in the source coordinates, one usually applies the reciprocal theorem and performs the differentiation in receiver coordinates. The reciprocal theorem is then applied again to the results to obtain expressions in the source coordinates. With known G_{ni}, this can be done for surface waves (e.g., Mendiguren, 1977) and body waves in a layered medium (see section 5). For a given set of observed displacements $\underline{u}$, M_{ij} can be found by applying the linear inverse operator $(\partial/\partial\xi_j \; G_{ni})^{-1}$.

Recently, Fitch et al. [1979] formulated such a formal inversion of the static seismic moment tensor from the amplitude of body waves. We briefly review the procedures here. The problem is simplified by reducing the amplitude data onto the focal sphere and simply using the inverse operator of the elastic response of a whole space to perform the inversion. Usually body wave data are deconvolved in the time domain to remove the instrument response and attenuation effects. The amplitudes of the resulting pulses corresponding to P, pP, and sP are then corrected for the geometrical spreading from empirical

amplitude-distance curves and for the reflection at the free surface over the source region for pP and sP with an assumed velocity model. Finally, these data are projected back onto the focal sphere using standard travel time curves to find the take-off angles just as in calculating fault plane solutions. Also the source is assumed to be a point.

For this procedure, it is most convenient to use spherical coordinates centered in the focal sphere. Expressions of the elastic response on a focal sphere due to the point seismic moment tensor can be found in McCowan [1977]. The moment tensor can be decomposed into a volumetric component, the monopole; and two non-volumetric components, the double couple and the compensated linear vector dipole (CLVD) [Fitch et al., 1979]. In general, regardless of whether the solution is constrained to have only a double couple mechanism or not, the inferred double couple component is found to be essentially the same [Fitch et al., 1979]. The formal uncertainties in the inversion process are probably not particularly meaningful because they do not take into account the possible errors associated with the reduction of the data such as noise on the seismogram, structural variations in the source region affecting the reflection coefficients and take-off angles, lateral inhomogeneity of structures and attenuation along the ray path,

particular receiver effects etc. For these reasons, Fitch et al. [1979] consider the results of the inversion with a non-double couple component to be artifacts of noise on the data.

Since apparently the focal depth for the event of September 14, 1976 is near 90 km, the depth phases are well separated from the direct P phase and from each other. Therefore we simply measured the peak amplitudes of P, pP, and sP with a digitizing table and performed the inversion. The amplitudes of pP and sP are corrected for reflections at the free surface with a half-space model, as in Kanamori and Stewart [1976]. Nine long-period WWSSN records within the distance range of 30° to 80° and with good sP signal to noise ratios were used (Table IV). Assuming a focal depth of 80 km the resulting moment tensor from the linear inversion has about 7.1% monopole component, 41.7% CLVD and 51.2% double couple. The double couple component resulting from the unconstrained linear inversion is shown in Fig. 8.

This solution is very close to the one obtained from P wave first motion polarities (Fig. 3b). The only obvious failing with the solution is that it is inconsistent with the compressional first motion of JER near one nodal plane. This does not trouble us greatly because the signal-to-noise ratio for the direct P phase at JER is not very large.

For this particular data set, the solution became unstable when it was constrained to be a double couple. In fact, the distribution of amplitude data on the focal sphere is probably barely sufficient to yield a stable solution for the unconstrained linear inversion. Although the direct P phase have poor signal-to-noise ratios, they are important in constraining the solution. When only sP phases are used, the resulting solution systematically gave amplitude ratios of P to sP phases that are too large and the resulting double couple component of the solution included about 50% strike-slip motion. Moreover, that solution is incompatible with several first-motion polarities.

In any case, solution 3 obtained from the amplitudes of P, pP and sP is similar to the range of solutions from the first motion data (solution 2). Both indicate a predominantly normal faulting mechanism with one north-south striking plane, and the results of the inversion suggest that a large strike slip component is unlikely.

5. Wave Form Matching of P Phases

In the last section we briefly reviewed the procedure of finding the elastic response to an arbitrary moment tensor. For a source embedded in a stack of homogeneous layers overlying a half-space, an efficient method of calculating such a response in the far field was given by Bouchon [1976] using the reciprocal theorem. At first,

the source is treated as being in a half space with the receiver in the layers. A good approximation to the far field Green's function in such a configuration can be calculated as the response of the layers to a plane wave incidence at the bottom of the layers using the Thompson-Haskell matrix algorithm [Haskell, 1953]. At this stage, one can simply differentiate the Green's function in the present receiver coordinates and then apply the reciprocal theorem to place the source in the layers. To obtain the proper source-receiver configuration when applying this method to the earth, knowledge of the take-off angle at the bottom of the layers in the source region, the angle of incidence at the base of the layers at the receiver (if so desired), geometrical spreading and attenuation in the mantle is required.

We generated synthetic seismograms for the 9 seismograms used in the seismic moment tensor inversion in section 4 following the procedures outlined above. The assumed velocity structure in the source region is that given in Table I except that the mantle is taken to be a half space with the same structure parameters for the layer between 70 to 90 km in Table I. The receiver region consists of a single layer of crust 30 km thick, with P wave velocity (V_p) of 6.1 km/s and density (ρ) of 3 gm/cm^3, overlying a half space with V_p of 8.0 km/s and ρ of 3.3 gm/cm^3. A Poisson's ratio of 0.25 is assumed for the reciver structure.

Corrections for the geometric spreading in the mantle, the take-off angles and the angles of incidence at the base of the crust in the receiver regions are all calculated from the smoothed travel time cruves of Herrin [1968]. An attenuation operator with a constant t* (travel time/ quality factor) = 1 and a rise time of 2 sec for the point source time function are assumed.

The digitized records and the synthetic seismograms for the double couple fault plane solution 3 (Table III) with a source depth of 90 km are shown in Fig. 8. All the observed wave forms have been normalized for an instrumental peak magnification of 1500 and with a vertical exaggeration of two except for the observed seismogram at DAV, for which the vertical exaggeration is 1/3. The synthetic seismograms correspond to a seismic moment of 7×10^{24} dyne-cm. We consider the agreement between the observed and synthesized wave forms to be very good except at DAV where the observed sP phase is too large.

Synthetic seismograms were also generated for fault plane solution 2 (Table III) both with $\lambda = 232°$ and $\lambda = 270°$ to explore the effects of variations in fault plane solutions. The differences in synthesized wave forms at SHI, TAB and TRI are negligible. The first motion of the

synthetic wave form at JER for solution 2 is consistent with the observation as expected, but for stations AAE, ATH and IST, solution 2 yields synthetic seismograms which have a much smaller P to sP amplitude ratio compared with the observations (Fig. 9). At MAT, the synthetic seismogram for solution 2 is inadequate to explain the observed wave forms while that for solution 3 matches the observation well (Fig. 9). The only recording difficult to match is from DAV. The observed wave form cannot be explained by small variations of fault plane solutions from solution 3, unless the nodal plane dipping to the east is moved very close to DAV. This would correspond to having a solution with a large strike-slip component. The observations near the nodal plane dipping to the west however, prohibit such a change in the fault plane solution, unless the nodal planes are not orthogonal or there are large lateral variations in the velocity structure that lead to large errors in the take-off angles.

An increase in take-off angle of about 10° is required to obtain a good fit to the observed wave form at DAV with solution 3. Such an increase corresponds to a take-off angle appropriate for epicentral distances 15° to 20° less than that reported distance by ISC.

Our preferred explanation

for the anomalous sP amplitude is the high noise level at DAV. The noise preceding the P arrival at DAV is very representative of that particular record (Fig. 10a). The closest WWSSN station to DAV is at BAG with a difference in azimuth of only 8° from the epicenter (Fig. 10a). Although the noise level at BAG is high, the sP amplitude is much smaller than that at DAV even without correcting for the geometrical spreading. The poor signal-to-noise ratios at LEM and small epicentral distance of SNG make these records unsuitable for quantitative analysis of the amplitude data, but the small amplitude ratios of sP to P at them (Fig. 10b) are consistent with a fault plane solution similar to fault plane solution 3 but are inconsistent with solutions with large strike-slip components.

The seismic moments calculated from the sP amplitudes average to 6.5×10^{24} dyne-cm (with an uncertainty of about a factor of 1.4) if the large sP amplitude at DAV is ignored. Otherwise the geometric average seismic moment is close to 8×10^{24} dyne-cm, with an uncertainty of about a factor of 2. The value of 6.5×10^{24} dyne-cm agrees with the estimated seismic moment of 5 to 6×10^{24} dyne-cm using 50 sec Rayleigh waves.

TECTONIC IMPLICATIONS

Normal Faulting at Depth

The epicenter of the earthquake of September 14, 1976 is about 50 km north of the suture where active subduction presumably ceased a few tens of m.y. ago. The fault plane solution not only is very different from low-angle underthrusting, characteristic of earthquakes in the Himalaya, but also is difficult to fit into any simple scheme of a sinking slab or bending of the lithosphere. Therefore, although it may have occurred in material that was once oceanic lithosphere, its occurrence probably should not be taken as evidence for an actively sinking slab. We believe that this earthquake probably represents deformation in the Tibetan mantle.

The approximately east-west trending T-axis is similar to the active normal faulting observed near the surface of Tibet. Since we studied only one event that clearly is in the mantle, it is risky to draw any firm conclusions about the style of deformation between the surface and this depth. If this event is representative of the deformation of the lower crust and upper mantle of Tibet, however, then it suggests that the small amount of the active east-west extension that occurs at the surface also occurs at depth.

Implications For The Temperature In the Mantle Beneath Tibet

The fact that this event occurred in the mantle and not in the lower crust enables us to investigate the possible temperature range in the source area of this earthquake. Chen and Molnar [1980] suggested that the average temperature of the uppermost mantle immediately beneath the Tibetan Moho is likely to be about 250°C warmer than that beneath stable platforms and shields. Thus the uppermost mantle temperature beneath Tibet could be around 750°C to 800°C if that beneath the stable platforms and shields were about 500°C.

To the best of our knowledge, the deepest intraplate earthquakes occur in periodic swarms about 60 km beneath the summit of Kilauea in Hawaii [Eaton, 1962]; and presumably are related to volcanic activity there. Using the cooling plate model for the thermal history of the oceanic lithosphere [Parsons and Sclater, 1977], the estimated temperature at 60 km depth in an oceanic plate about 100 m.y. old is about 750°C. The possible non-conductive heat transport associated with volcanic activities might increase this temperature estimate somewhat. Moreover, the solidus for basaltic material under water saturated conditions (corresponding to a lower bound of the solidus) is about 700°C at 20 kb of lithostatic pressure [e.g., Merrill et al., 1970]. Thus the temperature at 60 km beneath Kilauea could

be over 700°C if magma exists near that depth. This suggests that earthquake activity can occur in mantle materials at temperatures near 750°C if there are sufficient stress differences at these depths.

An application of flow laws for olivine, obtained from laboratory experiments [e.g., Goetze, 1978], indicates that at a strain rate of about 100% over the past 40 m.y. since the collision, only 1.1 Kb to 430 bars of differential stress is necessary to maintain steady state dislocation creep of olivine at temperatures of 750°C to 800°C respectively [Chen and Molnar, 1980]. This calculation is very crude because of uncertainties in the activation energy and temperatures. Nevertheless, this earthquake at 90 km beneath Tibet indicates that a very rapid deformation process is possible at temperatures over about 700°C and at pressures of about 30 kb, unless we have grossly over-estimated the temperature or unless the source region is anomalously cool compared with the average temperature at that depth.

CONCLUSIONS

The focal depth of the intermediate depth earthquake of September 14, 1976 is estimated to be about 90±10 km from the differences in arrival times of P, pP, and sP, from the synthetic seismograms for these phases, and from Rayleigh wave amplitude spectra. With the first-motion polarities of P phases, inversion of the relative amplitudes of

P, pP, and sP and matching of the P phases with synthetic seismograms, the fault plane solution is constrained to be predominantly normal faulting with at least one plane striking approximately north-south. The seismic moment of a point double couple source is estimated to be 5×10^{24} dyne-cm from the spectral densities of 50 sec Rayleigh waves and 6.5×10^{24} dyne-cm from the amplitude of the sP phases. Both estimates of the seismic moment are uncertain to a factor of about 1.4.

The apparently east-west trending T axis is consistent with the style of active deformation near the surface. If this mechanism is representative of the over-all deformation style of the Tibetan mantle, then a small amount of the east-west extension observed near the surface of Tibet also occurs at depth.

Since the average temperatures in the uppermost mantle beneath Tibet and 60 km beneath Hawaii could be 700 to 800°C, the occurrence of earthquakes in both regions indicates that rapid deformation can occur at these temperatures and at pressures over 20 kb.

Acknowledgements

We benefitted from several discussions with B. Evans on rock mechanics. This research was supported by the National Science Foundation Grant No. 77-23017 EAR and the United States Geological Survey Grant No. 14-08-0001-17759.

References

Ben-Menahem, A., Observed attenuation and Q values of seismic surface waves in the upper mantle, J. Geophys. Res., 70, 4641-4652, 1965.

Bouchon, M., Teleseismic body wave radiation from a seismic source in a layered medium, Geophys. J. Roy. Astron. Soc., 47, 515-530, 1976.

Brace, W.F., and J.D. Byerlee, California earthquakes: Why only shallow focus?, Science, 168, 1573-1576, 1970.

Chatelain, J.L., S.W. Roecker, D. Hatzfeld, and P. Molnar, Microearthquake seismicity and fault plane solutions in the Hindu-Kush region and their tectonic implications, J. Geophys. Res., (submitted) 1979.

Chen, W.P. and P. Molnar, Short-period Rayleigh wave dispersion across the Tibetan Plateau, Bull. Seism. Soc. Amer., 65, 1051-1057, 1975.

Chen, W.P., and P. Molnar, Constraints on the seismic wave velocity structure beneath the Tibetan Plateau and their tectonic implications, (submitted to) J. Geophys. Res., 1980.

Chung, W.Y., and H. Kanamori, Source process and tectonic implications of the Spanish deep-focus earthquake of March 29, 1954, Phys. Earth Planet. Inter., 13, 85-96, 1976.

Dewey, J.F., and K.C.A. Burke, Tibetan, Variscan, and Pre-Cambrian basement reactivation: Products of a

continental collision, J. Geol., 81, 683-692, 1973.

Dorman, J., M. Ewing, and F. Press, Study of shear-velocity distribution in the upper mantle by mantle Rayleigh waves, Bull. Seism. Soc. Amer., 50, 87-115, 1960.

Eaton, J.P., Crustal structure and volcanism in Hawaii, in The Crust of the Pacific Basin, G.A. MacDonald and H. Kuno (ed.), Geophys. Monograph, 6, Amer. Geophys. Un., Washington, DC, 1962.

Fitch, T.J., Earthquake mechanism in the Himalaya, Burmese, and Andaman regions and continental tectonics in central Asia, J. Geophys. Res., 75, 2699-2709, 1970.

Fitch, T.J., D.W. McCowan, and M.W. Shields, Estimation of the seismic moment tensor from teleseismic body wave data with applications to intraplate and mantle earthquakes, Submitted to J. Geophys. Res., 1979.

Goetze, C., The mechanism of creep in olivine, Phil. Trans. Roy. Soc. Lond., 288, 99-119, 1978.

Haskell, N.A., The dispersion of surface waves in multilayered media, Bull. Seism. Soc. Amer., 43, 17-34, 1953.

Herrin, E., Introduction to '1968 Seismological tables for P phases', Bull. Seism. Soc. Amer., 58, 1193-1241, 1968.

Isacks, B., and P. Molnar, Distribution of stresses in the descending lithosphere from a global survey of focal-mechanism solution of mantle earthquakes, Rev. Geophys. Space Phys., 9, 103-174, 1971.

Kanamori, H., and G.S. Stewart, Mode of the strain release along the Gibbs fracture zone, mid-Atlantic ridge, Phys. Earth Planet. Int., 11, 312-332, 1976.

McCowan, D.W., A moment-tensor representation of body wave displacement vectors on the focal sphere, in Semiannual Technical Summary, pp. 9-11, Lincoln Laboratory, Mass. Inst. of Tech., Lexington, MA, March, 1977.

Mendiguren, J.A., Inversion of surface wave data in source mechanism studies, J. Geophys. Res., 82, 889-894, 1977.

Merrill, R.B., J.K. Robertson, and P.J. Wyllie, Melting reactions in the system $NaAlSi_3O_8$-$KAlSi_3O_8$-SiO_2-H_2O to 20 kilobars compared with results for other feldspar-quartz-H_2O and rock - H_2O systems, J. Geol., 78, 558-569, 1970.

Molnar, P., W.P. Chen, T.J. Fitch, P. Tapponnier, W.E.K. Warsi, and F.T. Wu, Structure and tectonics of the Himalaya: A brief summary of relevant geophysical observation, in Himalaya: Sciences de la Terre, pp. 269-294, Centre National de la Recherche Scientifique, Paris, 1977.

Molnar, P., D. Freedman, and J.S.F. Shih, Lengths of intermediate and deep seismic zones and temperatures in downgoing slabs of lithosphere, Geophys. J. Roy. Astron. Soc., 56, 41-54, 1979.

Molnar, P., and P. Tapponnier, Cenozoic tectonics of Asia: Effects of a continental collision, Science, 189, 419-426, 1975.

Molnar, P., and P. Tapponnier, Active tectonics of Tibet, J. Geophys. Res., 83, 5361-5375, 1978.

Ni, J., and J.E. York, Late Cenozoic extensional tectonics of the Tibetan Plateau, J. Geophys. Res., 83, 5377-5387, 1978.

Parsons, B., and J.G. Sclater, An analysis of the variation of ocean floor bathymetry and heat flow with age, J. Geophys. Res., 82, 803-827, 1977.

Roecker, S.W., O.V. Soboleva, D. Hatzfeld, J.L. Chatelain, and P. Molnar, Seismicity and fault plane solutions of intermediate depth earthquakes in the Pamir-Hindu Kush region, J. Geophys. Res., (Submitted), 1979.

Tsai, Y.B., and K. Aki, Precise focal depth determination from amplitude spectra of surface waves, J. Geophys. Res., 75, 5729-5743, 1970.

Table I. Seismic Wave Velocity Structure Used For Tibet

Depth (km)	S wave velocity (V_s) (km/sec)	P wave velocity (V_p) (km/sec)	density (g/cm^3)
0-3.75	2.55	4.41	2.41
3.75-45	3.4	5.88	3.0
45-70	3.7	6.4	3.32
70-90	4.8	8.12	3.365
90-100	4.41	8.02	3.38

Table II. P Wave Travel Time Differences Between the Direct and Depth Phases at WWSSN Stations

Station	Δ (Deg.)	Azimuth (Deg.)	δT pP-P (sec)	δT sP-P (sec)	Instrument
AAE	51.7	257		38±2	LP
ATH	54.3	297	26±2	38±2	LP
COL	75.7	22	28±0.5		SP
DAV	40.7	116		37±2	LP
HKC	23.3	103		36±2	LP
IST	49.7	300		37±1	LP
JER	46.3	287	27±1	38±1	LP
MAL	75.8	304	27±1		LP
MAT	40.9	67		37±2	LP
POO	18.2	235		38±2	LP
SHI	32.1	279		38±2	LP
STU	62.2	312	27±0.5		SP
TRI	59.9	308	26±1	38±2	LP

long period instrument: LP
short period instrument: SP

Table III. Possible Fault Plane Solutions From P Wave First-Motion Polarities And Inversion of Amplitude Data

No.	Strike	dip (δ)	slip angle (λ)	Method of Analysis
1	0°	66°W	216°-228°	P wave first motion polarities, crustal depth
2	10°	57°W	232°-270°	P wave first motion polarities, upper mantle depth
3	26°	54°W	291°	Inversion of amplitudes of P phases, double couple component, upper mantle depth

For convention of defining the fault plane solutions, see Kanamori and Stewart [1976]. $\lambda = 270°$ corresponds to pure normal faulting and $\lambda = 0°$ to pure left-lateral strike-slip faulting.

Table IV. P Phase Amplitudes Used in the Moment Tensor Inversion

Station	Δ(deg.)	Azimuth (deg.)	Amplitude (cm)* P	pP	sP
AAE	51.7	257	-0.039	x	0.173
ATH	54.3	297	-0.041	0.037	0.131
DAV	40.7	116	-0.088	x	0.513
IST	49.7	300	-0.024	0.090	0.130
JER	46.3	287	0.022	0.060	0.222
MAT	40.9	67	-0.032	x	0.182
SHI	32.1	279	0.031	x	0.255
TAB	36.5	295	x	x	0.291
TRI	59.9	308	-0.036	0.053	0.080

*Normalized to peak magnification of 1500

Figure Captions

Fig. 1. Simplified map of active tectonics in Tibet and surrounding regions (adopted from [Molnar and Tapponnier, 1978]) showing the epicenter of the earthquake studied (⊕). Heavy lines are major faults (dahsed when less certain) recognized on the Landsat imagery. Dotted areas are sediment-filled basins presumably due to normal faulting. Thin dashed lines are a schematic outline of the 32°N fold belt. Cenozoic volcanism has not been represented. In fault plane solutions (lower hemisphere), solid areas are compressional quadrants, and open areas are dilatational quadrants; for smaller events (1961-1970), solid circles represent locations with more than 25 World Wide Standardized Seismograph Network Stations, and open circles those with more than 15 stations. Large closed and open circles are historic earthquakes with $M \geq 7.8$ and with $7.8 > M > 7.0$, respectively.

Fig. 2. Examples of vertical component long-period WWSSN seismograms which recorded at least one clear later phases (identified as sP) after the direct P arrival (top) and vertical component short-period WWSSN seismograms at COL and STU (bottom) where clear

pP phases can be easily identified.

Fig. 3. Equal area projections of the lower hemisphere of the focal sphere showing the P wave first motion polarities. (a) Crustal source. Take-off angles are calculated based on the Herrin P tables. Thus the assumed focal depth (25 km) is to approximate a lower crustal depth for Tibet. (b) Mantle source. Solid circles are compressional first motions and open circles are dilatational first motions. Two different southeast dipping nodal planes are extreme solutions allowed by the data.

Fig. 4. Examples of the traces of the digitized vertical component long-period WWSSN seismograms with clear Rayleigh wave signals. Note the apparent absence of Rayleigh wave energy with periods less than about 20 sec.

Fig. 5. Observed vertical component Rayleigh wave spectra after corrections for the instrument response in the period range of 10 to 50 sec at 13 WWSSN stations with scales shown to the right of each diagram. The spectra are not smoothed and only peaks and troughs are plotted (open circles). Theoretical spectra (scales shown to the left of each diagram) at three different depths with different fault plane solutions are shown for comparison: 45 km depth with solution 1, 85 km with solution 2, $\lambda = 270°$, 95 km with solution 3 (Table III). Representative examples showing the negligible effects

of possible different fault plane solutions on the theoretical spectra are shown in (d) and (j). In (a), (f) and (k) the theoretical spectra of solution 3 with a source depth of 70 km is also shown. The observed spectra have a resolution of about $\pm$10 km on a source depth near 90 km. All theoretical spectra are generated for the structure model SE (Table I) with a seismic moment of 1×10^{27} dyne-cm and corrected with appropriate geometrical spreading factors for each station. No attenuation correction is applied since we are only interested in the shape of these spectra.

Fig. 6. Observed vertical component Rayleigh wave spectral densities (50 sec period) at 14 WWSSN stations (solid circles) normalized to the source assuming an attenuation coefficient of $1.5 \times 10^{-4} km^{-1}$. The solid curve shows the theoretical spectral densities predicted for a source at 90 km depth with fault plane solution 3 (Table III). The dashed curve shows those for a source at 85 km depth with fault plane solution 2 ($\lambda = 232°$). The assumed seismic wave velocity structure is shown in Table I and the assumed seismic moment is 5.5×10^{24}dyne-cm. Station JER is not used in Fig. 5 because the latter part of the dispersed Rayleigh wave train overlaps a calibration pulse.

Fig. 7. Schematic diagram showing a force couple corresponding to a M_{ij} term in the seismic moment tensor acting at source $\underline{\xi}$ with a source coordinate $\hat{i}$ and $\hat{j}$ and the resulted displacement field $\underline{u}$ at receiver $\underline{\chi}$ with receiver coordinates $\hat{n}$ and $\hat{m}$. $G_{ni}(\underline{\chi},\underline{\xi}, t)$ is the Green's function where t is time. The third dimension is not shown for simplicity.

Fig. 8. Equal area projection of the lower focal sphere showing the nodal planes of the double couple component of the seismic moment tensor obtained from the linear inversion of the amplitudes of the P phases. Also plotted are the P wave first motion polarities (solid circles for compressional, open circles for dilatational, and X for nodal), pP polarities (+ for compressional and - for dilatational), and positions of the sP reflections (with the symbol '2'). Digitized vertical component long-period WWSSN seismograms (top trace) and synthetic seismograms (bottom trace) are shown for each of the 9 stations used in the inversion. For the synthetic seismograms, we used double couple solution 3 (Table III) at 90 km depth with a seismic moment of 7×10^{24} dyne-cm. The beginning of the synthetic seismograms marks the onsets of the direct P phases. The lack of clarity of the initial P phases is due to the digitizing, which does not allow the change in

intensity of the original trace at the P onset to be seen. The originals are clear (Fig. 2). The peak instrument response is normalized to 1.5 k with a vertical exaggeration of 2 except that the observed trace from DAV has a vertical exaggeration of 1/3. The point source has a rise time of 2 sec and the attenuation is parameterized by $t^* = 1$.

Fig. 9. Examples of digitized vertical component long-period seismograms (top trace) and synthetic seismograms for three different fault plane solutions: solution 2 with $\lambda = 232°$, solution 2 with $\lambda = 270°$, and solution 3 (Table III) with arbitrary seismic moments. The source depth is at 90 km and all the seismograms have been normalized to the maximum peak-to-peak amplitude of the observed trace. Solution 3 yields a good match between the synthetic and observed seismograms.

Fig. 10. (a). Digitized vertical component long-period WWSSN records from DAV and BAG. The azimuths from the epicenter to both stations are similar (116° for DAV, $\Delta = 40.7°$; 108° for BAG, $\Delta = 31.4°$). Note the large apparent sP phase is observed at DAV but not at BAG. Both stations have high noise levels. The expected P arrival times are based on the P arrival times on the short-period records.

(b) Digitized vertical component long-period WWSSN

records at LEM and SNG showing comparable amplitudes of p and sP which is qualitatively consistent with a fault plane similar to solution 3 (Table III).

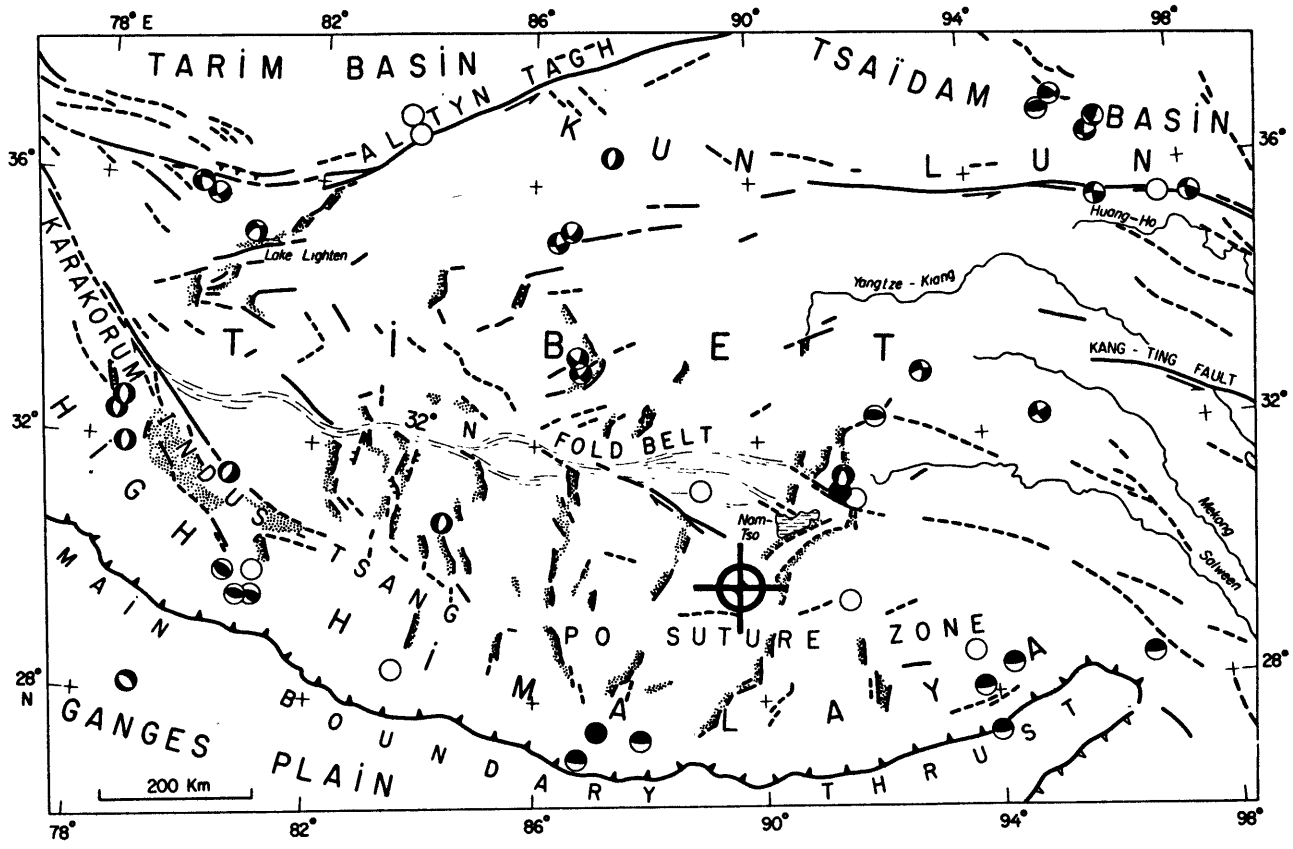
78° E
82°
86°
90°
94°
98°
36°
32°
28° N
TARİM BASİN
ALTYN TAGH
KUN-LUN
TSAİDAM BASİN
Huang-Ho
Lake Lighten
KARAKORUM
Yangtze - Kiang
TİBET
KANG - TING FAULT
HIGH
INDUS TSANG
32° N FOLD BELT
Nam-Tso
Mekong
Salween
MAIN
HİMA
PO SUTURE ZONE
LAYA
BOUNDARY THRUST
GANGES PLAİN
200 Km

Fig. 1

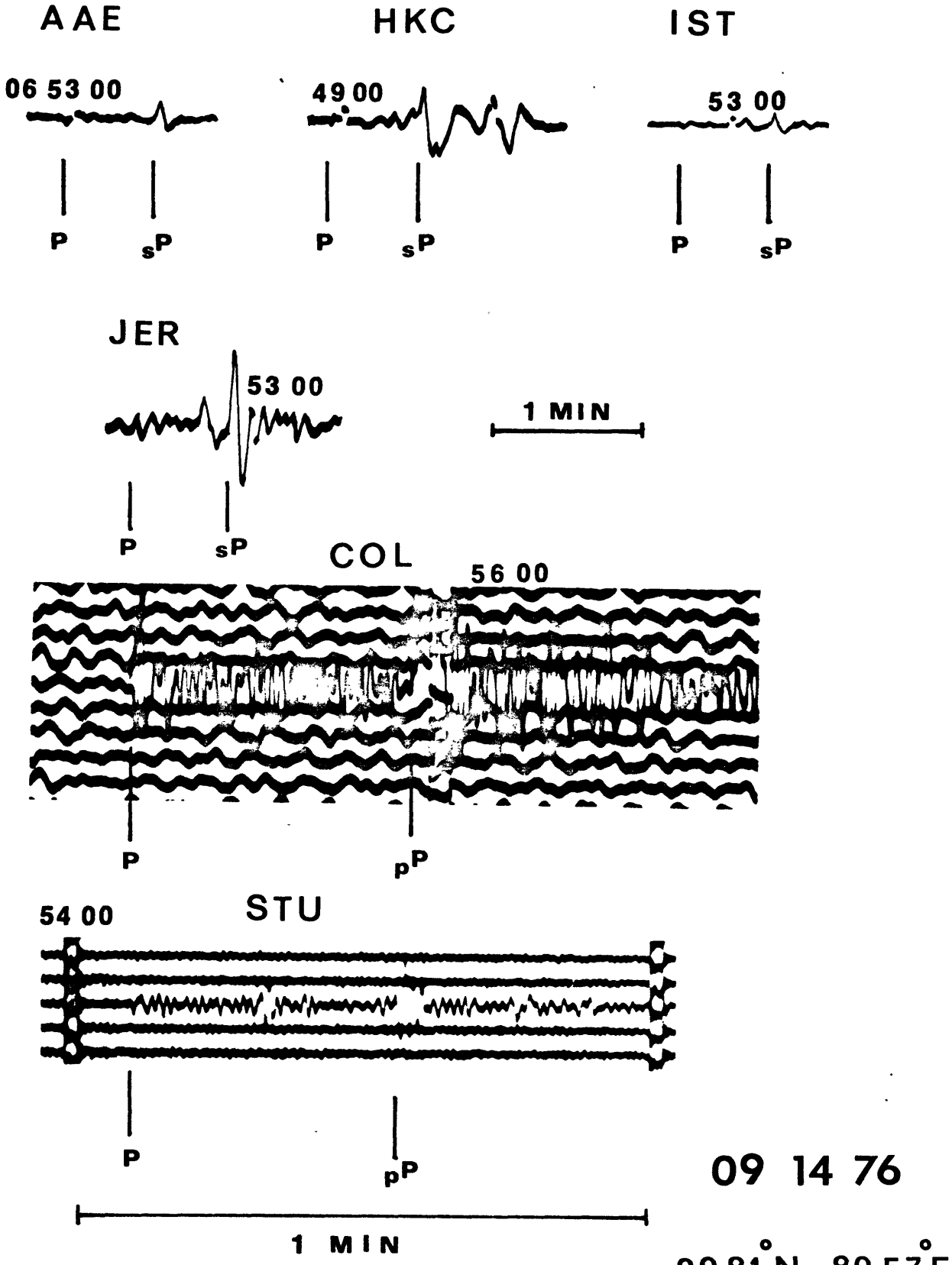
AAE
HKC
IST
06 53 00
49 00
53 00
P
sP
P
sP
P
sP
JER
53 00
1 MIN
P
sP
COL
56 00
P
pP
54 00
STU
P
pP
1 MIN
09 14 76
29.81°N 89.57°E
TIBET

Fig. 2

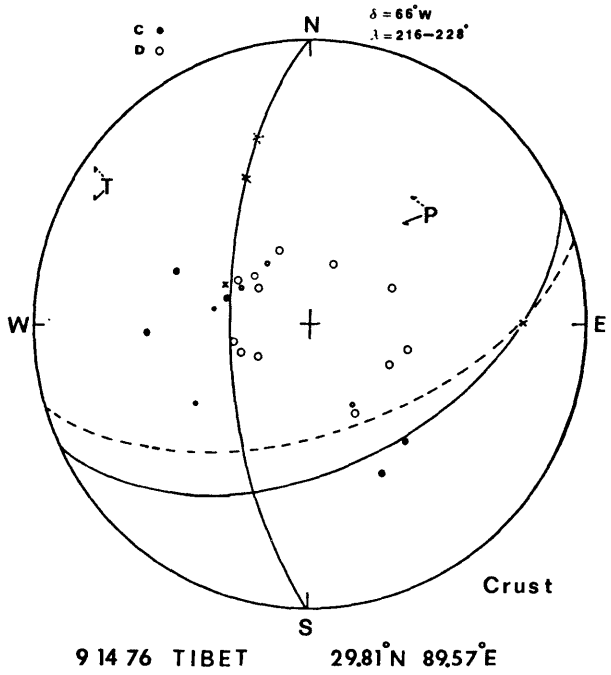

Fig. 3a

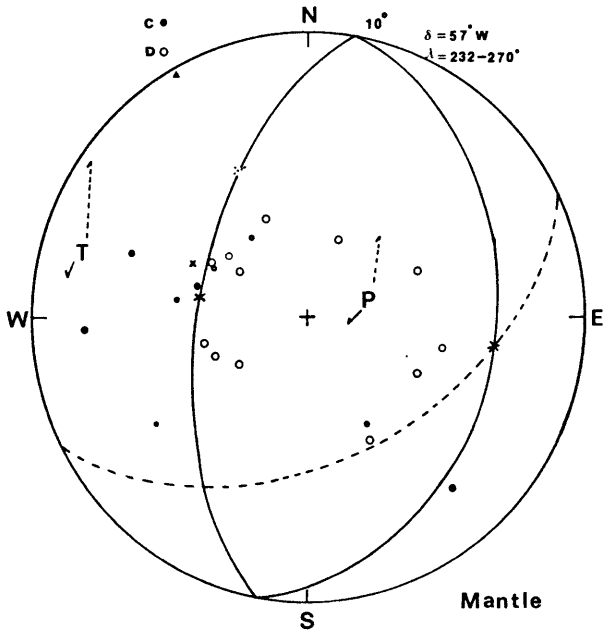

9 14 76 TIBET 29.81°N 89.57°E

Fig. 3b

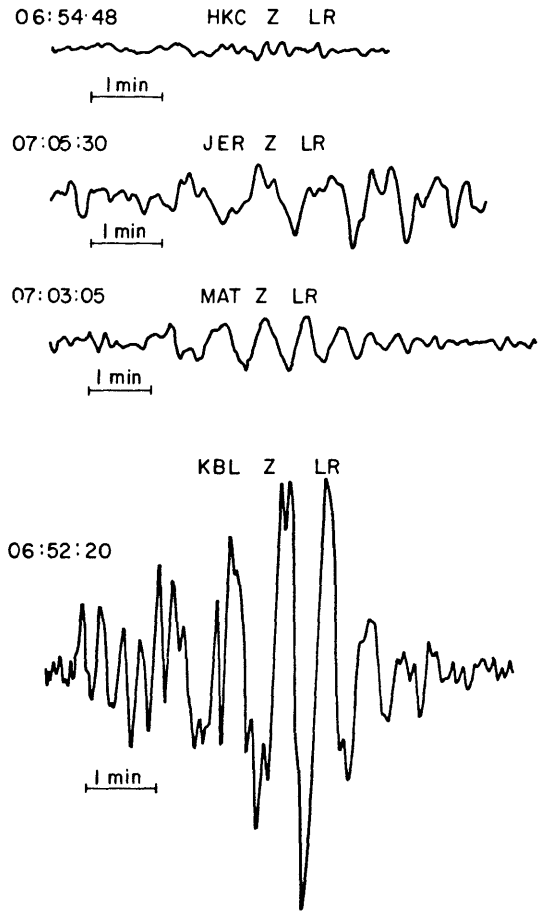

September 14, 1976 29.81°N 89.57°E
Tibet 90 km

Fig. 4

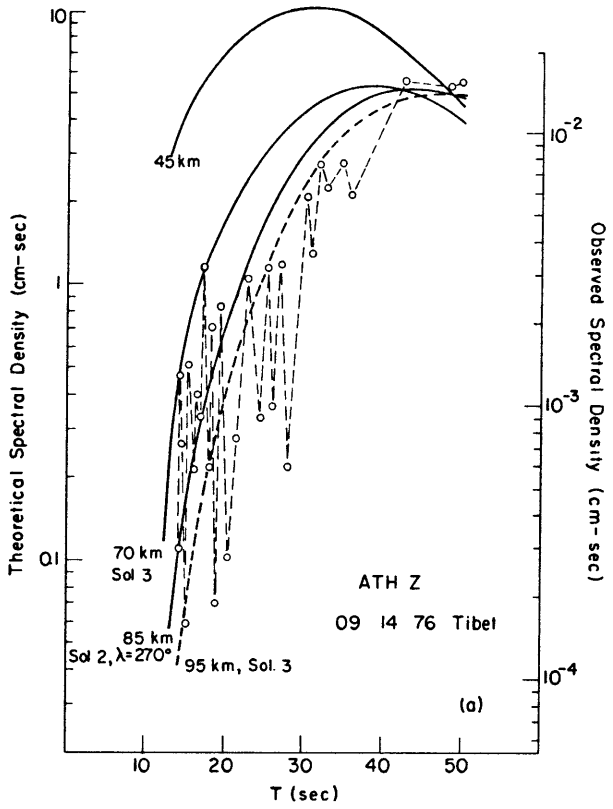
10
1
0.1
45km
70 km
Sol 3
85 km
Sol 2, λ=270°
95 km, Sol. 3
ATH Z
09 14 76 Tibet
(a)
10
20
30
40
50
T (sec)
Theoretical Spectral Density (cm-sec)
Observed Spectral Density (cm-sec)
10^-2
10^-3
10^-4

Fig. 5

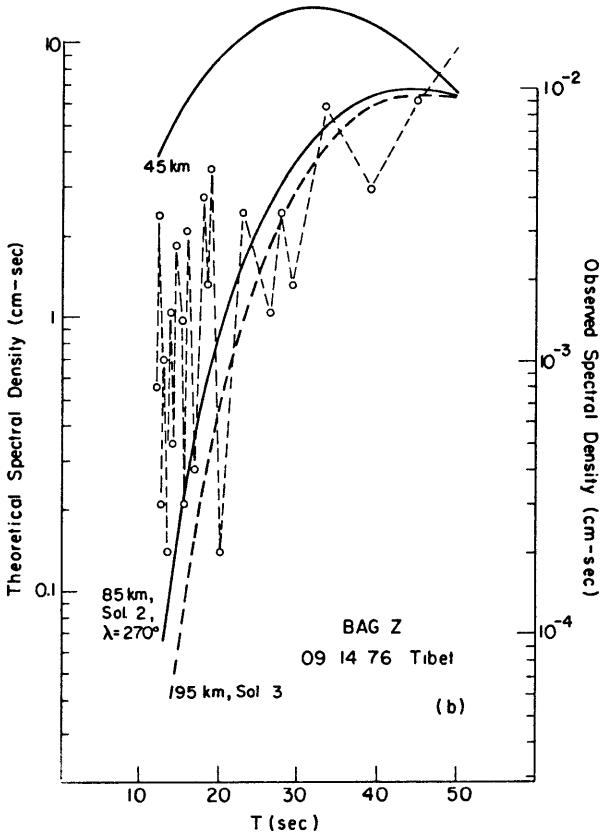
10
1
0.1
45 km
85 km,
Sol 2,
λ=270°
195 km, Sol 3
BAG Z
09 14 76 Tibet
(b)
10
20
30
40
50
T (sec)
Theoretical Spectral Density (cm-sec)
Observed Spectral Density (cm-sec)
10^-2
10^-3
10^-4

Fig. 5
(cont.)

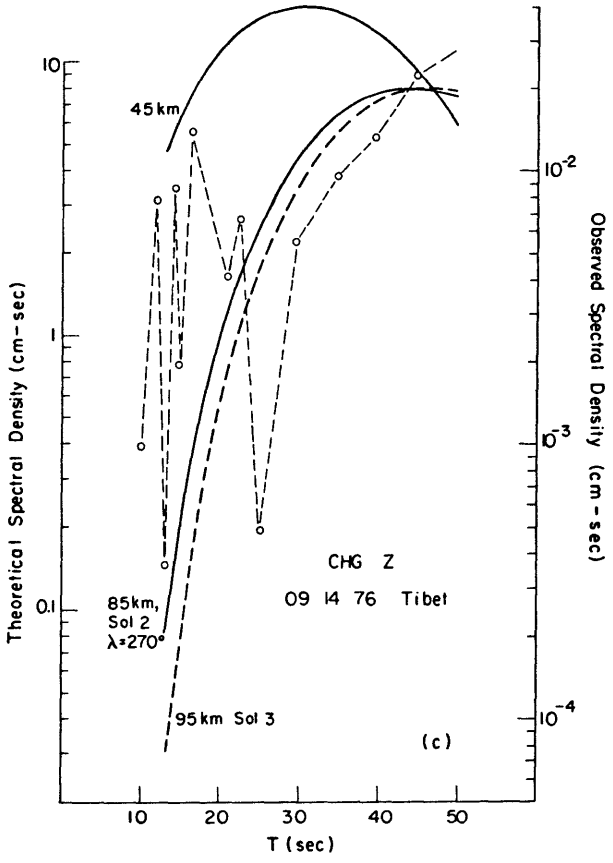
10
1
0.1
45km
85km,
Sol 2
λ=270°
95km Sol 3
CHG Z
09 14 76 Tibet
(c)
10
20
30
40
50
T (sec)
Theoretical Spectral Density (cm-sec)
Observed Spectral Density (cm-sec)
10-2
10-3
10-4

Fig. 5
(cont.)

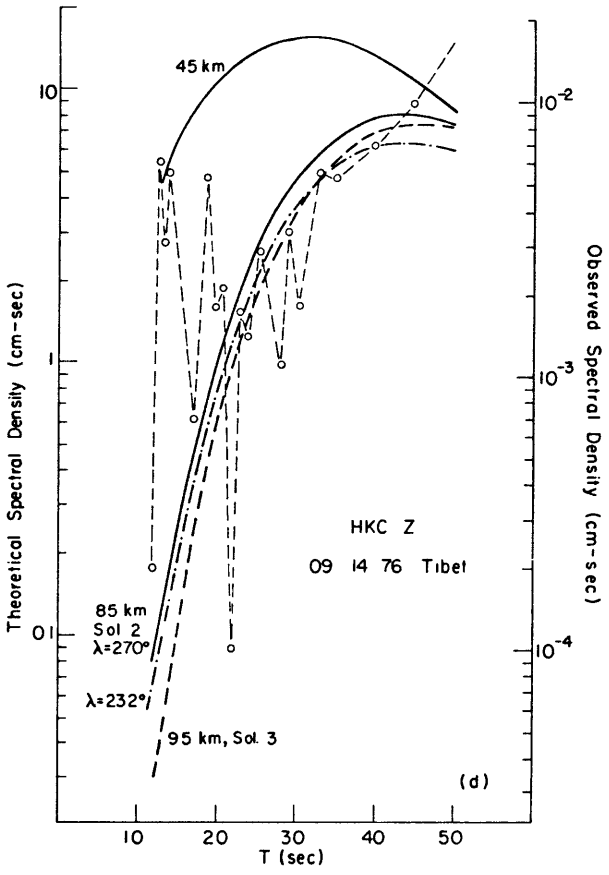
45 km
10
1
0.1
10⁻²
10⁻³
10⁻⁴
Theoretical Spectral Density (cm-sec)
Observed Spectral Density (cm-sec)
HKC Z
09 14 76 Tibet
85 km
Sol 2
λ=270°
λ=232°
95 km, Sol 3
(d)
10
20
30
40
50
T (sec)

Fig. 5
(cont.)

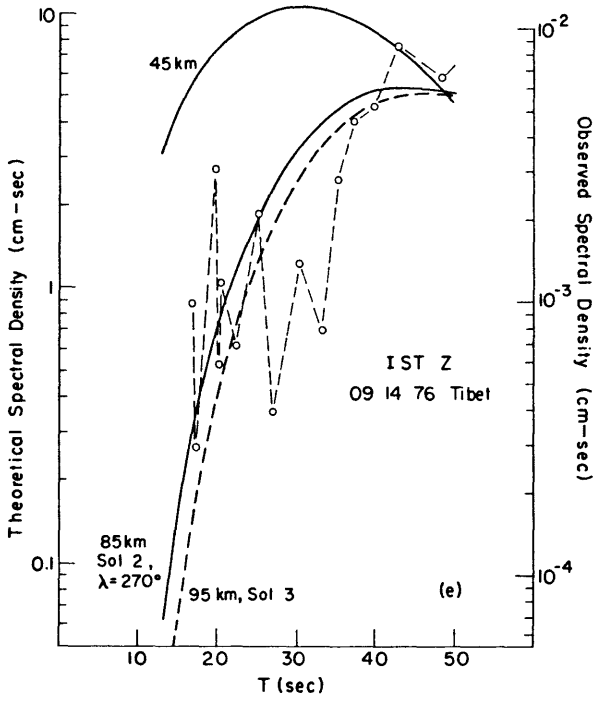
10
1
0.1
45 km
85km
Sol 2,
λ= 270°
95 km, Sol 3
(e)
IST Z
09 14 76 Tibet
10
20
30
40
50
T (sec)
Theoretical Spectral Density (cm-sec)
Observed Spectral Density (cm-sec)
10-2
10-3
10-4

Fig. 5
(cont.)

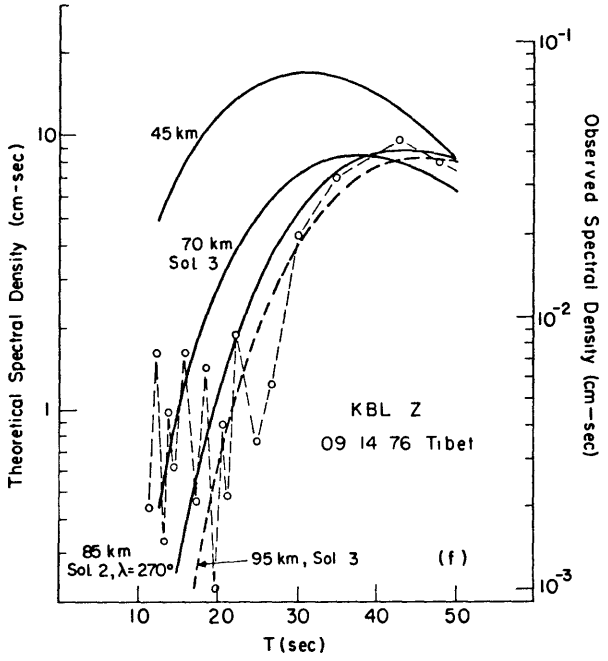
Theoretical Spectral Density (cm-sec)
Observed Spectral Density (cm-sec)
T(sec)
45 km
70 km
Sol 3
85 km
Sol 2, λ=270°
95 km, Sol 3
KBL Z
09 14 76 Tibet
(f)
10
1
10^-1
10^-2
10^-3
10
20
30
40
50

Fig. 5
(cont.)

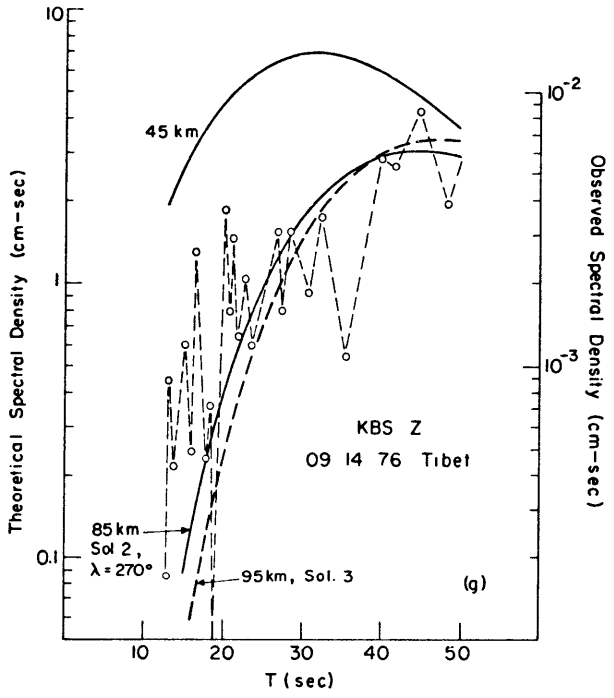
10
1
0.1
45 km
85 km
Sol 2,
λ = 270°
95km, Sol. 3
KBS Z
09 14 76 Tibet
(g)
10
20
30
40
50
T (sec)
Theoretical Spectral Density (cm-sec)
Observed Spectral Density (cm-sec)
10-2
10-3

Fig. 5
(cont.)

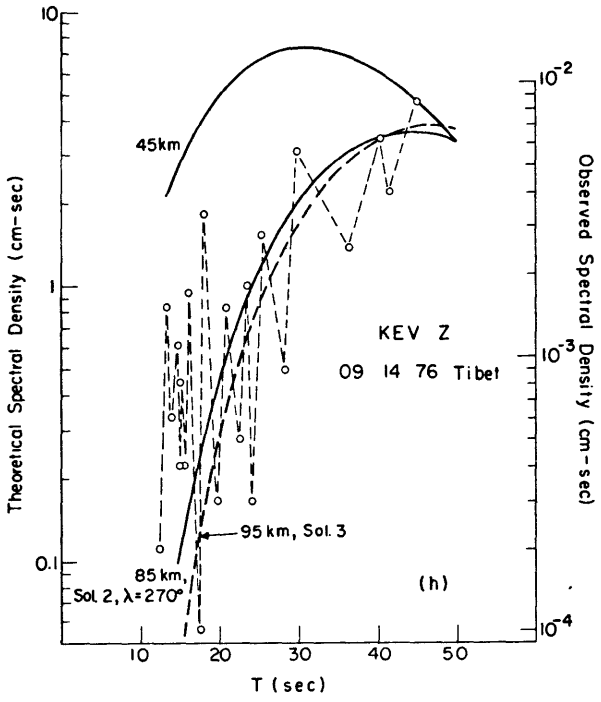
10
1
0.1
Theoretical Spectral Density (cm-sec)
45km
KEV Z
09 14 76 Tibet
95 km, Sol. 3
85 km,
Sol. 2, λ=270°
(h)
10
20
30
40
50
T (sec)
10^{-2}
10^{-3}
10^{-4}
Observed Spectral Density (cm-sec)

Fig. 5
(cont.)

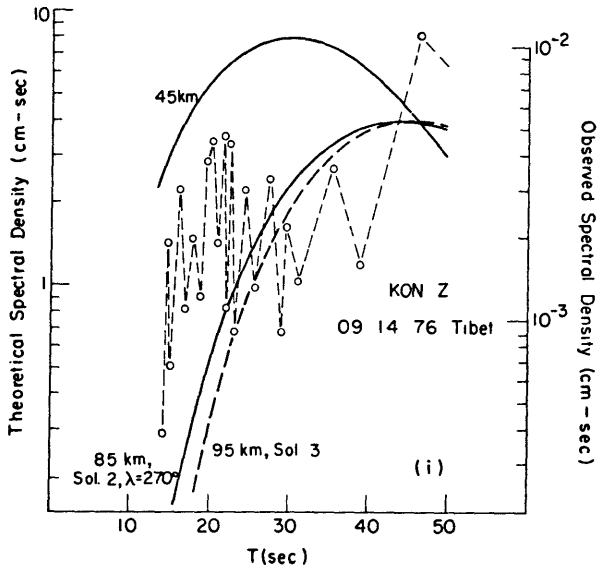
10
1
Theoretical Spectral Density (cm-sec)
45km
85 km,
Sol. 2, λ=270°
95 km, Sol 3
KON Z
09 14 76 Tibet
(i)
10
20
30
40
50
T(sec)
10^-2
10^-3
Observed Spectral Density (cm-sec)

Fig. 5
(cont.)

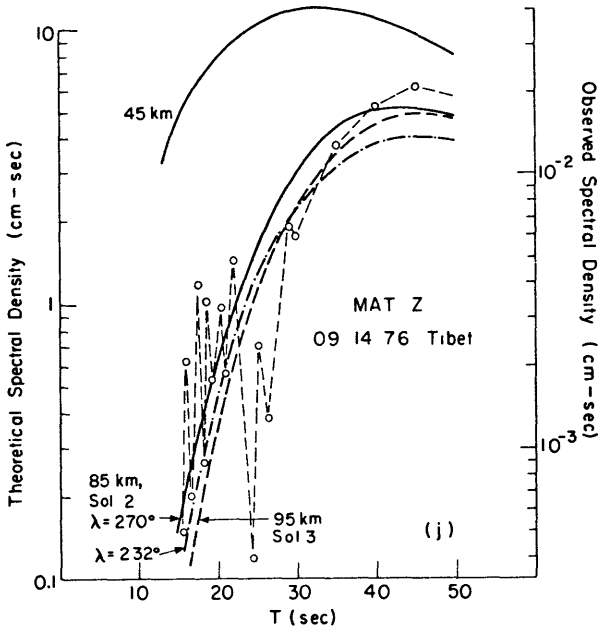
10
1
0.1
45 km
MAT Z
09 14 76 Tibet
85 km,
Sol 2
λ = 270°
λ = 232°
95 km
Sol 3
(j)
10
20
30
40
50
T (sec)
Theoretical Spectral Density (cm - sec)
Observed Spectral Density (cm - sec)
10^{-2}
10^{-3}

Fig. 5
(cont.)

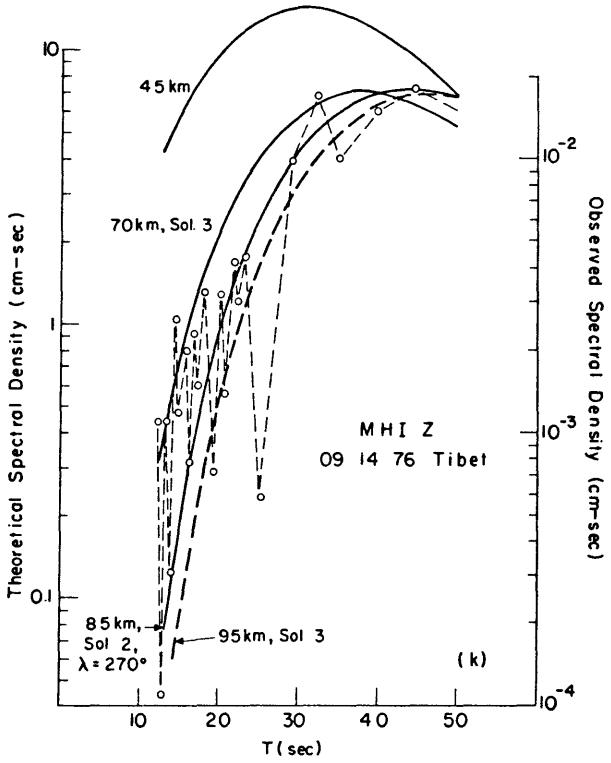
10
1
0.1
45 km
70km, Sol. 3
MHI Z
09 14 76 Tibet
85 km,
Sol 2,
λ = 270°
95km, Sol 3
(k)
10
20
30
40
50
T (sec)
Theoretical Spectral Density (cm-sec)
Observed Spectral Density (cm-sec)
10^{-2}
10^{-3}
10^{-4}

Fig. 5
(cont.)

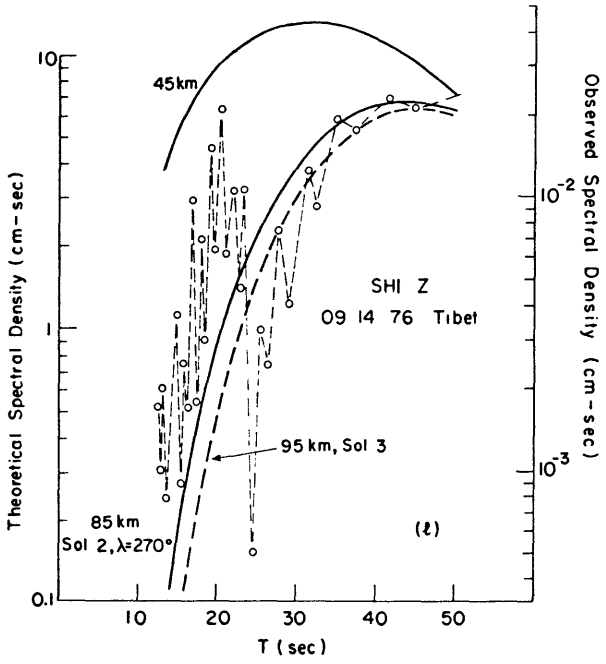
10
1
0.1
45km
95 km, Sol 3
SHI Z
09 14 76 Tibet
85 km
Sol 2, λ=270°
(ℓ)
10
20
30
40
50
T (sec)
Theoretical Spectral Density (cm-sec)
Observed Spectral Density (cm-sec)
10^{-2}
10^{-3}

Fig. 5
(cont.)

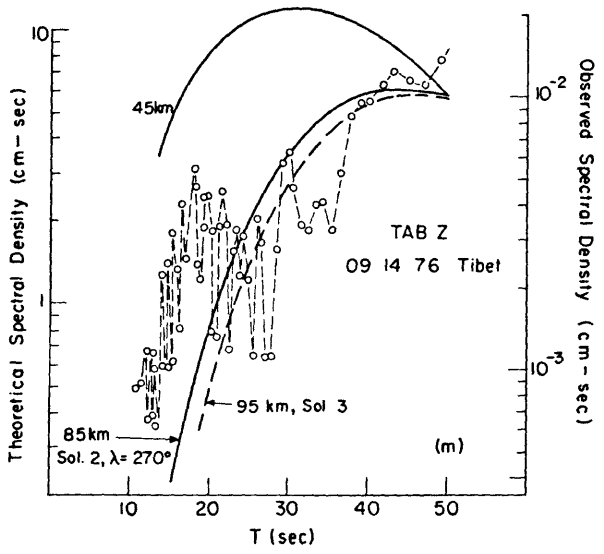
Theoretical Spectral Density (cm - sec)
Observed Spectral Density (cm - sec)
10
1
10^{-2}
10^{-3}
45km
TAB Z
09 14 76 Tibet
95 km, Sol 3
85km
Sol. 2, λ= 270°
(m)
10
20
30
40
50
T (sec)

Fig. 5
(cont.)

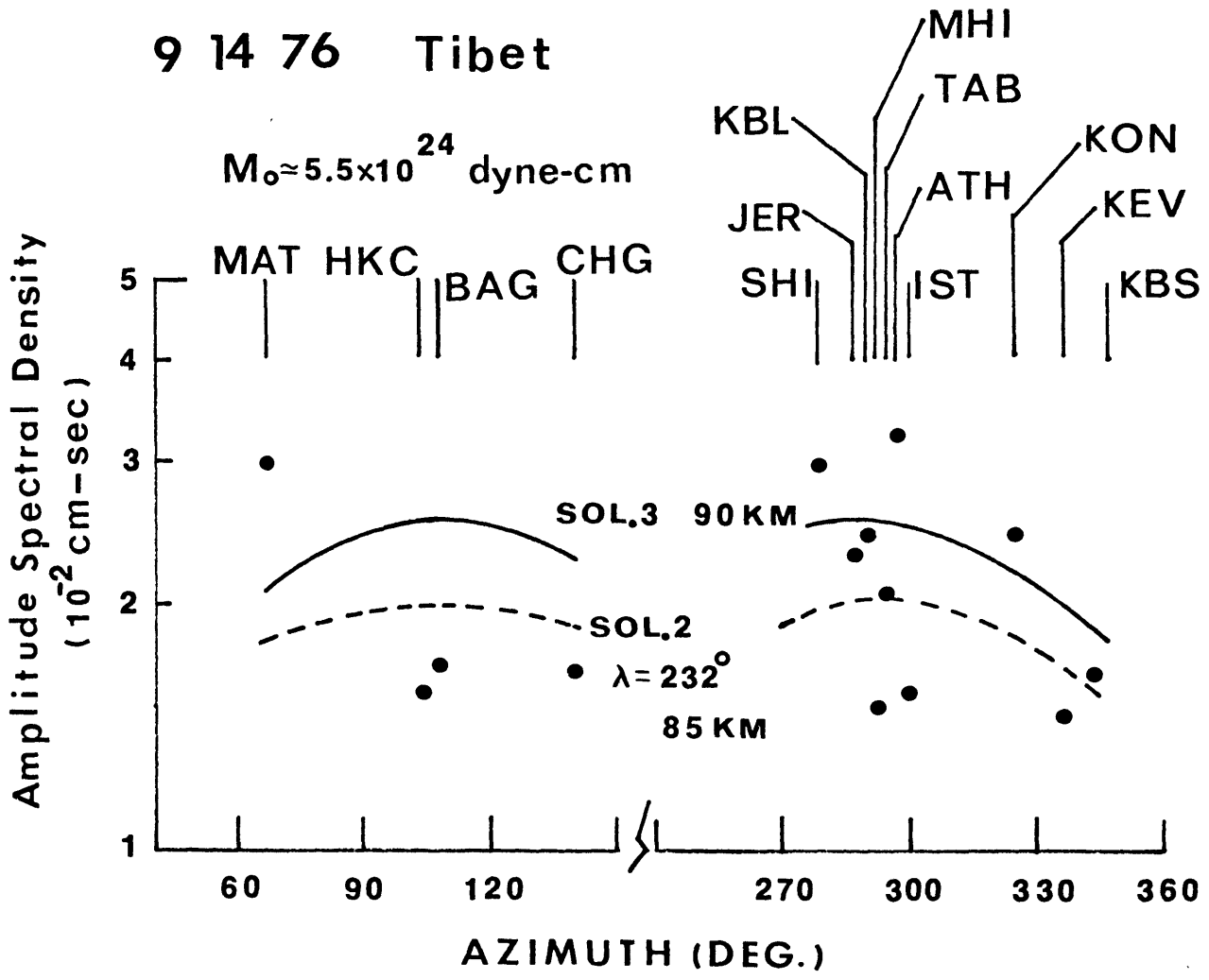
9 14 76 Tibet
$M_o \simeq 5.5 \times 10^{24}$ dyne-cm
MHI
TAB
KBL
KON
ATH
JER
KEV
MAT HKC
BAG
CHG
SHI
IST
KBS
Amplitude Spectral Density
(10^{-2} cm-sec)
SOL.3 90KM
SOL.2
λ = 232°
85 KM
1
2
3
4
5
60
90
120
270
300
330
360
AZIMUTH (DEG.)

Fig. 6

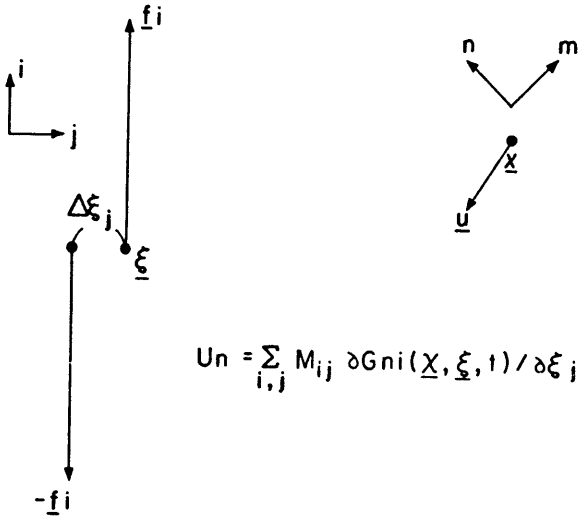

Fig. 7

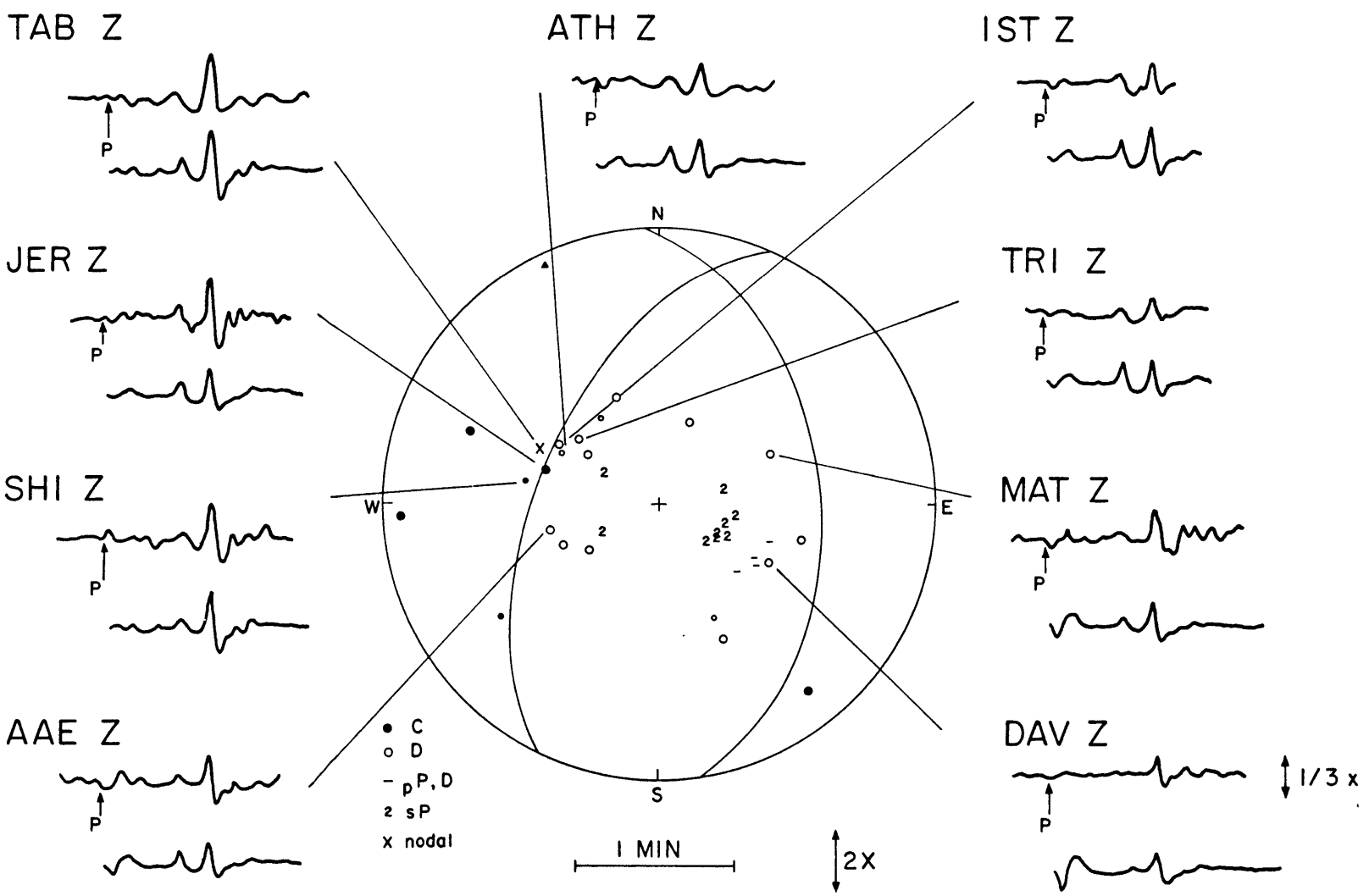

September 14, 1976 Tibet 29.81° N, 89.57°E 90 km

Fig. 8

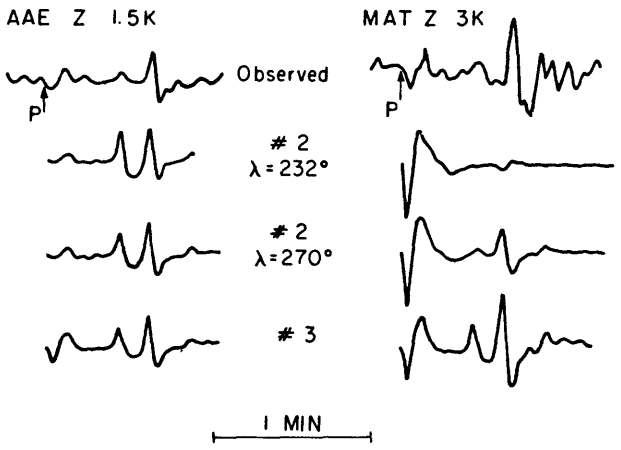
AAE Z 1.5K
MAT Z 3K
Observed
P
P
2
λ=232°
2
λ=270°
3
1 MIN
Sept. 14, 1976
29.81°N 89.57°E 90 km
Tibet

Fig. 9

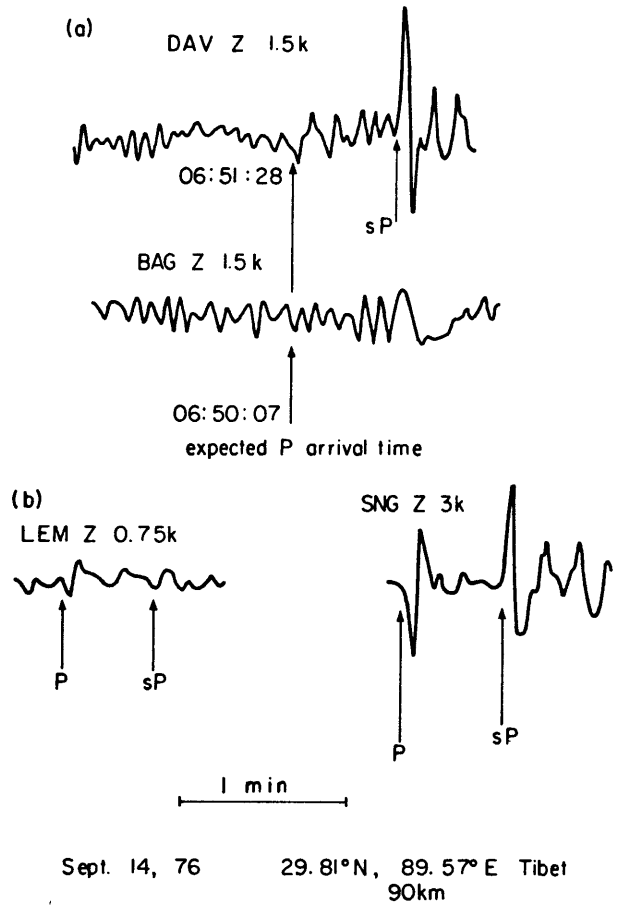
(a)
DAV Z 1.5k
06:51:28
sP
BAG Z 1.5k
06:50:07
expected P arrival time
(b)
LEM Z 0.75k
P
sP
SNG Z 3k
P
sP
1 min
Sept. 14, 76
29.81°N, 89.57°E Tibet
90km

Fig. 10

BIOGRAPHIC NOTE

The author was born on November 28, 1951 to Mr. S.K. Chen and Mrs. P.Y.C. Chen in Taipei, Taiwan, R.O.C. He attended public schools in Taipei from 1958 to 1970 and received B.S. degree in geology from National Taiwan University in June, 1974.

The Massachusetts Institute of Technology is the only institute the author attended outside Taiwan since his arrival in the U.S. in late August, 1974. After leaving an earthquake country to study geophysics in quiet New England, the list of author's publication includes the following:

Chen, W.P. and P. Molnar, Short-period Rayleigh-wave dispersion across the Tibetan Plateau, Bull. Seismol. Soc. Amer., 65, 1051-1057, 1975.

Molnar, P., W.P. Chen, T.J. Fitch, P. Tapponnier, W.E.K. Warsi, and F.T. Wu, Structure and tectonics of the Himalaya: A brief summary of relevant geophysical observations, in Himalaya: Sciences de la Terre, pp. 269-294, Centre National de la Recherche Scientifique, Paris, 1977.

Chen, W.P. and P. Molnar, Seismic moments of major earthquakes and the average rate of slip in central Asia, J. Geophys. Res., 82, 2945-2969, 1977.

Molnar, P. and W.P. Chen, Evidence of large Cainozoic crustal shortening of Asia, Nature, 273, 218-220, 1978.

Chen, W.P. and P. Molnar, Constraints on the seismic wave velocity structure beneath the Tibetan Plateau and their tectonic implications, Submitted to J. Geophys. Res., 1979.

Chen, W.P., T.J. Fitch, J.L. Nabelek, and P. Molnar, An intermediate depth earthquake beneath Tibet: source characteristics of the event of September 14, 1976, Submitted to J. Geophys. Res., 1979.

Chen, C.Y., W.P. Chen, and P. Molnar, The uppermost mantle P wave velocities beneath Turkey and Iran, Submitted to Geophys. Res. Lett., 1979.

Appendix A:

We solve analytically the one-dimensional time-dependent heat conduction problem with a constant heat flux at one end (z=h) and zero temperature at the other (z=o). The particular cases that we consider are appropriate for a layer with heat sources in it and initially at steady state. Then the layer is thickened instantaneously so that both the distribution and the amount of heat sources changes but with the same flux at the bottom.
We solve for the temperature as a function of depth and time in the thickened layer.

We start with the steady state solution of the one-dimensional heat conduction equation $\nabla^2 T = -A(z)/k$ (A1)
subject to the boundary conditions: $T(0) = 0$, $-k \partial T/\partial z \big|_{z=h} = -Q_h$
where T is the temperature, A(z) is the heat producing rate between depth (z, downward positive) 0 and h, Q_h is a constant heat flux at depth h and k is the thermal conductivity.

(1) If $A(z) = 0$, then $T = Q_h z/k$ (A2)

(2) If $A(z) = \begin{cases} A_0, & 0 \le z \le D \\ 0, & D < z \le h \end{cases}$,

then $T = (-A_0/2k) z^2 + (Q_h + A_0 D) z/k$, $0 \le z \le D$
$T = Q_h z/k + A_0 D^2/2k$, $D < z \le h$ (A3)

(3) If $A(z) = A_0 e^{-z/D}$,

then $T = -A_0 D^2/k \cdot \exp(-z/D) + [Q_h - A_0 D \cdot \exp(-h/D)]\, z/k + A_0 D^2/k$ (A4)

Conditions (2) and (3) satisfy the linear relationship between surface heat production rate (A_0) and surface heat flow (Q_s)

$$Q_s = Q_o + D\, A_o \qquad (A5)$$

where Q_o is the reduced heat flow and D is a constant with units of depth. Letting $Q_h = Q_o$ corresponds to an upper bound of the heat flux from the mantle estimated from equation (A5). For an exponential dependence of A(Z), for which equation (A5) remains valid after differential erosion, D/h must be much less than one [Lachenbruch, 1970].

Now consider the solution to the one-dimensional time-dependent heat conduction equation:

$$\nabla^2 T - 1/\kappa \; \partial T/\partial t = - A(z)/k \qquad (A6)$$

where κ is the thermal diffusivity, $\kappa = k/\rho C_p$, ρ is the density, and C_p is the heat capacity at constant pressure. The boundary conditions are

$$T(0, t) = 0$$

and $$-k\, \partial T/\partial z \Big|_{z=h'} = - Q_h \quad \text{with} \quad h' = a h \quad \text{and} \quad a > 1.$$

The initial condition $T^\circ = T(z,0)$, can be obtained by substituting z/a for z in equations A2 to A4. The steady state solution $T^\infty(z) = u(z)$, can also be obtained from equations A2 to A4 with the appropriate constants Ao and D. Thus equation (A6) can be easily solved by finding the solutions of the form $T(z,t) = u(z) + w(z,t)$. The equation for the transient part, $w(z,t)$, is

$$\nabla^2 w - \frac{1}{k}\frac{\partial w}{\partial t} = -A(z)/k$$

with boundary conditions

$$w(0,t) = 0 \quad \text{and} \quad -k\,\partial w/\partial z\Big|_{z=h'} = 0$$

the initial condition is $w(z,o) = T(z,o) - u(z)$. Note that $u(z)$ satisfies $d^2u/dz^2 = 0$ with $u(0) = 0$ and $-k\,\partial u/\partial z\Big|_{z=h'} = -Q_h$.

$w(z,t)$ will have the form $\sum_{n=0}^{\infty} A_n \sin(pz)\exp(-p^2 k t)$ and from boundary condition of zero flux at h', $p = (2n+1/2)\pi/h'$. We have

$$w(z,t) = \sum_{n=0}^{\infty} A_n \sin\left[(2n+1/2)\pi z/h'\right] \exp\left[-k t (2n+1)^2 \pi^2/4h'^2\right] \qquad (A7)$$

where

$$A_n = \frac{2}{h'}\int_0^{h'} w(z,0)\sin\left[(2n+1/2)\pi z/h'\right] dz \qquad (A8)$$

From equations (A2) to (A4) and (A8), it is clear that the solution can be written as $T(z,t) = T_m(z,t) + T_R(z,t)$ where $T_m(z,t)$ is proportional to Q_h and $T_R(z,t)$ is

proportional to Ao. The following three cases consider different possible distributions of heat producing elements for a crust thickened by horizontal shortening. In each case the amount of thickening is given by the factor a.

(a) $A(z) = A_0 \quad , \quad 0 \le z \le D$

$= 0 \quad , \quad D < z \le h$

Initial conditions: from (A3) with z replaced by z/a

$$T^0(z) = -A_0 z^2/2k a^2 + (Q_h + A_0 D) z/k a \,, \quad 0 \le z \le aD$$
$$= Q_h z/k a + A_0 D^2/2k \quad , \quad aD < z \le h' \qquad (A9)$$

Steady state: from (A 3) with D = aD

$$T^\infty(z) = -A_0 z^2/2k + (Q_h + A_0 aD) z/k \quad , \quad 0 \le z \le aD$$
$$= Q_h z/k + A_0 a^2 D^2/2k \quad , \quad aD < z \le h' \qquad (A10)$$

Thus, $T(z,t) = w(z,t) + T^\infty(z)$ with

$$A_n = 2/h' \sum_i D_i I_i \qquad (A11)$$

and

$$D_1 = -A_0/2k \cdot (1/a^2 - 1)$$
$$D_2 = Q_h/k \cdot (1/a - 1)$$
$$D_3 = A_0 D/k \cdot (1/a - a)$$
$$D_4 = A_0 D^2/2k \cdot (1 - a^2)$$

$$I_1 = \frac{1}{\rho^3}\left\{\left[2-(\rho D')^2\right]\cos(\rho D') + 2\rho D'\sin(\rho D') - 2\right\}$$

$$I_2 = (-1)^n/\rho^2$$

$$I_3 = \frac{1}{\rho^2}\left[\sin(\rho D') - \rho D'\cos(\rho D')\right]$$

$$I_4 = \frac{1}{\rho}\cos(\rho D')$$

where $D' = aD$ (A 12)

(b) $A(z) = A_o e^{-z/D}$, assuming that the migration of heat producing elements towards z = o is very slow compared with heat conduction (i.e., A_o is the same before and after crustal thickening).

Initial condition: from (A4), with z replaced by z/a

$$T^o(z) = -A_o D^2/k \cdot \exp(-z/Da) + \left[Q_h - A_o D\cdot\exp(-h/D)\right] z/k\,a + A_o D^2/k \quad (A13)$$

Steady state: from (A4) with D = D' = aD

$$T^\infty(z) = -A_o D'/k \cdot \exp(-z/D') + \left[Q_h - A_o D'\cdot\exp(-h/D')\right] z/k + A_o D'^2/k \quad (A14)$$

Thus, as in (A11)

$$D_1 = -A_o/k \cdot D^2(1-a^2)$$

$$D_2 = -A_o D/k \cdot \exp(-h/D)\cdot(1/a - a)$$

$$D_3 = Q_h/k \cdot (1/a - 1)$$

$$D_4 = -D_1$$

$$I_1 = \frac{1}{\left(\frac{1}{D'^2} + p^2\right)} \cdot \left[\frac{(-1)^{n+1}}{D'} \cdot \exp\left(-\frac{h}{D}\right) + p\right]$$

$$I_2 = (-1)^n / p^2$$

$$I_3 = I_2$$

$$I_4 = 1/p \qquad (A15)$$

(c) $A(z) = A_o e^{-z/D}$, and the migration of heat producing elements is very fast compared with heat conduction (i.e., D is the same before and after crustal thickening).

Initial conditions are the same as (A13)

Steady state: from (A4) with $A_o = aA_o$

$$T^{\infty}(z) = -aA_o D^2/k \cdot \exp\left(-\frac{z}{D}\right) + \left[Q_h - aA_o D \cdot \exp\left(-\frac{h'}{D}\right)\right] z/k + aA_o D^2/k \qquad (A16)$$

Thus, as in (A11)

$$D_1 = -A_o D^2/k$$

$$D_2 = -aD_1$$

$$D_3 = Q_h/k \cdot (1/a - 1)$$

$$D_4 = -A_o D/k \cdot \left[\frac{1}{a} \cdot \exp\left(-\frac{h}{D}\right) - a \exp\left(-\frac{h'}{D}\right)\right]$$

$$D_5 = -D_1 \cdot (1 - a)$$

$$I_1 = 1/(1/D'^2 + p^2) \cdot [(-1)^{n+1}/D' \cdot \exp(-h/D) + p]$$

$$I_2 = 1/(1/D^2 + p^2)\ [(-1)^{n+1}/D \cdot \exp(-h'/D) + p]$$

$$I_3 = (-1)^n/p^2$$

$$I_4 = I_3$$

$$I_5 = 1/p \qquad (A17)$$

The solution $T_m(z,t)$ for $A_o = 0$ (no heat production) is also found in Carslaw and Jaeger [1959, p. 113] with zero temperature as the initial condition and a steady state of $T = Q_h\ z/k$:

$$T_m'(z,t) = Q_h z/k - 2Q_h/h'k \sum_{n=0}^{\infty} (-1)^n/p^2 \cdot \sin(pz) \cdot \exp(-p^2 \kappa t) \qquad (A18)$$

Thus $T_m = T_m' + T_m^\circ = T_m' + (1/a)\, Q_h z/k$, (A19)

We plotted T_m' as function of time (Fig. A1) for three different depths z = h', 0.786h' and h'/2 (70 km, 55 km and 35 km for h' = 70 km). Time is given in million years for the cases with h' = 70 km and $\kappa = 0.01$ cm^2/sec. These can be scaled easily for different values of h' and κ by h'^2/κ. Since T_m° and T_m^∞ are readily calculated by (A2). Any T_m' can be found by using Fig.A1. For instance, at z = h', with h' = 70 km, a = 2, $k = 6 \times 10^{-3}$ cal/(cm°-C-sec) and $Q_h = 0.94$ HFU (μcal/cm^{2}sec), $T_m^\circ = 550$°C and $T_m'^\infty = 550$°C.

After 20 m.y., $T_m' = 550 \times 0.4$ (Fig. A1) so that $T_m = 220 + T_m° = 770°C$.

For T_R, we calculated the values at three different depths of z: 70 km, 55 km, and 35 km (Fig. A2, A3 and A4). We have used a = 2 and h = 35 km to approximate the situation in Tibet. The time scale is the same as in Fig. A1 and T_R is normalized by the steady state values, T_R^{∞}. Both $T_R°$ and T_R^{∞} and their asymptotes for $D/h \rightarrow 0$ are shown in Fig. A5 for the three cases considered above, at the three given depths. Ao is normalized to 1 HGU (10^{-13}cal/cm^{3}sec) for case (a) and 10 HGU for (b) and (c). With these values any T_R for a given D and time can be found. For example, at 70 km depth and 20 m.y. for D = 20 km and A_o = 1 HGU, with uniform distribution of heat producing elements in the crust (a), $T_R = 133.3 \times 0.36 = 48°C$ (Fig. A5a). Therefore $T = T_m + T_R = 818°C$.

Appendix A Figure Captions

Fig. A1 (a) Temperature change T_m' at z = h' due to mantle heat flux, Q_h, normalized by the steady state value $T'm^{\infty}$, as a function of time. See equations (A18) and (A19). Time scale is in m.y., if h' = 70 km, and κ = 0.01 cm^2/s, but can be scaled by h'^2/κ. (b) Temperature change as in (a) but at depths z = 0.786 h' and z = h'/2.

Fig. A2 (a) Temperature change due to radioactivity (T_R) at z = h', normalized by its steady state value T_R^{∞}, as a function of time, for different values of D. The distribution of radioactive elements are uniform with a thickness of D from the surface (case (a), Appendix A). See equations (A11) and (A12).

Fig. A2 (b) Temperature change due to radioactivity (T_R) at z = h', normalized by the steady state value T_R^{∞}, as a function of time (as in Fig. A1) for different values of D. The distribution of radioactive elements decays exponentially with depth. Surface heat production rate is kept constant during crustal thickening (case (b), Appendix A). See equations (A11) and (A15).

Fig. A2 (c) Temperature change due to radioactivity (T_R) at z = h', normalized by the steady state value T_R^{∞}, as a function of time (as in Fig. A1) for different values of D. The distribution of radioactive elements decays exponentially with depth, but D is kept constant during crustal thickening (case (c), Appendix A). See equations (A11) and (A17).

Fig. A3 (a) T_R as a function of time at z = 55 km, for h' = 70 km and for different values of D. See Fig. A2 (a) for details.

Fig. A3 (b) T_R as a function of time at z = 55 km, for h' = 70 km and for different values of D. See Fig. A2 (b) for details.

Fig. A3 (c) T_R as a function of time at z = 55 km for h' = 70 km and for different values of D. See Fig. A2 (c) for details.

Fig. A4 (a) T_R as a function of time at z = 35 km, for h' = 70 km and for different values of D. See Fig. A2 (a) for details.

Fig. A4 (b) T_R as a function of time at z = 35 km, for h' = 70 km and for different values of D. See Fig. A2 (b) for details.

Fig. A4 (c) T_R as a function of time at z = 35 km, for h' = 70 km and for different values of D. See Fig. A2 (c) for details.

Fig. A5 (a) Contribution to steady state temperature due to radioactivity (T_R^{∞}) as a function of D at three different depths: 70 km, 55 km and 35 km. The distribution of radioactive elements are uniform with a thickness of D from the surface (case (a), Appendix A). See equations (A9) and (A10).

Fig. A5 (b) Steady state contribution to temperature change due to radioactivity (T_R^{∞}) as a function of D at three different depths = 70 km, 55 km, and 35 km. The distribution of radioactive elements decays exponentially with depth. Surface heat production rate is kept constant during crustal thickening (case b, Appendix A). See equations

(A13) and (A14).

Fig. A5 (c) Steady state contribution to temperature change due to radioactivity (T_R^{∞}) as a function of D at three different depths: 70 km, 55 km and 35 km. The distribution of radioactive elements decays exponentially with depth, but D is kept constant during crustal thickening (case (c), Appendix A). See equations (A13) and (A16).

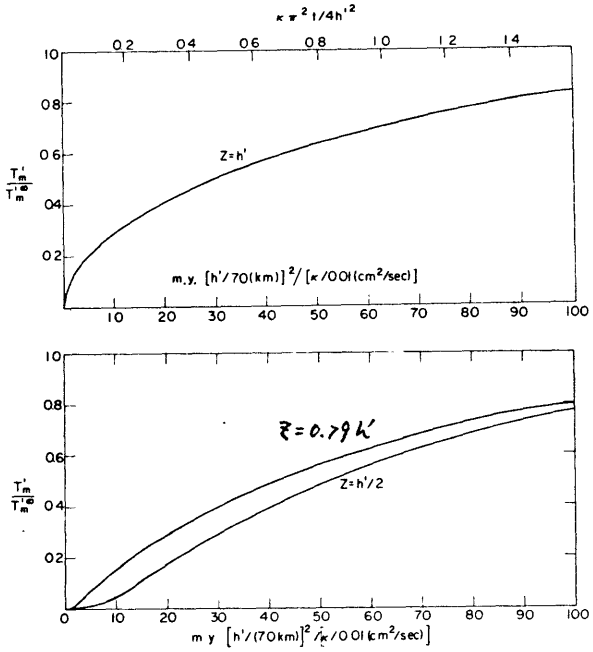
κπ²t/4h'²
0.2 0.4 0.6 0.8 1.0 1.2 1.4
Z=h'
m,y, [h'/70(km)]²/[κ/.001(cm²/sec)]
10 20 30 40 50 60 70 80 90 100
Z=0.79h'
Z=h'/2
m y [h'/(70km)]²/κ/.001(cm²/sec)]

(a)

(b)

Fig. A1

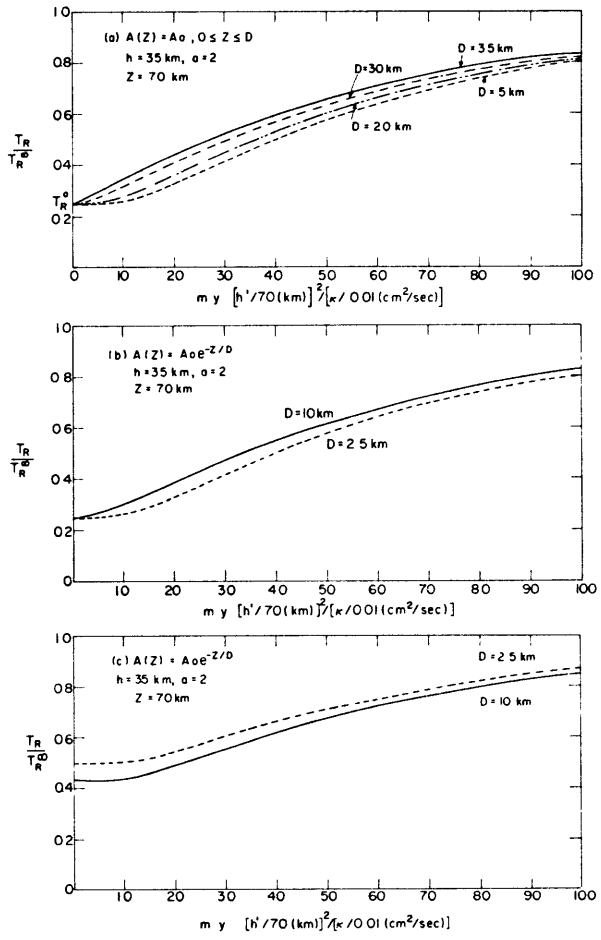
(a) A(Z) = Ao , 0 ≤ Z ≤ D
h = 35 km, a = 2
Z = 70 km
D = 35 km
D = 30 km
D = 5 km
D = 20 km
$\frac{T_R}{T_R^0}$
T_R^0
m y [h'/70(km)]²/[κ/.001(cm²/sec)]
(b) A(Z) = Aoe^{-Z/D}
h = 35 km, a = 2
Z = 70 km
D = 10 km
D = 2.5 km
(c) A(Z) = Aoe^{-Z/D}
h = 35 km, a = 2
Z = 70 km
D = 2.5 km
D = 10 km

Fig. A2

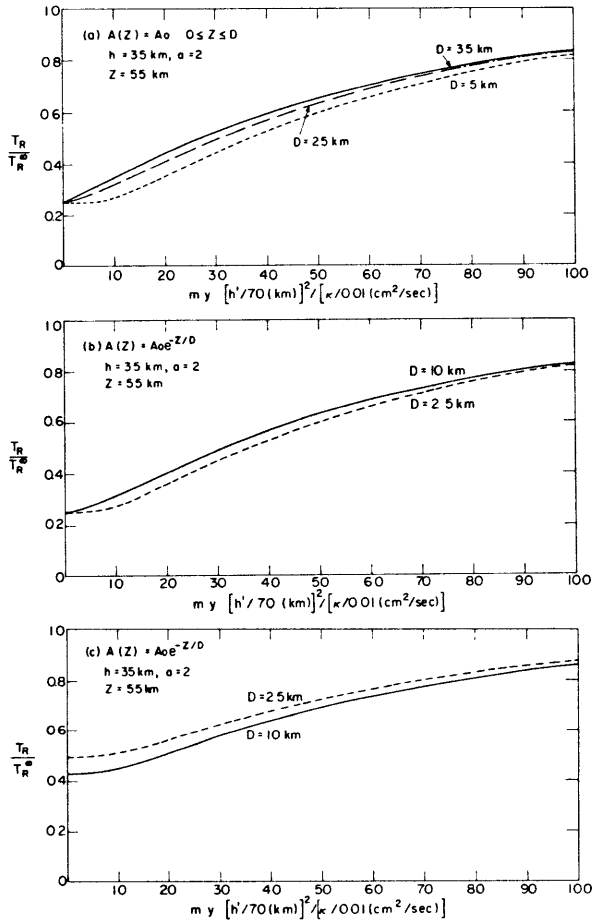
(a) A(Z) = Ao 0 ≤ Z ≤ D
h = 35 km, a = 2
Z = 55 km
D = 35 km
D = 5 km
D = 25 km
$\frac{T_R}{T_R^\infty}$
m y [h'/70 (km)]²/[κ/001 (cm²/sec)]
(b) A(Z) = Aoe^{-Z/D}
h = 35 km, a = 2
Z = 55 km
D = 10 km
D = 2 5 km
$\frac{T_R}{T_R^\infty}$
m y [h'/ 70 (km)]²/[κ/001 (cm²/sec)]
(c) A(Z) = Aoe^{-Z/D}
h = 35 km, a = 2
Z = 55 km
D = 2 5 km
D = 10 km
$\frac{T_R}{T_R^\infty}$
m y [h'/70 (km)]²/[κ/001 (cm²/sec)]

Fig. A3

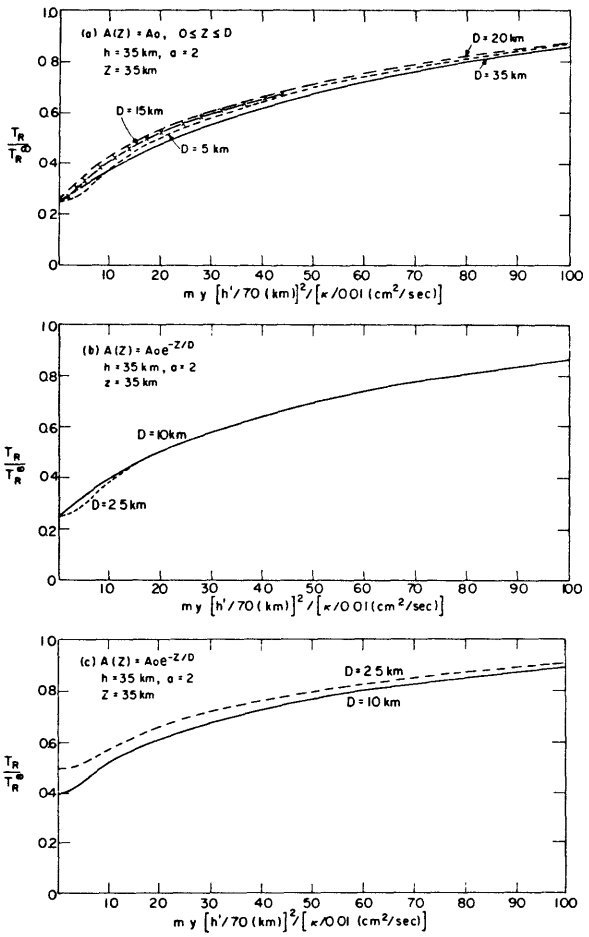
(a) A(Z) = Ao, 0 ≤ Z ≤ D
h = 35 km, a = 2
Z = 35 km
D = 20 km
D = 35 km
D = 15 km
D = 5 km
$\frac{T_R}{T_{R\infty}}$
m y [h'/70 (km)]²/[κ/.001 (cm²/sec)]
(b) A(Z) = Ae^{-Z/D}
h = 35 km, a = 2
z = 35 km
D = 10 km
D = 2.5 km
(c) A(Z) = Ae^{-Z/D}
h = 35 km, a = 2
Z = 35 km
D = 2.5 km
D = 10 km

Fig. A4

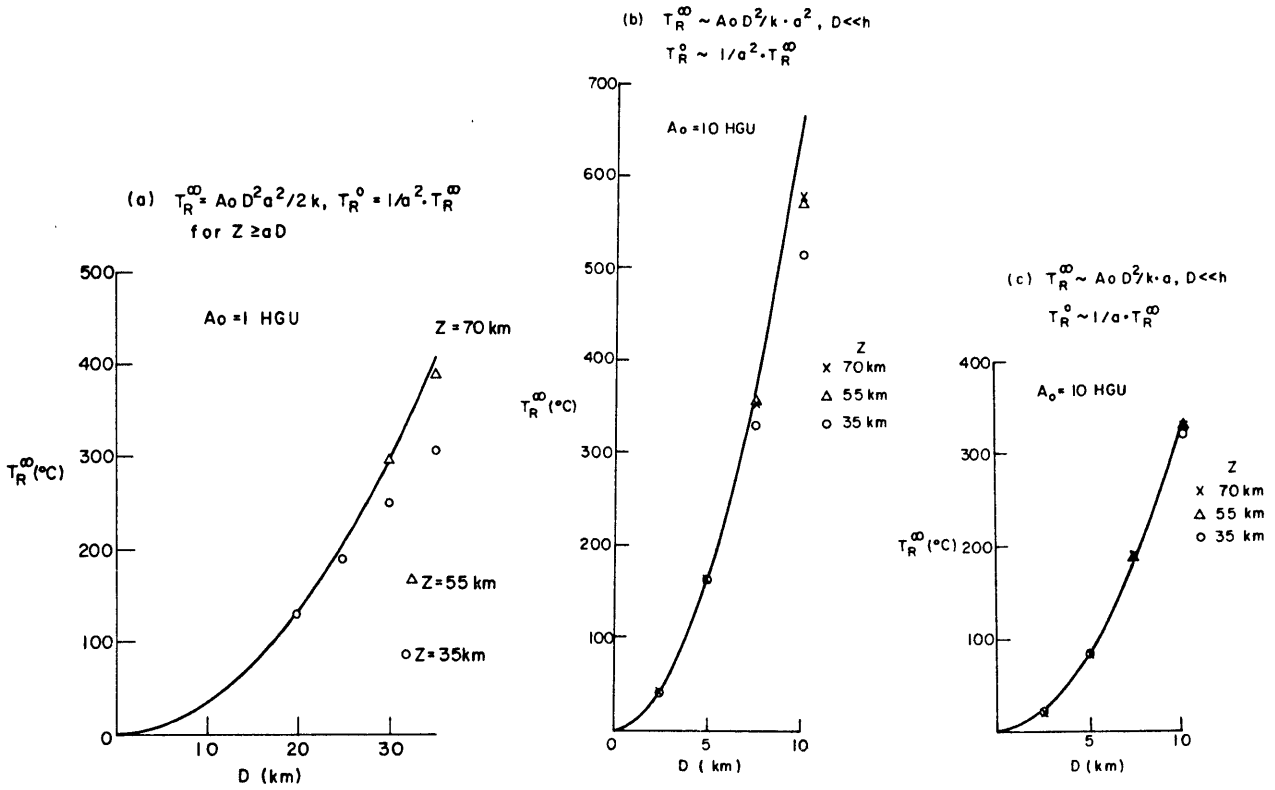
(a) $T_R^{\infty} = A_o D^2 a^2/2k$, $T_R^{o} = 1/a^2 \cdot T_R^{\infty}$
for $Z \geq aD$
A_o = 1 HGU
Z = 70 km
Δ Z = 55 km
o Z = 35 km
T_R^{∞} (°C)
D (km)
(b) $T_R^{\infty} \sim A_o D^2/k \cdot a^2$, D<<h
$T_R^{o} \sim 1/a^2 \cdot T_R^{\infty}$
A_o = 10 HGU
Z
x 70 km
Δ 55 km
o 35 km
T_R^{∞} (°C)
D (km)
(c) $T_R^{\infty} \sim A_o D^2/k \cdot a$, D<<h
$T_R^{o} \sim 1/a \cdot T_R^{\infty}$
A_o = 10 HGU
Z
x 70 km
Δ 55 km
o 35 km
T_R^{∞} (°C)
D (km)

Fig. A5

APPENDIX B

This section describes the contribution of the co-authors in the co-authored papers which appear in Chapter II, III and IV.

Three quarters of the old seismograms used in Chapter II. were collected by P. Molnar and he digitized several of them. He also wrote a prototype of the computer program for analyzing these old seismograms. I collected and digitized the rest of the seismograms and revised the computer program into its present form. I am also responsible for the processing of the seismograms, calculating the seismic moment tensors and the average strain tensor, relocating the aftershocks, and reading the P-pP delays.

Most of the seismograms used in the surface wave and P_L phase studies in Chapter III are also collected and digitized by P. Molnar. I processed all the seismograms and calculated the observed and theoretical dispersion curves. I also generated all the synthetic seismograms and wrote programs for calculating the refraction profiles and the numerical values of the heat conduction problem. P. Molnar checked some of my analytical solutions to the heat conduction problem and he also pointed out that equation A18 can be found in Carslaw and Jaeger's book.

In Chapter IV, the original version of the computer program for inverting the body wave amplitude data and synthesizing P wave signals are due to T.J. Fitch and J.L. Nabelek, respectively, while Peter Molnar determined most

of the P wave first motion polarities. The collection, digitizing and processing of the seismograms, generation of the synthetic seismograms, and the interpretation of the results are the author's responsibility except that P. Molnar pointed out the Hawaiian earthquakes and the estimated temperatures for that source region using a cooling plate model.